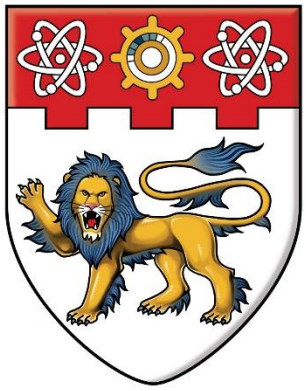

NANYANG TECHNOLOGICAL UNIVERSITY

MOLECULAR CHARACTERIZATION OF CELLULAR STRESS RESPONSES DURING CORONAVIRUS INFECTION

FUNG TO SING

SCHOOL OF BIOLOGICAL SCIENCES

2 0 1 5

MOLECULAR CHARACTERIZATION OF CELLULAR STRESS RESPONSES DURING CORONAVIRUS INFECTION

FUNG TO SING

School of Biological Sciences

A thesis submitted to the Nanyang Technological University in partial fulfillment of the requirement for the degree of Doctor of Philosophy

2015

Acknowledgements

I would like to express my utmost gratitude to my supervisor, Associate Professor Liu Ding Xiang, for giving me the opportunity to undertake this project and providing me with the greatest guidance and continuous support. The four years of study in Dr Liu's lab helps me to regain my confidence in biological research after a major setback in Hong Kong. The scientific attitude and logical thinking I learned in this lab will stay with me in the future career; and all the experiences will become unforgettable memories in my life.

I would like to thank Professor James Tam and Assistant Professor Tang Kai for their helpful feedback and encouragement during the thesis advisory committee meetings.

I would also like to extend my appreciation to the wonderful senior fellows from Dr Liu's and Dr Tam's laboratories, especially Dr Huang Mei, Dr Fang Shuo Guo, Dr Zhong Yan Xin, Dr Chen Guang, Dr Tan Yong Wah and Dr Nguyen Quoc Thuc Phuong, for their professional advice and kind assistance. I would also like to show my thankfulness to all the friends and fellow students in School of Biological Sciences (SBS) – Jong Fu, Kelvin, Ashley, Heidi, Zheng Jie, Emma and Liang Xiao, for their friendship and encouragement.

I would like to thank Nanyang Technological University (NTU) for the research scholarship during the PhD candidature. I would also like to thank SBS for supporting me to present my data in the XIIIth International Nidovirus Symposium.

This work would not have been possible without the support from my family, who are always listening to me, encouraging me and inspiring me.

Table of Contents

CHAPTER 4. ACTIVATION OF JNK PATHWAY DURING IBV INFECTION AND ITS INVOLVEMENT IN REGULATING IBV-INDUCED APOPTOSIS AND INNATE IMMUNE RESPONSE

CHAPTER 5. CONCLUSIONS AND FUTURE DIRECTIONS

ABBREVIATIONS

BCoV	Bovine coronavirus
CHIKV	Chikungunya virus
HCoV-229E	Human coronavirus 229E
HCoV-HKU1	Human coronavirus HKU1
HCoV-NL63	Human coronavirus NL63
HCoV-OC43	Human coronavirus OC43
HIV-1	Human immunodeficiency virus type I
IBV	Infectious bronchitis virus
MERS-CoV	Middle East respiratory syndrome coronavirus
MHV	Mouse hepatitis virus
PEDV	Porcine epidemic diarrhea virus
SARS-CoV	Severe acute respiratory syndrome coronavirus
TGEV	Transmissible gastroenteritis coronavirus

ACE2	Angiotensin-converting enzyme 2
Akt	RAC-alpha serine/threonine-protein kinase
AP-1	Activator protein 1
APAF1	Apoptotic protease activating factor 1
ASK1	Apoptosis signal-regulating kinase 1
ATF4	Activating transcription factor 4
ATF6	Activating transcription factor 6
ATG	Autophagy-related gene
Bad	Bcl2-associated death promoter
Bak	Bcl2 homologous antagonist killer
Bax	Bcl2-associated X protein
Bcl2	B-cell lymphoma 2
Bcl-X_L	B-cell lymphoma-extra-large
BECN1	Coiled-coil, myosin-like Bcl2 interacting protein 1
Bid	BH3-interacting domain death agonist
Bim	Bcl2-interacting mediator of cell death
Bmf	Bcl2 modifying factor

bZIP	Basic-region leucine zipper
C/EBPβ	CCAAT/enhancer binding protein beta
CHOP	C/EBP homologous protein
CLR	C-type lectin receptor
COX-2	Cyclooxygenase-2
CPE	Cytopathic effect
CREB	Cyclic AMP response element binding protein
DC	Dendritic cell
DMV	Double membrane vesicles
DPP4	Dipeptidyl peptidase 4
dsRNA	Double stranded RNA
DUSP1	Dual specificity protein phosphatase 1
E	Envelope protein
EDEM1	ER degradation enhancer, mannosidase alpha-like 1
eIF2B	Eukaryotic initiation factor 2B
eIF2α	Eukaryotic initiation factor 2 alpha subunit
ER	Endoplasmic reticulum
ERAD	ER-associated degradation
ERdj4	ER DNA J domain-containing protein 4
ERGIC	Endoplasmic reticulum-Golgi intermediate compartment
ERK	Extracellular signal-related kinase
ERO1α	ER oxidoreductin 1 alpha
ERSE	ER stress response element
GADD34	Growth arrest and DNA damage-inducible protein 34
GCN2	General control non-derepressible 2
GCN4	General control non-derepressible 4
GRP78/BiP	Glucose-regulated protein 78/immunoglobulin heavy chain-binding protein
GRP94	Glucose-regulated protein 94
HA	Hemagglutinin protein
HE	Hemagglutinin-esterase protein
HRI	Heme-regulated inhibitor kinase
IFNβ	Interferon beta

IKK	IκB kinase
IL-6	Interleukin 6
IL-8	Interleukin 8
IRE1	Inositol-requiring protein 1
IRF3/7	Interferon regulatory factor 3/7
ISR	Integrated stress response
ISRE	Interferon stimulated response element
IκBα	Inhibitor of NF-κB alpha
JIP	JNK interacting protein
JNK	c-Jun N-terminal kinase
kDa	Kilo Dalton
LAMP2	Lysosomal associated membrane protein 2
LC3	Microtubule-associated proteins 1A/1B light chain 3C
LPS	Lipopolysaccharide
M	Membrane protein
MAPK	Mitogen-activated protein kinase
mCEACAM1	Murine carcinoembryonic antigen-related adhesion molecules 1
Mcl-1	Myeloid cell leukemia 1
MEF	Mouse embryonic fibroblast
MKK	MAP kinase kinase
MKKK	MAP kinase kinase kinase
M^{pro}	Main protease
mTOR	Mammalian target of rapamycin
MYD88	Myeloid differentiation primary-response protein 88
N	Nucleocapsid protein
NF-κB	Nuclear factor kappa-light-chain-enhancer of activated B cells
NLR	NOD-like receptor
nsp	non-structural protein
OAS	2’5’-oligoadenylate synthetase
ORF	Open reading frame
PAMP	Pathogen-associated molecular pattern
PE	Phosphotidylethanolamine
PERK	PKR-like ER protein kinase

PIP3	Phosphatidylinositol-3-phosphate
PKR	Protein kinase RNA-activated
$PL1^{pro}/PL2^{pro}$	Papain-like protease 1/2
PP1	Protein phosphatase 1
pp1a/pp1ab	polyprotein 1a / polyprotein 1ab
PPARγ	Peroxisome proliferator-activated receptor gamma
PRR	Pattern recognition receptor
PTP1B	Protein tyrosine phosphatase 1B
PUMA	p53 up-regulated modulator of apoptosis
Rab7	Ras-related protein 7
RBD	Receptor binding domain
RdRp	RNA-dependent RNA polymerase
RIDD	IRE1-dependent mRNA decay
RIG-I	Retinoic acid inducible gene 1
RLR	RIG-I-like receptor
RTC	Replication-transcription complex
S	Spike protein
TAK1	TGFβ activated kinase 1
TBK1	TANK-binding kinase 1
TGFβ	Transforming growth factor beta
TIR	Toll and IL-1 receptor domain
TLR	Toll-like receptor
TNFα	Tumor necrosis factor alpha
TRAF2	TNF receptor-associated factor 2
TRIF	TIR domain containing adaptor protein inducing IFNβ
TRS	Transcription-regulated sequence
ULK1/2	Unc51-like kinase 1 and 2
UPR	Unfolded protein response
UTR	Untranslated region
VLP	Virus-like particle
Vsp34	Vacuolar protein sorting 34
WIPI	WD-repeat protein interacting with phosphoinositides
XBP1	X-box protein 1

LIST OF FIGURES

LIST OF TABLES

PUBLICATIONS

1. **Fung TS**, Huang M, Liu DX (2014) Coronavirus-induced ER stress response and its involvement in regulation of coronavirus–host interactions. Virus research 194: 110-123.

2. **Fung TS,** Liao Y, Liu DX (2014) The ER stress sensor IRE1α protects cells from apoptosis induced by coronavirus infectious bronchitis virus. Journal of Virology 88: 12752-12764.

3. **Fung TS**, Liu DX (2014) Coronavirus infection, ER stress, apoptosis and innate immunity. Frontiers in Microbiology 5: 1-13.

4. Liu DX, **Fung TS**, Chong KKL, Shukla A, Hilgenfeld R (2014) Accessory proteins of SARS-CoV and other coronaviruses. Antiviral Research. 109:97-109.

5. Liao Y, **Fung TS**, Huang M, Fang SG, Zhong Y, Liu DX (2014). RNA isolation and northern blot analysis. Bio-protocol 4(6): e1077. http://www.bio-protocol.org/e1077

6. Liao Y*, **Fung TS***, Huang M, Fang SG, Zhong Y, et al. (2013) Up-regulation of CHOP/GADD153 during coronavirus infectious bronchitis virus infection modulates apoptosis by restricting activation of the extracellular signal-regulated kinase pathway. Journal of virology 87: 8124-8134. **(*First authorship shared)**

ABSTRACT

Coronaviruses are important animal and human pathogens. In this study, two stress pathways – the unfolded protein response (UPR) and c-Jun N-terminal kinase (JNK) pathway are shown to be activated in cells infected with infectious bronchitis virus (IBV). The inositol requiring protein 1 (IRE1) branch of UPR protects infected cells from apoptosis by splicing the mRNA of X-box protein 1 (XBP1) and differentially modulating the activation of two kinases. The PKR-like ER protein kinase (PERK) branch of UPR promotes IBV-induced apoptosis by up-regulating C/EBP homologous protein (CHOP). JNK is phosphorylated by MKK7 during IBV infection, and it promotes apoptosis by modulating the level of B cell lymphoma-2 (Bcl2) family proteins. Moreover, IRE1 mediates autophagy induction whereas XBP1 and JNK contribute to the induction of pro-inflammatory cytokines (interleukin-8) and type-I interferon in the IBV-infected cells. Therefore, these stress pathways modulate critical cellular events and contribute to pathogenesis during coronavirus infection.

Chapter One:

Literature Review

1.1 MOLECULAR BIOLOGY OF CORONAVIRUS

Coronavirus is a family of enveloped virus with a large RNA genome. Coronavirus infections in domestic animals have long been an important veterinary issue, leading to severe economic loss worldwide. The emergence of two highly pathogenic human coronaviruses – the severe acute respiratory syndrome coronavirus (SARS-CoV) and the Middle East respiratory syndrome coronavirus (MERS-CoV), has clearly demonstrated that coronaviruses can cross the species barrier and become lethal zoonotic human pathogens. Therefore, understanding the pathogenesis of coronavirus is essential for identifying antiviral agents and developing effective vaccines. In the following sections, current knowledge of coronavirus will be reviewed, with a focus on its molecular biology and replication cycle.

1.1.1 Human and animal diseases caused by coronaviruses

As early as in the 1960s, infection of coronaviruses such as Human Coronavirus 229E (HCoV-229E) or HCoV-OC43 has been associated with mild upper respiratory symptoms [1,2]. To date, four human coronaviruses (HCoV-229E, HCoV-OC43, HCoV-NL63 and HCoV-HKU1) have been demonstrated to be globally distributed and responsible for about one third of common cold in human adults [3]. Sometimes, these viruses may also cause severe lower respiratory infections in infants, the elderly and immunocompromised individuals.

In 2002-2003, an outbreak of severe acute respiratory syndrome (SARS) in southern China rapidly spread to other countries, which eventually infected over 8000 people worldwide with a mortality rate of ~9.6% [4]. The etiologic agent for SARS was identified as a highly pathogenic coronavirus and named SARS-CoV [5]. After an incubation period of 2-10 days, most SARS patients would develop pneumonia, which in severe cases could lead to respiratory failure and acute respiratory distress syndrome [6]. Apart from the respiratory infection, SARS-CoV has also been shown to infect multiple organs (such as liver, kidney, intestine and brain) and the immune system according to autopsy of SARS patients [7]. Initially, the SARS-CoV was proposed to origin from bat, adapt to the intermediate host palm civet and finally gain the ability to infect humans [8,9]. Recently a live SARS-like coronavirus has been isolated from bats, suggesting that direct human infection by some bat coronavirus may also be possible [10].

In 2012, a novel human coronavirus – MERS-CoV emerged in Saudi Arabia, which was associated with severe acute respiratory illness with a high mortality rate (~40%) in patients with comorbidities [11,12]. Although sustained human-to-human transmission is considered low, MERS-CoV has managed to persist and spread to other countries in the Middle East and Europe. Current evidence strongly suggests the dromedary camels to be the natural reservoirs of MERS-CoV, adding to the list of zoonotic coronaviruses that are highly pathogenic in humans [13].

Coronavirus also infects a wide range of animals. The murine hepatitis virus (MHV) has been the most extensively studied prototype coronavirus prior to the SARS pandemic. Being extremely contagious, MHV has been considered as the most important pathogen of laboratory mice [14]. There are about 25 strains of MHV, which differ in tissue tropism and virulence. Mice experimentally infected with the neurotropic strains of MHV (such as A59 and JHM) develop acute encephalitis and chronic demyelination, which are commonly used as animal models for multiple sclerosis [15]. On the other hand, natural MHV infection of laboratory mice drastically affects host physiology and compromises their value as research subjects [14].

Coronavirus infections in domestic animals are also a significant concern in the livestock industry. Bovine coronavirus (BCoV) and transmissible gastroenteritis coronavirus (TGEV) mainly infect the gastrointestinal tract, which cause high mortality in neonates and reduce yield in adults [16,17]. In 2013, the outbreak and spreading of porcine epidemic diarrhea virus (PEDV), which has a mortality rate approaching 100% in suckling piglets, has caused major economic impact to the swine industry in North America [18].

Finally, the infectious bronchitis coronavirus (IBV) causes highly contagious respiratory disease in chickens [19]. Apart from the upper respiratory tract, IBV may also replicates in other epithelial tissues such as the gastrointestinal tract, kidney and reproductive organs. Infection with IBV reduces the performance of both meat-type and egg-laying chickens and causes severe economic loss to the poultry industry worldwide [19].

1.1.2 Classification

The family *Coronaviridae*, together with *Arteriviridae* and *Roniviridae*, are grouped under the order *Nidovirales*, which are characterized by the 3'-nested set of subgenomic RNAs (sgRNAs) during viral replication. Coronaviridae is divided into two subfamilies, the *coronavirinae* and the *torovirinae*. The Coronavirinae is further classified into four genera, namely the Alphacoronavirus, Betacoronavirus, Gammacoronavirus and Deltacoronavirus [20]. The classification was originally based on antigenic relationships and later confirmed by sequence comparisons of viral genomic sequences [21]. Current evidence supports that Alphacoronavirus and Betacoronavirus evolve from coronaviruses in bats and establish tropism in mammals, whereas Gammacoronavirus and Deltacoronavirus origin from coronaviruses in birds and adapt to mainly avian hosts [22].

Within the genus Betacoronavirus, four lineages (A, B, C and D) can be distinguished based on phylogenetic analysis. MHV, HCoV-OC43 and HCoV-HKU1 belong to the lineage A. Lineage B includes the SARS-CoV and its likely precursor, the SARS-like coronavirus WIV1 that infects bats. The newly emerged MERS-CoV, together with two bat coronaviruses HKU4 and HKU5, belongs to the C lineage, whereas lineage D only contains one species of bat coronavirus (HKU9). The up-to-date classifications of coronaviruses, as well as prototypes or clinically important species of each genus, are summarized in **Figure 1-1**.

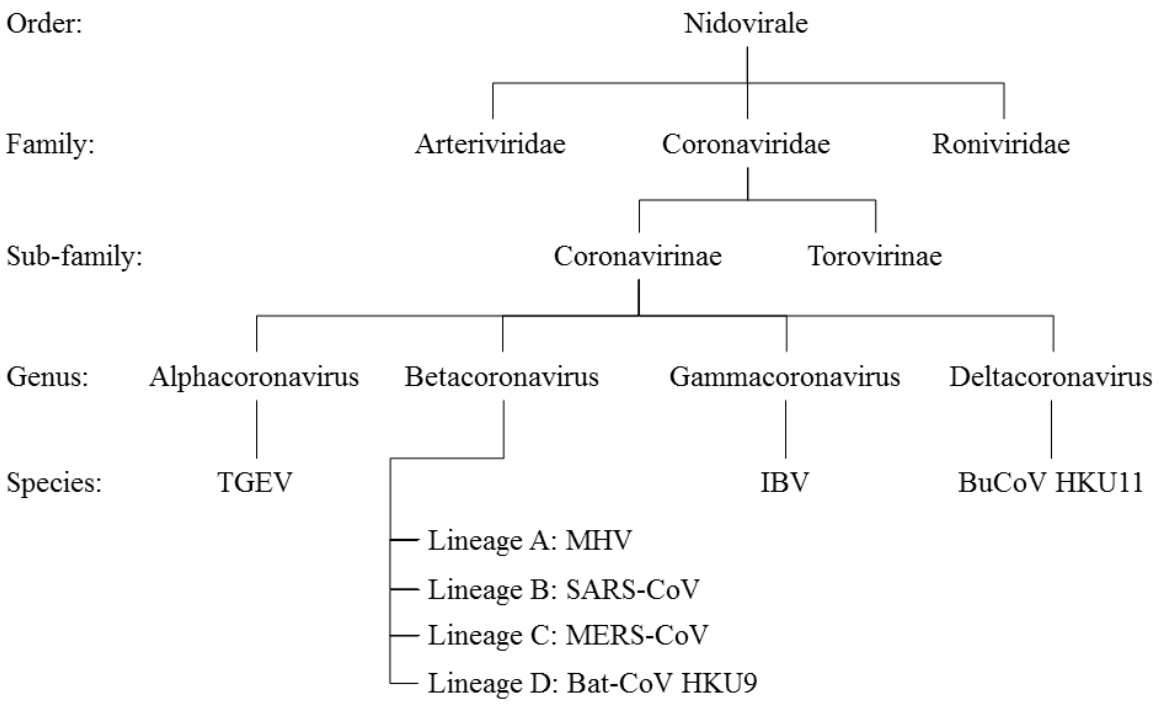

Figure 1-1 Taxonomy of coronaviruses

Taxonomic classification of coronaviruses and the representative viruses. The taxonomic ranks are presented on the left. TGEV, transmissible gastroenteritis coronavirus; MHV, murine hepatitis coronavirus; SARS-CoV, severe acute respiratory syndrome coronavirus; MERS-CoV, Middle East respiratory syndrome coronavirus; Bat-CoV HKU9, bat coronavirus HKU9; IBV, infectious bronchitis coronavirus and BuCoV HKU11, Bulbul coronavirus HKU11.

1.1.3 Virion morphology and structures

Under electron microscope, coronavirus is generally spherical or moderately pleomorphic in shape, with a mean diameter of 80 to 120 nm. The virus particle contains distinct "club-like" projections on the surface that resemble sonar corona, giving rise to the name coronavirus (**Figure 1-2A**). Formed by the trimers of the spike (S) proteins, these protrusions have thin bases anchoring in the envelope, which swell to about 10 nm at the distal end and project to 20 nm from the virion surface [23]. In some Betacoronaviruses, a second type of shorter projections (5 to 10 nm) can be found under the major spikes, which are contributed by the homodimers of the hemagglutinin-esterase (HE) protein [24]. Apart from the prominent S and HE proteins, the envelop is also embedded with the membrane (M) protein and a much lower amount of the envelope (E) protein. The interior of the coronavirus virion is occupied by a helically symmetric nucleocapsid, which is comprised of the RNA genome closely associated with the nucleocapsid (N) protein. A schematic diagram demonstrating the morphological features of a typical coronavirus particle is shown as in **Figure 1-2B**.

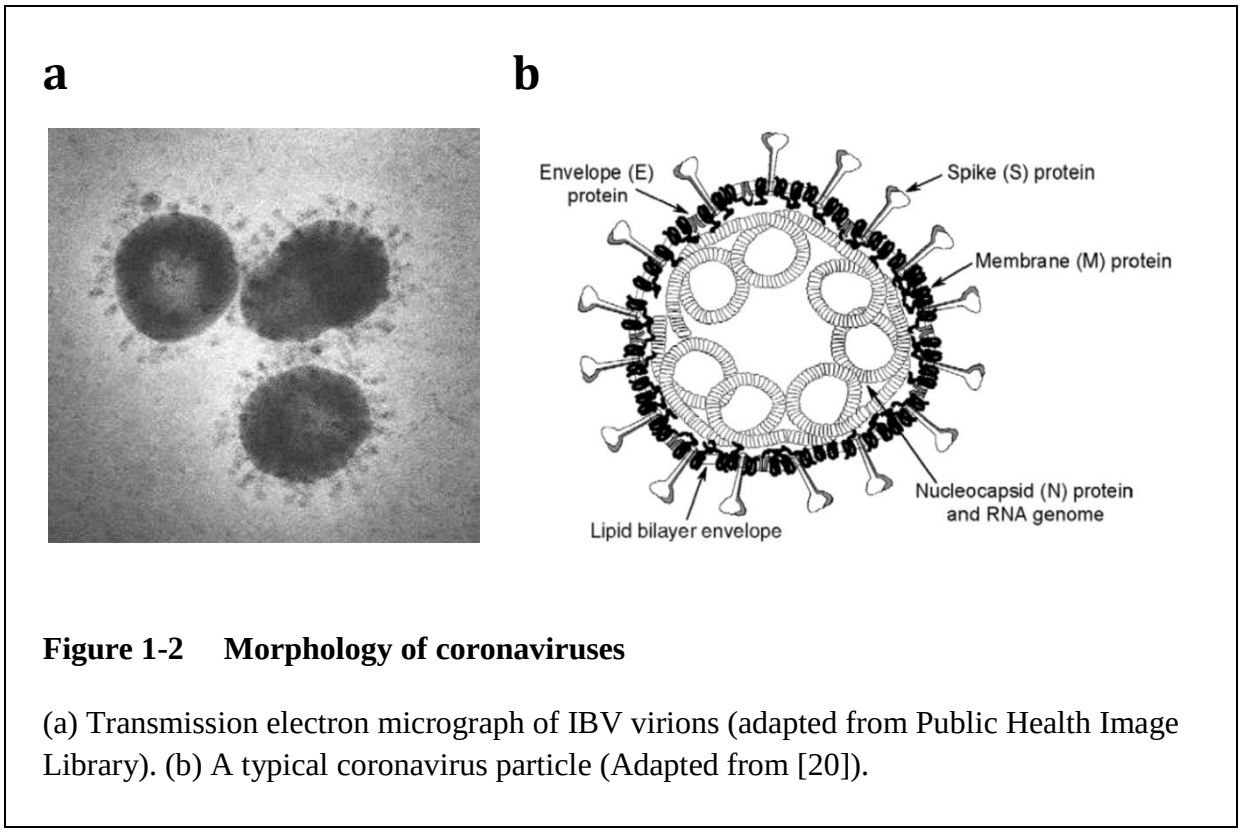

Figure 1-2 Morphology of coronaviruses

(a) Transmission electron micrograph of IBV virions (adapted from Public Health Image Library). (b) A typical coronavirus particle (Adapted from [20]).

1.1.4 Genome organization

Coronavirus has a non-segmented, single-stranded RNA genome. The genome is positive sense (same as mRNAs) and is infectious when transfected into permissive host cells. Similar to eukaryotic mRNAs, the genomic RNA contains a 5'-caps and is modified by 3'-polyadenylation. The coronavirus genome is the largest among RNA viruses, ranging from 27,000 to 32,000 nucleotides. There are two untranslated regions (UTRs) flanking the coronavirus genomic RNAs. The 5'-UTR, ranging from 210 to 530 nucleotides in length, contains a leader sequence at the 5'-terminal that is 70 to 100 nucleotides long. The 3'-UTR ranges from 270 to 500 nucleotides and contains a highly conserved octameric sequence (GGAAGAGC) 70 to 80 nucleotides upstream from the poly(A) tail [20].

Unlike most eukaryotic mRNAs, the coronavirus genomic RNAs have multiple open reading frames (ORFs). Nearly two-thirds of the genome at the 5' end is occupied by the viral replicase gene with two ORFs (ORF1a and ORF1b). The remaining one third of the genome encodes the four structural proteins: the S, E, M and N protein [25]. Although the invariant gene order in a coronavirus is 5'-replicase-S-E-M-N-3', rearrangement of the gene order is found to be tolerated by the virus [26]. In addition to the canonical genes, the coronavirus genome also contains numerous ORFs coding for accessory proteins, which are interspersed among the structural protein genes. With a few exceptions, these accessory proteins share low sequence homology to any known proteins and are not essential for viral replication in the cell culture. A color-coded schematic diagram of the genome organization for TGEV, MHV, SARS-CoV, MERS-CoV and IBV is shown in **Figure 1-3**.

During coronavirus replication, the genome has three main functions. Immediately after entry and uncoating, the genome serves as an mRNA encoding the replicase polyprotein. Secondly, the genomic RNA acts as the template for the transcription of subgenomic RNAs and for the replication of progeny genomes. Finally, during virus assembly, the genomes are encapsidated by the N proteins and incorporated into progeny virions [20].

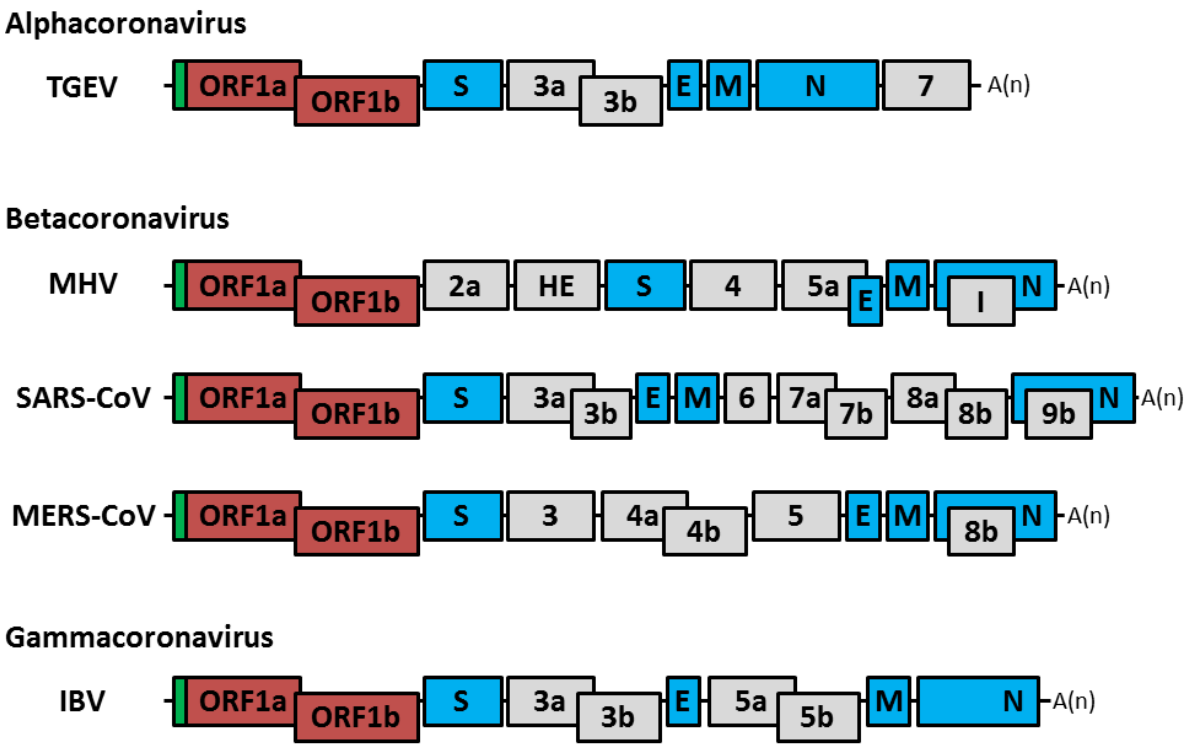

Figure 1-3 Genome organization of coronaviruses

Schematic diagram showing the genome organization of TGEV, MHV, SARS-CoV, MERS-CoV and IBV, respectively. The 5' leader sequences are shown in green boxes. The replicase genes (ORF1a and ORF1b) are indicated with red boxes. Structural protein genes are shown in blue boxes, whereas genes encoding the accessory proteins are represented by gray boxes (not drawn to scale).

1.1.5 Coronavirus structural proteins

The four structural proteins, namely the S, E, M and N protein, are the major protein components of the mature coronavirus particles, although some accessory proteins and host proteins are also recruited into the virion at low abundance. In the following section, structural and functional characteristics of the coronavirus structural proteins will be briefly reviewed.

1.1.5.1 Spike (S) protein

Being the largest structural protein, the S protein is about 128-160 kilo Dalton (kDa) in size, and reaches 150-200kDa after glycosylation (exclusively N-linked) [20]. It is a type I transmembrane protein, with a large N-terminal ectodomain, a single transmembrane domain and a short C-terminal endodomain (**Figure 1-4**). In most coronaviruses, the S protein is cleaved by host proteases into two functional subunits of roughly the same size, an N-terminal S1 domain and a C-terminal S2 domain [27]. The S protein cleavage may be mediated by furin or furin-like protease during exocytosis of the virion (as for IBV), by endosomal cathepsin proteases during cell entry (as for SARS-CoV) or by proteases present in the extracellular milieu [28-30].

The S1 domain makes up the globular head of the S protein and harbors the receptor binding domain (RBD). The RBD has been mapped to different regions in the S1 domain in different coronaviruses, namely the N-terminal of S1 for MHV, center of S1 for SARS-CoV and C-terminal of S1 for TGEV [31-33]. The S2 domain constitutes the stem of the S protein and contains an upstream buried fusion peptide, followed by two heptad repeat regions (HR1 and HR2), a transmembrane domain and a short cytoplasmic tail. The fusion peptide and heptad repeats are important for virus-cell membrane fusion after receptor binding by RBD. For some coronaviruses like TGEV and IBV, the S protein is retained intracellularly by a tyrosine motif located in the cytoplasmic tail [34,35].

Due to the large size and the formation of numerous disulfide bonds in the luminal domain, the S protein folds slowly and trimerizes in the ER before it is transported to the assembly sites [36]. Based on the fusion mechanisms, the coronavirus S protein is classified as class I fusion proteins, which also include the influenza virus hemagglutinin (HA) and the human immunodeficiency virus type I (HIV-1) *env* protein [27]. Due to its fusion activity, the S protein often causes cell-cell fusion (syncytia) in the infected cells or when it is overexpressed [37].

1.1.5.2 Membrane (M) protein

Although the S protein is the most prominent component on the viral envelope, the M protein is the most abundant protein in the virion. Composing of 220 to 260 amino acids, the M protein contains a short N-terminus exposed on the outside of the virion, three hydrophobic transmembrane domains, and a large C-terminal tail inside the virion (**Figure 1-4**). Coronavirus M protein is modified by glycosylation on the N-terminal domain, which is O-linked for most betacoronavirus and N-linked for alpha- and gammacoronavirus [38-40]. Homotypic interaction between M proteins is thought to provide the scaffold for the assembly of envelope, and therefore pivotal for the virion morphogenesis [41]. Moreover, the M protein also interacts with the S, E, N protein and the genomic RNA, thereby orchestrating the proper recruitment of viral components at the assembly sites [42]. The M protein also interacts with cellular proteins such as β-actin, and has been implicated in viral pathogenesis as a type I interferon antagonist [43,44].

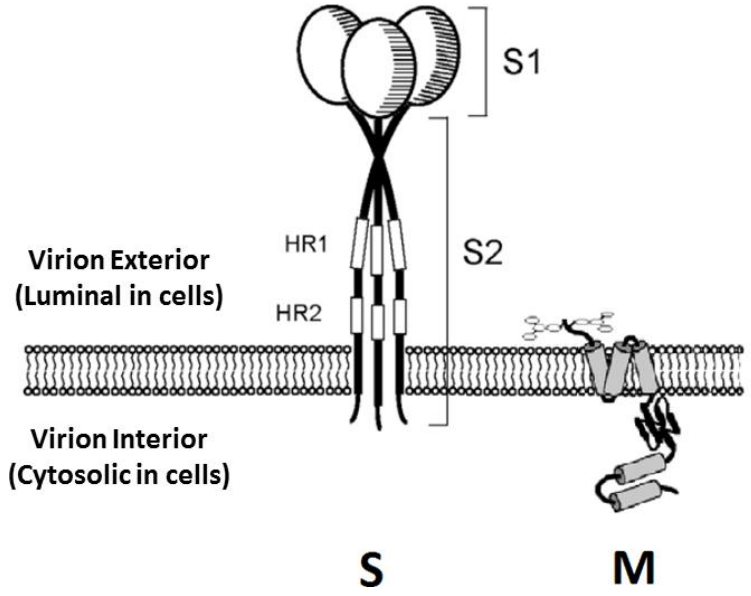

Figure 1-4 Membrane topology of the coronavirus S protein and M protein

Schematic diagram showing the membrane topology of coronavirus S and M proteins. The two sub-units (S1 and S2) of S protein and the heptad repeat regions (HR1 and HR2) for membrane fusion are also indicated (modified from [20]).

1.1.5.3 Envelope (E) protein

The E protein is non-glycosylated, very small in size (~8-10kDa) and presents at a low amount in the virion, which explains its late discovery and recognition as a virion component [45]. Although the E protein has been shown to be an integral membrane protein, its membrane topology is still under debate [46,47]. Certain coronavirus E proteins are palmitoylated, although the function of this modification is unknown [47,48].Nevertheless, E protein is important for coronavirus assembly, which is likely mediated by its ability to induce membrane curvature and its physical interaction with the M protein [49,50]. In fact, co-expression of the M and E protein is necessary and sufficient for the formation of virus-like particles (VLPs) in cells [50,51]. Interestingly, the E protein is not essential for certain coronavirus such as MHV and SARS-CoV, although deletion of the E protein gene results in severely crippled virions with significantly lower titers [52,53]. Notably, the E protein has also been shown to exhibit viroporin activity, as it can alter membrane permeability and function as an ion channel [48,54,55]. Indeed, recent studies have clearly elucidated the pentameric α-helical bundle of SARS-CoV E Protein, which shows voltage independent ion conductance that are also regulated by lipid charges [56,57].

1.1.5.4 Nucleocapsid (N) protein

The N protein is a phosphoprotein ranging from 43 to 50kDa in size. The primary function of N protein is to bind the coronavirus genomic RNA in a beads-on-a-string fashion, thereby encapsidating it into a helical nucleocapsid within the mature virion [58]. The N-terminal of the N protein is rich in positively charged arginine and lysine residues, which facilitate its binding to the negatively charged genome. The C-terminal, however, is rich in basic residues and is proposed to interact with M protein during viral assembly [59]. The N protein has been found to bind RNA in both sequence-specific and sequence non-specific manner [60,61]. Interestingly, *in vitro* studies have found that phosphorylation of N protein allows binding to viral RNA substrates with higher affinity compared to non-viral RNA [60,62]. Phosphorylation of N protein may also play a role in virus assembly and maturation [63]. Being a multifunctional protein, the N protein has also been implicated in viral RNA transcription and replication [64], viral mRNA translation [65], and RNA chaperone activity [66].

1.1.6 Coronavirus non-structural proteins

As mentioned above, the replicase gene of all coronaviruses consists of two ORF (ORF1a and ORF1b). Translation of ORF1a produces the polyprotein 1a (pp1a). Meanwhile, ribosomal frame shifting can occur at the junction of ORF1a and ORF1b, allowing translation to continue from ORF1a to ORF1b, producing a larger polyprotein 1ab (pp1ab) [67]. Both pp1a and pp1ab are co- or post-translationally cleaved by two ORF1a-encoded proteases. Cleavage of pp1a produces 11 non-structural proteins (nsp1-nsp11), while cleavage of pp1ab produces 15 non-structural proteins (nsp1-nsp10, nsp12-nsp16). Notably, due to the lack of a cleavage site that usually lies between nsp1 and nsp2 in other coronaviruses, IBV doesn't have a counterpart of nsp1 and only produces 15 non-structural proteins. Autoproteolytic cleavage of pp1a and pp1ab is mediated by the two papain-like proteases ($PL1^{pro}$ and $PL2^{pro}$) activity of nsp3 and the chymotrypsin-like main protease (M^{pro}) activity within nsp5 [68].

The functions of some non-structural proteins have been partially characterized. The multi-pass transmembrane proteins nsp3, nsp4 and nsp6 are required for the formation of double membrane vesicles (DMVs), which are closely associated with the coronavirus replication transcription complexes (RTCs) [69]. The critical RNA-dependent RNA polymerase (RdRp) activity is encoded by nsp12 [70]. Nsp8 also possess RdRp activity, but it has low-processivity and acts as a putative primase to synthesize short oligonucleotides primers [71]. The multifunctional nsp13 is essentially an RNA helicase with 5' to 3' polarity, while also possessing NTPase, dNTPase and RNA 5'-triphosphatase activity [72]. Nsp14 has 3' to 5' exoribonuclease (ExoN) activity, which is proposed to ensure the fidelity during RNA transcription and replication [73,74]. Nsp15 possesses the uridylate-specific endoribonuclease (NendoU) activity, which is conserved in all nidoviruses and plays critical (but currently unknown) function during coronavirus replication [75,76]. Interestingly, nsp14 also mediates RNA capping by a (guanine-N7)-methyltransferase (N7-MTase) activity, while nsp16 caps RNA by an S-adenosyl-L-methione-dependent RNA (nucleoside-2-O)-methyltransferase (2'O-MT) activity [77,78]. The known functions of all coronavirus non-structural proteins are summarized in Table-1-1.

Table 1-1: Summary of the known functions of coronavirus non-structural proteins.

Protein	Functions
Nsp1	Suppression of host gene expression by mRNA degradation [79]; inhibition of translation initiation [80]; induction of G_0/G_1 cell cycle arrest [81]; inhibition of IFN signaling by suppressing STAT1 phosphorylation [82].
Nsp2	Unknown; dispensable for replication in cell culture [83].
Nsp3	Papain-like protease activity for polyprotein processing [68]; ADP-ribose 1"-phosphatase activity [84]; deubiquitinating enzyme activity [85]; type I IFN antagonist [86]; NF-κB signaling antagonist [87]; DMV formation [69].
Nsp4	DMV formation [69,88].
Nsp5	Main protease activity for polyprotein processing [68]
Nsp6	Induction of autophagosome formation [89]; DMV formation [69].
Nsp7	Interacts with nsp8 to form a hexadecameric complex [90].
Nsp8	Interacts with nsp7 to form a hexadecameric complex [90]; noncanonical RNA-dependent RNA polymerase activity, may serves as primase [71].
Nsp9	Single-stranded RNA (ssRNA) binding protein [91]; interacts with nsp8 [92].
Nsp10	RNA binding protein [93].
Nsp11	Unknown.
Nsp12	Primer-dependent RNA-dependent RNA polymerase [70].
Nsp13	RNA helicase with 5' to 3' polarity [72]; NTPase; dNTPase; RNA 5'-triphosphatase activity [94].
Nsp14	3' to 5' exoribonuclease activity [74]; RNA capping by a (guanine-N7)-methyltransferase activity [77].
Nsp15	Uridylate-specific endoribonuclease (NendoU) activity [75].
Nsp16	RNA capping by S-adenosyl-L-methione-dependent RNA (nucleoside-2-O)-methyltransferase (2'O-MT) activity[78].

1.1.7 Coronavirus replication cycle

The replication cycle of coronaviruses can be artificially divided into several stages: attachment and entry, translation and assembly of the RTC, transcription and replication, translation of structural proteins, virion assembly and finally budding of the mature virions (**Figure 1-5**). The mechanistic detail of each stage will be briefly described as below.

1.1.7.1 Attachment and entry

Coronavirus infections start with the binding of virion to the cell surface receptor via the S protein. The interaction between the receptor and S protein is the major determinant of host and tissue tropism of a coronavirus. In most cases, forced expression of a coronavirus receptor in a non-permissive cell line renders it permissive to infection by the corresponding coronavirus. On the other hand, mutations in the S protein, especially in the RBD of the S1 subunit, have been associated with changes in host specificity. For instance, a single point mutation within the RBD of a SARS-CoV animal isolate (SZ16) is sufficient to allow for efficient binding to human cells [95]. As another example, when the ectodomain of MHV S protein is swapped with that of FIPV (Feline Infectious Peritonitis Virus), the virus is said to be felinized and acquires the ability to infect feline cells while losing the ability to infect murine cells *in vitro* [96].

Most alphacoronaviruses use the metallopeptidase callsed aminopeptidase N (APN) as their receptors. The receptors of betacoronaviruses are more diverse: murine carcinoembryonic antigen-related adhesion molecules 1 (mCEACAM1) for MHV, angiotensin-converting enzyme 2 (ACE2) for SARS-CoV and dipeptidyl peptidase 4 (DPP4) for MERS-CoV respectively [97-99]. To date no receptors have been identified for gammacoronaviruses, although neuraminidase treatment rendered permissive cells resistant to IBV infection, indicating a role of sialic acid in the attachment stage [100].

For most coronaviruses receptor binding alone can initiate the fusion process, although others (such as SARS-CoV and IBV) requires additional activations such as proteolytic cleavage or acidic pH [27]. Fusion may occur either on the plasma membrane or the endosomal membrane depending on the different routes of entry. In both cases, extensive conformational changes occur

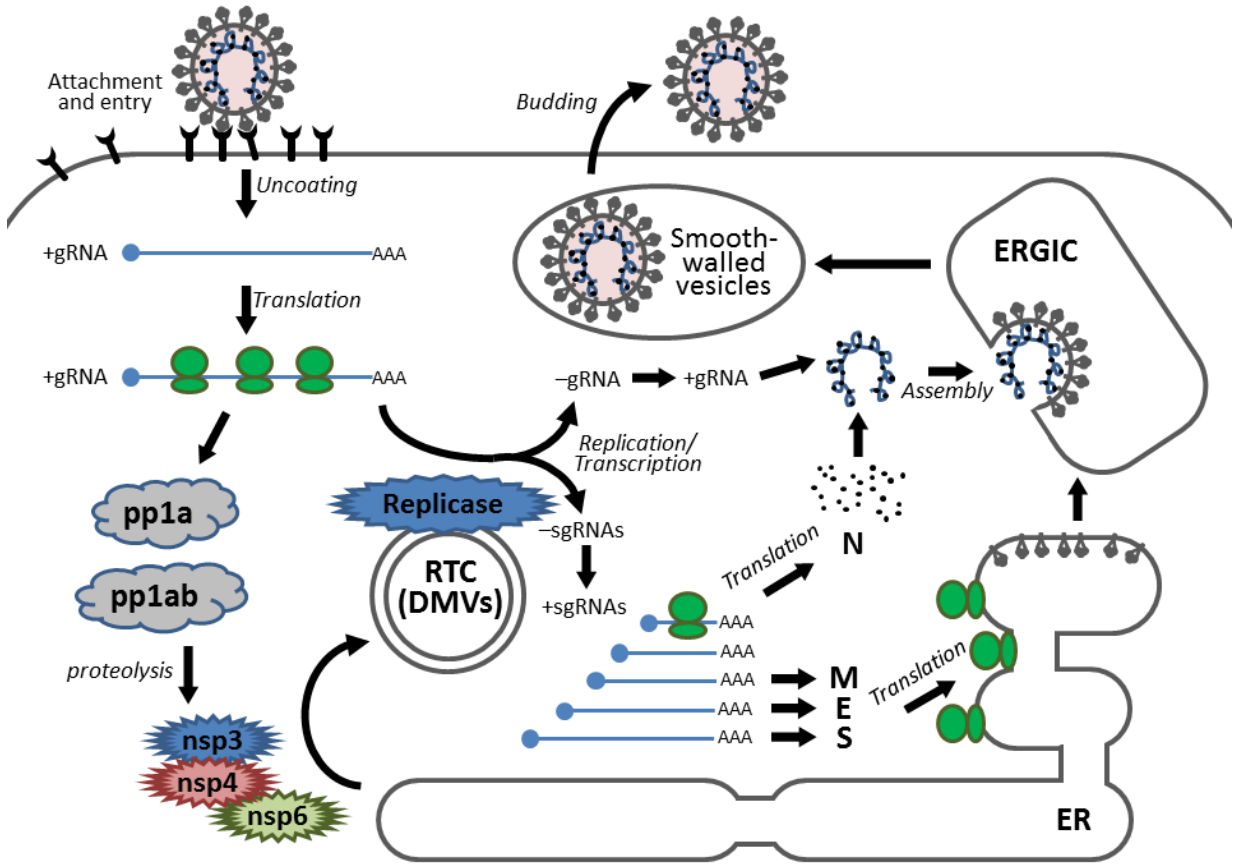

Figure 1-5 Replication cycle of coronaviruses

Schematic diagram showing the replication cycle of coronaviruses. Infection starts with receptor binding and entry by membrane fusion. After uncoating, the genomic RNA is translated into polyproteins (pp1a and pp1ab), which are processed by auto-proteolytic cleavage into replicase proteins. The genomic RNA is used as a template to synthesize progeny genomes via a negative sense intermediate. Discontinuous transcription of the genomic RNA results in a nested set of subgenomic RNAs. The replication transcription centre (RTC) is closely associated with double membrane vesicle (DMV), which is proposed to be originated from the ER. The S, E and M proteins are synthesized and inserted in the ER, while the N protein is translated by free ribosomes in the cytosol. Assembly takes place in the ER-Golgi intermediate compartment (ERGIC) and the mature virions are released via smooth-walled vesicles by exocytosis.

in the S protein, exposing a hydrophobic fusion peptide in the S2 subunit. After inserting the fusion peptide into the host membrane, two heptad repeats in each of the three S monomers come together to form a six-helix bundle. This enables close juxtaposition of the viral envelope and the cellular membrane, allowing for fusion of the lipid bilayers and delivery of the nucleocapsid into the cytosol. This is followed by uncoating – the dissociation of the N proteins from the genomic RNA. The uncoating process in coronavirus is poorly characterized, and may involve the activities of host factors and dephosphorylation of the N protein [101,102].

1.1.7.2 Translation and assembly of the replication transcription complex

Because the coronavirus genomic RNA consists of a 5'-methylated cap and a 3'-poly(A) tail, it resembles cellular mRNAs and is recognized by the host translation machinery. Cap-dependent translation of the ORF1a produces the polyprotein pp1a. In between ORF1a and ORF1b, there is a "slippery sequence" (UUUAAAC) and a downstream hairpin-type pseudoknot. By virtue of these two RNA elements, around 25-30% of the ribosomes undergo -1 frameshifting and continue translation on ORF1b, thereby producing the longer polyprotein pp1ab [20]. As mentioned above, protease activities residing in nsp3 and nsp5 enable auto-proteolytic cleavage of the replicase polyprotein into 15-16 non-structural proteins with diverse functions (see 1.1.6).

To enhance the efficiency of RNA synthesis, the replicase proteins are concentrated and anchored to intracellular membranes in the perinuclear region of infected cells. Through membrane association and protein-protein interactions, the coronavirus RTC is assembled, which is also referred to as "viral factory" [103]. Notably, the RTC associated membranous structure is originated and modified from the ER, usually in the form of DMV or spherule [104,105]. Membrane rearrangement is likely mediated by the multi-pass transmembrane non-structural proteins nsp3, nsp4 and nsp6 [69].

1.1.7.3 Genome replication and transcription

Coronavirus RNA synthesis in the RTC comprises of two distinct but related events: replication and transcription. Genome replication refers to the synthesis of full-length positive sense genomic RNA for the assembly of progeny virions, whereas transcription refers to the

production of a 3’-nested set of subgenomic RNAs (sgRNAs) that encode structural and accessory proteins. To replicate the genome, the replicase synthesizes full-length negative sense genomic RNA in a continuous fashion, which is in turn used as the template to synthesize large amounts of positive-stranded genomic RNA. The synthesis of sgRNA is not so straight forward and involves discontinuous transcription of the genome.

Coronavirus sgRNAs are 3’-nested, meaning that they share the same 3’ ends but contain 5’ ends of different lengths. Moreover, all sgRNAs possess an identical leader sequence (~70 to 100 nt in length) at the 5’ end, which is also present in the genomic RNA. Immediate downstream of the leader sequence is a consensus motif called the transcription-regulated sequence (TRS), which is conserved in each coronaviruses genus. In the genomic RNA, TRSs are also located in the intergenic sequences where discontinuous transcription occurs. In the current model, during the synthesis of negative sense sgRNAs, an RNA segment between an internal TRS and the TRS downstream of the 5’ leader in the genomic RNA template loops out, enabling the polymerase to switch template and finish transcription on the 5’ leader sequence. This results in a 5’-nested set of negative sense sgRNAs, which in turn serve as template for the synthesis of positive sense sgRNAs [106,107].

1.1.7.4 Translation of structural and accessory proteins

Translated by a cap-dependent mechanism, most of the coronavirus sgRNAs are functionally monocistronic, meaning that only the most 5’ ORF is translated. For example, in the case of IBV, sgRNA2, sgRNA4 and sgRNA6 only encode the S, M and N protein, respectively. In contrast, some of the sgRNAs are polycistronic. For instance, the sgRNA3 of IBV encodes the accessory proteins 3a and 3b, as well as the structural protein E. While 3a is translated by a cap-dependent mechanism, 3b is translated by ribosome leaky scanning and translation of E is mediated by internal entry of ribosome [108]. Similarly, the sgRNA5 of IBV is bi-cistronic, encoding another two accessory proteins 5a and 5b [109].

Membrane bound structural proteins (S, M and E) are translated, inserted and folded in the ER. These proteins are also post-translationally modified by ER resident enzymes, before transported to the ER-Golgi intermediate compartment (ERGIC) for assembly. On the other

hand, the N protein is translated by free ribosomes in the cytoplasm and encapsidates the nascent progeny genomic RNA to form the nucleocapsid.

1.1.7.5 Virion assembly and budding

The ERGIC is generally considered as the site of virion assembly, morphogenesis and budding for coronaviruses [110,111]. Virion assembly is likely to be orchestrated by the M protein [20]. Homotypic interaction of the M protein provides scaffold for the formation of viral envelope. Moreover, the C-terminal cytosolic tail of M protein also interacts with S and N protein, thereby recruiting them to the assembly sites [112,113]. Importantly, the M protein may also be responsible for the selective encapsidation of the coronavirus genomic RNA by interacting with a cis-acting packaging signal [114]. Finally, virion budded into the ERGIC is exported through cellular secretory pathway in the smooth-wall vesicle, which ultimately fuses with the plasma membrane, releasing the progeny virus into the extracellular milieu for a new round of infection cycle. For some coronavirus, a portion of the S protein escapes from viral assembly and is inserted into the plasma membrane by the secretary pathway. These surface S proteins cause fusion of the infected cell with neighboring uninfected cells, forming a large multinucleated cell known as a syncytium. Syncytia formation is a hallmark of the cytopathic effect (CPE) in cells infected with IBV.

1.2 APOPTOSIS AND AUTOPHAGY

Apoptosis and autophagy are two cellular events involved in diversities of physiological and pathophysiological processes. Both apoptosis and autophagy are known to be activated during coronavirus infections, but detailed mechanisms are only partially characterized. In the following section, the core signaling pathways of apoptosis and autophagy will be briefly reviewed, followed by their involvements in coronavirus infections.

1.2.1 Apoptosis

Apoptosis is a mode of cell death morphologically characterized by cell shrinkage, plasma membrane blebbing, nuclear condensation and fragmentation. Apoptosis is a highly controlled and self-limited process, in which cellular structures are dismantled from within, packaged in membrane bound vesicles (apoptotic bodies) that are engulfed by phagocytes [115]. In this manner, apoptosis prevents leakage of intracellular contents and minimizes activation of the immune system, which distinguishes it from necrosis – the immunogenic form of cell death. The controlled demolition in apoptosis is coordinated by a family of protease known as cysteine aspartic acid-specific protease (caspase), which can be activated by either the extrinsic pathway or the intrinsic pathway (**Figure 1-6**) [116].

1.2.1.1 Intrinsic pathway of caspase activation

The B-cell lymphoma (Bcl2) family proteins play essential roles in the regulation of apoptosis. Based on the number of Bcl2 homology (BH) domains, these proteins can be classified into three groups. The Bcl2 like proteins (such as Bcl2, B-cell lymphoma-extra-large [Bcl-X_L] and myeloid cell leukemia 1 [Mcl-1]), contain all four BH domains and are anti-apoptotic. The Bcl2-associated X protein (BAX)-like proteins (such as BAX and Bcl2 homologous antagonist killer [BAK]), contain BH1, BH2 and BH3 but lack BH4. They promote apoptosis by forming pores in the mitochondrial outer membrane. BH3-only proteins (such as Bcl2-interacting mediator of cell death [Bim], Bcl2-associated death promoter [Bad] and BH3 interacting-domain death agonist [Bid]) only contain the BH3 domain and are pro-apoptotic [117].

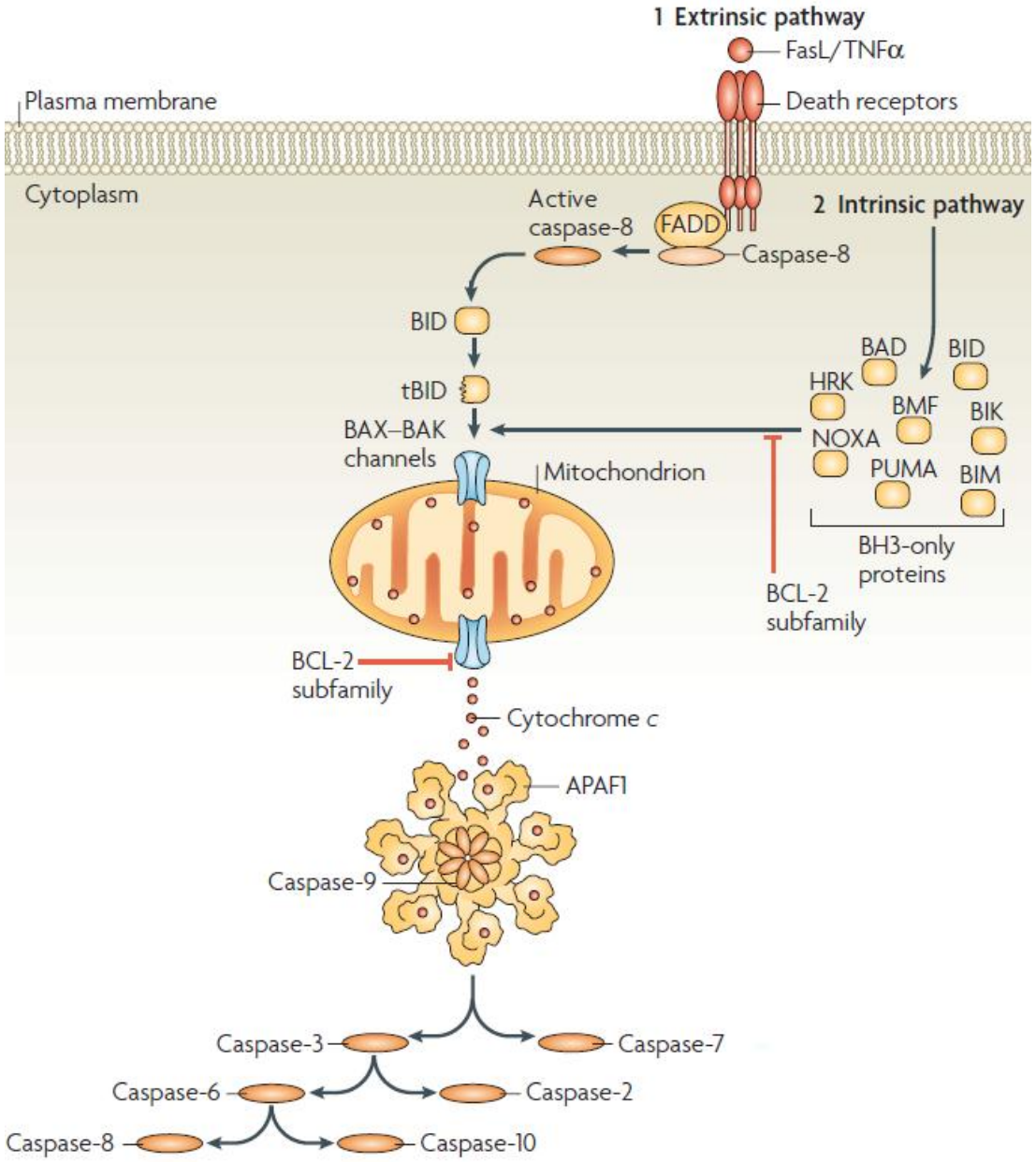

Figure 1-6 The extrinsic and intrinsic pathway of caspase activation in apoptosis.

The intrinsic pathway is mediated by the BH3-only proteins, which induces channel formation in the mitochondrial outer membrane and release of cytochrome c. This is followed by the subsequent activation of the caspase cascade. The extrinsic pathway is activated when the death receptors binds to extracellular death ligands, which leads to activation of caspase 8 or cross-activation of the intrinsic pathway. See text for details (modified from [115]).

In the intrinsic pathway, BH3-only proteins act as pathway specific sensors to monitor various stimuli that cause cell stress or damage. For example, p53 up-regulated modulator of apoptosis (PUMA) is activated by p53 under DNA damage response; Bad is activated by growth factor deprivation; and Bim is activated when the cytoskeleton is disrupted. When the BH3-only proteins are activated beyond a threshold, they can overcome the inhibitory effect of Bcl2 like proteins and promote the assembly of BAX-BAK channels in the mitochondrial outer membranes. This leads to the release of cytochrome c from the intermembrane space into the cytosol. Cytochrome c forms a complex called apoptosome by interacting with Apoptotic Protease Activating Factor 1 (APAF1) and pro-caspase 9, resulting in proteolytic activation of caspase 9. Caspase 9 subsequently cleaves and activates caspase 3 and caspase 7, which targets key substrates in the cells and set off series of events associated with apoptosis [118].

1.2.1.2 Extrinsic pathway of caspase activation

Cells can also be induced to undergo apoptosis by extracellular death signals via the extrinsic pathway. The tumor necrosis factor (TNF) super-family of death receptors (such as Fas) are mediators of the extrinsic pathway. Upon binding to extracellular death ligands (such as Fas ligand [FasL]), the death receptors recruit adaptor proteins such as the Fas-associated death domain protein (FADD). FADD contains two domains, the death domain (DD) that associates with the DD in Fas and the death effector domain (DED) that associates with the DED in caspase 8. The complex of FasL-Fas-FADD-caspase 8 is called the death-inducing signaling complex (DISC) and its formation leads to autocatalysis and activation of caspase 8. Like caspase 9, caspase 8 can directly cleaves and activates caspase 3 and caspase 7 [117]. On the other hand, caspase 8 also cleaves the BH3-only protein Bid into truncated Bid (tBid), which promotes cytochrome c release and apoptosis activation via the intrinsic pathway [119].

1.2.1.3 Coronavirus-induced apoptosis

It has been shown that cell death induced by coronavirus infections can proceed via either apoptosis or necrosis, or both. Actually, in the infected tissues obtained from autopsy studies of SARS patients, both apoptotic and necrotic tissues have been observed [120]. In cell culture studies, various coronaviruses (TGEV, IBV, SARS-CoV, ect) have been found to induce caspase-dependent apoptosis [121-123]. The coronavirus induced apoptosis is dependent on viral

replication, and it can be inhibited by caspase inhibitors such as z-VAD-FMK or forced expression of the anti-apoptotic protein Bcl2 [124,125]. However, inhibition of apoptosis does not severely affect the coronavirus replication, suggesting that apoptosis may not be essential for replication *in vitro* [121,124,125].

For SARS-CoV, it has been found all four structural proteins (S, E, M, N), the main protease, and the accessory proteins 3a, 3b, and 7a can all induce apoptosis when overexpressed in cells [120]. However, the mechanisms for apoptosis induction by these proteins are not fully understood. The E protein and 3a protein have been shown to form ion channels, and it has been proposed that they may induce apoptosis by perturbing the mitochondrial permeability [126,127]. Other proteins could modulate the mitogen-activated protein kinase (MAPK) pathways or cell cycle control proteins, thus leading to apoptosis [128,129]. Interestingly, the N protein of some coronaviruses has been found to be cleaved by activated caspases during viral induced apoptosis, although the physiological significance remains unknown [130,131].

1.2.2 Autophagy

Macroautophagy (hereafter referred to as autophagy) is an evolutionarily conserved "self-eating" process where part of the cytoplasm and/or organelles are sequestered within a double membrane vesicle (named autophagosome), which ultimately fuses with the lysosome for bulk degradation [132]. Under basal conditions, autophagy allows cells to break down long-lived proteins and damaged organelles (such as mitochondria). Autophagy is also activated under starvation or growth factor deprivation, so that cells can recycle amino acids and fatty acids to maintain metabolism for cell survival. In fact, it has been found that mice defective in autophagy cannot survive the nutrient deprivation following birth [133].

Autophagy is also activated under a variety of cellular stress, such as hypoxia, reactive oxygen species, DNA damage, protein aggregates, or infection of intracellular pathogens [134]. In most scenarios, autophagy facilitates stress adaptation and cell survival. However, in other settings, autophagy constitutes an alternative pathway of cell death called autophagic cell death [135]. Complete autophagy pathway can be divided into four steps: initiation, isolated membrane nucleation, elongation and lysosomal fusion (**Figure 1-7**). Each step is tightly regulated by numerous highly conserved autophagy-related genes (ATGs) [136].

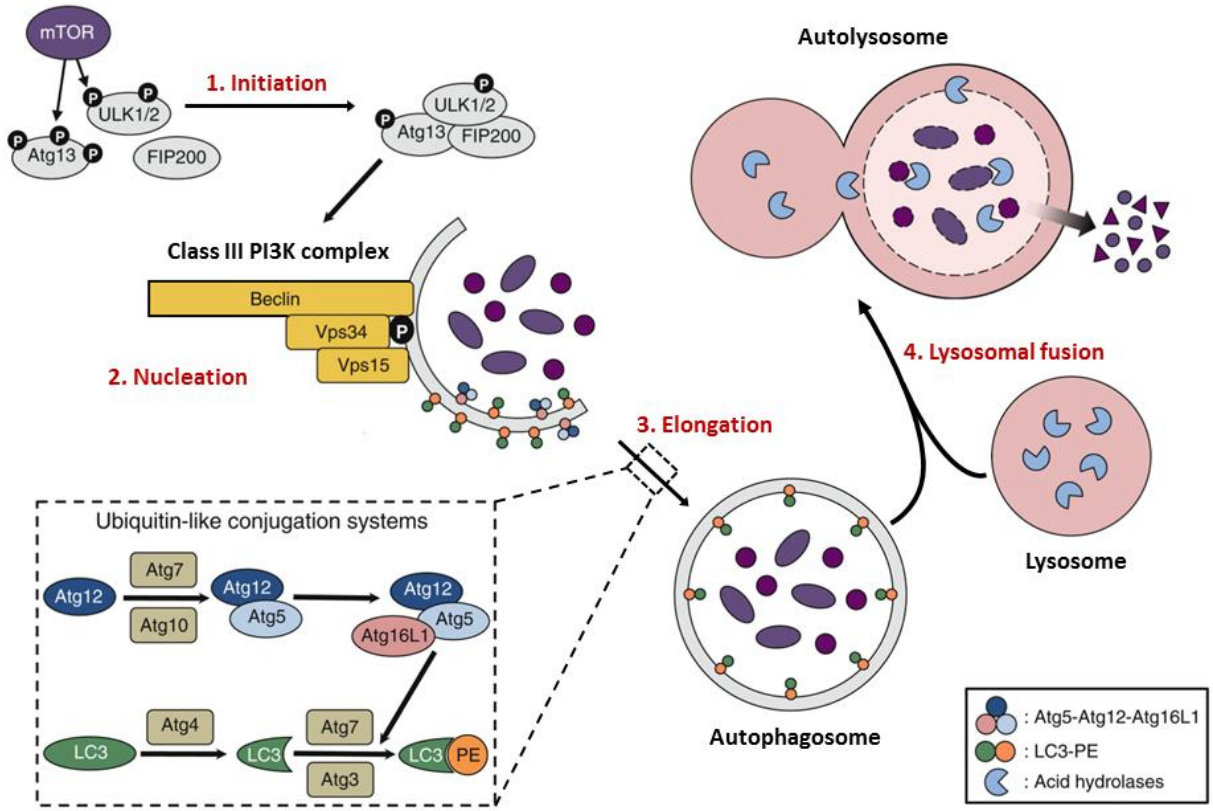

Figure 1-7 The autophagy signaling pathways.

Initiation of autophagy is triggered by inactivation of mTOR and the formation of the ULK complex. This is followed by nucleation of isolated membrane on the ER by the class III PI3K complex. The elongation of autophagic vesicles is mediated by two ubiquitin-like conjugation systems, which decorate the autophagosomes with lipidated LC3-II marker. Finally, the autophagosomes fuse with lysosomes and the contents are degraded by lysosomal enzymes for recycle to the cytoplasm. See text for detail. (Modified from [137])

1.2.2.1 Signaling pathways of autophagy

Inititation Under nutrition replete conditions, the mammalian target of rapamycin (mTOR) is active and inhibit autophagy by phosphorylating the Unc-51-like kinase 1 and 2 (ULK1/2) and Atg13. During starvation, mTOR is inactivated, leading to hypo-phosphorylation of ULK1/2 and Atg13. This leads to the formation of the ULK1/2-Atg13-FIP200 complex and its translocation from cytosol to certain domains of the ER where autophagy is initiated [138].

Isolated membrane nucleation The ULK complex then recruits the class III phosphatidylinositol-3-OH kinase (PI3K) complex, which includes vacuolar protein sorting 34 (Vsp34), Vps15 and coiled-coil, myosin-like Bcl2 interacting protein 1 (beclin1, or BECN1). Vsp34 is allosterically activated by beclin 1 and generates phosphotidylinositol-3-phosphate (PI3P). PIP3 recruits effectors such as the double FYVE domain-containing protein 1 (DFCP1) and WD-repeat protein interacting with phosphoinositides (WIPI). DFCP1 initiates the formation of ER-associated membrane structures with Ω-shape, termed omegasomes, whereas WIPI acts downstream of DFCP1 to transform omegasomes into isolated membranes [139].

Vesicle elongation Two ubiquitin-like conjugating systems play essential role in the elongation of autophagic vesicles. In the first system, Atg12 is conjugated to Atg5, with the help of the E1-like enzyme Atg7 and E2-like enzyme Atg10. The Atg5-Atg12 conjugate non-covalently associates with Atg16 to form a multimeric Atg12-Atg5-Atg16 complex, which is present on the outer side of the isolation membrane and is essential for proper elongation of the isolation membrane. In the second system, microtubule-associated proteins 1A/1B light chain 3C (LC3) is first cleaved by Atg4 at the C-terminal to form LC3-I, which is soluble and localizes in the cytosol. A lipid moiety, phosphatidylethanolamine (PE), is then conjugated to LC3-I to form LC3-II with the help of the E1-like enzyme Atg7, E2-like enzyme Atg3 and the Atg12-Atg5-Atg16 complex mention above, which functions as the E3 ligase [139]. LC3 is stably associated with both the inner and outer membrane of the autophagosomes, and its biochemical and microscopic detection has been widely used to monitor autophagy [140].

Lysosomal fusion The last stage of autophagy involves the fusion of autophagosomes with lysosome or late endosome for cargo degradation. The detailed mechanism regulating vesicle fusion remains poorly understood. However, the small GTPase Ras-related protein 7

(Rab7), the lysosomal associated membrane protein 2 (LAMP2) and other proteins have been proposed to mediate lysosomal fusion [141]. The vesicles after fusion are called autolysosome and the sequestered cargos are degraded by lysosomal hydrolytic enzymes to recycle essential biomolecules to the cytoplasm.

1.2.2.2 Coronavirus-induced autophagy

As mentioned above, coronaviruses induce formation of DMVs in the infected cells and the replication transcription complexes are targeted to the DMVs. Since cellular stress induced autophagosomes are also double membrane vesicles, there have been some speculations that coronaviruses may hijack the autophagy machinery. Early studies have demonstrated that the DMVs induced by MHV and SARS-CoV may be adopted from autophagosomes, because immune-staining against the autophagy marker LC3 co-localize with proteins of the replication complexes [142,143]. However, follow-up studies have not been able to corroborate these results, and no co-localization of autophagosomes and replication complexes were detected [144,145]. Recenly, it has been found that the non-structural protein 6 (nsp6) of IBV and other coronaviruses, is responsible for coronavirus induced autophagy [89]. However, nsp6 does not activate the mTOR pathway or induces ER stress. Therefore, the detailed mechansisms of how coronaviruses induce autophagy remain elusive.

Previous studies have also shown different result regarding the role of autophagy in coronavirus replication in cells. Whereas Prentice et al have reported that MHV growth is reduced in ATG5 -/- cells, studies by others have shown that MHV replication is not affected in autophagy defective cells [143,146,147]. Moreover, a recent paper has demonstrated that IBV replicates normally in cells after ATG5 silencing or treatment of autophagy inhibitor wortmannin [89]. Therefore, although coronavirus infections induce autophagy, it is likely that replication does not rely on autophagy. Interestingly, although knockdown of LC3 significantly reduces MHV replication in cells, this can be completely restored by transfection of non-lipidable LC3. Thus MHV replication only requires the autophagy-independent activity of LC3 [146].

1.3 ER STRESS AND UNFOLDED PROTEIN RESPONSE (UPR)

Inside a eukaryotic cell, the endoplasmic reticulum (ER) is the major site for the synthesis, folding, modification and sorting of secreted and transmembrane proteins. In cells undergoing certain physiological changes (such as cell differentiation) or affected by environmental stimulations (such as amino acid deficiency), the amount of proteins entering the ER can fluctuate substantially [148]. If the ER protein influx saturates its folding capacity, unfolded proteins will accumulate in the ER, leading to ER stress. In order to re-establish ER homeostasis, signaling pathways known as the unfolded protein response (UPR) are activated, which are mediated by the three ER transmembrane sensors – PKR-like ER protein kinase (PERK), inositol-requiring protein 1 (IRE1) and activating transcriptional factor 6 (ATF6) [148]. The following section will summarized current knowledge of UPR signaling pathways, as well as their implications during coronavirus infections.

1.3.1 ER stress induced by coronavirus infections

Coronavirus replication of in the cytoplasm is closely associated with ER and other cellular membrane organelles. Recent studies have strongly suggested that coronavirus replication causes ER stress and induces UPR in the infected cells. Increase expression of ER protein chaperones, such as the immunoglobulin heavy chain-binding protein (BiP, also known as glucose-regulated protein 78, or GRP78) or glucose-regulated protein 94 (GRP94), is generally accepted as an indicator of ER stress [15]. The mRNA levels of BiP and GRP94, together with other ER stress related genes, have been shown to increase in SARS-CoV-infected cells or in cells overexpressing the SARS-CoV spike protein, as determined by micro-array studies [149,150]. Consistently, luciferase reporters under the control of BiP or GRP94 promoters is activated in SARS-CoV-infected cells [151]. Induction of ER stress has also been detected in cells overexpressing SARS-CoV accessory protein 3a, 6 or 8ab [152-154], or in cells infected with other coronaviruses such as MHV [155] and IBV [156]. Therefore, ER stress is likely to be a common outcome in cells infected with coronaviruses [157]. Although not completely understood, coronavirus-induced ER stress has been mainly attributed to the following three mechanisms.

Massive production of the S glycoprotein Except for the N protein, all coronavirus structural proteins are transmembrane proteins synthesized in the ER. Among them, the large and highly glycosylated S protein is massively produced for virion assembly during coronavirus infections [20]. N-linked glycosylation significantly increases the size of the S protein, and has been shown to promote its folding and trimerization [158]. The folding and maturation of spike protein presumably depends heavily on the ER protein chaperones, such as calreticulin and calnexin. In fact, physical interaction between calnexin and the SARS-CoV S protein has been determined, and inhibition of calnexin function has been shown to reduce the infectivity of pseudotyped lentivirus bearing the SARS-CoV S protein [159]. The folding, modification and assembly of the gigantic trimeric S protein undoubtedly increase the workload of the ER. Indeed, overexpression of the spike protein of SARS-CoV or MHV, but not other structural proteins, has been shown to induce potent ER stress in cell culture studies [151,155]. Interestingly, a HCoV-OC43 variant with two point mutations in the spike protein has been found to induce a stronger ER stress and UPR in the infected neurons as compared to the wild type virus, which may also contribute to the increased virulence and persistence in mice [160].

Membrane modifications Modification of cellular membranes has been observed in cells infected with various RNA viruses [161]. Among them, coronaviruses have been shown to induce the formation of double membrane vesicles (DMVs) in the infected cells [162]. Using immunocytochemistry and electron microscopy, these DMVs are found to closely associate with the coronavirus replication transcription complexes (RTCs) where viral RNAs are synthesized [144,163]. As mentioned above, DMVs formation is presumably mediated by the multi-pass transmembrane non-structural proteins nsp3, nsp4 and nsp6 [69]. Using high resolution electron tomography, it has been shown that the DMVs formed in SARS-CoV-infected cells are modified from a reticulovesicular network derived from the ER, which also contains convoluted membranes and vesicle packets [104]. Moreover, Reggiori et al. have recently uncovered a mechanism whereby MHV obtains DMV membrane from the ER [146]. Specifically, the protein ER degradation enhancer, mannosidase alpha-like 1 (EDEM1) is normally exported from the ER in COPII-independent vesicles called EDEMosomes. MHV hijacks these EDEMosomes and uses the membrane to construct the DMVs, which further supports the ER-origin of the DMVs [146]. Last but not the least, alternative membrane rearrangements such as zippered ER and ER spherules have also been observed in IBV-infected cells [105].

Membrane depletion during coronavirus assembly It has been well established that the site for coronavirus assembly and budding is the ER-Golgi intermediate compartment (ERGIC), which is a structural and functional extension of the ER [110,111]. Undoubtedly, continuous morphogenesis and budding of mature virions into the ERGIC will in effect deplete the ER membrane component. Previous studies have demonstrated that depletion of phosphatidylcholine (the major lipid component of ER) affects the morphology of ER and impairs protein trafficking in the Golgi [164]. This in turns induces ER stress and UPR, and the affected cells respond by increasing lipid biosynthesis and ER membrane biogenesis [165,166]. Apart from the budding process, coronavirus infections also induce autophagy, and the autophagosome also obtained its membrane from the ER [89]. Therefore, it is likely that membrane depletion during coronavirus replication contribute to ER stress.

To summarize, ER stress induced by coronavirus infections may be attributed to: (1) massive production of the S glycoprotein in the ER; (2) dramatic membrane rearrangement in the ER for DMVs formation; and (3) ER membrane depletion due to virion assembly and induction of autophagy. In response to the ER stress, the infected cells will activate the UPR (**Figure 1-8**). In the following section, signaling pathways of the three UPR branches and their induction during coronavirus infections will be discussed in detail.

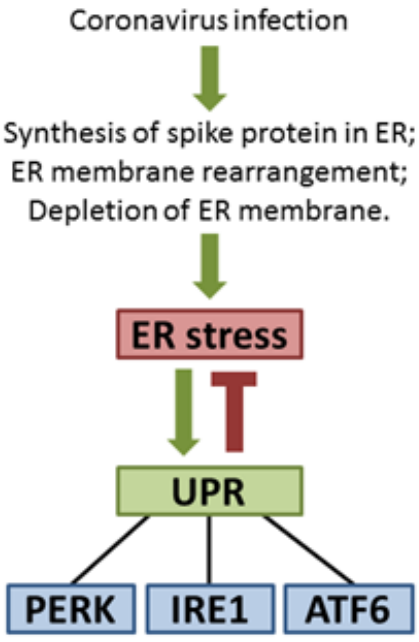

Figure 1-8 Coronavirus-induced ER stress

Coronavirus replication causes ER stress by: synthesis of the spike glycoprotein, ER membrane modification and depletion of ER membrane. The ER stress sensors PERK, IRE1, and ATF6 are activated and trigger UPR in an attempt to counter ER stress. See text for detail.

1.3.2 The PERK branch of UPR and the integrated stress response (ISR)

1.3.2.1 PERK and ISR Signaling pathways

Among the three UPR branches, PERK is generally considered to be the first sensor activated in response to ER stress [148,167]. In unstressed cells, the luminal domain of PERK is bound by the ER chaperone BiP and held inactive. Under ER stress, BiP is recruited to interact with the excessive influx of unfolded proteins and dissociate from PERK. The dissociation of BiP results in the oligomerization, auto-phosphorylation, and ultimately activation of the tyrosine kinase activity of PERK [168]. Phosphorylated PERK is usually dephosphorylated and inactivated by the protein tyrosine phosphatase 1B (PTP1B). In cells under ER stress, however, PTP1B is inhibited by sulfhydration, and active PERK is thus kept in the active form [169]. The most well characterized substrate for PERK is the α-subunit of eukaryotic initiation factor 2 (eIF2α) [170]. When phosphorylated at serine 51, eIF2α forms a stable complex with eukaryotic initiation factor 2B (eIF2B) and inhibits its enzymatic activity. EIF2B is a guanine nucleotide exchange factor that converts the inactive GDP-bound eIF2α to its active GTP-bound form, which is required for the binding of initiator methionine-transfer RNA (tRNA) to the 40S ribosome to form the 43S pre-initiation complex [171]. Thus, phosphorylation of eIF2α results in the inhibition of translation initiation and a general suppression of cellular protein synthesis [172]. Translation attenuation aims to reduce the influx of newly synthesized proteins into the already stressed ER. Moreover, eIF2α phosphorylation liberates ribosomes and translation factors from mRNAs, allowing for preferential translation of UPR specific genes and reprograming the ER for the stress condition [173].

Apart from PERK, three other proteins have been identified as eIF2α kinases, namely the heme-regulated inhibitor kinase (HRI), the general control non-derepressible 2 (GCN2) and the protein kinase RNA-activated (PKR) [148]. Expressed predominantly in erythroid cells and hepatocytes, HRI is activated by low heme level and coordinates the synthesis of heme and the protein moieties of hemoglobin in red blood cells and P450 cytochromes in hepatocytes [174,175]. GCN2 is the only known eIF2α kinase with a homolog in yeast, which is activated by uncharged tRNA under amino acid deprivation [176]. In the context of virus infection, PKR is probably the most relevant eIF2α kinase, because it is induced by interferon and activated by the binding of double-stranded RNA (dsRNA), a common intermediate during the replication of a

diversities of DNA and RNA viruses [177]. Binding of dsRNA to the two dsRNA binding motifs leads to dimerization and auto-phosphorylation of PKR, thereby switching on its kinase activity [178]. Although the upstream stimuli are different, activation of all four eIF2α kinases results in translation attenuation and activates similar signaling pathways, which are collectively known as the integrated stress response (ISR) **(Figure 1-9)** [148].

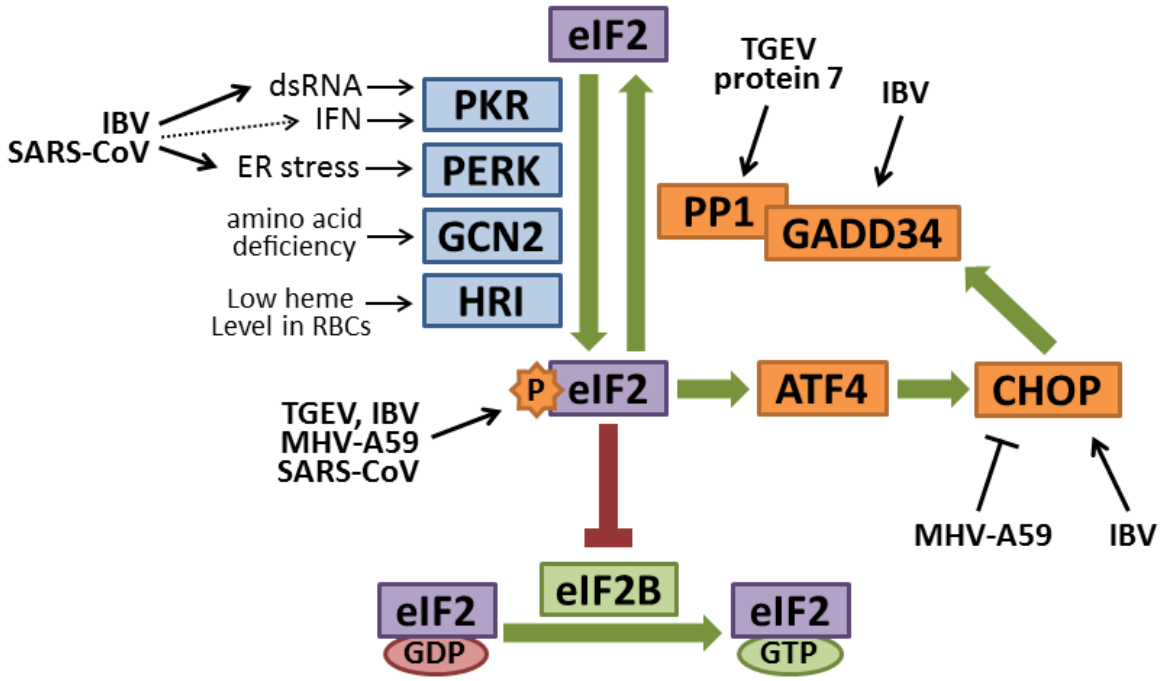

Figure 1-9 PERK and ISR signaling pathway during coronavirus infections.

Phosphorylation of eIF2α by PKR, PERK, GCN2 or HRI leads to sequestration of eIF2B and inhibits recycling of GTP-bound eIF2α, resulting in translation attenuation and the activation of the ISR. Negative feedback mediated by CHOP and GADD34 aims to restore translation by promoting dephosphorylation of eIF2α. Infection with MHV-A59, SARS-CoV, and IBV has been shown to cause eIF2α phosphorylation, which is most likely mediated by PKR and/or PERK. Other proteins in the signaling pathway such as CHOP, GADD34 and PP1 are also modulated by coronavirus infections. See text for detail.

Translation of cellular mRNAs is generally suppressed under ISR. However, mRNAs of certain genes consist of small upstream ORFs (uORFs) in their 5'UTR, and they are actually preferentially translated under ISR [179]. These include one gene called the activating transcription factor 4 (ATF4), the mammalian homolog of the general control non-derepressible 4 (GCN4) in yeast [173,180]. ATF4 belongs to a large family of transcription factors featured by a basic-region leucine zipper (bZIP) DNA binding domain [181]. ATF4 induces the expression of genes involved in amino acid biosynthesis [182], antioxidant response [183], and another important bZIP transcription factor – the C/EBP homologous protein (CHOP, also known as growth arrest and DNA damage-inducible protein 153, or GADD153) [184]. Acting together, CHOP and ATF4 further induces the growth arrest and DNA damage-inducible protein 34 (GADD34), which is a regulatory subunit of the protein phosphatase 1 (PP1) [185]. GADD34 interacts with and activates PP1, which mediates the de-phosphorylation of eIF2α to switch off the translation suppression **(Figure 1-9)** [186]. The negative feedback enables normal translation initiation to resume after ER stress is resolved. However, if ER stress persists, restoration of protein synthesis can also aggravate the ER stress and contribute to cell death [185,187].

1.3.2.2 Activation of ISR during coronavirus infections

There have been diverging results regarding ISR activation during coronavirus infections. An early study performed in cells infected with MHV-1 has detected minimal transcriptional activation of PKR and another interferon-stimulated gene, 2'5'-oligoadenylate synthetase (OAS) [188]. Later experiments using MHV-A59 also confirms that PKR and eIF2α are not phosphorylated and that host protein translation was not inhibited in the infected cells [189]. The inability to activate PKR in MHV-A59 infected cells was attributed to the inhibition of the IFN response by the virus [189,190]. However, in a separate study using the same virus strain (MHV-A59), significant eIF2α phosphorylation has been observed starting from 8 hours post infection (hpi) [191]. Although activation of the corresponding upstream kinases has not been determined, the protein level of downstream ATF4 is clearly up-regulated, with no apparent induction of CHOP and GADD34 [191]. It has been proposed that virus may adopt certain uncharacterized mechanisms to down-regulate the CHOP/GADD34/PP1 feedback loop, allowing for sustained translation attenuation of the host proteins **(Figure 1-9)** [191]. Meanwhile, translation of MHV mRNAs is not affected even when eIF2α is phosphorylated, although the reason is not known.

In terms of SARS-CoV, significant phosphorylation of PKR and PERK, but not GCN2 has been detected in the infected cells [192]. Phosphorylation of eIF2α was also detected, although changes in the host protein synthesis have not been determined. Unexpectedly, knock-down of PKR has no effect on SARS-CoV replication or eIF2α phosphorylation, indicating that SARS-CoV is resistant to the antiviral function of PKR *in vitro* and that eIF2α phosphorylation in SARS-CoV-infected cells is mediated by other kinases.[192]. On the other hand, overexpression of SARS-CoV structural proteins has been shown to activate the PERK branch of UPR. For example, expression of the SARS-CoV S protein activates BiP and GRP98 promoters in a dosage dependent manner [151]. Induction of BiP and GRP98 is likely mediated through PERK and eIF2α, because co-transfection of dominant negative forms of PERK or eIF2α drastically suppresses the reporter activities [151]. Recently, the PERK activating domain of the SARS-CoV S protein is mapped to the central region of the S1 subunit and appears to function independent of N-linked glycosylation [193]. Interestingly, the accessory protein 3a of SARS-CoV, a small multi-pass transmembrane protein with ion channel activity, has also been found to activate ATF4 and CHOP promoters, and may be involved in SARS-CoV-induced ISR [152].

As for Alphacoronaviruses, TGEV replication has been shown to induce PKR and eIF2α phosphorylation in the infected cells, although the involvement of PERK has not been determined [194]. Interestingly, Cruz et al. have generated a recombinant TGEV virus deficient in the accessory gene 7 (rTGEV-Δ7). Compared with the wild type virus, cells infected with rTGEV-Δ7 have a much higher level of eIF2α phosphorylation, more severe translation attenuation and also a stronger induction of GADD34 [194]. Moreover, the protein 7 of TGEV has been shown to physically interact with PP1, thereby promoting eIF2α de-phosphorylation. Although the implication of other signaling intermediates (such as ATF4 and CHOP) have not been determined, it is likely that TGEV infection induces the PKR-eIF2α-GADD34 pathway, which is in turn modulated by the accessory protein 7.

In terms of Gammacoronaviruses, previous studies done by this group have demonstrated that IBV triggers PKR and PERK phosphorylations at the early stage of infection (2-8 hpi), which diminish quickly afterwards [156,195]. The inhibition of PKR (and likely also PERK) phosphorylation has been attributed to the nsp2 protein, which display weak antagonistic activity towards PKR [195]. The kinetic of eIF2α phosphorylation is similar to that of PKR and PERK,

peaking at early time points of infection but dramatically reduces thereafter [156,195]. Consequently, *de novo* synthesis of host proteins is not significantly affected in cells infected with IBV [195]. Besides the inactivation of the upstream kinases, rapid de-phosphorylation of eIF2α could also be attributed to the induction of GADD34 by ATF4 and CHOP, all of which are significantly up-regulated at later stage of IBV infection [156,195]. RNA interference and inhibitor experiments further confirms the activation of PKR/PERK-eIF2α-ATF4-CHOP pathway in IBV-infected cells and the negative feedback by GADD34/PP1. Knock-down of PKR or PERK, as well as chemical inhibition of PKR or eIF2α, greatly reduces IBV-induced CHOP up-regulation [156]. On the other hand, PP1 inhibition by okadaic acid dosage dependently inhibits IBV replication and enhances IBV-induced eIF2α phosphorylation [195]. Moreover, IBV replication is not affected by PKR or PERK knock-down, indicating that similar to SARS-CoV, IBV is not sensitive to the antiviral activities of PKR or PERK *in vitro* [156].

1.3.3 The IRE1 branch of UPR

1.3.3.1 The IRE1 signaling pathways

The IRE1 branch of UPR is highly conserved from yeast to humans [196]. Initial studies have suggested that IRE1 is activated via a similar mechanism as PERK, which involved ER stress induced dissociation of BiP followed by oligomerization and trans-phosphorylation [168,197]. This idea is further strengthened by the high sequence homology (~47%) of the two proteins' N-terminal luminal domains (NLDs), and the fact that their NLDs are interchangeable *in vivo* [198]. However, recent studies have demonstrated that the NLD of IRE1 can directly bind unfolded proteins [199]. Moreover, the dissociation of BiP may not be the primary switch for IRE1 activation, but rather serves as a buffer to modulate the sensitivity and dynamics of IRE1 [200].

Phosphorylation of IRE1 activates its cytosolic RNase domain, which results in the unconventional splicing of the mRNA of homologous to Atf/Creb1 (HAC1) in yeast and X-box binding protein 1 (XBP1) in Metazoans [201,202]. The sequence flanking the spliced intron is highly conserved, which forms secondary structures recognized by IRE1 [203]. In human, splicing of the 26-nucleotide intron leads to a frame-shift transcript, which encodes the spliced XBP1 protein (XBP1s) [202]. XBP1s is a potent bZIP transcription factor that induces expression of genes harboring the UPR element (UPRE) or the ER stress response element (ERSE) in the promoter sequences [204]. To counteract ER stress, XBP1s regulates genes

involved in protein entry into ER, folding, glycosylation, ER-associated degradation (ERAD), lipid biogenesis and vesicular trafficking [205]. The expression of at least two genes, the ER DNA J domain-containing protein 4 (ERdj4) and the protein kinase inhibitor of 58 kDa ($p58^{IPK}$) have been shown to be specifically induced by XBP1s, but not other UPR transcription factors [206]. XBP1s also induces the E3 ubiquitin ligase synoviolin, which promotes ubiquitination and degradation of IRE1, forming a negative feedback loop [207,208]. The unspliced mRNA (XBP1u) is also translated, which contains only the bZIP domain but not the transactivation domain. XBP1u has been shown to negatively regulate the activity of XBP1s and undergoes rapid proteasome dependent degradation **(Figure 1-10)** [209,210].

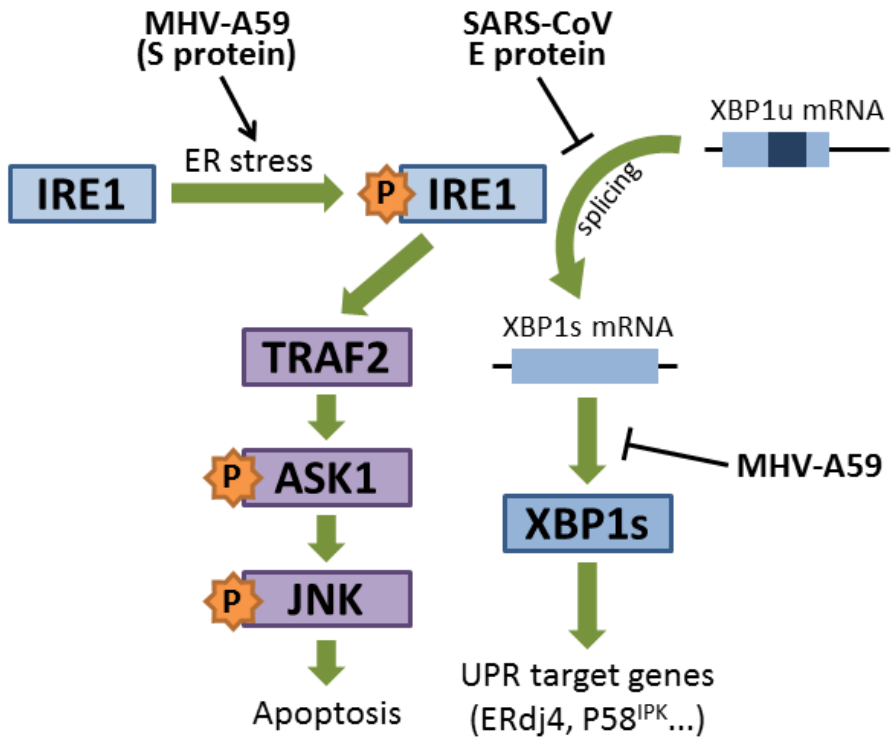

Figure 1-10 IRE1 signaling pathway during coronavirus infections.

IRE1 mediates splicing of XBP1, which induces UPR genes such as ERdj4 and $p58^{IPK}$. IRE1 can also recruit TRAF2 and activate JNK-mediated apoptosis. Overexpression of the spike proteins of IBV and MHV-A59 has been shown to activate IRE1, whereas the SARS-CoV E protein inhibits XBP1 splicing. See text for detail.

Previously, the mRNA of XBP1 has been considered the only splicing substrate for IRE1. Recently, Hollien et al. have identified degradation of ER-localized mRNAs by IRE1 under ER stress, which is termed regulated IRE1-dependent mRNA decay (RIDD) [211,212]. Although most RIDD substrates identified harbor XBP1-like consensus sequences [213], IRE1-mediated XBP1 splicing and RIDD seems to operate via two distinct mechanisms [214]. Whereas basal level of RIDD removes ER-associated mRNA to facilitate ER homeostasis, prolonged RIDD has been shown to degrade mRNAs encoding pro-survival proteins and contribute to ER-stress induced cell death [215].

Apart from mediating XBP1 splicing, the kinase domain of phosphorylated IRE1 has been shown to recruit the tumor necrosis factor (TNF) receptor-associated factor 2 (TRAF2) [216]. The IRE1-TRAF2 complex further interacts with the Apoptosis signal-regulating kinase 1 (ASK1), which ultimately activates the c-Jun N-terminal kinase (JNK) and induces ER stress dependent apoptosis **(Figure 1-10)** [217]. The IRE1-JNK pathway is also required for autophagy activation after pharmacological induction of ER stress [218]. The decision between autophagy and apoptosis in cells under ER stress may be intricately regulated by multiple mechanisms, including the JNK-mediated phosphorylation of Bcl2 and the stress integrator Bax-inhibitor 1 [219,220]. In short, IRE1 facilitates the resolution of ER stress by activating the UPR gene master control XBP1 and induction of autophagy, but prolonged activation of IRE1 can also trigger RIDD and apoptosis via the JNK pathway.

1.3.3.2 Activation of IRE1 pathway during coronavirus infections

MHV infection or overexpression of its spike protein has been shown to induce significant splicing of XBP1 mRNA [155,191]. However, XBP1s protein cannot be detected in the infected cells and downstream genes such as ERdj4, EDEM1 and $p58^{IPK}$ are not up-regulated. It is possible that sustained translation attenuation by MHV-induced eIF2α phosphorylation blocks the translation of XBP1s protein and suppresses the activation of this branch of UPR [191]. In contrast to MHV, infection of SARS-CoV or transfection of SARS-CoV spike protein fails to induce XBP1 mRNA splicing [155,221]. This observation have been attributed to the ability of SARS-CoV E protein to suppress host stress response [221]. A recombinant SARS-CoV with the E gene deleted (rSARS-CoV-ΔE) has been generated, and significant XBP1 splicing and higher expression levels of UPR genes are observed in the

infected cells, compared with wild type SARS-CoV. Furthermore, transfection of E protein strongly inhibits ER stress induced by chemicals or RSV infection [221]. The UPR modulating function of E protein may explain why SARS-CoV lacking E protein is attenuated in animal models [52], but its detail mechanisms remain to be investigated. Activation of the IRE1 pathway in cells infected with Gammacoronaviruses has not been systematically studied before. In this project, IBV is used as a model Gammacoronavirus to study the involvement of IRE1 pathway in coronavirus-host interactions, with an emphasis on viral induced apoptosis.

1.3.4 The ATF6 branch of UPR

1.3.4.1 The ATF6 signaling pathways

Unlike PERK or IRE1, the ATF6 protein is a Type-II transmembrane protein with an N-terminal bZIP signaling domain and an ER luminal domain that is modified by glycosylation and disulfide bonding. Similar to PERK, ATF6 is activated by ER-stress induced dissociation of BiP [222], although underglycosyltion [223] and reduction of disulfide bonds [224] have also been suggested as alternative activation mechanisms. Activated ATF6 is translocated to Golgi apparatus and processed by the Site-1 protease (S1P) and Site-2 protease (S2P) [225]. The intramembrane proteolysis releases the cytosolic DNA binding domain, which translocates into the nucleus and switches on genes harboring ERSE or ERSE-II in the promoters [226]. The major target genes of ATF6 consist of ER chaperones (such as BiP, GRP94 and calreticulin) and some ERAD components, thus activation of the ATF6 branch promotes protein folding and restoration of ER homeostasis (Figure 1-11) [227].

1.3.4.2 Activation of ATF6 pathway during coronavirus infections

Compared with PERK and IRE1, there have been limited studies on the activation of ATF6 pathway during coronavirus infections. The cleavage of ATF6 can be observed in cells infected with MHV, but the level of both full length and cleaved ATF6 protein diminish at late stage of infection, with no activation of target genes determined by ERSE reporter constructs [191]. Similar to XBP1s, the lack of ATF6 transactivation may be a result of sustained translation suppression mediated by eIF2α phosphorylation. As for SARS-CoV, no significant ATF6 cleavage is observed compared with mock infected cells [221]. Overexpression of the SARS-CoV spike protein also fails to activate ATF6 reporter constructs [151]. In contrast, ATF6

cleavage and nuclear translocation have been determined in cells transfected with the SARS-CoV accessory protein 8ab, which has also been shown to physically interact with the luminal domain of ATF6 [154]. The SARS-CoV 8ab protein was only detected in early human isolates during the SARS-CoV pandemic. In the later isolants, genome deletion resulted in the splitting of ORF8 into two smaller ORFs, encoding two truncated protein 8a and 8b respectively [228]. Therefore, further experiments on the 8a and 8b proteins, as well as studies using recombinant SARS-CoV deletion mutants are required. There has been no published study regarding the activation of the ATF6 pathway in cells infected with Gammacoronaviruses.

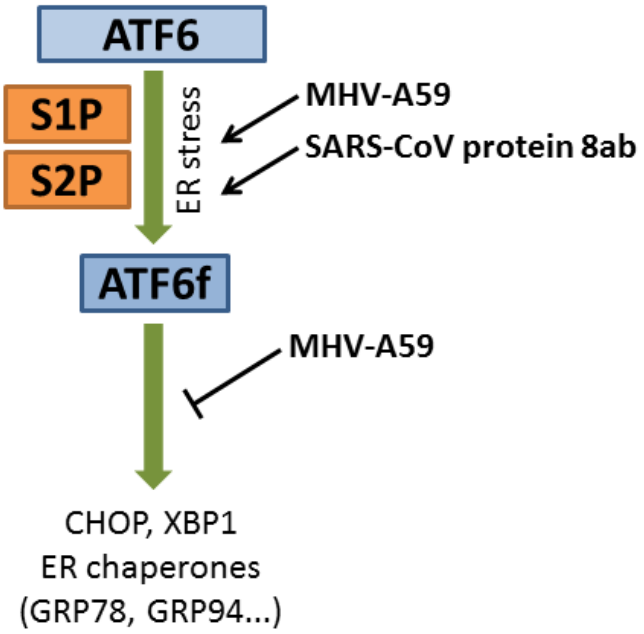

Figure 1-11 ATF6 signaling pathway during coronavirus infections.

ATF6 protein is cleaved by S1P and S2P under ER stress. The released fragment (ATF6f) translocates to the nucleus and induces UPR genes such as CHOP, XBP1 and ER chaperones. Transfection of SARS-CoV accessory protein 8ab or infection with MHV-A59 has been shown to induce ATF6 cleavage. See text for detail.

1.3.5 UPR and coronavirus-induced apoptosis

Prolonged UPR activation is known to cause apoptotic cell death and has been reviewed in detailed [167,229]. It has also been demonstrated that coronavirus infections induce apoptosis *in vitro* [230,231] and *in vivo* [232,233], which is caspase-dependent but p53-independent [234,235]. Also, coronavirus-induced apoptosis is dependent on but not essential for virus replication [124,125]. However, there have been limited studies on the involvement of UPR in coronavirus-induced apoptosis [236]. Here, we summarize current knowledge on ER stress induced apoptosis and the implications of UPR during coronavirus infections.

1.3.5.1 Apoptosis induction and regulation: PERK and the ISR

The early phase of ISR, characterized by eIF2α phosphorylation and translation attenuation, aims to restrict ER stress and is pro-survival in nature. However, at late stage of persistent ER stress, with the induction of CHOP and restoration of protein synthesis by GADD34, the pathway becomes pro-apoptotic. First, resuming protein translation in a stressed ER aggravates the ER burden and allows for the expression of pro-apoptotic proteins, such as CHOP and ER oxidoreductin-1α (ERO1α) [185]. Secondly, CHOP promotes the intrinsic pathway of apoptosis by inhibiting the transcription of anti-apoptotic Bcl2 [237] and inducing the pro-apoptotic protein Bcl2-interacting mediator of cell death (Bim) [238]. Moreover, CHOP also promotes the extrinsic pathway of apoptosis by inducing the cell-surface death receptor 5 (DR5), which mediates apoptosis via caspase-8 cleavage [239]. Previously studies in this lab have shown that both the mRNA and protein level of CHOP are significantly induced in IBV-infected cells at late stage infection [156]. Knock-down of PKR or PERK significantly reduces IBV-induced CHOP up-regulation and apoptosis. Knock-down of CHOP almost completely abolishes IBV-induced apoptosis in the infected cells, which is associated with the hyper-phosphorylation of the pro-survival extracellular signal-related kinase (ERK) **(Figure 1-12)** [156]. Induction of CHOP is either not observed or not determined in cells infected with other coronaviruses, although Krähling et al have shown that PKR is required for SARS-CoV-induced apoptosis, which is independent of eIF2α phosphorylation [192]. On the other hand, increased eIF2α phosphorylation has been associated with enhanced cytopathic effect and apoptosis in cells infected with TGEV lacking the accessory gene 7 [194].

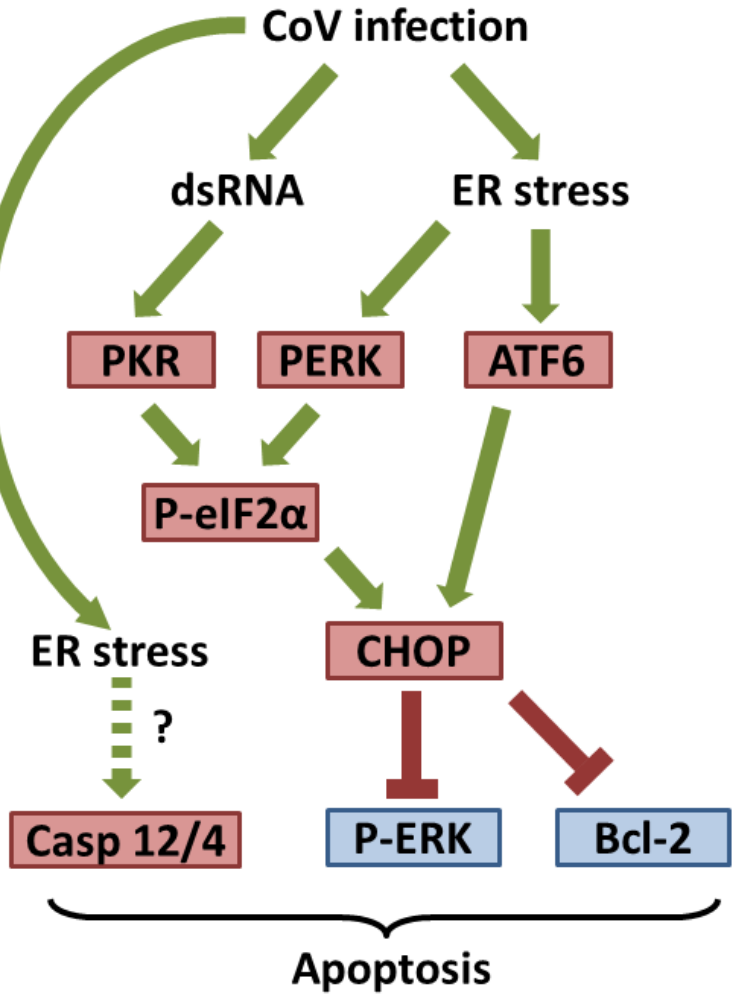

Figure 1-12 Involvement of UPR in coronavirus-induced apoptosis.

Under prolonged ER stress, phosphorylation of eIF2α by PKR/PERK up-regulates CHOP, which has been shown to suppress the pro-survival kinase ERK and the anti-apoptotic mitochondrial protein Bcl2. ATF6 potentially facilitates apoptosis by induction of CHOP. ER-stress induced apoptosis has also been associated with cleavage of caspase 12 (Casp 12) in mouse or caspase 4 (Casp4) in human, although their involvement during coronavirus infections is unknown. Pro-apoptotic factors are shown in red boxes, while pro-survival proteins in blue boxes. See text for detail.

1.3.5.2 Apoptosis induction and regulation: IRE1, ATF6 and other mechanisms

Similar to PERK, IRE1 can be either pro-survival or pro-apoptotic depending on the strength of activation and the downstream signaling pathways. Enhancement of protein folding and ERAD through the IRE1-XBP1 pathway, as well as basal RIDD of ER-associated mRNAs are considered beneficial for adaptation to ER stress and cell survival [167]. In contrast, signaling through the IRE-JNK pathway and prolonged RIDD activation are considered detrimental and induce apoptotic cell death [215]. As mentioned above, compared with the wild type virus, SARS-CoV lacking the E gene induces XBP1 splicing and a high level of stress response, which is also associated with a higher degree of apoptosis [221]. This may suggest a pro-apoptotic role of IRE1 during SARS-CoV infection, although further functional experiments are required. The involvement of the IRE1 pathway in apoptosis induced by other coronaviruses has not been determined so far.

The involvement of ATF6 in coronavirus-induced apoptosis has not been characterized. Interestingly, preliminary results from this group have suggested a pro-apoptotic role of ATF6 during IBV infection, which is contrary to the common believe that ATF6 facilitates adaptation to ER stress and promote cell survival [167]. Moreover, several recent findings have demonstrated that under certain conditions ATF6 activation may also induce apoptosis via transcriptional activation of CHOP and/or suppression of myeloid cell leukemia sequence I (Mcl-1) [240-242]. Aside from the three UPR branches, ER stress induced apoptosis has been shown to be mediated by other mechanisms, such as fluctuation of ER calcium concentration [229] and activation of murine caspase 12 [243] or human caspase 4 [244]. However, the involvement of these UPR-independent pathways in coronavirus-induced apoptosis remains undetermined.

1.3.6 UPR and innate immunity during coronavirus infections

The innate immunity constitute a pivotal anti-viral response against coronavirus infections, although over-activated inflammatory response also causes extensive tissue damage and other immunopathologies associated with SARS-CoV infection [245]. In fact, highly elevated production of pro-inflammatory cytokines/chemokines such as interleukin-1 (IL-1), IL-6, IL-8, Interferon gamma-induced protein 10 (IP-10) and monocyte chemoattractant protein-1 (MCP-1) has been detected in the lung tissues and serum samples from SARS-CoV patients

[246,247]. Recent studies have suggested that the UPR may cross-talk with the innate immune signaling pathways and modulate the production of type-I interferons and/or pro-inflammatory cytokines in virus infected cells [248]. In the following section, implications of UPR in the innate immunity in the context of coronavirus infections will be briefly discussed.

1.3.6.1 UPR-mediated NF-κB activation

For decades, the transcription factor nuclear factor kappa-light-chain-enhancer of activated B cells (NF-κB) has been well established as the master regulator of innate immunity and pro-inflammatory response [249]. Expression of pro-inflammatory cytokines (such as IL-6 and IL-8) and the early expression of type-I interferon has been shown to be induced by NF-κB together with other transcription factors, such as activator protein 1 (AP-1), interferon regulatory factor 3 (IRF3) and IRF7 [250-253]. Specifically, the SARS-CoV spike protein dosage-dependently induces the production of TNF-α, IL-6 and IL-8 in transfected cells, which is mediated by the NF-κB pathway [254,255].

In its inactive form, NF-κB is sequestered by the inhibitor of NF-κB alpha (IκBα), which prevent the nuclear translocation of NF-κB [256]. The protein level of IκBα is determined by the rate of synthesis and its degradation by the proteasome. Degradation of IκBα is in turn facilitated by the IκB kinases (IKK), since phosphorylated IκBα is efficiently modified by poly-ubiquitination and targeted for proteasomal degradation [257]. The PERK and IRE1 branches of UPR have been shown to activate NF-κB **(Figure 1-13)**. Translation attenuation mediated by eIF2α phosphorylation effectively decreases the synthesis of IκBα protein in cells under various stress conditions [258]. On the other hand, IRE1 has been shown to complex with TRAF2 and activate the basal activity of IKK in cells under ER stress, thus facilitating the phosphorylation and degradation of IκBα [259]. With less synthesis and more degradation, the protein level of IκBα is reduced, and NF-κB is in turn activated.

NF-κB activation in cells under ER stress may be mediated by UPR via other mechanisms. For example, ER stress induces expression of CHOP, which forms a heterodimer with the CCAAT/enhancer binding protein β (C/EBPβ), preventing it from trans-activating another transcription factor called peroxisome proliferator-activated receptor γ (PPARγ) [260]. Because PPARγ is a negative regulator of NF-κB, up-regulation of CHOP in cells under ER

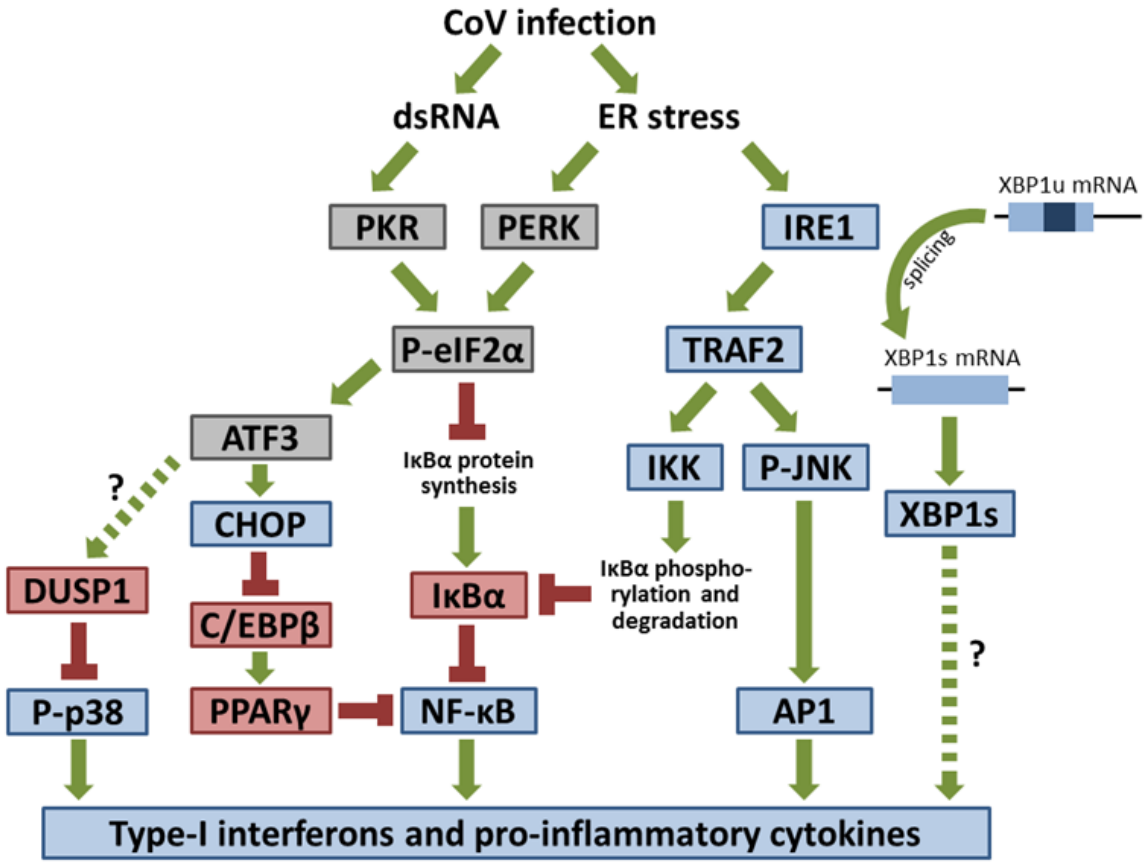

Figure 1-13 Involvement of UPR in innate immunity during coronavirus infections.

The PKR/PERK mediated eIF2α phosphorylation leads to translation attenuation and lower level of IκBα synthesis. On the other hand, IRE1 recruits TRAF2 and activates IKK to phosphorylate IκBα, promoting its ubiquitination and degradation. The outcome is a lower protein level of IκBα, releasing NF-κB for activation of type-I interferons and/or cytokines. The PERK branch also activates NF-κB by up-regulation of CHOP, which forms heterodimer with C/EBPβ and prevent it from activating PPARγ that suppresses NF-κB activation. The MAP kinases p38 and JNK activate AP-1 and promote cytokine production. Under ER stress, JNK is phosphorylated by IRE1/TRAF2 complex, while ATF3 has been shown to induce DUSP1 that de-phosphorylates p38. Several proteins, such as GADD34 or the spliced form of XBP1, have been shown to cross-talk with the innate immune signaling. Refer to text for detailed description. See text for detail.

stress thus in effect activates NF-κB and induces the expression of IL-8 [260] (**Figure 1-13**). Activation of NF-κB has also been associated with the ATF6-dependent phosphorylation of RAC-alpha serine/threonine-protein kinase (Akt), although the detail mechanisms have not been determined [261]. Finally, it should be noted that during coronavirus infections, mediators of innate immunity may be targeted and modulated by the virus. Therefore, functional studies need to be performed to validate the involvement of these signaling pathways in the context of coronavirus infections.

1.3.6.2 UPR-mediated p38 activation

Previously, the induction of IL-6 in cells infected with MHV has been shown to be mediated by the MAP kinase p38 [262]. Studies from this group have also demonstrated that induction of IL-6 and IL-8 in IBV-infected cells is dependent on p38 phosphorylation [263]. Also, as a negative feedback mechanism, IBV induces the expression of the dual specificity protein phosphatase 1 (DUSP1), which de-phosphorylates p38 and suppresses cytokine production [263]. Previous studies have indicated that DUSP1 is up-regulated in cells under ER stress [264,265], possibly via the action of ATF3 in the PERK branch of UPR [266]. In fact, one recent study has detected a reduced activation of the PERK-eIF2α pathway in cystic fibrosis airway cells, resulting in a higher level of phosphorylated p38 and increased production of IL-6 [267]. Therefore, the signaling through PERK-ATF3-DUSP1 may be used by coronavirus to down-regulate p38 activation and cytokine induction in the infected cells **(Figure 1-13).**

1.3.6.3 GADD34, XBP1, RIDD and innate immunity

Besides the well characterized involvement of UPR in NF-κB and MAP kinase activation, UPR has also been shown to modulate innate immune response by other mechanisms. In particular, the UPR proteins GADD34 and XBP1, as well as the RIDD activity of IRE1, have been implicated in the production of type-I interferons and pro-inflammatory cytokines.

As mentioned above, GADD34 is a co-factor of PP1 that mediates the de-phosphorylation of eIF2α to reverse translation attenuation. Interestingly, when dendritic cells (DCs) are treated with polyriboinosinic:polyribocytidylic acid (polyI:C), expression of GADD34 is induced via the PKR-eIF2α-ATF4 pathway [268]. Although GADD34 does not significantly affect protein synthesis, it is required for the polyI:C induced production of interferon β (IFN-β)

and IL-6 [268]. Importantly, similar GADD34-dependent induction of IFN-β and IL-6 has also been observed in mouse embryonic fibroblasts and mouse neonates infected with Chikungunya virus (CHIKV) [269]. In a separate study, however, GADD34 is shown to suppress the production of pro-inflammatory cytokines TNF-α and IL-6 in macrophages triggered by toll-like receptor 3 (TLR3), TLR4, and TLR9 [270]. This inhibition is mediated by the GADD34/PP1 dependent de-phosphorylation of TGF-β-activated kinase 1 (TAK) in the TLR signaling pathway. Therefore, the activity of GADD34 in innate immune response seems to be cell type and stimulus-specific. Since induction of GADD34 has been observed in IBV-infected cells [195], it would be desirable to examine its involvement in cytokine production induced by IBV and other coronaviruses.

The transcription factor XBP1 downstream of IRE1 pathway has also been implicated in innate immune response (**Figure 1-13**). In mouse macrophages treated with TLR2 agonist Pam3CSK4 or TLR4 agonist lipopolysaccharide (LPS), significant IRE1 activation and XBP1 mRNA splicing has been detected [271]. Moreover, TLR-activated XBP1 is required for the optimum and sustained production of IFN-β and pro-inflammatory cytokines (such as IL-6 and TNF-α) [271]. Similar XBP1-dependent induction of IFN-β has also been observed in murine DCs treated with polyI:C [272]. Notably, recent studies have identified putative XBP1 binding to the promoter/enhancer sequences of IL-6, TNF-α and IFN-β [271,273]. In terms of coronavirus infections, induction of IL-8 has been associated with ER stress and XBP1 splicing in cells infected with MHV or in cells overexpressing the MHV spike protein [155].

Intriguingly, one recent study has pointed to the innate immune signaling function of IRE1, which is mediated via RIDD and is independent of XBP1. In their study, Cho et al. have shown that the A subunit of Cholera toxin (CTA) induces ER stress and activates the RIDD activity of IRE1, which degrades endogenous mRNA into small fragments [274]. These mRNA fragments are recognized by the cytosolic sensor retinoic acid-inducible gene 1 (RIG-I), which activates NF-κB and induces the production of pro-inflammatory cytokines such as IL-6 and IL-8. Similar observations have been obtained with Shiga toxin and SV40 virus, both of which also enter the ER to induce disease [274]. Therefore, the IRE1-RIDD dependent signaling may be a general mechanism to bridge ER stress and innate immune response, and its implication during coronavirus infections deserves further investigation.

1.4 JNK – THE STRESS-ACTIVATED MAP KINASE

The mitogen activated (MAP) kinases are evolutionarily conserved protein kinases that regulate a diversity of critical cellular signaling pathways in response to extracellular stimuli, such as cell division, differentiation, autophagy, apoptosis, innate immunity and pro-inflammatory response [275]. So far, four subgroups of MAP kinases have been identified in metazoans, namely the extracellular regulated kinase 1/2 (ERK1/2), ERK5, the p38 MAP kinase and the c-Jun N-terminal kinases (JNK) [276,277]. In the following sections, the JNK signaling pathways, as well as the involvement in apoptosis and innate immunity will be reviewed.

1.4.1 JNK signaling pathways

JNK, also known as the stress-activated protein kinase, is activated by a variety of environmental stress, such as oxidative stress, DNA damage, ionizing radiation, protein synthesis inhibition etc. [276]. JNK is also activated by pro-inflammatory cytokines such as TNF-α and IL-1 [278,279], or by growth factors such as transforming growth factor β (TGF-β) [280]. Similar to other MAP kinases, JNK is activated through a kinase signaling cascade. The signal initiators responding to cellular stresses are small GTPases of the Ras homolog (Rho) family, such as Rho, Ras-related C3 botulinum toxin substrate (Rac) and cell division control protein 42 (cdc42). These GTPases activate the MAP kinase kinase kinase (MKKK), which include at least 14 kinases differentially regulated by protein interactions and covalent modifications [281] . The MKKK in turn activates the MAP kinase kinase (MKK). The N-lobe presents in the kinase domain of MKKK interacts with the domain for versatile docking (DVD) site in MKK, facilitating the dual phosphorylation of two residues in the MKK's catalytic domain [282]. Two MKKs – MKK4 and MKK7 have been associated with JNK activation, which involves the dual phosphorylation of a threonine and a tyrosine residue within a conserved Thr-Pro-Tyr motif inside JNK's catalytic domain. Whereas MKK7 is specific for JNK only, MKK4 has been shown to also phosphorylate p38. Moreover, the two MKKs are differentially activated by upstream kinases, with MKK4 primarily activated by environmental stress and MKK7 primarily activated by cytokines [281]. Apart from the interactions via docking domains, the MKKK-MKK-JNK signaling module is also organized by scaffold proteins, such as JNK interacting proteins (JIP). The assembly of the JNK signaling module is demonstrated in **Figure 1-14**.

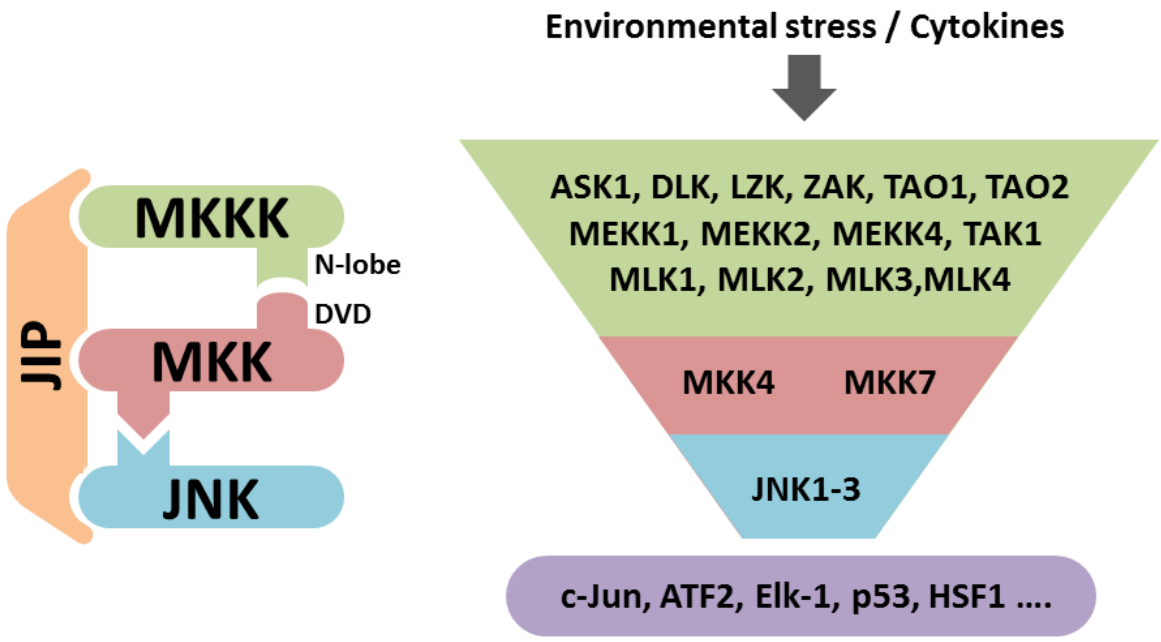

Figure 1-14 The JNK signaling module and kinase cascade.

Left, the assembly of the JNK signaling module is facilitated by physical interactions between substrates and upstream kinases via docking domains and bindings of scaffold proteins such as JIP. Right, the inverted pyramid of kinase cascade in JNK signaling. At least 14 MKKKs activates two MKKs, which in turns activates JNK. JNK phosphorylates substrates such as c-Jun to enhance their transcription activity. ASK1, apoptosis signal-regulating kinase 1; DLK, dual leucine zipper-bearing kinase; LZK, leucine zipper-bearing kinase; ZAK, zipper sterile alpha motif kinase; TAO1/2, thousand and one amino acid protein kinase 1/2; MEKK1-4, MAPK/ERK kinase kinase 1-4; TAK1, transforming growth factor beta-activated kinase 1; MLK1-4, mixed-lineage kinase 1-4. See text for detail.

The JNK protein kinases are encoded by three genes: JNK1, JNK2 and JNK3. Whereas JNK1 and JNK2 are expressed ubiquitously, JNK3 is primarily expressed in the brain, heart and testis [281]. Moreover, alternative splicing of the transcripts results in at least ten JNK isoforms, although functional significance of these isoforms is still unknown. When resolved by SDS-PAGE and detected by Western blot, two bands of 46kDa and 55kDa are usually observed. Although mice deficient of JNK1 or JNK2 are morphologically normal, they are defective in T

cell function and thus immunodeficient [283]. The best characterized function of JNK is phosphorylation of the transcription factor c-Jun at Ser 63 and Ser 73, thus the name c-**J**un **N**-terminal **K**inases [284] (**Figure 1-14**). Apart from c-Jun, JNK has also been shown to phosphorylate other transcription factors such as activating transcription factor 2 (ATF2), ETS domain-containing protein (Elk-1), p53 and heat-shock factor 1 (HSF1), to name just a few [285-288]. JNK mediated phosphorylation generally activates the transcription factors. For example, phosphorylated c-Jun heterodimerizes with FBJ murine osteosarcoma (c-Fos) to form the activator protein 1(AP-1) complex, which binds to promoters harboring the 12-O-tetradecanoylphorbol-13-acetate (TPA) response element and activates gene expression [289]. The kinase activity of JNK is negatively regulated by various mechanisms, such as dephosphorylation by the dual-specificity phosphatases (DUSPs) [290].

1.4.2 Activation of the JNK pathway during coronavirus infections

JNK phosphorylation has been detected in cells infected with MHV or SARS-CoV [262,291]. Activation of the JNK pathway has also been demonstrated in cells overexpressing the N protein, accessory protein 3a, 3b or 7a of SARS-CoV [128,292,293]. In a study using specific inhibitors, Mizutani et al have shown that the JNK and Akt signaling pathways are required for establishing persistent SARS-CoV infection in Vero E6 cells, suggesting a pro-survival function for these kinases [294]. Phosphorylation of JNK and Akt is likely induced by the SARS-CoV N protein, and the anti-apoptotic Bcl2 and Bcl-xL proteins may also contribute to the persistent infection [295]. JNK activation has also been observed in HEK293 cells overexpressing the SARS-CoV S protein [296]. The spike protein of SARS-CoV activates the protein kinase C epsilon (PKCε), which induces JNK phosphorylation in a calcium independent manner. Moreover, JNK is required for the activation of cyclic AMP response element binding proteins (CREB) and the expression of cyclooxygenase-2 (COX-2) gene induced by the SARS-CoV spike protein [296]. To conclude, it is generally accepted that JNK is activated during coronavirus infections, but the detail mechanisms of the upstream signaling pathways and the implications in regulating host innate immune response are still largely unknown.

1.4.3 The role of JNK in apoptosis signaling

Previous studies have demonstrated that the JNK pathway is closely associated with apoptotic signaling [297]. In fact, *JNK1-/-JNK2-/-* mouse embryonic fibroblasts (MEFs) were found to be resistant to apoptosis in response to UV irradiation, DNA damage and translation inhibition [298]. Moreover, MEFs with non-phosphorylatable alanine mutation in c-Jun showed a similar resistance to UV-induced apoptosis [299]. The pro-apoptotic role of JNK is further supported by studies using JNK inhibitors. Apoptotis of hepatocytes and cardiomyocytes following ischemia/reperfusion injuries has been shown to be attenuated in rats treated with JNK inhibitors [300,301]. JNK-mediated apoptosis is likely mediated by two mechanisms: transactivation of pro-apoptotic genes in the nucleus and interactions with the Bcl2 family of proteins in the mitochondria [297].

Upon phosphorylated by MKKs, JNK translocates into the nucleus and activates substrate transcription factors [281]. JNK dependent activation of AP-1 has been shown to up-regulate the expression of pro-apoptotic genes such as BAK1, FasL and TNF-α [302]. However, under certain conditions, JNK-mediated apoptosis could occur independent of AP-1 [303]. It is proposed that whether JNK activation of AP-1 is required for apoptosis seems to be highly dependent on the cell type and the type of apoptotic stimuli [304]. This is not unexpected, because other transcription factors have been identified as JNK substrates. For example, JNK has been shown to phosphorylate p53 and inhibit its ubiquitin-mediated degradation [287]. Later studies have further demonstrated that JNK is required for p53-dependent apoptosis in cells overexpressing 10-formyltetrahydrofolate dehydrogenase [305]. JNK-dependent phosphorylation and stabilization is also required for DNA damage induced apoptosis mediated by p73, another transcription factor from the p53 family [306]. After activated by JNK, p53 and p73 most likely promote apoptosis by inducing the expression of pro-apoptotic Bcl2 proteins such as BAX and PUMA (**Figure 1-15**).

In addition to the nuclear activities, JNK has been shown to translocate to the mitochondria and modulate the function of Bcl2 family proteins [307]. For example, a pro-apoptotic BH3-only protein called Bid, has been found to be cleaved by JNK independent of caspase 8 [308]. The resulting fragment – jBid then translocates to mitochondria and promote the release of the pro-apoptotic protein Second mitochondria-derived activator of caspase (Smac,

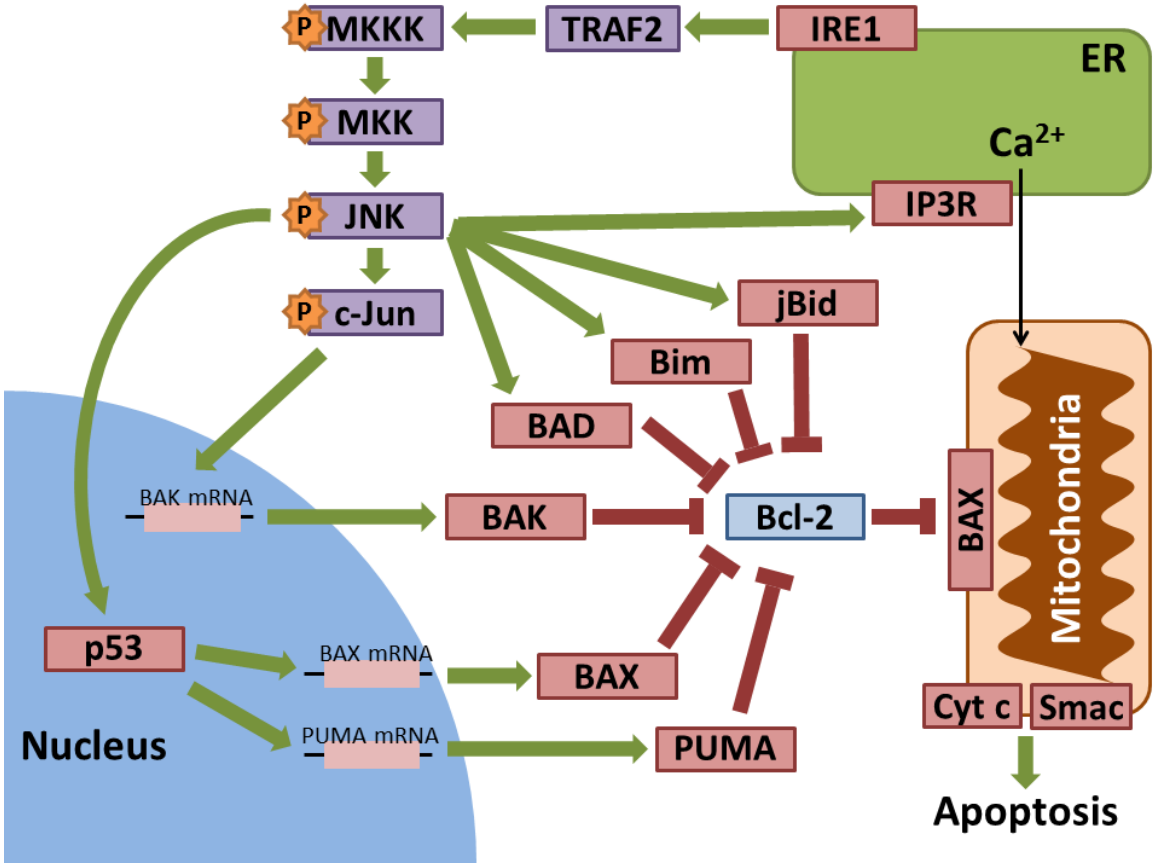

Figure 1-15 The role of JNK in apoptotic signaling.

JNK promotes apoptosis by nucleus- and mitochondria-targeted signaling. Phosphorylated JNK translocates into the nucleus and activates pro-apoptotic proteins such as p53 and BAK. The p53 family of transcription factors induces the expression of pro-apoptotic protein BAX and PUMA. Some pro-apoptotic Bcl2 family proteins (such as BAD, Bim, Bmf) are directly phosphorylated and activated by JNK. Bid is known to be cleaved and activated by JNK. JNK are also involved in apoptosis signaling crosstalk between ER and mitochondria. ER stress activates IRE1, which is known to activate JNK via TRAF2. JNK is also required for calcium ion release from the ER, which is taken up by the mitochondria and induces apoptosis by disrupting the outer membrane permeability. Inhibition of Bcl2 by pro-apoptotic Bcl2 family proteins, release BAX from sequestration, allowing it to form pores on the mitochondrial outer membrane. This leads to the release of cytochrome c (Cyt c) and Smac, formation of the apoptosome, activation of the caspase cascade and induction of apoptosis. See text for detail.

also known as direct IAP-binding protein with low pI, or DIABLO). JNK-dependent phosphorylation of Bim and Bcl2 modifying factor (Bmf) has been shown to dissociate them from sequestering motor protein complexes and allow for their pro-apoptotic activity [309]. Moreover, JNK has been shown to phosphorylate BAD and its inhibitory binding partner 14-3-3 protein [310,311]. This releases BAD from sequestration and allows it to inhibit the anti-apoptotic Bcl2 proteins, thereby promoting apoptosis [312]. Finally, JNK has also been demonstrated to directly phosphorylate Bcl2 at Ser70 and inhibit its anti-apoptotic activity during apoptosis induced by pacilitaxel [313] (**Figure 1-15**).

Recent studies have also suggested the pro-apoptotic role of JNK in the crosstalk between ER and mitochondria [314]. As mentioned above, JNK is activated by the kinase activity of IRE1 during ER stress and accounts for ER-stress induced apoptosis [216]. Also, during IL-1β-mediated cell death, JNK is required for the ER Ca^{2+} release via the inositol 1,4,5-triphosphate receptor [315]. The perturbation of ER Ca^{2+} induces ER stress and activates the pro-apoptotic pathways of the UPR [316]. Moreover, Ca^{2+} release from ER is taken up by the mitochondria, resulting in mitochondrial outer membrane permeabilization and induction of apoptosis [315]. Therefore, JNK may act both upstream and downstream of the UPR pathway in the apoptotic signaling (**Figure 1-15**).

1.4.4 JNK and innate immunity

It is generally accepted that activation of the MAP kinases, in conjunction with NF-κB and the interferon-regulatory factors (IRFs), are crucial in regulating the innate immune response. Innate immune cells, such as macrophages and DCs, use a limited number of pattern recognition receptors (PRRs) to recognize the pathogen-associated molecular patterns (PAMPs). The PRRs identified so far include the Toll-like receptors (TLRs), RIG-I-like receptors (RLRs), NOD-like receptors (NLRs) and C-type lectin receptors (CLRs). Although these PRRs are activated by different mechanisms, all of them can activate both the MAP kinase and NF-κB pathways, which in turn induces genes related to pro-inflammatory response [317]

Activation of JNK in innate immune cells is most well characterized in the context of TLR pathway (**Figure 1-16a**). TLRs are transmembrane proteins that recognized extracellular or endosomal PAMPs with their leucine-rich repeats. Upon activation, cytoplasmic Toll and IL-1

receptor (TIR) domains of TLRs interact with TIR-containing adaptor proteins, such as the myeloid differentiation primary-response protein 88 (MYD88) or TIR domain containing adaptor protein inducing IFN-β (TRIF). The MYD88 recruit the IL-1 receptor associated kinase 4 (IRAK4), which in turn recruits IRAK1, IRAK2 and TNF receptor associated factor 6 (TRAF6). The TRAF6 complex catalyses K63-linked polyubiquitination on TRAF6 and IRAK1 [318].

A critical MKKK called transforming growth factor beta-activated kinase 1 (TAK1) is essential for transducing the signal to JNK and NF-κB. Mediated by the TAK1-binding protein 1 (TAB1) and the ubiquitin-binding protein TAB2 and TAB3, TAK1 is recruited to and activated by the TRAF6 complex. TAK1 then activates MKK4 and /or MKK7, which in turn activates JNK. The essential function of TAK1 in TLR-mediated JNK activation is clearly demonstrated with Tak1-/- MEFs, in which NF-κB and AP-1 activation are severely impaired when cells are treated with TNF-α, IL-1 or LPS [319]. In addition, studies using mice with B-cell specific deletion of TAK1 have confirmed the importance of TAK1 in TLR4-mediated activation of JNK and p38 [320]. Furthermore, TAK1 is known to phosphorylate IKK, which promote degradation of IκBα and activation of NF-κB [321]. On the other hand, TLR signaling mediated by the adaptor protein TRIF recruits the TANK-binding kinase 1 (TBK1) and IKK inducible (IKKi), which mediates the phosphorylation of IRF3 and IRF7 [322]. Activated IRF3 and IRF7 translocate into the nuclei and regulate genes harboring the interferon stimulated response element (ISRE). TRIF has also been shown to cross-talk with the NF-κB pathway by activating the receptor-interacting protein 1 (RIP1) [323].

Cytokines and chemokines are secreted by innate immune cells to induce pro-inflammatory response for recruitment of additional immune cells and subsequent induction of the adaptive immune response. In fact, expression of cytokines and chemokines is regulated by the synergistic action of AP-1, NF-κB and IRFs, as evidenced by the presence of respective response elements in the promoter sequences (**Figure 1-16b**). Co-operative binding of these transcription factors has been shown to recruit additional co-activator proteins, such as CREB-binding protein (CBP, also known as p300). The resulting protein complex, called the enhanceosome, facilitates the opening of chromatin structure and promotes transcription of the cytokine/chemokine genes [324].

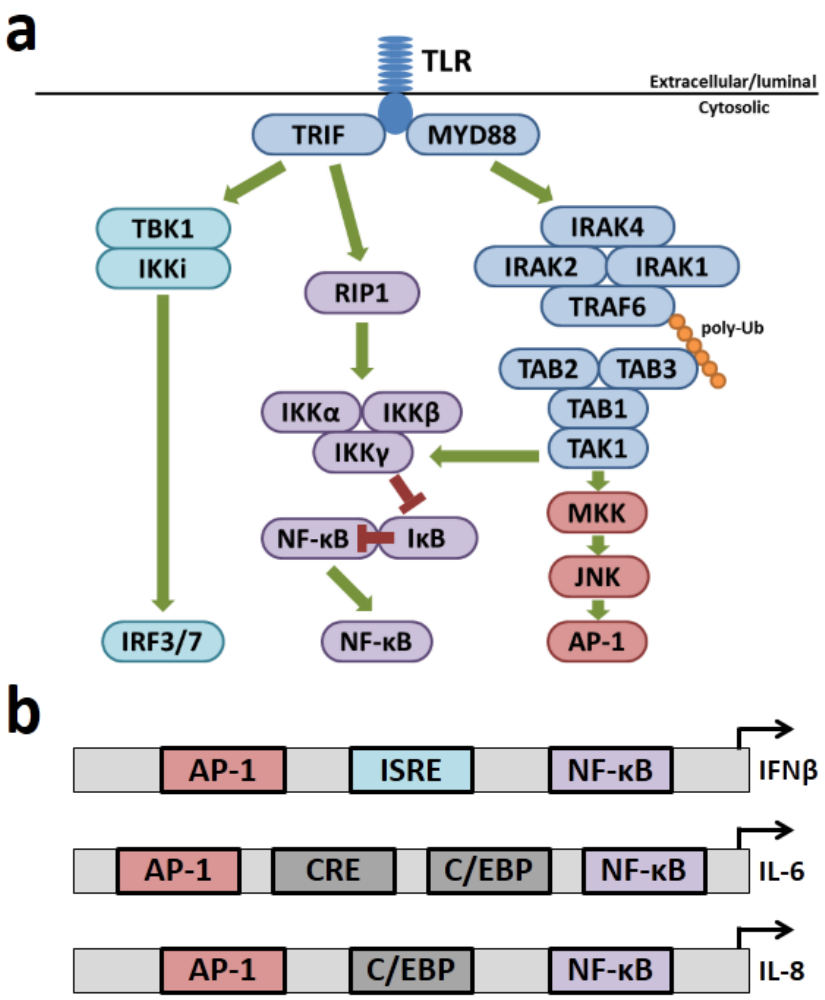

Figure 1-16 The involvement of JNK signaling pathway in innate immunity.

(a) Schematic diagram of the TLR signaling pathway leading to the activation of IRF3/7, NF-κB and AP-1. Upon activation, the adaptor protein MYD88 recruit the TRAF6 complex that catalyses poly-ubiquitination. With the help of adaptor protein TAB1/2/3, TAK1 is recruited to and activated by the TRAF6 complex. TAK1 phosphorylate MKK, ultimately activating AP-1 via the JNK kinase cascade. TAK1 also activate the IKKs, which promote the degradation of IkB and activation of NF-κB. The adaptor protein TRIF activates TBK1 and IKKi, which phosphorylate and activates IRF3 and IRF7. TRIF also activates the NF-κB pathway by activating the kinase RIP1. (b) Schematic diagram showing the response elements presents in the promoters of IFNβ, IL-6 and IL-8. Binding sites for AP-1 are highlighted in red and binding sites for NF-κB are highlighted in purple. IRF3 and IRF7 bind to the ISRE highlighted in blue. The response elements for CRE and C/EBP are shown in grey boxes.

Among the three MAP kinases, JNK is known to regulate cytokine expression by directly phosphorylation of c-Jun and activation of AP-1 [325]. Indeed, previous studies have shown that overexpression of the SARS-CoV S protein induces the IL-8 promoter, which is dependent on the activation of JNK but not NF-κB [326]. Moreover, the induction of pro-inflammatory cytokines TNF-α and IL-6 in primary mouse astrocytes infected with MHV-A59 is dependent on the activation of JNK, but not NF-κB, ERK or p38 [327]. However, the detailed mechanisms of JNK-dependent cytokine induction during coronavirus infections remain largely unknown.

1.5 OBJECTIVES

As obligate intracellular parasites with small genomes, RNA viruses are known to co-opt host factors and remodel subcellular structures to benefit their replication. From the host's perspective, timely recognition of a viral infection is a prerequisite to elicit effective and specific antiviral response. Therefore, studies on host-virus interactions are pivotal in understanding viral pathogenesis and development of antiviral agents.

The UPR and the JNK kinase are both evolutionarily conserved cellular stress response mechanisms, which cross-talk with crucial signaling pathways and constitute a major aspect of coronavirus-host interaction. Although preliminary studies implicate the involvement of UPR and JNK during coronavirus infections, the detailed mechanisms of the upstream triggers and the downstream effector functions remain largely unexplored.

Using IBV as a model, this study aims to characterize the activation of UPR and JNK pathway in coronavirus-infected cells and study their roles in host-virus interactions. Specifically, the objectives of this study are:

1. To determine the induction of UPR during IBV infection, with an emphasis on the activation of the IRE1-XBP1 and the PERK-eIF2α-CHOP pathway (Chapter Three);
2. To investigate the potential involvement of UPR in the regulation of IBV-induced apoptosis, autophagy and pro-inflammatory cytokines production (Chapter Three);
3. To characterize the activation of JNK in cells infected with IBV (Chapter Four);
4. To explore the role of JNK signaling pathway in regulating apoptosis and innate immune response under the context of IBV infection (Chapter Four);

It is hoped that mechanisms unraveled by this study can contribute to the understanding of host-virus interactions and viral pathogenesis, providing insights to the development of novel anti-viral therapies and vaccines for emerging and re-emerging viruses.

Chapter Two:

Materials and Methods

2.1 MATERIALS

2.1.1 Reagents and chemicals

The reagents and chemicals used in this study, together with the product brands or providers, are summarized in **Table 2-1** as below.

Table 2-1: List of reagents and chemicals

Reagent/Chemical	Brand/Provider
3,5-Dibromosalicylaldehyde (DBSA)	Sigma-Aldrich
6X DNA loading dye	Thermo Scientific
Agarose	Vivantis
Ampicillin	Calbiochem
Chloroquine	Sigma-Aldrich
Deoxyribonucleotides (dNTPs)	Bio-Run
Dithiothreitol (DTT)	Sigma-Aldrich
DNA ladder – 50bp, 100bp, 1kb	Bio-Run
Dulbecco's Modified Eagle Medium (DMEM)	PAA
Ethidium bromide	Bio-Rad
Fetal bovine serum (FBS)	Gibco
Formaldehyde	Sigma-Aldrich
Geneticin Reagent (G418)	Gibco
Kanamycin	Calbiochem
Luminol	Sigma-Aldrich
p-Coumaric acid	Sigma-Aldrich
Penicillin-Streptomycin stock solution	PAA
Protein Ladder	Bio-Rad
Roswell Park Memorial Institute medium (RPMI)	PAA
Sodium Dodecyl Sulfate (SDS)	Merck

SP600125	Sigma-Aldrich
Staurosporine (STS)	Millipore
Triton X-100	Merck
Trizol reagent	Ambion
Trypsin	Gibco
Tween 20	Bio-Rad
β-mercaptoethanol	Sigma-Aldrich

2.1.2 Enzymes

All restriction enzymes were purchased from New England Biolabs. T4 DNA ligase was from Promega. *Taq* DNA polymerase was provided by Bio-Run. High fidelity (HiFi) DNA polymerase was obtained from Kapa Biosystems. Master mixture for quantitative PCR (qPCR) was provided by Life technologies. Reverse transcriptase (ImProm-II) was from Promega.

2.1.3 Antibodies

Table 2-2 summarizes the provider, catalogue number and animal source of primary antibodies used in this study.

Table 2-2 List of primary antibodies

Antibody	Provider	Cat. #	Source
Akt	Cell Signaling Technology	4691	Rabbit
BAK1	Santa Cruz Biotechnology	sc-832	Rabbit
Bcl2	Cell Signaling Technology	2870	Rabbit
Caspase-3	Cell Signaling Technology	9662	Rabbit
Caspase-8	Cell Signaling Technology	9746	Rabbit
Caspase-9	Cell Signaling Technology	9502	Rabbit
c-Jun	Cell Signaling Technology	9165	Rabbit
ERK	Cell Signaling Technology	9102	Rabbit
FLAG-tag	Cell Signaling Technology	2044	Rabbit

GADD153/CHOP	Cell Signaling Technology	2895	Mouse
GFP	Clontech	632381	Mouse
IRE1	Cell Signaling Technology	3294	Rabbit
JNK	Cell Signaling Technology	9258	Rabbit
LC3B	Cell Signaling Technology	3868	Mouse
MKK4	Cell Signaling Technology	9152	Rabbit
MKK7	Cell Signaling Technology	4172	Rabbit
PARP	Cell Signaling Technology	9532	Rabbit
PERK	Cell Signaling Technology	3192	Rabbit
Phospho-Akt	Cell Signaling Technology	4060	Rabbit
Phospho-Bcl2	Cell Signaling Technology	2827	Rabbit
Phospho-c-Jun	Cell Signaling Technology	9261	Rabbit
Phospho-ERK	Cell Signaling Technology	9101	Rabbit
Phospho-JNK	Cell Signaling Technology	4668	Rabbit
Phospho-MKK4	Cell Signaling Technology	9151	Rabbit
Phospho-MKK7	Cell Signaling Technology	4171	Rabbit
Phospho-PERK	Cell Signaling Technology	3191	Rabbit
XBP1	Santa Cruz Biotechnology	sc-7160	Rabbit
β-actin	Cell Signaling Technology	4967	Rabbit
β-tubulin	Santa Cruz Biotechnology	sc-9104	Rabbit

The anti-serum against IBV S protein and N protein were raised in rabbits immunized with bacterial expressed fusion proteins as previously described [45,328].

Horseradish peroxidase (HRP)-conjugated secondary antibodies used for Western blot analysis were purchased from Dako. Fluorochrome-conjugated secondary antibodies used for fluorescent microscopy were purchased from Life technologies.

2.1.4 Compositions of buffer solutions

Table 2-3 summarizes the chemical compositions of buffer solutions used in this study

Table 2-3 List of buffer solutions and their compositions

Buffer	Application	Composition (per liter)
10X gel running buffer	SDS-PAGE	30.2g Tris base (250mM) 144g glycine (1.92M) 10g SDS (1%)
10X wet transfer buffer	Western blot	30.2g Tris base (250mM) 144g glycine (1.92M)
10X Tris buffer saline (TBS)	Western blot	60.6g Tris base (0.5M) 87.8g NaCl (1.5M) Adjust pH to ~7.4 with HCl
1X Membrane stripping buffer (without β-mercaptoethanol)	Western blot	7.6g Tris base (62.5mM) 20g SDS (2%) Adjust pH to ~6.8 with HCl
50X Tris-Acetate-EDTA (TAE)	DNA electrophoresis	242g Tris base (2M) 18.6g EDTA (50mM) Adjust pH to ~8.4 with acetic acid
10X Phosphate buffer saline (PBS)	Cell culture Immunofluorescence	80g NaCl (1.37M) 2g KCl (27mM) 14.4g Na_2HPO_4 (0.1M) 2.4g KH_2PO_4 (20mM) Adjust pH to ~7.4 with HCl

2.2 CELLS AND VIRUSES

2.2.1 Cell culture

H1299 cells (ATCC CRL-5803) were cultured in RPMI 1640 supplemented with 5% fetal bovine serum (FBS) and 1% Penicillin-Streptomycin (PS). Vero cells (ATCC CCL-81) were cultured in high glucose (4,500 mg/L) DMEM supplemented with 5% FBS and 1% PS. HEK293/BOSC23 (ATCC CRL 11270), DF1 (ATCC CRL-12203) and Huh-7 cells were cultured in high glucose (4,500 mg/L) DMEM supplemented with 10% FBS and 1% PS. All cells were grown in a 37^{o}C incubator supplied with 5% CO_2.

Cells in monolayer approaching 100% confluent were sub-cultured in a routine basis. Briefly, medium was removed and cells were washed twice with PBS before incubated with 0.05% trypsin at room temperature. Dissociated cells were collected with medium containing FBS and centrifuged at 500 g for 2 minutes. The cell pellet was re-suspended with fresh culture medium and plated to new culture dishes. Alternatively, the cell pellet was re-suspended with freezing medium (DMEM with 20% FBS and 10% DMSO) and stored at -80°C as cell stock. Only low passage cells (<20 passages) were used for all experiments.

2.2.2 Preparation of IBV stocks

The egg-adapted Beaudette strain of IBV (ATCC VR-22) was obtained from American Type Culture Collection (ATCC) and adapted to Vero cells as previously described [329]. To prepare virus stock, monolayers of Vero cells were infected at a multiplicity of infection (MOI) of approximately 0.1 and cultured in plain Dulbecco modified Eagle medium (DMEM) at 37°C. When the cytopathic effect (CPE) reached 100%, cells were frozen at -80°C and subjected to three freeze/thaw cycles. The cell lysate was clarified by centrifugation at 1,500 g at 4°C for 15 min. The supernatant was aliquot and stored at -80°C as virus stock. The titer of the virus preparation was determined by plaque assays. Mock cell lysate was prepared by same treatment of uninfected Vero cells. Inactivation of IBV was done by exposing the virus stock to 254-nm shortwave UV radiation for 15 minutes with a CL-1000 cross-linker (UVP).

2.2.3 IBV infection

For all experiments involving IBV infection, confluent monolayers of cells were washed twice with respective medium (without FBS or PS) before infected with IBV at the indicated MOI or incubated with same volume of mock Vero cell lysate. After 1-2 hours of adsorption, cells were washed twice with plain medium and incubated at 37°C until harvested for protein or RNA at the indicated time points.

2.2.4 Determination of virus titer by plaque assay

IBV stocks or culture supernatants of IBV infected cells were clarified by centrifugation and 10-fold serially diluted using DMEM. The viral titers were determined by plaque assay. Briefly, 200µl diluted supernatants were applied to confluent monolayers of Vero cells in 6-well plates. The plate was agitated every 10 minutes to ensure proper coverage of the monolayers.

After 1-2 hours of adsorption, unbound viruses were removed and cells were washed twice with DMEM. To each well, 2ml overlay medium (0.4% agarose in DMEM) was added and the plates were incubated at 37ºC for two days before plaques formed. The agarose overlay was removed and cells were fixed with 4% formaldehyde before staining with crystal violet. Finally plaque numbers were count and the titers of individual samples were expressed in the unit of logarithm of plaque forming unites (PFU) per ml. Each sample was titrated in triplicate.

2.3 MOLECULAR CLONING

2.3.1 Preparation of chemically competent cells

Glycerol stock of *Escherichia coli* (*E. coli*) strain DH5α was streaked onto a LB plate and incubated at 37ºC overnight. A single colony was inoculated into a starter culture of 5ml LB broth and cultured overnight at 37ºC with shaking at 250 rpm. Then the starter culture was diluted 100 times in a conical flask and kept incubated at 37ºC with shaking. The growth of bacteria was monitor by optical absorbance at 660nm (OD660) using a spectrophotometer. When OD660 reached 0.8, the culture was chilled on ice for 30 minutes and centrifuged at 4000 rpm for 15 minutes at 4ºC. The pellet was re-suspended in 50ml of ice-cold 0.1M $CaCl_2$ solution and incubated for 30 minutes. After that, the suspension was centrifuged at 4000 rpm for 15 minutes at 4ºC and the pellet was re-suspended in 5ml of 0.1M $CaCl_2$ with 20% glycerol. The competent cells were aliquot in tubes, snap-frozen in liquid nitrogen and stored at -80ºC.

2.3.2 Polymerase chain reaction (PCR) for molecular cloning

PCR was used to amplify the coding sequence (CDS) of genes, as a first step of cloning into expression vectors. The compositions and the thermo cycler program for a typically 50µL PCR reaction is listed as follows:

5µL	High fidelity buffer
2µL	Template: complementary DNA (cDNA) from reverse transcription (RT) reaction
1.5µL	Forward primer (10µM)
1.5µL	Reverse primer (10µM)
1.5µL	dNTPs (10µM)
0.5µL	Kapa HIFI DNA polymerase
38µL	Autoclaved ultrapure water

PCR thermo cycler program:

94°C, 5 min	Initial denaturation	
94°C, 20 sec	Denaturation	┐
60°C, 15 sec	Annealing	├ 30-35 cycles
72°C, 60 sec/kb	Extension	┘
72°C, 5 min	Final extension	

The duration of extension was determined by the expected size of the amplicon (~60 seconds required to synthesize 1 kb DNA). After PCR amplification, the product was resolved using gel electrophoresis to determine the efficiency and specificity of the reaction. For site-directed mutagenesis, approximately 100ng parental plasmid was used as PCR template and the cycle number was reduced to 16 cycles to prevent unwanted mutations.

2.3.3 Agarose gel electrophoresis of DNA

Agarose gel was prepared by dissolving calculated amount of agarose in 1X TAE buffer with heating. Different agarose percentages were chosen based on the size of DNA fragments to be resolved. Typically, 0.8% gel was used for DNA larger than 3kb, 1% gel for DNA between 300bp to 3kb and 2.5% gel for XBP1 splicing assay. Agarose gel was supplemented with 1μg/ml ethidium bromide (EtBr) for detection. DNA samples were mixed with 6X DNA loading dye and loaded to the agarose gel. Electrophoresis was carried out at constant 80-100V and monitored with the migration of indicator dyes. DNA bands were visualized under UV shadowing.

2.3.4 PCR purification and gel purification of DNA

After resolved by electrophoresis, DNA bands in the EtBr-stained agarose gel were visualized with UV light, and the fragments of interest were excised using a scalpel. Gel slices were weighted and 100μL QG buffer per 100mg gel was used to dissolve the agarose gel. Melting of the gel slices was accelerated with heating at 55°C and occasional vortex. Alternatively, if a single specific band was detected with electrophoresis, the PCR product could be directly mixed with 3 times volume of PBI buffer. The dissolved or diluted DNA fragments in respective buffers were then applied to QIAquick columns and centrifuged at 13000 rpm for 1 minute. After one round of washing with wash buffer and one round of dry spin, the DNA fragments were eluded with 50μL nuclease free water. The DNA concentration was determined using a NanoDrop 1000 spectrophotometer.

2.3.5 Molecular cloning with restriction enzymes

To perform directional cloning, PCR products or vectors were digested with one pair of suitable restriction enzymes under conditions recommended by NEB. Briefly, ~2-3μg DNA was mixed with 2μL of each restriction enzyme, 5μL NEB buffer, 0.5μL 100X BSA and topped up with nuclease free water to a final volume of 50μL. The mixtures were incubated at 37°C overnight before subjected to DNA electrophoresis. Purified vector and insert were ligated at a molar ratio of 1:3 using T4 DNA ligase at room temperature for more than 5 hours. For site-directed mutagenesis, the PCR product was precipitated with absolute ethanol and digested with DpnI to remove the parental plasmid.

For transformation, 10μL ligation product or DpnI-digested product was added to 100μL DH5α and incubated on ice for 30 minutes. The bacteria were heat shocked at 42°C for 1 minute and rapidly returned on ice for 5 minutes. After that, 500μL LB broth was added and the bacteria were recovered at 37°C for 1 hour with vigorous shaking. Subsequently, all the bacteria were spread on LB agar plates with suitable antibiotic (100μg/μL of ampicillin or 50μg/μL of kanamycin) and incubated at 37°C overnight. Finally, 4-6 colonies were inoculated into LB broth to screen for correct insertion of the desired DNA fragment.

2.3.6 Plasmid minipreparation (miniprep)

The Axygen Axyprep Plasmid MiniPrep Kit was used for isolation of plasmid DNA from transformed DH5α cells. Briefly, the bacteria were pelleted from 3ml overnight culture by centrifugation at 13,000 rpm for 1 minute. After complete removal of supernatant, the pellet was re-suspended with 250μL S1 buffer (supplemented with 100mg/ml RNase A). This was followed by addition of 250μL S2 cell lysis buffer and gentle inversion of the tube for 6-8 times. After that, 350μL S3 neutralization buffer was added and the tube was again gently inverted for 8-10 times before subjected to centrifugation at 13,000 rpm for 15 minutes at 4°C. The supernatant was applied to the spin column and centrifuged at 13,000 rpm for 1 minute. After one round of washing with W2 buffer and one round of dry spin, the plasmid DNA was eluded with 50μL nuclease water. The DNA concentration and quality were determined using a NanoDrop 1000 spectrophotometer. Plasmid DNAs were validated by DNA sequencing and stored at -20°C.

2.3.7 Plasmids

For transfection and overexpression in mammalian cells or chicken fibroblast cells, the expression vector *pXJ40-FLAG, pEGFP-C1* (clontech) and *pcDNA3.1-HA* were extensively used in this study. The *pXJ40-FLAG* vector was previously develop by J.H. Xiao, containing a CMV promoter, a T7 promoter and an N-terminal FLAG-tag (DYKDDDDK) coding sequence upstream of the multiple cloning site (MCS). The vector *pcDNA3.1-HA* was generated by M. Huang, which consist of a HA-tag (YPYDVPDYA) coding sequence inserted between the *NotI* and *XbaI* sites in the parental vector *pcDNA3.1* (Invitrogen).

The plasmids generated for this study, as well as the primer sequences for directional cloning and site-directed mutagenesis, are summarized in **Table 2-4** below.

The plasmid *pKT-S* was constructed by H. Xiao in this lab as described previously [330]. Other plasmids used in this study were either purchased from Addgene or requested from labs where they were constructed. Specifically, the autophagy reporter construct *pmRFP-GFP-LC3* was obtained from Addgene as previously described [331]. The constitutively active JNK *pcDNA-Flag-MKK7-JNK1* and its dominant negative control *pcDNA-Flag-MKK7-JNK1(APF)* were also obtained from Addgene as previously described [332]. The expression plasmid for constitutively active Akt *pcDNA-myr-AKT1* was a generous gift from Dr. Jean-Ehrland Ricci as described before [333]. The IL8 luciferase reporter constructs: *pIL8-Fluc, pIL8-ΔAP1-Fluc, pIL8-ΔNFκB-Fluc* and *pIL8-ΔCEBPβ-Fluc* were described previously [334] and obtained from Dr. Mukaida in Kanzawa University (Kanzawa, Japan).

Table 2-4 Summary of expression plasmids and sequence of primers used for cloning

Plasmid name	Vector	Insertion or Mutation(s)	Restriction enzyme sites	Forward primer sequence (5'→ 3')	Reverse primer sequence (5'→ 3')
pEGFP-LC3	pEGFP-C1	LC3	*EcoRI/KpnI*	CCGGAATTCCATGCCGTCGGAGAAGAC	CGGGGTACCAACAATTCTAGAAGAGCTGCA
pcDNA-IRE1-HA	pcDNA-HA	IRE1	*EcoRI/NotI*	CGGGAATTCGGCCGAGTCCTCGCCATG	CAAGCGGCCGCCTTTCCCAACTATCACCACGCT
pcDNA-IRE1-K599A-HA	pcDNA-HA	IRE1, K599A	*EcoRI/NotI*	GACGTGGCCGTGGCGAGGATCCTCCCC	GGGGAGGATCCTCGCCACGGCCACGTC
pcDNA-IRE1-ΔRNase-HA	pcDNA-HA	IRE1, delete L835-L977	*EcoRI/NotI*	CGGGAATTCGGCCGAGTCCTCGCCATG	CAAGCGGCCGCCGCTCCAGAAGAACGGGTG
pEGFP-XBP1u	pEGFP-C1	XBP1U	*BglII/KpnI*	GGAAGATCTGGAGCTATGGTGGTG	CGGGGTACCTTAGTTCATTAATGGCTTCCAGC
pEGFP-XBP1s	pEGFP-C1	XBP1S	*BglII/KpnI*	GGAAGATCTGGAGCTATGGTGGTG	CGGGGTACCTTAGACACTAATCAGCTGG
pXJFLAG-XBP1u	pXJ40-FLAG	XBP1U	*BamHI/KpnI*	GGAAGATCTGGAGCTATGGTGGTG	CGGGGTACCTTAGTTCATTAATGGCTTCCAGC
pXJFLAG-XBP1s	pXJ40-FLAG	XBP1S	*BamHI/KpnI*	GGAAGATCTGGAGCTATGGTGGTG	CGGGGTACCTTAGACACTAATCAGCTGG

pXJFLAG-XBP1-DN	pXJ40-FLAG	XBP1U M1-V193	*BamHI/KpnI*	GGAAGATCTGGAG CTATGGTGGTG	CGGGGTACCTTATA CCGCCAGAATCCAT GGGGAGATG
pXJFLAG-CHOP	pXJ40-FLAG	CHOP	*BamHI/XhoI*	CCCGGATCCGCAGC TGAGTCATTGCCTT TC	GCCGCTCGAGTCAT GCTTGGTGCAGATT CACC
pXJFLAG-CHOP-S79/82A	pXJ40-FLAG	CHOP, S79A/S82A	*BamHI/XhoI*	AGCACCTCCCAGGC CCCTCACGCTCCAG ATTCCAGT	ACTGGAATCTGGAG CGTGAGGGGCCTGG GAGGTGCT
pXJFLAG-CHOP-L134/141A	pXJ40-FLAG	CHOP, L134A/L141A	*BamHI/XhoI*	GGCACAGGCAGCT GAAGAGAATGAAC GGGCCAAGCAGG	CCTGCTTGGCCCGT TCATTCTCTTCAGC TGCCTGTGCC
pXJFLAG-CHOP-ΔN9	pXJ40-FLAG	CHOP, delete A2-S9	*BamHI/XhoI*	CGCGGATCCTTCGG GACACTGTCCAGCT GG	GCCGCTCGAGTCAT GCTTGGTGCAGATT CACC
pXJFLAG-CHOP-ΔN18	pXJ40-FLAG	CHOP, delete A2-L18	*BamHI/XhoI*	CGCGGATCCGAAGC CTGGTATGAGGACC TG	GCCGCTCGAGTCAT GCTTGGTGCAGATT CACC
pXJFLAG-CHOP-ΔN36	pXJ40-FLAG	CHOP, delete A2-G36	*BamHI/XhoI*	CGCGGATCCACCTA TGTTTCACCTCCTG GA	GCCGCTCGAGTCAT GCTTGGTGCAGATT CACC
pXJFLAG-CHOP-ΔN70	pXJ40-FLAG	CHOP, delete A2-P70	*BamHI/XhoI*	CGCGGATCCGCAGA GGTCACAAGCACCT CC	GCCGCTCGAGTCAT GCTTGGTGCAGATT CACC
pXJFLAG-MKK4	pXJ40-FLAG	MKK4	*BamHI/KpnI*	CCCGGATCCATGGC GGCTCCGAGCCCGA G	CTTGGTACCTCAAT CGACATACATGGGA GAGCTGGGAG

pXJFLAG-MKK7	pXJ40-FLAG	MKK7	*BamHI/KpnI*	CCCGGATCCATGGCGGCGTCCTCCCTGGAAC	CTTGGTACCCTACCTGAAGAAGGGCAGGTGGGG
pXJFLAG-MKK7-K149M	pXJ40-FLAG	MKK7, K149M	*BamHI/KpnI*	CATTGCCGTTATGCAAATGCGGC	GCCGCATTTGCATAACGGCAATG
pXJFLAG-MKK7-STS-E3	pXJ40-FLAG	MKK7, S271E /T275E/S277E	*BamHI/KpnI*	GAGAAAGCCAAGGAGCGGGAAGCCGGCTGTGCCGCC	TTCCCGCTCCTTGGCTTTCTCGTCCACCAGGCGGCC
pXJFLAG-MKK7-STS-A3	pXJ40-FLAG	MKK7, S271A /T275A/S277A	*BamHI/KpnI*	GCCAAAGCCAAGGCGCGGGCCGCCGGCTGTGCCGCC	GGCCCGCGCCTTGGCTTTGGCGTCCACCAGGCGGCC
pXJFLAG-Bcl2	pXJ40-FLAG	Bcl2	*BamHI/XhoI*	CGCAGATCTGCGCACGCTGGGAGAACAGGGTAC	GCCGCTCGAGTCACTTGTGGCCCAGATAGGCACC
pXJFLAG-Bcl2-S70A	pXJ40-FLAG	Bcl2, S70A	*BamHI/XhoI*	GTCGCCAGGACCGCGCCGCTGCAGAC	GTCTGCAGCGGCGCGGTCCTGGCGAC
pXJFLAG-c-Jun	pXJ40-FLAG	c-Jun	*BamHI/KpnI*	CCCGGATCCATGACTGCAAAGATGGAAACGACC	CTTGGTACCTCAAAATGTTTGCAACTGCTGCG
pXJFLAG-c-Jun-AA	pXJ40-FLAG	c-Jun, S63A/S73A	*BamHI/KpnI*	CCTCCTCACCGCGCCCGACGTG	CAGCTCGGGCGCCGCCAGCTTG
pXJFLAG-DUSP1	pXJ40-FLAG	DUSP1	*BamHI/XhoI*	CGCGGATCCGTCATGGAAGTGGGCACCCTG	GCCGCTCGAGTCAGCAGCTGGGAGAGGTCGTAATG

2.4 RNA MANIPULATION

2.4.1 Total RNA extraction from mammalian cells

Total RNA from cultured cells was extracted with TRIzol reagent (Invitrogen) according to the manufacturer's instructions. Briefly, cells were washed twice with PBS and lysed with 1ml TRIzol per 10 cm^2 effective growth area. The lysates were mixed with one-fifth volume of chloroform, vortex for 20 seconds and incubated at room temperature for 5 minutes. After centrifugation at 12,000g at 4^oC for 15 min, the aqueous phase was mixed with equal volume of isopropanol. RNA was pelleted by centrifugation at 12,000g at 4^oC for 15 min, washed twice with 70% ethanol and dissolved in RNase-free water. The concentration of the total RNA was measured using a NanoDrop 1000 Spectrophotometer (Thermo Fisher Scientific).

2.4.2 Reverse transcription

The extracted total RNA was reverse transcribed using the ImProm-II™ Reverse Transcription System (Promega) according to the manufacturer's instructions. Briefly, 5µg total RNA was mixed with 1µl oligo-dT primer (10µM) and incubated at 70^oC for 5 minutes to denature RNA higher structures. This pre-RT mixture was then rapidly transferred on ice and incubated for 5 minutes to allow annealing of the oligo-dT primer to the 3' polyadenylate tails present in most host mRNAs and all IBV positive-stranded RNA species. Then, 4µl 5X RT buffer, 0.5µl dNTP (10mM), 0.5µl RNAse inhibitor (20U, Thermo Scientific) and 1µl RT enzyme (50U) were added to the mixture. The RT reaction mix was incubated at 42^oC for 1 hour to synthesize the complementary DNA (cDNA) product. Finally, the mixture was incubated at 70^oC for 15 minutes to inactivate the RT enzyme and stored at -20^oC. The cDNA could be used for semi-quantitative PCR and quantitative real-time PCR (qPCR) described below.

2.4.3 Semi-quantitative PCR

To determine the relative abundance of a transcript, semi-quantitative PCR was performed. Briefly, 1µl cDNA was mixed with 2µl 10X PCR buffer, 0.8µl forward primer (10µM), 0.8µl reverse primer (10µM), 0.4µl dNTP (10mM), 0.1µl *Taq* DNA polymerase and 15µl PCR grade H_2O to make up a typical 20µl PCR reaction. The mixture was then incubated in a thermo cycler with 94^oC initial denaturation for 5 minutes, followed by 20-36 cycles of

Table 2-5 Summary of primers used for semi-quantitative PCR

Gene Name	Accession number	Amplicon size (bp)	Forward primer sequence (5'→ 3')	Reverse primer sequence (5'→ 3')
ATF6	NM_007348.3	340	CATCCGCAGAAG GGGAGACACA	CTATTGTAATGA CTCAGGGA
CHOP	NM_001195053.1	300	GATTCCAGTCAG AGCTCCCT	GTAGTGTGGCCC AAGTGGGG
c-Jun	NM_002228.3	198	TCCAAGTGCCGA AAAAGGAAG	TCAAAATGTTTG CAACTGCTGCG
EDEM1	NM_014674.2	462	CTACCAGGCAAC CAAGAATC	CCAACCATCTGG TCAATCTG
ERdj4	NM_012328.2	414	GATACACTTGGA CACAGTGC	CTACTGTCCTGA ACAGTCAG
GAPDH	NM_002046.4	444	GACAACTTTGGT ATCGTGGAA	CCAGGAAATGAG CTTGACA
HERPUD1	NM_014685.2	378	GGACCTATTCAG CAGCTACA	ATCAGTTTGCGA TGGCTGGG
IFNB	NM_002176.2	168	AAACTCATGAGC AGTCTGCA	AGGAGATCTTCA GTTTCGGAGG
IL8	NM_000584.3	349	TGGAGAAGTTTT TGAAGAGGGCT	GCCCTTGGCCTC AATTTTGC
IRE1	NM_001433.3	387	GAAAAGGAATCC CTGGATGG	TCAGAGGGCGTC TGGAGTC
NF-κB	NM_001145138.1	151	ATGTGGAGATCA TTGAGCAGC	CCTGGTCCTGTG TAGCCATT
P58IPK	NM006260.4	204	GGCTCGGTATTC CCCTTCCT	AGTAGCCCTCCG ATAATAAGCAA
PERK	NM_004836.5	320	TCTATTTGAATT GCTGTATC	CTTAAGGCTAAT TGCTTGGC
XBP1	NM_005080.3 NM_001079539.1	289/263	TTACGAGAGAAA ACTCATGGCC	GGGTCCAAGTTG TCCAGAATGC
IBVgRNA	NC_001451.1	410	GAGTAACATAAT GGACCTGT	TGCTGTACCCTC GATCGTAC
IBVsgRNA2	NC_001451.1	415	CTATTACACTAG CCTTGCGCTAGA	CTCTGGATCCAA TAACCTAC

denaturation (94ºC,30 seconds), annealing (55ºC, 30 seconds) and extension (72ºC, 30 seconds). After a final extension at 72ºC for 5 minutes, 10µl PCR product was mixed with 2µl 6X loading dye and subjected to agarose electrophoresis as described in **section 2.3.3**. The semi-quantitative PCR primers used in this study is summarized in **Table 2-5**.

2.4.4 Quantitative real-time PCR

Quantitative real time RT-PCR (qPCR) was performed using the SYBR select PCR kit (Life technologies) according to manufacturer's instructions. Briefly, 1µl cDNA product was mixed with 0.3µl forward primer (10µM), 0.3µl reverse primer (10µM), 7.5µl 2X SYBR select master mixture and 5.9µl PCR grade H_2O to make up a typical 15µl qPCR reaction. The mixture was then subjected to thermo cycling in a 7500 real-time PCR system (Applied Biosystems). The standard protocol include enzyme activation at 50ºC for 2 minutes, initial denaturation at 95ºC for 2 minutes, followed by 40 cycles of denature (95ºC, 15 seconds) and annealing/extension (60ºC, 1 minute) with fluorescent acquisition at the end of each cycle. The results obtained were in the form of threshold cycles (C_T values). The relative abundance of the mRNA was calculated using GAPDH as an internal control and normalized to 0 hours post infection samples (in time course experiments) or siEGFP transfected samples (in knockdown experiments). **Table 2-6** summarizes the primers used for qPCR in this study.

2.4.5 RNA interference

Small interfering RNA (siRNA) was used to transiently knockdown the expression of specific host genes. The siRNA sequences (sense strands, 5' → 3') used in this study are: siEGFP, GCUGACCCUGAAGUUCAUCTT; siBECN1, GAUUGAAGACACAGGAGGCTT; siATG5, GCAACUCUGGAUGGGAUUGTT; siATF6, GCAACCAAUUAUCAGUUUATT; siIRE1, GGACGUGAGCGACAGAAUATT; siXBP1, ACAGCAAGUGGUAGAUUUATT; siCHOP, GGCUCAAGCAGGAAAUCGATT; siJNK, AAAGAAUGUCCUACCUUCUTT; siPKR, GCGAGAAACUAGACAAAGUTT; siGADD34, GGACACUGCAAGGUUCUGATT. The siRNA duplexes were purchased from Sigma-Aldrich, dissolved in nuclease-free H_2O for a working concentration of 20µM and stored at -20ºC.

Table 2-6 Summary of primers used for quantitative real-time PCR

Gene Name	Accession number	Amplicon size (bp)	Forward primer sequence (5'→ 3')	Reverse primer sequence (5'→ 3')
ATF6	NM_007348.3	76	GACAGTACCAA CGCTTATGCC	CTGGCCTTTAGT GGGTGCAG
CHOP	NM_001195053.1	80	GAACGGCTCAA GCAGGAAATC	TTCACCATTCGG TCAATCAGAG
c-Jun	NM_002228.3	78	TCCAAGTGCCGA AAAAGGAAG	CGAGTTCTGAGC TTTCAAGGT
EDEM1	NM_014674.2	96	CGGACGAGTAC GAGAAGCG	CGTAGCCAAAG ACGAACATGC
ERdj4	NM_012328.2	81	TCTTAGGTGTGC CAAAATCG	TGTCAGGGTGGT ACTTCATGG
GAPDH	NM_002046.4	102	CCACTCCTCCAC CTTTGAC	ACCCTGTTGCTG TAGCCA
IFNB	NM_002176.2	168	AAACTCATGAG CAGTCTGCA	AGGAGATCTTCA GTTTCGGAGG
IL8	NM_000584.3	102	ATAAAGACATA CTCCAAACCTTT CCAC	AAGCTTTACAAT AATTTCTGTGTT GGC
IRE1	NM_001433.3	115	CGGGAGAACAT CACTGTCCC	CCCGGTAGTGGT GCTTCTTA
NF-κB (p65)	NM_001145138.1	151	ATGTGGAGATC ATTGAGCAGC	CCTGGTCCTGTG TAGCCATT
P58IPK	NM006260.4	204	GGCTCGGTATTC CCCTTCCT	AGTAGCCCTCCG ATAATAAGCAA
PERK	NM_004836.5	111	GGAAACGAGAG CCGGATTTATT	ACTATGTCCATT ATGGCAGCTTC
XBP1 (spliced)	NM_001079539.1	169	TGCTGAGTCCGC AGCAGGTG	GCTGGCAGGCTC TGGGGAAG
XBP1 (Total)	NM_005080.3	88	TTGTCACCCCTC CAGAACATC	TCCAGAATGCCC AACAGGAT
IBV+gRNA	NC_001451.1	100	AGTAGCTTGGA AACGAACGGT	CGGCACTGGCAT CTTTAGAC

Transfection of siRNAs to H1299 cells was performed using DhamaFECT2 transfection reagent (Thermo Fisher Scientific) according to the manufacturer's instructions. Briefly, H1299 cells were seeded at ~150000 cells per well in a 12-well plate the day before transfection. For each well, 2.5µL siRNA (20µM) was diluted with 100µL plain RPMI and 2µL DhamaFECT2 was diluted with 100 µL plain RPMI in a separate tube and incubated at room temperature for 5 minutes. The diluted siRNA was then mixed with the diluted DhamaFECT2 by gentle vortex and incubated for 20 minutes at room temperature. Culture medium was removed and 800µL RPMI containing 5% FBS was added to each well. Finally, 200µL transfection mixture was added to respective wells and the cells were incubated at 37ºC. Culture medium was changed 6-8 hours post transfection. Transfection of siRNAs to Huh-7 cells was performed using Lipofectamine RNAiMAX transfection reagent (Life technologies) similarly, but 5µl siRNA (20µM) and 3µl RNAiMAX were used per well in a 12-well plate. At 48 hours post-transfection, cells were infected with IBV at an MOI of 2 or mock infected and continued incubated before harvested for protein and/or RNA analysis at indicated time points.

2.5 PROTEIN EXPRESSION AND DATA ANALYSIS

2.5.1 Transient expression of plasmid DNA in mammalian cells

Transfection of plasmids to H1299 cells was performed using Lipofectamine 2000 reagent (Invitrogen) according to the manufacturer's instructions. Briefly, H1299 cells were seeded at ~150000 cells per well in a 12-well plate the day before transfection. For each well, 0.8µg plasmid DNA was diluted with 100µL plain RPMI and 2µL Lipofectamine 2000 was diluted with 100 µL plain RPMI in a separate tube and incubate at room temperature for 5 minutes. The diluted plasmid was then mixed with the diluted Lipofectamine 2000 by gentle vortexing and incubated for 20 minutes at room temperature. Culture medium was removed and 800µL RPMI containing 5% FBS was added to each well. Finally, 200µL transfection mixture was added to respective wells and the cells were incubated at 37ºC. Culture medium was changed at 6-8 hours post transfection to minimize cytotoxicity of Lipofectamine 2000. The protocol for transfection of Huh-7, HEK293 and DF1 cells is similar, but 1.6µg plasmid DNA was used per well in a 12-well plate and DMEM was used instead of RPMI.

In some experiments, cells were transfected using a recombinant vaccinia virus system. Cells were seeded at ~200000 cells per well in a 12-well plate the day before transfection. Cells were infected with a recombinant vaccinia virus harboring the T7 RNA polymerase (vTF7) at a MOI of 1 for 3-4 hours before transfected with plasmid DNA using Lipofectamine 2000.

2.5.2 Sodium dodecyl sulfate-polyacrylamide gel electrophoresis (SDS-PAGE)

Cells were harvested at indicated times points using cell scrapers (Corning). After centrifugation at 13,000 rpm for 1 min, the supernatant was discarded and the pellets were washed twice with PBS and lysed in radioimmunoprecipitation assay (RIPA) buffer. After clarifying by centrifugation and determination of protein concentration by spectrophotometer, the cell lysates were mixed with Laemmli sample buffer containing 100 mM dithiothreitol [335]. The protein samples were boiled at 90^{o}C for 5 min and centrifuged at 13,000 rpm for 5 min. Equal amount of protein samples were subjected to SDS-PAGE. Resolving gels of different concentrations (8%, 10%, 12% or 15%) were used. Electrophoresis was performed using the Bio-Rad Mini-PROTEAN II system at constant 20 microampere in the presence of 1X running buffer (25mM Tris-HCl, 192mM glycine and 0.1% SDS). The resolved proteins were transferred to 0.2 µm nitrocellulose membranes using the Bio-Rad Trans-Blot system at 4^{o}C in the presence of 1X transfer buffer (25mM Tris-HCl, 192mM glycine and 20% ethanol).

2.5.3 Immunoblotting

After the nonspecific antibody binding sites were blocked with 5% bovine serum albumin (BSA) in Tris-buffered saline (20 mM Tris-HCl pH 7.4, 150 mM NaCl and 0.1% Tween 20), the membranes were incubated with 1 µg/ml primary antibodies at 4 ^{o}C overnight. After washing with Tris-buffered saline, the membranes were incubated with 1:2000 diluted anti-mouse or anti-rabbit IgG antibodies conjugated with horseradish peroxidase (HRP) at room temperature for 2 h. The membranes were washed and the proteins detected with a chemiluminescence detection kit (Amersham Biosciences) and medical X-ray films (Fujifilm) according to the manufacturer's instructions. To re-probe the same membrane with another antibody, the membrane was incubated with 10ml stripping buffer (62.5mM Tris-HCl pH 6.7, 100mM β-mercaptoethanol and 2% SDS) at 55^{o}C for 20-30 minutes, washed extensively with Tris-buffer saline and blocked with BSA before incubated with a different antibody.

2.5.4 Immunofluorescence

Cells plated on glass coverslips were fixed with 4% formaldehyde in PBS at room temperature for 30 minutes, permeabilized with 0.3% Triton X-100 in PBS and incubated with primary antibodies diluted in blocking solutions (5% goat serum, 0.3% Triton X-100 in PBS). The dilution factor for anti-IBV N or IBV S antiserum was 1 to 300. After 1 hour incubation at room temperature, cells were washed three times with PBS and incubated with anti-rabbit secondary antibodies conjugated with AlexaFluo488 (Life technologies) for 1 hour in dark. Cell nuclei were stained with DAPI at a dilution of 1:10000. Fluorescent images were captured using a Zeiss LSM 510 confocal microscope according to manufacturer's instructions.

2.5.5 Luciferase assays

HEK293 cells plated on 12-well plate were co-transfected with 30ng pRL-TK, 0.4µg firefly luciferase reporter constructs and 0.4µg respective plasmids for 24 hours before infected with IBV. Luciferase assay was performed using the Dual-Luciferase reporter assay system (Promega) according to manufacturer's instructions. Briefly, cells were lysed with 200µl passive lysis buffer and clarified by brief centrifugation. 20µl cell lysate was mixed with 50µl substrate and the luminescent signal was determined using an Infinite 200 PRO plate reader (Tecan). Following that 50µl Stop & Glo reagent was added to the mixture to quench the firefly luciferase and the luminescent signal specific for the Renilla luciferase was similarly determined. The reporter activity was calculated by normalizing the firefly luciferase readout to that of the Renilla luciferase. Each transfection and luciferase assay was performed at least three times.

2.5.6 Densitometry and statistical analysis

Films from Western blot or DNA gel photos were saved as 8-bit images and semi-quantitative measurement of band intensity was performed using ImageJ developed by the National Institute of Health (NIH). The band intensities were normalized with the corresponding loading controls, such as β-actin in Western Blot and GAPDH in semi-quantitative RT-PCR. Quantitative or semi-quantitative data were reported as the mean +/- standard deviation from at least three independent experiments. P-values determined by 2-sample t-test were used to indicate the significance levels. Asterisks indicate significant differences between the indicated samples and the control sample (*, $P<0.05$; **, $P<0.01$).

Chapter Three:

Induction of UPR during IBV infection and its involvement in regulating IBV-induced apoptosis, autophagy and innate immune response

3.1 BACKGROUND AND INTRODUCTION

Numerous RNA viruses have been documented to cause ER stress and induce UPR in the infected cells. For coronaviruses, previous studies related to UPR have been mainly performed using betacoronaviruses (such as MHV and SARS-CoV) as models [191,192]. Moreover, a lot of these studies have been based on overexpression experiments where viral proteins are transiently transfected in culture cells. Therefore, it is uncertain whether similar conclusions will hold true under the setting of actual coronavirus infections. Finally, despite of its importance in host-virus interaction, the mechanisms underlying coronavirus-induced UPR and its cross-talks with other cell signaling pathways have remained largely unexplored.

To gain a better understanding of coronavirus-induced UPR, we use the gamma-coronavirus IBV as a model. The Vero cells-adapted IBV strain can efficiently infect various mammalian cell lines, and unlike SARS-CoV, its manipulation does not require BSL3 facilities. This system provides a powerful model to study host-virus interaction, because host genes expression can be easily manipulated by ectopic transfection or RNA interference, while targeted modification of the virus genome is also possible with reverse genetics techniques.

In this chapter, the induction of UPR during IBV infection will be characterized, with a particular emphasis on the IRE1 branch. Utilizing knockdown and overexpression approaches, it is concluded that the IRE1 pathway is activated during IBV-infection and plays a pro-survival role to protect infected cells from IBV-induced apoptosis. Moreover, XBP1 in the IRE1 pathway is required for the production of IL-8 and IFN-β in IBV-infected cells, suggesting its possible involvement in regulating the pro-inflammatory and innate immune response against coronavirus infections.

At the beginning of this project, studies performed in this group have already shown that IBV infection activates the PERK branch of UPR as well as the PKR kinase. Thus, follow-up experiments in this thesis will mainly focus on molecular characterization of the downstream transcription factor – CHOP, and its role in host responses during IBV infection. Our result has demonstrated that CHOP is a pro-apoptotic protein and may contribute to the regulation of cytokine production in the IBV-infected cells.

3.2 ACTIVATION OF THE IRE1 PATHWAY DURING IBV INFECTION AND ITS INVOLVEMENT IN REGULATING IBV-INDUCED APOPTOSIS

3.2.1 IBV infection activates the IRE1-XBP1 pathway

To determine whether the IRE1 pathway is activated during IBV infection, H1299 cells were either infected with IBV at MOI~2 or incubated with UV-inactivated IBV (UV-IBV). DTT, a chemical that induces potent ER stress by reducing disulfied bonds, was added to the cells in the positive control. Total RNA was extracted at the indicated time points and subjected to semi-quantitative RT-PCR analysis. The IBV genomic RNA could be detected from 12 hpi onward, indicating robust replication of the virus genome (**Figure 3-1a**). HERPUD1 is a component of the ERAD pathway, and its induction is commonly used as a marker for ER stress [155,336]. A drastic increase in the mRNA level of HERPUD1 could be detected in cells infected with IBV or treated with DTT, but not in cells incubated with UV-IBV (**Figure 3-1a**). Therefore, similar to MHV and SARS-CoV, IBV also induced ER stress in the infected cells. Expression of IRE1 and XBP1 at the mRNA level was also determined by RT-PCR. As shown in **Figure 3-1a**, the mRNA level of IRE1 gradually increased through the course of infection and slighly reduced at 24 hpi, possibly due to extensive cell death at the late stage of infection. The mRNA of total XBP1 also stably accumulated overtime, whereas the mRNA levels of both IRE1 and XBP1 remained unchanged in cells incubated with UV-IBV. IRE1 and XBP1 were also induced at the transcription level in cells treated with DTT (**Figure 3-1a**).

Upon activation, IRE1 mediates splicing of the XBP1 mRNA by removing a 26-nt intron [337]. The spliced (XBP1s) and unspliced (XBP1u) mRNAs can be differentiated by RT-PCR followed by high percentage agarose gel electrophoresis. In fact, the percentage of XBP1 splicing (band intensity of XBP1s divided by total intensities of XBP1u and XBP1s) has been a standard measurement of IRE1 activity. As shown in **Figure 3-1a**, DTT induces high level of XBP1 splicing (~90%) in H1299 cells. In cells infected with IBV, a significantly lower but detectable XBP1 splicing (~15%) was observed at 24 hpi, whereas no XBP1 splicing could be detected at earlier time points or in cells incubated with UV-IBV. The result suggested that IBV activated IRE1 and induced XBP1 splicing at the late stage of infection.

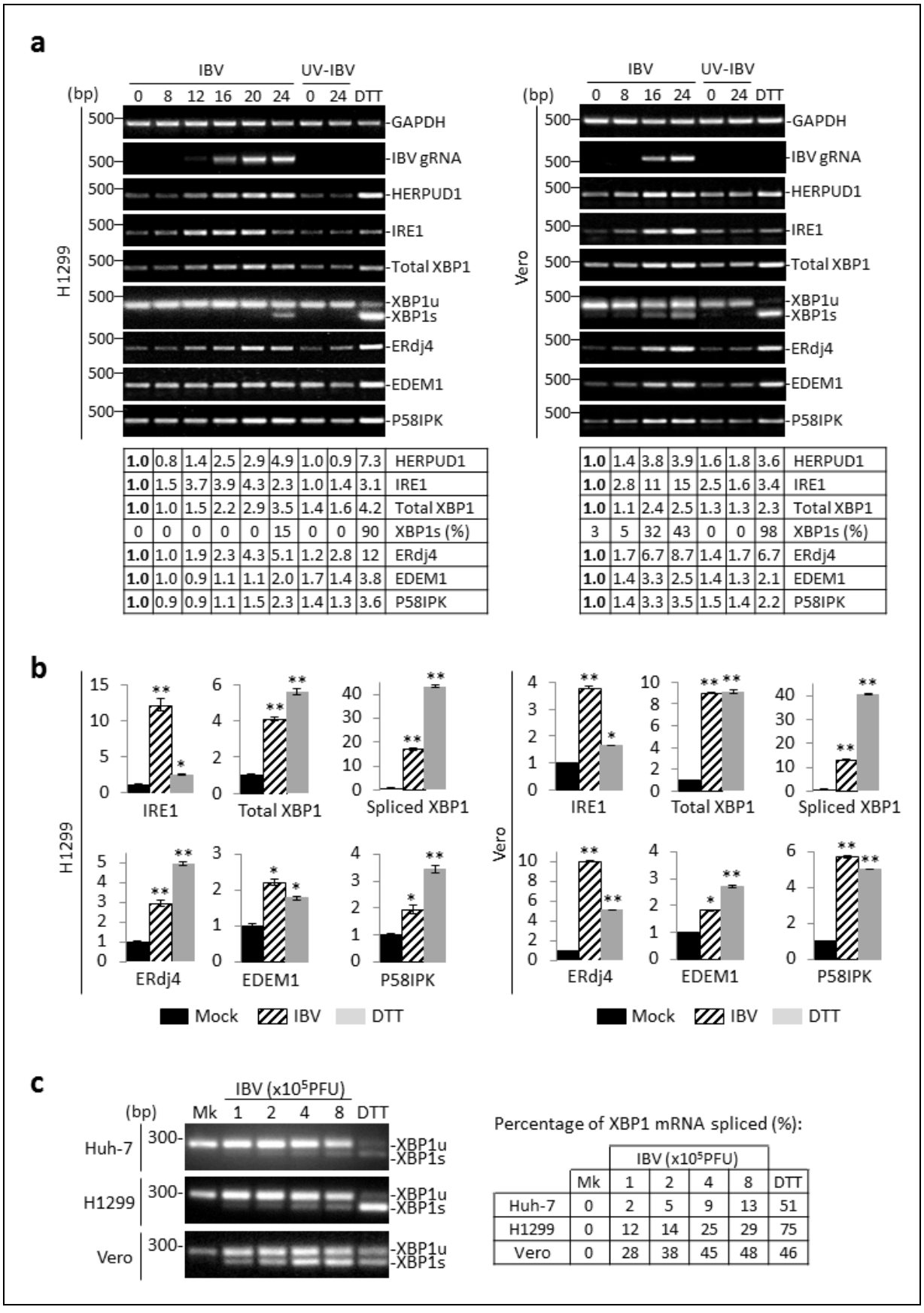

1.0	0.8	1.4	2.5	2.9	4.9	1.0	0.9	7.3	HERPUD1
1.0	1.5	3.7	3.9	4.3	2.3	1.0	1.4	3.1	IRE1
1.0	1.0	1.5	2.2	2.9	3.5	1.4	1.6	4.2	Total XBP1
0	0	0	0	0	15	0	0	90	XBP1s (%)
1.0	1.0	1.9	2.3	4.3	5.1	1.2	2.8	12	ERdj4
1.0	1.0	0.9	1.1	1.1	2.0	1.7	1.4	3.8	EDEM1
1.0	0.9	0.9	1.1	1.5	2.3	1.4	1.3	3.6	P58IPK

1.0	1.4	3.8	3.9	1.6	1.8	3.6	HERPUD1
1.0	2.8	11	15	2.5	1.6	3.4	IRE1
1.0	1.1	2.4	2.5	1.3	1.3	2.3	Total XBP1
3	5	32	43	0	0	98	XBP1s (%)
1.0	1.7	6.7	8.7	1.4	1.7	6.7	ERdj4
1.0	1.4	3.3	2.5	1.4	1.3	2.1	EDEM1
1.0	1.4	3.3	3.5	1.5	1.4	2.2	P58IPK

Percentage of XBP1 mRNA spliced (%):

	IBV (x10⁵PFU)					
	Mk	1	2	4	8	DTT
Huh-7	0	2	5	9	13	51
H1299	0	12	14	25	29	75
Vero	0	28	38	45	48	46

Figure 3-1 IBV infection activates the IRE1-XBP1 pathway.

(a) IBV infection leads to ER stress and activates the IRE1-XBP1 pathway in H1299 cells and Vero cells. H1299 cells (left) or Vero cells (right) were infected with IBV (MOI~2) or incubated with UV-IBV and harvested at the indicated time points. As a positive control, cells were treated with 2mM DTT for 2 hours. Total RNA was extracted and subjected to RT-PCR using primers specific for the indicated genes. The PCR products were resolved using 1% agarose gel electrophoresis, except for XBP1u/XBP1s, in which 4% agarose gel was used. The band intensities of HERPUD1, IRE1, Total XBP1, ERdj4, EDEM1 and P58IPK were determined by densitometry and normalized to the intensities of corresponding GAPDH bands. Percentage of XBP1 splicing [XBP1s (%)] was calculated as the band intensity of XBP1s divided by the total intensities of XBP1u and XBP1s. Sizes of DNA ladders in base pairs (bp) were indicated on the left. The experiment was repeated three times with similar results and the result of one representative experiment is shown.

(b) H1299 cells and Vero cells were infected with IBV or mock infected for 20 hours, or treated with DTT as in (a). Total RNA was extracted and subjected to real time RT-PCR analysis. Fold inductions of genes were calculated using GAPDH as internal references and normalized to the mock infected samples. The experiment was repeated three times with similar results and the result of one representative experiment is shown. Asterisks indicate significant differences between indicated samples and mock (*, $P<0.05$; **, $P<0.01$).

(c) Huh-7, H1299 and Vero cells seeded in 6-well plate were infected with different dosages of IBV or incubated with mock cell lysate for 24 hours. In the positive control, cells were treated with 2mM DTT for 2 hours. Total RNA was extreacted and subjected to RT-PCR as in (a). Sizes of DNA ladders in bp were indicated on the left. Percentage of XBP1 splicing was calculated as in (a) and summarized on the right.

ERdj4, EDEM1 and P58IPK are three UPR-related genes known to be specifically induced by the spliced form of XBP1 [206], and their expression during IBV infection was also determined by RT-PCR. As shown in **Figure 3-1a**, treatment of DTT significantly induced the mRNA levels of ERdj4, EDEM1 and P58IPK, suggesting that the observed XBP1s mRNA was indeed translated into a potent transcription factor that up-regulated the expression of downstream genes. In H1299 cells infected with IBV, considerable induction of ERdj4 and moderate induction of P58IPK and EDEM1 was detected (**Figure 3-1a**). It is interesting to note that the mRNA levels of ERdj4 and P58IPK were significantly elevated from 12-20 hpi, when XBP1 splicing was bearly detectable. It is possible that IBV might induce P58IPK and ERdj4 by some unknown mechanisms independent of XBP1s. Alternatively, it is also likely that low level of XBP1 splicing might have occurred at earlier time points of IBV infection, but the semiquantitative RT-PCR was not sensitive enough to detect it.

The same time course experiment was performed in Vero cells. Similarly, the mRNA levels of HERPUD1, IRE1α and total XBP1 were significantly up-regulated in IBV-infected and DTT-treated Vero cells. Compared with H1299 cells, the degree of XBP1 splicing was much higher in IBV-infected Vero cells, reaching ~43% at 24 hpi (**Figure 3-1a**). This may be attributed by different origins of the cell lines, resulting in cell type specific phenotypes. Consistent with the higher percentage of XBP1 splicing, the IBV-induced up-regulation of ERdj4, EDEM1 and P58IPK was also more prominent in Vero cells compared with H1299 cells (**Figure 3-1a**). Taken together, the RT-PCR result demonstrated that IBV infection caused ER stress and induced the IRE1-XBP1 pathway in H1299 and Vero cells.

To validate the semi-quantitative RT-PCR results, real time RT-PCR was performed on RNA samples harvested from H1299 and Vero cells infected with IBV (20 hpi), incubated with mock lysate or treated with DTT. As shown in **Figure 3-1b**, IBV infection induced ~12-fold increase in IRE1 mRNA and ~4-fold increase in total XBP1 mRNA in H1299 cells at 20 hpi, whereas the mRNA levels were induced by ~4-fold and ~9-fold respectively in IBV-infected Vero cells. Previously, a pair of real time RT-PCR primers was validated to specifically amplify only the spliced form of XBP1 [338]. Using these primers, it was found that IBV infection induced ~17-fold and ~13-fold increase in the mRNA level of XBP1s in the infected H1299 and Vero cells, respectively (**Figure 3-1b**). Notably, XBP1 splicing was undetectable at 20 hpi in

H1299 cells using semi-quantitative RT-PCR (**Figure 3-1a**). Therefore, real time RT-PCR analysis seemed to be a more sensitive method to determine XBP1 splicing compared to the traditional agarose gel-based XBP1 splicing assay. As expected, ~2-3 fold increase of ERdj4, EDEM1 and P58IPK mRNA levels was observed in IBV-infected H1299 cells, while significant induction of ERdj4 (~10-fold) and P58IPK (~6-fold) was also detected in IBV-infected Vero cells (**Figure 3-1b**). Therefore, real time RT-PCR result supported that IRE1was activated in H1299 and Vero cells infected with IBV, leading to splicing of XBP1 mRNA and up-regulation of downstream UPR genes.

In the experiments describe above, cells were infected with IBV at MOI~2. To see whether activation of the IRE1 pathway was dependent on the dose of infection, H1299 and Vero cells were infected with different amount of IBV for 24 hours and XBP1 splicing was determined. Also, another mammalian cell line of different origin (Huh7, from human liver cancer) was included. As shown in **Figure 3-1c**, XBP1 splicing was undetectable in mock infected cells. More than 50% XBP1 splicing could be observed in cells treated with DTT. In all three cell types, the degree of XBP1 splicing gradually increased as the IBV dosage used for infection increased. Therefore, XBP1 splicing was a general outcome in IBV-infected cells and was indeed dependent on the dose of infection. Notably, at the same IBV dose, the percentage of XBP1 splicing was lowest in Huh-7 cells, intermediate in H1299 cells and highest in Vero cells (**Figure 3-1c**). Again this demonstrated the cell type dependent responsiveness to IBV infection. Since IBV-induced XBP1 splicing was very inefficient in the Huh-7 cells, we refrained from using this cell line in future IRE1-related experiments.

3.2.2 Overexpression of IBV S protein is sufficient for IRE1 activation

In a previous study, efficient XBP1 splicing was detected in cells transfected with the S protein of MHV using a vaccinia virus T7 polymerase system [155]. To see whether the S protein of IBV would similarly activate the IRE1-XBP1 pathway, Vero cells were transfected with different doses (0.2, 0.4 or 0.8μg) of the T7 promoter-driven construct pKT-IBV-S. Expression of the inserted genes was dramatically enhanced by the T7 RNA polymerase, which is encoded by the recombinant vaccinia virus innoculated prior to transfection. This expression system was used because transient transfection of CMV promoter-driven constructs encoding IBV S failed to be expressed in all cell line tested (data not shown). As a negative control, empty vector (pKT0) or pKT-EGFP was transfected to Vero cells in the same manner. As positive control, Vero cells were infected with IBV as described above. As shown in **Figure 3-2a**, expression of S protein could be clearly detected in IBV-infected cells as well as pKT-IBV-S transfected cells. The cleavage bands (lower than 100kDa) for S protein are different between the infected cells and transfected cells, possibly due to different post-translational modifications. Expression levels of IBV S were similar in cells transfected with 0.4μg or 0.8μg plasmid, and only slightly lower in cells transfected with 0.2μg plasmid, indicating that the expression system was highly efficient and the amount of DNA was not a limiting factor. Expression of the transfected IBV S protein could also be determined by IF (**Figure 3-2b**), which showed massive syncytia formation as compared with the single cell pattern of EGFP expressing cells. As shown above, IBV induced XBP1 splicing in the infected cells (**Figure 3-2a**). Notably, overexpression of the IBV S protein also resulted in considerable degree (~30%) of XBP1 mRNA splicing, although lower compared with cells infected with IBV for 24 hours. Therefore, similar to MHV, the S protein of IBV might be the major viral component responsible for the induction of ER stress and activation of the IRE1-XBP1 pathway.

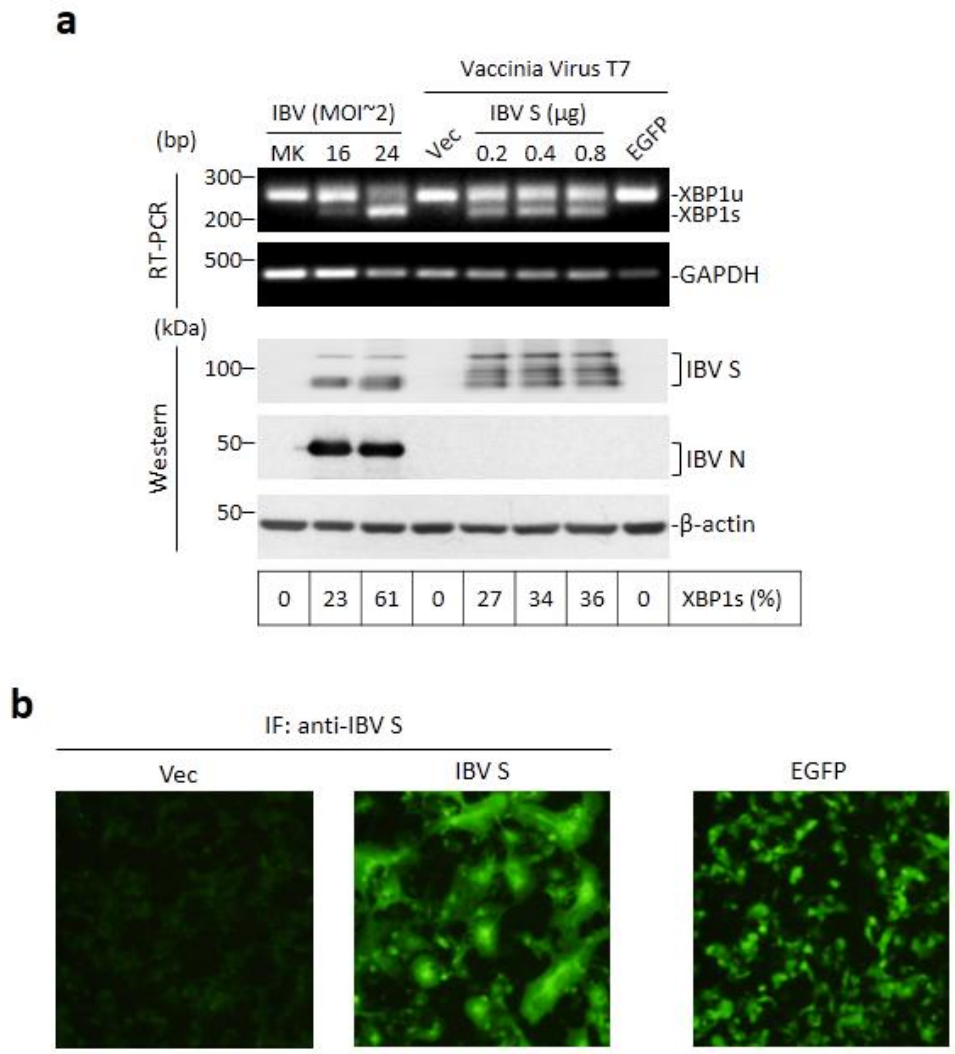

Figure 3-2 Overexpression of IBV S protein activates the IRE1-XBP1 pathway.

(a) Overexpression of the IBV S protein induces XBP1 splicing in Vero cells. Vero cells were infected with IBV at MOI~2 or mock infected. Alternatively, Vero cells were infected with with vTF7 at MOI~1 for 4 hours before transfecting with 0.8μg pKT0 (vec), 0.2-0.8μg pKT-IBVS, or 0.8μg pKT-EGFP for 24 hours. In one set of cells, total RNA was extracted and subjected to RT-PCR as in Figure 3-1a. Percentage of XBP1 splicing was calculated as in Figure 3-1a. Another set of cells were harvested for protein and subjected to Western blot using indicated antibodies.

(b) Another set of Vero cells in (a) transfected with 0.8μg pKT0 or pKT-IBVS was subjected to immunofluorescent (IF) using antibody against IBV S. Expression of EGFP in Vero cells transfected with 0.8μg pKT-EGFP was also determined.

3.2.3 IRE1 inhibition attenuates IBV-induced activation of the IRE1-XBP1 pathway in Vero cells but reduces IBV replication in H1299 cells

To confirm and further characterize activation of the IRE1-XBP1 pathway during IBV infection, a recently identified IRE1 inhibitor (3,5-dibromosalicylaldehyde, or DBSA) was used. DBSA is a non-competitive, reversible inhibitor blocking the RNAse activity of IRE1 [339]. Vero cells were treated with DBSA or the solvent control DMSO 4 hours after innoculation of IBV. The inhibitor was not added before or at the time of IBV innoculation, so as to prevent possible non-specific inhibition of virus adsorption or entry. As shown in **Figure 3-3a**, compared with the control, treatment of DBSA at 5μM or 10 μM did not significantly affect IBV replication in Vero cells, as indicated by similar levels of IBV genomic RNA (gRNA) at 8 hours post drug treatment. Although the amount of IBV gRNA was slightly lower in cells treated with DBSA for 16 hours, plaque assay analysis of the culture supernatant showed no significant reduction in the virus titer (**Figure 3-3b**). As expected, IBV infection induced ~47% XBP1 splicing at 16 hours post treatment (20 hpi) in the DMSO control. Notably, addition of DBSA dosage dependently inhibited IBV-induced XBP1 splicing. Percentage of XBP1 splicing was reduced to ~29% in cells treated with 5μM DBSA and to ~13% in cells treated with 10μM DBSA (**Figure 3-3a**). Consistently, the mRNA levels of downstream UPR genes ERdj4, EDEM1 and p58IPK were all dosage dependently reduced in Vero cells treated with DBSA, as compared with the DMSO control. It should be noted that IBV infection still induced ~4-fold increase in the mRNA level of ERdj4 in cells treated with 10μM DBSA (**Figure 3-3a**). This might be contributed by the remaining 13% of XBP1s, suggesting that ERdj4 expression was highly responsible to the splicing of XBP1.

Similar experiments were also performed in H1299 cells. However, it was observed that treatment of DBSA at 5μM significantly inhibited IBV replication in H1299 cells, as evidenced by the dramatically reduced levels of IBV gRNA and virus titers in the supernatant compared with the DMSO control (**Figure 3-3c and d**). Although XBP1 splicing was inhibited in H1299 cells treated with DBSA, it could not be concluded whether the inhibition was due to a direct inhibition of IRE1 by DBSA or an indirect effect due to the reduced IBV infection. Thus, we refrained from further analysis of the downstream UPR genes, and the specific effect of DBSA on IBV-induced activation of the IRE1-XBP1 pathway in H1299 cells were undetermined.

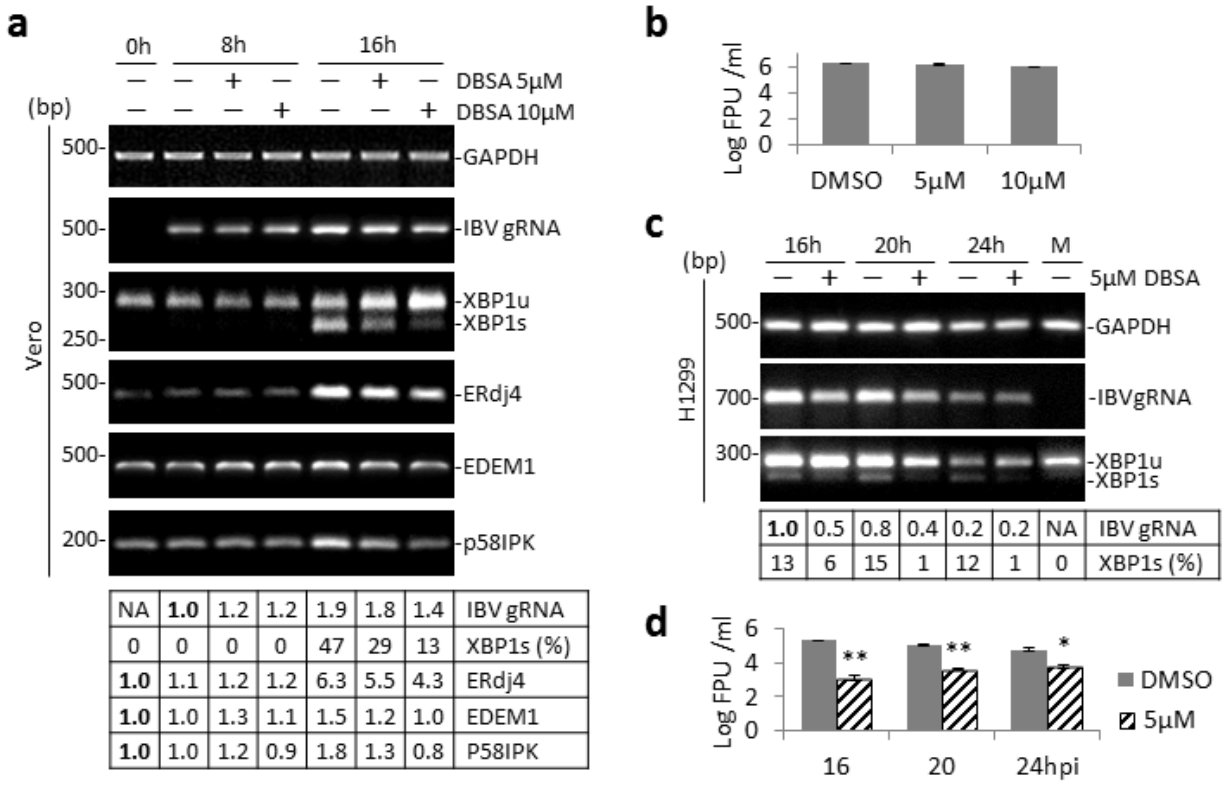

NA	**1.0**	1.2	1.2	1.9	1.8	1.4	IBV gRNA
0	0	0	0	47	29	13	XBP1s (%)
1.0	1.1	1.2	1.2	6.3	5.5	4.3	ERdj4
1.0	1.0	1.3	1.1	1.5	1.2	1.0	EDEM1
1.0	1.0	1.2	0.9	1.8	1.3	0.8	P58IPK

1.0	0.5	0.8	0.4	0.2	0.2	NA	IBV gRNA
13	6	15	1	12	1	0	XBP1s (%)

Figure 3-3 IRE1 inhibition attenuates IBV-induced activation of the IRE1-XBP1 pathway in Vero cells but reduces IBV replication in H1299 cells

(a) Vero cells were infected with IBV at MOI~2 for 4 hours before treated with 5μM or 10μM of DBSA, or same volume of DMSO. Total RNA was extracted and subjected to RT-PCR as in Figure 3-1a. Sizes of DNA ladders in bp were indicated on the left. Relative fold-induction of genes and percentage of XBP1 splicing was calculated as in Figure 3-1a.

(b) The culture supernatants from 16 hours post-treatment samples in (a) were clarified by centrifugation and subjected to plaque assay analysis. Virus titers were expressed as the logarithm of plaque forming units (PFU) per ml of supernatants.

(c) H1299 cells were infected with IBV at MOI~2 for 4 hours before treated with 5μM of DBSA, or same volume of DMSO for the indicated period of time. RNA extraction and semi-quantitative RT-PCR analysis was performed as in (a).

(d) The culture supernatant from IBV-infected samples in (c) were subjected to plaque assay analysis as in (b). Virus titers were expressed as the logarithm of PFU per ml of supernatants. Asterisks indicate significant differences between indicated samples and DMSO-treated sample of the same time point (*, $P<0.05$; **, $P<0.01$).

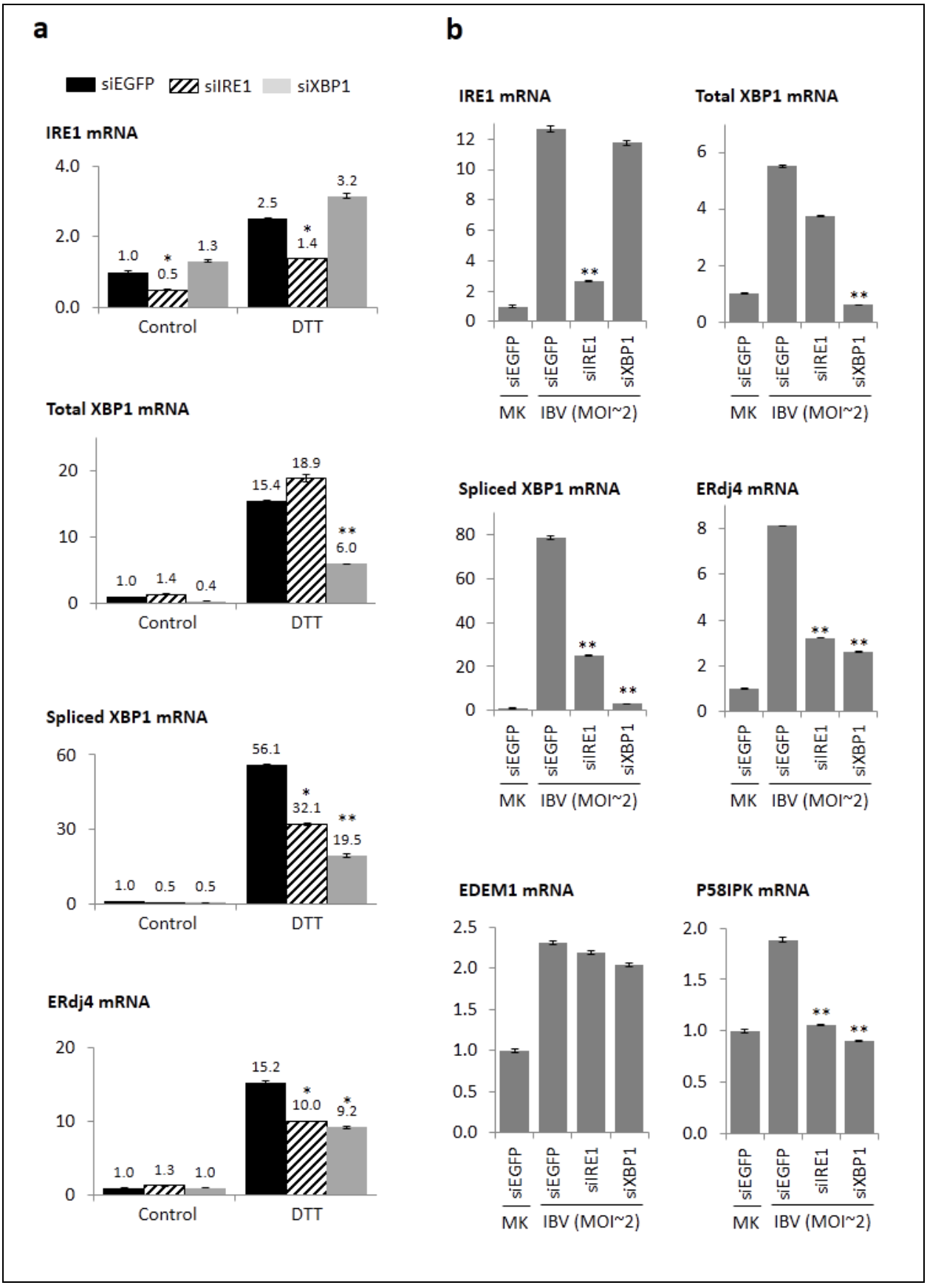
a
siEGFP
siIRE1
siXBP1
IRE1 mRNA
4.0
2.0
0.0
1.0
0.5
1.3
2.5
1.4
3.2
Control
DTT
Total XBP1 mRNA
20
10
0
1.0
1.4
0.4
15.4
18.9
6.0
Control
DTT
Spliced XBP1 mRNA
60
30
0
1.0
0.5
0.5
56.1
32.1
19.5
Control
DTT
ERdj4 mRNA
20
10
0
1.0
1.3
1.0
15.2
10.0
9.2
Control
DTT
b
IRE1 mRNA
Total XBP1 mRNA
Spliced XBP1 mRNA
ERdj4 mRNA
EDEM1 mRNA
P58IPK mRNA
siEGFP
siEGFP
siIRE1
siXBP1
MK
IBV (MOI~2)

Figure 3-4 Knockdown of IRE1 or XBP1 attenuates IBV-induced activation of the IRE1-XBP1 pathway in H1299 cells

(a) H1299 cells were transfected with siEGFP, siIRE1 or siXBP1 before treated with 2mM DTT for 2 hours. Another set of control cells were treated with PBS for the same period of time. Total RNA was extracted and subjected to real time RT-PCR analysis. Fold induction of specific genes were calculated using GAPDH as internal references and normalized to the siEGFP transfected PBS-treated sample. Asterisks indicate significant differences between the indicated samples and siEGFP (*, $P<0.05$; **, $P<0.01$).

(b) Knockdown of IRE1 or XBP1 attenuates IBV-induced activation of the IRE1-XBP1 pathway in H1299 cells. H1299 cells were transfected with siRNAs before infected with IBV (MOI~2) for 20 hours. Total RNA extraction, real time RT-PCR and data analysis were performed as in (a). Asterisks indicate significant differences between the indicated samples and the siEGFP transfected IBV-infected sample (**, $P<0.01$)..

3.2.4 Knockdown of IRE1 or XBP1 attenuates IBV-induced activation of the IRE1-XBP1 pathway

To achieve more specific loss-of-function analysis of the IRE1-XBP1 pathway, we adopted the RNA interference (RNAi) approach. It should be noted that knockdown experiments were only performed in H1299 cells but not Vero cells, due to its extremely low transfection efficiency. Short interfering RNAs (siRNA) specifically targeting IRE1 or XBP1 were transfected into H1299 cells, and one siRNA targeting EGFP was used as a negative control. To see if knockdown of IRE1 or XBP1 suppressed the pathway, transfected H1299 cells were treated with the ER stress inducer DTT. As shown in **Figure 3-4a**, the mRNA levels of IRE1, total XBP1, XBP1s and ERdj4 significantly increased in the siEGFP transfected DTT-treated cells, compared with PBS-treated control. In cells transfected with siIRE1, DTT-induced up-regulation of IRE1 significantly decreased by ~50% compared with siEGFP control. On the other hand, transfection of siXBP1 drastically reduced the mRNA level of total XBP1 by ~70% in DTT-treated cells. Notably, the mRNA level of spliced XBP1 induced by DTT treatment was also reduced by ~50% in IRE1-knockdown cells and by ~70% in XBP1-knockdown cells compared with the siEGFP control. Moreover, knockdown of either IRE1 or XBP1 also reduced ERdj4 expression at the mRNA level by 30-40% in the DTT-treated cells (**Figure3-4a**).

H1299 cells were then similarly transfected before infected with IBV. Quantitative real time RT-PCR was again used to determine induction of related UPR genes. As shown in **Figure 3-4b**, increased mRNA expression of genes related to the IRE1-XBP1 pathway was observed in the IBV-infected cells compared with mock infected control. Transfection with siIRE1 and siXBP1 resulted in ~75% and ~90% knockdown of the endogenous IRE1 and total XBP1 at the mRNA level, respectively. The knockdown efficiency seemed higher compared to the DTT treatment experiment (**Figure 3-4a**), which might be due to a longer incubation time of siRNA transfection before cell harvest. Notably, transfection of siXBP1 almost completely abolished the up-regulation of XBP1s in IBV-infected cells, whereas knockdown of IRE1 also reduced the level of XBP1s mRNA by ~75% (**Figure 3-4b**). Knockdown of either IRE1 or XBP1 also significantly reduced up-regulation of ERdj4 and p58IPK by ~ 50% or more in the infected cells, but the mRNA level of EDEM1 was only minimally affected (**Figure 3-4b**). Taken together, the knockdown experiments demonstrated that IBV infection indeed activated the IRE1-XBP1 pathway, and up-regulations of ERdj4 and p58IPK were dependent on both IRE1 and XBP1.

.

3.2.5 Knockdown of IRE1 potentiates IBV-induced apoptosis

One of the possible outcomes for cells under prolonged ER stress is the induction of apoptosis [216,340,341]. Since previous studies have shown that IBV triggers caspase dependent apoptosis in the infected cells [234], we moved on to investigate the involvement of IRE1 and XBP1 in this process. As shown in **Figure 3-5a**, H1299 cells transfected with siIRE1, siXBP1 and siEGFP were infected with IBV or mock infected. Knockdown of IRE1 was determined by Western blot, as revealed by the significantly weaker bands in siIRE1-transfected cells compared with the siEGFP control. Transfection of siXBP1 also reduced the protein level of unspliced XBP1 in the cells, although we were not able to detect the spliced form of XBP1 by Western blot. Successful knockdown of IRE1 and XBP1 were also reflected by the differences in XBP1 splicing determined by RT-PCR. Consistent with the real time PCR data (**Figure 3-4b**), whereas knockdown of IRE1 reduced the mRNA level of XBP1s, knockdown of XBP1 depleted the mRNA of both XBP1u and XBP1s compared to the siEGFP control (**Figure 3-5a)**. Poly (ADP-ribose) polymerase (PARP), a well characterized apoptosis marker and a substrate of caspase 3, was used to monitor apoptosis. In cells transfected with siEGFP, significant PARP cleavage

(~27%) could be detected at 22 hpi. Interestingly, in IRE1-knockdown cells, PARP cleavage was observed at an earlier time point (~19 hpi). Moreover, at 22 hpi, a more prominent PARP cleavage (~49%) was detected in the IRE1-knockdown cells, compared with the siEGFP control (**Figure 3-5a**). Surprisingly, knockdown of XBP1 did not result in a similar phenotype. Indeed, in XBP1-knockdown cells, no significant PARP cleavage could be detected at either 19 or 22 hpi (**Figure 3-5a**). The same experiment was performed multiple times, and the observed differences were reproducible and statistically significant (**Figure 3-5b**).

Because apoptosis induction in the infected cells were dependent on IBV replication [234], the more prominent PARP cleavage in the IRE1-knockdown cells might be attributed to more robust IBV replication. To see whether knockdown of IRE1 or XBP1 affect IBV replication, the IBV N protein was determined by Western blot. As shown in **Figure 3-5a**, the levels of N protein were similar in the cells transfected with siIRE1 or siXBP1, compared with the siEGFP control. The two minor bands of lower molecular weight represent the cleavage product of the N protein, which is known to be processed by caspases [131,342]. Interestingly, the cleavage patterns of the N protein seems to agree with that of PARP, as cleavage of N also occurred earlier and was more complete in the IRE1-knockdown cells compared with the control (**Figure 3-5a**). To confirm that knockdown of IRE1 or XBP1 did not affect IBV replication, culture supernatants of the infected cells were subjected to plaque assay analysis. As shown in **Figure 3-5c**, virus titers in the supernatants were similar for cells transfected with siIRE1 or siXBP1, compared with the control of the same time points. The results thus suggested that the observed differences in IBV-induced apoptosis were not due to changes of IBV replication in the knockdown cells.

To further validate the results, we also determined the activation of caspases (caspase 3, 8 and 9) during IBV infection in the knockdown cells. Samples collected at 22 hpi and siEGFP trasnfected mock infected sample in **Figure 3-5a** were probed with individual caspase antibodies. As shown in **Figure 3-5d**, the cleavage of caspase 3, 8 and 9 were significantly higher in the IRE1-knockdown cells and lower in the XBP1-knockdown cells, as compared with the siEGFP control, which was consistent with the PARP cleavage pattern (**Figure 3-5a**). Moreover, the observed effects in all three caspases tested suggested that the anti-apoptotic activity of IRE1 might function at apoptotic signaling factors upstream of caspase activation.

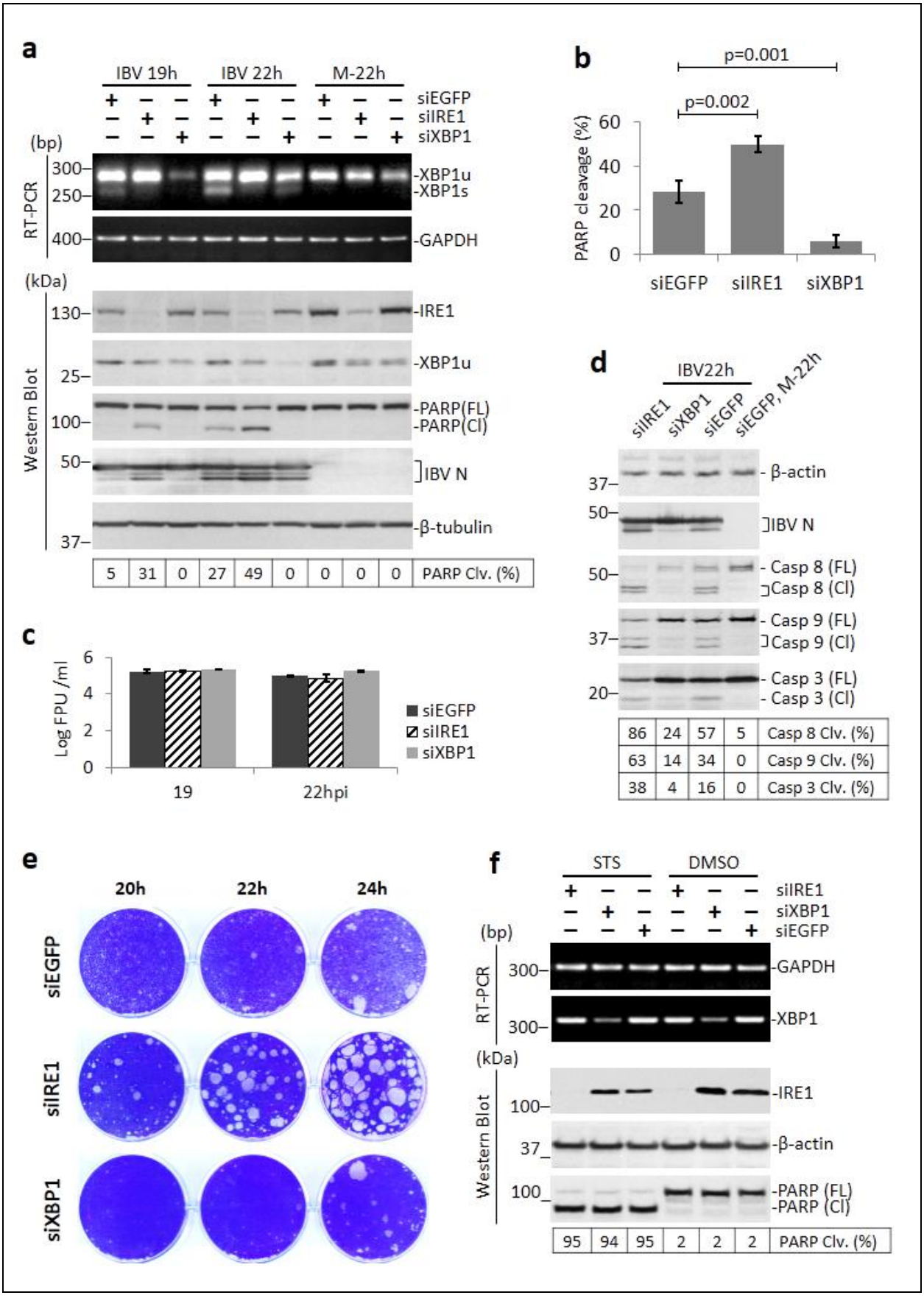
a
IBV 19h
IBV 22h
M-22h
siEGFP
siIRE1
siXBP1
(bp)
RT-PCR
300–
250–
-XBP1u
-XBP1s
400–
-GAPDH
(kDa)
Western Blot
130–
-IRE1
-XBP1u
25–
100–
-PARP(FL)
-PARP(Cl)
50–
IBV N
-β-tubulin
37–
5 31 0 27 49 0 0 0 0 PARP Clv. (%)
b
p=0.001
p=0.002
PARP cleavage (%)
60
40
20
0
siEGFP
siIRE1
siXBP1
c
Log FPU /ml
6
4
2
0
19
22hpi
siEGFP
siIRE1
siXBP1
d
IBV22h
siIRE1
siXBP1
siEGFP
siEGFP, M-22h
37–
- β-actin
50–
IBV N
50–
- Casp 8 (FL)
Casp 8 (Cl)
37–
- Casp 9 (FL)
Casp 9 (Cl)
20–
- Casp 3 (FL)
- Casp 3 (Cl)
86 24 57 5 Casp 8 Clv. (%)
63 14 34 0 Casp 9 Clv. (%)
38 4 16 0 Casp 3 Clv. (%)
e
20h
22h
24h
siEGFP
siIRE1
siXBP1
f
STS
DMSO
siIRE1
siXBP1
siEGFP
(bp)
RT-PCR
300–
-GAPDH
300–
-XBP1
(kDa)
Western Blot
100–
-IRE1
37_
-β-actin
100_
-PARP (FL)
-PARP (Cl)
95 94 95 2 2 2 PARP Clv. (%)

Figure 3-5 knockdown of IRE1 potentiates IBV-induced apoptosis in H1299 cells

(a) Effects of IRE1- or XBP1-knockdown on IBV-induced PARP cleavage. H1299 cells in duplicate were transfected with siIRE1, siXBP1 or siEGFP. At 48 hours post transfection, cells were infected with IBV at MOI~2 or mock infected. One set of cells were harvested at the indicated time points and subjected to Western blot analysis using antibodies against IRE1, XBP1, IBV N and PARP. β-tubulin was included as loading control. Sizes of protein ladders in kDa were indicated on the left. Percentage of PARP cleavage [PARP Clv. (%)] was calculated as the intensity of cleaved PARP [PARP(Cl)] divided by the total intensities of full length PARP [PARP(FL)] and PARP(Cl). In the second set of cells, total RNA was extracted and subjected to RT-PCR using primers specific for XBP1 and GAPDH. Sizes of DNA ladders in bp were indicated on the left.

(b) Quantification of PARP cleavage in siRNA-transfected cells infected with IBV. PARP cleavage was determined as in (a). The bar chart shows results from three independent experiments and indicates standard deviations and p values.

(c) The supernatants from IBV-infected samples in (a) were subjected to plaque assay analysis. Virus titers were expressed as the logarithm of PFU per ml of supernatants.

(d) Effects of IRE1- or XBP1-knockdown on IBV-induced activation of caspase 3, 8 and 9. The IBV-infected, 22 hpi protein samples and the siEGFP-transfected mock infected protein sample from (a) were subjected to Western blot analysis using antibodies against IBV N, caspase 8, caspase 9 and caspase 3 respectively. β-actin was included as loading control. Percentage of caspase cleavage was calculated as the intensity of cleaved caspases divided by the total intensities of the corresponding full length and cleaved caspases.

(e) Effect of IRE1- or XBP1-knockdown on the viability of IBV-infected cells. H1299 cells transfected with siRNAs were infected with IBV at MOI~2 for the indicated perriod of time or mock infected. After removing the supernatant, cells were fixed with 3.7% formaldehyde for 1 hour and stained with crystal violet.

(f) Effect of IRE1- or XBP1-knockdown on apoptosis induced by staurosporine (STS). H1299 cells in duplicate were transfected with siIRE1, siXBP1 or siEGFP. At 48 hours post transfection, cells were treated with 5 μg/ml STS or same volume of DMSO for 12 hours before harvested. Sizes of protein ladders in kDa or sizes of DNA ladders in bp were indicated on the left. Western blot and RT-PCR analysis were performed as in (a). Percentage of PARP cleavage was calculated as in (a).

The effect of IRE1-knockdown on IBV-induced apoptosis could also be revealed by the viability of infected cells. As shown in **Figure 3-5e**, the knockdown cells were infected with IBV for the indicated time points before fixed and stained with crystal violet. In the siEGFP control, the intensity of crystal violet gradually reduced throughout the course of infection, indicating a decrease in viable cells. Large plaques could be observed in the 24 hpi well, due to massive cell death and detachment. In cells transfected with siIRE1, plaques could be observed at an earlier time point (20 hpi) and much more extensive cell death was detected at later time points. In contrast, cells transfected with siXBP1 exhibited minimal decrease in stain intensities as infection proceeded, although some plaques were also observed at 24 hpi similar as in the siEGFP control (**Figure 3-5e**).

To rule out the possibility that off-target effects of siRNAs may affect normal apoptotic signaling, H1299 cells were transfected with the siRNAs, before treated with a widely-used apoptosis inducer staurosporine (STS) or the DMSO solvent control. As shown in **Figure 3-5f**, similar levels of PARP cleavage were observed in STS-treated cells transfected with siIRE1, siXBP1 or siEGFP, and minimum levels of PARP cleavage were observed in cells treated with DMSO. This result demonstrated that cells transfected with the siRNAs have normal apoptotic signaling and the observed differences in IBV-induced apoptosis were specific for IBV infection.

Taken together, these data suggest that although IRE1 was not essential for IBV replication, it protected the infected cells from IBV-induced apoptosis. The seemingly opposite effect of XBP1 knockdown on apoptosis was unexpected, since XBP1 is the main target of IRE1-mediated splicing. However, it is well known that whereas XBP1s serves as a potent activator of downstream UPR genes, XBP1u is actually a negative regulator of UPR [209]. Thus it is possible that XBP1u and XBP1s may also demonstrate opposite effects on IBV-induced apoptosis. Because siXBP1 used in the experiments targets both XBP1u and XBP1s, it is difficult to elucidate the function of individual isoforms. As shown in **section 3.2.7**, when we shifted to the overexpression approach using wild type and dominant negative XBP1, it became appearent that XBP1u and XBP1s indeed play opposing roles on IBV-induced apoptosis.

3.2.6 Overexpression of IRE1 protects cells from IBV-induced apoptosis

To further characterize the anti-apoptotic function of IRE1, we adopted the transient overexpression approach. A plasmid encoding full-length human IRE1 with an HA-tag at the C-terminus was constructed. N-terminal epitope tag was not used to prevent undesired effect on the signal peptide at the N-terminus of IRE1. H1299 cells were transfected with the construct or the vector control (pcDNA3.1), before infected with IBV at an MOI ~2 or mock infected. As shown in **Figure 3-6a**, ectopic expression of IRE1-HA was detected by Western blot using antibodies against the HA-tag. Transfection of IRE1 did not significantly affect the replication of IBV, as indicated by the similar level of N protein compared with the control (**Figure 3-6a**). In the vector control, prominent PARP cleavage was observed at 20 hpi (~20%) and 24 hpi (~46%). However, in cells transfected with IRE1-HA, IBV-induced PARP cleavage was partially reduced to ~9% at 20 hpi and ~24% at 24 hpi. The experiment was performed multiple times and the result was reproducible and statistically significant (**Figure 3-6b**). Therefore, transient overexpression of IRE1 was pro-survival and sufficient to partially protect cells from IBV-induced apoptosis.

The full length IRE1 protein contains a lumenal domain that recognizes unfolded protein, a transmembrane domain, a kinase domain that catalyses autophosphorylation and dimerization, and an RNase domain that mediates mRNA splicing (**Figure 3-6c**). To investigate which domain of IRE1 harbors the anti-apoptotic activity, two mutants were generated by mutagenesis. In the K599A mutant, the critical lysine residue was mutated to alanine and the kinase activity was abolished. In the ΔRNase mutant, coding sequence for RNase domain was deleted (**Figure 3-6c**).

H1299 cells were transfected with the pcDNA3.1 vector control, wild type IRE1, or the two mutants before infected with IBV at MOI~2 or mock infected. As shown in **Figure 3-6d**, the expression levels for the two mutants were slightly higher than that of the wild type IRE1. This was not unexpected, because IRE1 has been shown to undergo ubiquitin-dependent degradation upon activation. Removal of the kinase or RNase activity possibly reduced basal activation and rendered the protein more stable. Overexpression of wild type IRE1 significantly enhanced IBV-induced XBP1-splicing and up-regulation of ERdj4, as compared with the vector control (**Figure 3-6d**). In contrast, transfection of the K599A mutant only slightly increased XBP1 splicing,

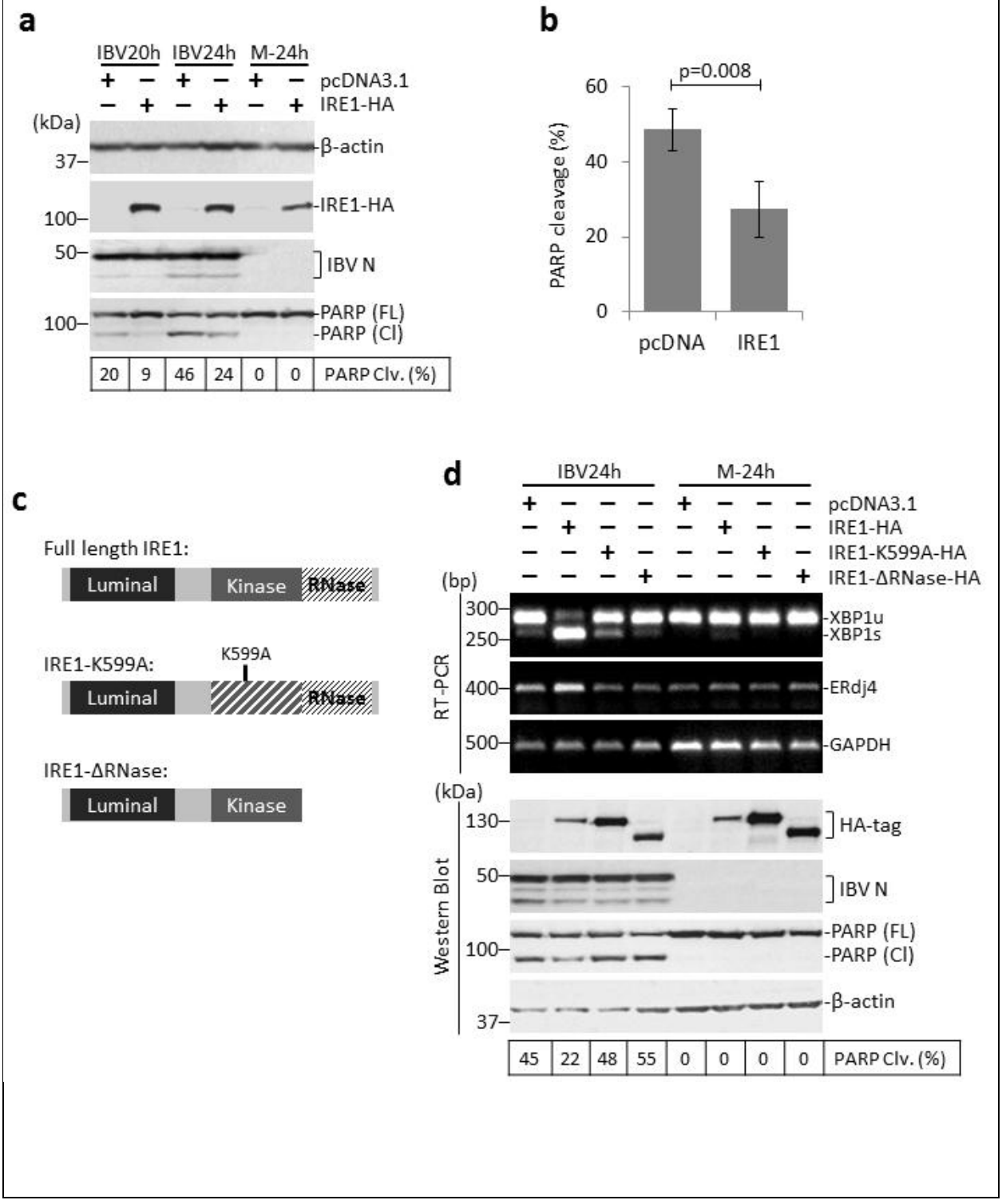
a
IBV20h
IBV24h
M-24h
pcDNA3.1
IRE1-HA
(kDa)
37–
β-actin
100–
IRE1-HA
50–
IBV N
100–
PARP (FL)
PARP (Cl)
20 9 46 24 0 0 PARP Clv. (%)
b
p=0.008
PARP cleavage (%)
60
40
20
0
pcDNA
IRE1
c
Full length IRE1:
Luminal
Kinase
RNase
IRE1-K599A:
K599A
Luminal
RNase
IRE1-ΔRNase:
Luminal
Kinase
d
IBV24h
M-24h
pcDNA3.1
IRE1-HA
IRE1-K599A-HA
IRE1-ΔRNase-HA
(bp)
300–
250–
XBP1u
XBP1s
RT-PCR
400–
ERdj4
500–
GAPDH
(kDa)
130–
HA-tag
50–
IBV N
Western Blot
PARP (FL)
100–
PARP (Cl)
β-actin
37–
45 22 48 55 0 0 0 0 PARP Clv. (%)

Figure 3-6 Overexpression of full-length IRE1 protects cells from IBV-induced apoptosis.

(a) H1299 cells were transfected with pcDNA3.1-IRE1-HA or pcDNA3.1. At 24 hours post transfection, cells were infected with IBV at MOI~2 or mock infected. Cells were harvested at indicated time points and the protein lysates were subjected to Western blot analysis using antibodies against HA-tag, IBV N and PARP. Beta-actin was included as loading control. Sizes of protein ladders in kDa were indicated on the left. Percentage of PARP cleavage was calculated as in Figure 3-5a and summarized at the bottom.

(b) Quantification of PARP cleavage in plasmid transfected cells infected with IBV. Percentage of PARP cleavage in cells transfected with pcDNA3.1 or pcDNA3.1-IRE1-HA and infected with IBV for 24 hours was determined as in (a). The bar chart shows results from three independent experiments and indicates standard deviations and p values.

(c) Schematic diagrams showing the functional domains of IRE1 protein. A lysine to alanine mutation at K599 results in loss of IRE1 kinase activity. The RNase domain of IRE1 is deleted to generate the ΔRNase mutant. Not drawn to scale.

(d) H1299 cells were transfected with pcDNA3.1-IRE1-HA, pcDNA3.1-IRE1-K599A-HA, pcDNA3.1-IRE1-ΔRNase-HA or pcDNA3.1 in duplicate. At 24 hours post transfection, cells were infected or mock infected as in (a). In one set of the cells, Western blot analysis was performed as in (a). In the second set, total RNA was extracted and subjected to RT-PCR using primers specific for XBP1, ERdj4 and GAPDH. Sizes of protein ladders in kDa or sizes of DNA ladders in bp were indicated on the left. Percentage of PARP cleavage was calculated as in (a).

whereas transfection of the ΔRNase mutant has no effect on XBP1 splicing induced by IBV infection. Expression of both mutants also failed to increase the IBV-induced up-regulation of ERdj4, suggesting that both the kinase and RNase domains of IRE1 were required for its activation and function during IBV infection.

Similar to the result shown in **Figure 3-6a**, overexpression of wild type IRE1 partially reduced IBV-induced PARP cleavage, as compared with the vector control. Importantly, transfection of the two mutant forms of IRE1 failed to protect cells from IBV-induced apoptosis. In fact, compared with the vector control, IBV-induced PARP cleavage was slightly higher in K599A or ΔRNase transfected cells (**Figure 3-6d**). No PARP cleavage could be detected in the mock infected cells, so the observed differences in PARP cleavage could not be attributed to changes in the basal level of apoptosis in cells transfected with the mutant constructs. Moreover, the similar levels of IBV N protein suggested that overexpression of the wild type or mutants of IRE1 did not significantly alter the replication of IBV (**Figure 3-6d**). Taken together, the result demonstrated that both the kinase and RNase domains are necessary for the anti-apoptotic activity of IRE1 during IBV infection.

3.2.7 Overexpression of XBP1s protects cells from IBV-induced apoptosis

As presented in **Figure 3-5a**, knockdown of XBP1 inhibited IBV-induced apoptosis in H1299 cells, suggesting that XBP1 may be pro-apoptotic during IBV infection. This is quite unexpected, since both knockdown and overexpression experiments revealed an anti-apoptotic role of its immediate upstream factor IRE1 (**section 3.2.5 and 3.2.6**). Because the mRNAs of XBP1u and XBP1s differ only by the 26-nt intron (which contains repeated sequence), specific knockdown of one isoform is practically impossible. Thus, the siXBP1 used in **Figure 3-5** indeed targeted both XBP1u and XBP1s at the same time. As mentioned above, XBP1u and XBP1s exert distinct or even opposing cellular functions (XBP1u is potentially a transcription repressor and XBP1s is a potent transcription activator). Therefore, the siRNA approach that non-specifically knocked down both XBP1u and XBP1s rendered it difficult to attribute the observed phenotype to individual isoforms.

As a result, the overexpression approach was also adopted to study the function of XBP1u and XBP1s during IBV infection. Initially, coding sequence of XBP1u or XBP1s was

inserted into the C-terminal HA-tagged pcDNA3.1 vector as for the IRE1 constructs. However, the protein expression levels for both XBP1u-HA and XBP1s-HA were very low when transfected in H1299 cells (data not shown). This might be attributed to the non-optimized kozak sequence and/or proteasome degradation of the protein products. To enhance the expression level as well as to monitor the transfection efficiency, coding sequence of XBP1u or XBP1s was fused with an N-terminal EGFP-tag. Previous studies have shown that the fused EGFP would not significantly affect the sub-cellular localization and activity of XBP1 [343]. H1299 cells were transfected with pEGFP-C1 (vector control), pEGFP-XBP1u or pEGFP-XBP1s for 24 hours before infected with IBV or mock infected. As shown in **Figure 3-7a**, the expression of EGFP as well as both fusion proteins could be clearly detected using an antibody against EGFP. Apart from the full-length EGFP-XBP1u protein, multiple low molecular weight bands were observed. This was not unexpected, because the XBP1u protein has been shown to harbor proteasome degradation motif (PDM) in the C-terminus, rendering it unstable in transfected cells [209]. Two major bands were detected in cells transfected with EGFP-XBP1s (**Figure 3-7a**). The upper band represented the full-length fusion protein, whereas the low molecular weight band might be due to premature termination and/or degradation by uncharacterized mechanisms.

As compared with the vector control, transfection of EGFP-XBP1u or EGFP-XBP1s did not significantly affect IBV replication, as determined by the similar levels of IBV N protein and the similar levels of IBV positive-stranded genomic RNA (**Figure 3-7a**). Notably, overexpression of EGFP-XBP1s but not EGFP-XBP1u significantly enhanced the IBV-induced up-regulation of ERdj4 mRNA. This confirmed that the ectopically expressed EGFP-XBP1s retained its normal function as a potent transcription activator. Detectable PARP cleavage could be observed at 24 hpi in the vector control. Importantly, in cells transfected with EGFP-XBP1u, a low level of PARP cleavage was detected at an earlier time point (20 hpi), and a slightly higher percentage of PARP cleavage was also observed at 24 hpi. This suggested that overexpression of XBP1u partially potentiated IBV-induced apoptosis. In contrast, PARP cleavage was slightly weaker at 24 hpi in cells transfected with EGFP-XBP1s compared with the vector control, suggesting that overexpression of XBP1s reduced IBV-induced apoptosis (**Figure 3-7a**). Although the difference was small, multiple experiments yielded repeatable results that were statistically significant (**Figure 3-7b**). Taken together, whereas XBP1u was weakly pro-apoptotic, XBP1s exhibited anti-apoptotic activity during IBV infection.

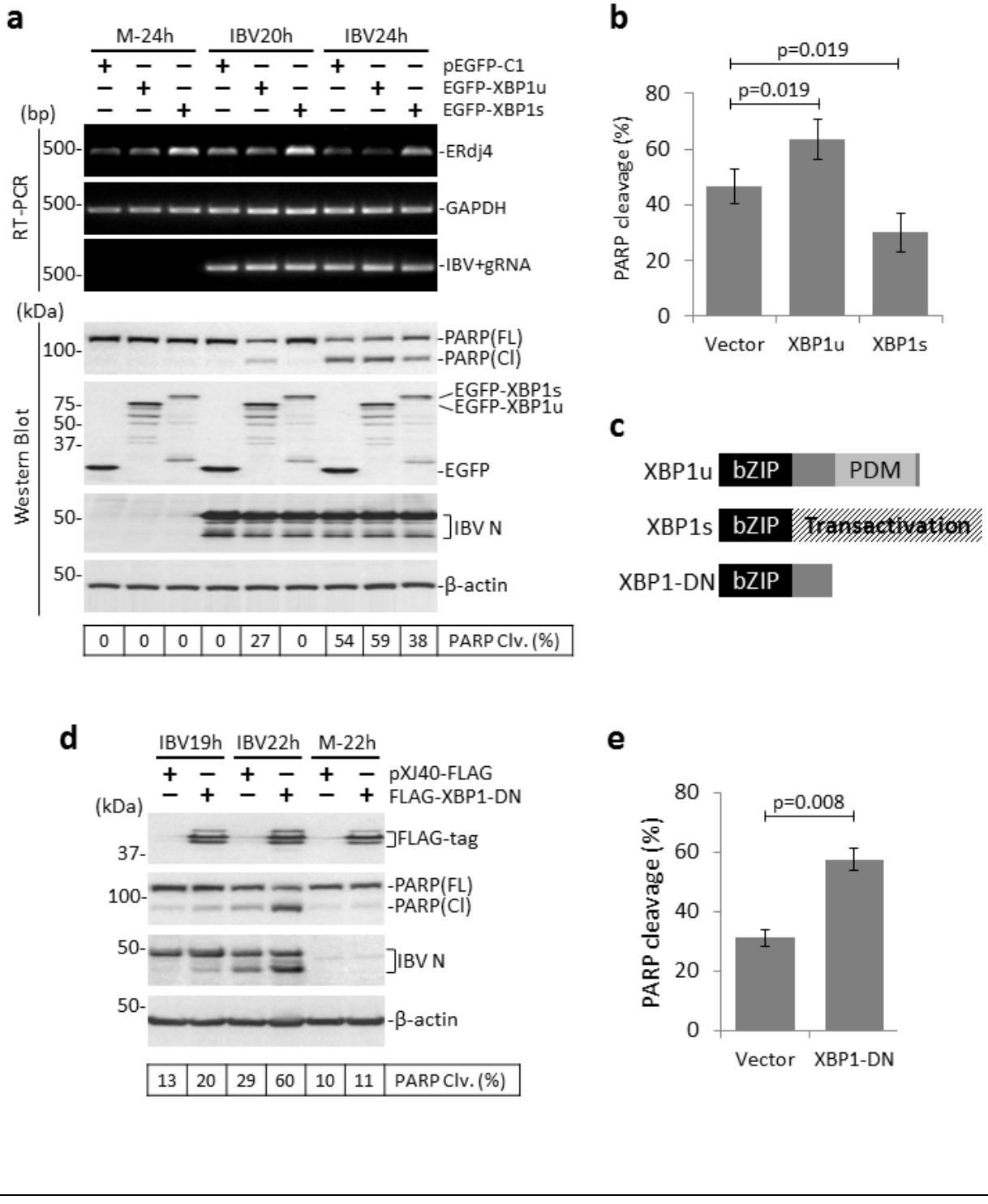
a
M-24h
IBV20h
IBV24h
pEGFP-C1
EGFP-XBP1u
EGFP-XBP1s
(bp)
RT-PCR
500-
ERdj4
GAPDH
IBV+gRNA
(kDa)
Western Blot
100-
PARP(FL)
PARP(Cl)
75-
50-
37-
EGFP-XBP1s
EGFP-XBP1u
EGFP
IBV N
β-actin
0 0 0 0 27 0 54 59 38 PARP Clv. (%)
b
p=0.019
p=0.019
PARP cleavage (%)
80
60
40
20
0
Vector
XBP1u
XBP1s
c
XBP1u bZIP PDM
XBP1s bZIP Transactivation
XBP1-DN bZIP
d
IBV19h
IBV22h
M-22h
pXJ40-FLAG
FLAG-XBP1-DN
(kDa)
37-
FLAG-tag
100-
PARP(FL)
PARP(Cl)
50-
IBV N
β-actin
13 20 29 60 10 11 PARP Clv. (%)
e
p=0.008
PARP cleavage (%)
80
60
40
20
0
Vector
XBP1-DN

Figure 3-7 Effect of XBP1s and XBP1u overexpression on IBV-induced apoptosis

(a) Overexpression of XBP1s, but not XBP1u, protects cells from IBV-induced apoptosis. H1299 cells were transfected with pEGFP-C1, pEGFP-XBP1u or pEGFP-XBP1s in duplicate. At 24 hours post transfection, cells were infected with IBV at MOI~2 or mock infected. Cells were lysed for protein at the indicated time points and subjected to Western blot analysis using antibodies against EGFP, IBV N and PARP. Beta-actin was included as loading control. Percentage of PARP cleavage was calculated as in Figure 3-5a. Sizes of protein ladders in kDa were indicated on the left. Percentage of PARP cleavage was calculated as in Figure 3-5a and summarized at the bottom. In the second set of cells, total RNA was extracted and subjected to RT-PCR using primers specific for ERdj4, IBV positive-stranded genomic RNA and GAPDH. Size of DNA ladders in bp were indicated on the left.

(b) Quantification of PARP cleavage in transfected H1299 cells infected with IBV. Percentages of PARP cleavage in cells transfected with pEGFP-C1, pEGFP-XBP1u or pEGFP-XBP1s, and infected with IBV for 24 hours were determined as in (a). The bar chart shows results from three independent experiments and indicates standard deviations and p values.

(c) Schematic diagrams showing the functional domains of XBP1u, XBP1s and XBP1-DN. All three proteins contain the basic leucine zipper (bZIP) DNA binding domain. The proteasome degradation motif (PDM) in XBP1u is deleted to generate XBP1-DN.

(d) Overexpression of dominant negative XBP1potentiates IBV-induced apoptosis. H1299 cells were transfected with pXJ40-FLAG or pXJ40-FLAG-XBP1-DN. At 24 hours post transfection, cells were infected with IBV at MOI~2 or mock infected. Cells were harvested at indicated time points and the lysates subjected to Western blot analysis using antibodies against FLAG-tag, IBV N and PARP. Beta-actin was included as loading control. Percentage of PARP cleavage was calculated as in (a).

(e) Quantification of PARP cleavage in transfected H1299 cells infected with IBV. PARP cleavage in cells transfected with pXJ40-FLAG or pXJ40-FLAG-XBP1-DN, and infected with IBV for 24 hours was determined as in (d). The bar chart shows results from three independent experiments and indicates standard deviations and p values.

A closer inspection of the function domains in XBP1u and XBP1s reveals that both proteins contain the basic leucine zipper (bZIP) DNA binding domain (**Figure 3-7c**). The 26-nt intron is located downstream of the bZIP coding sequence. Due to the IRE1-mediated splicing and the consequent frame shifting, the two isoforms differ from each other in the C-terminal amino acid sequences. In XBP1u, the presence of a proteasome degradation motif renders it highly unstable in cells. On the other hand, XBP1s encodes a transactivation domain at the C-terminus that accounts for its ability to transactivate downstream UPR genes. Previous studies have shown that if the proteasome degradation motif of XBP1u is deleted, the resulted protein is stabilized [210]. Moreover, by competing with XBP1s for DNA binding, the truncated protein in fact serves as a dominant negative inhibitor of XBP1s (**Figure 3-7c**). Because overexpression of dominant negative XBP1 (XBP1-DN) could selectively inhibit the activity of XBP1s, we decided to investigate its effect on IBV-induced apoptosis.

The proteasome degradation motif of XBP1u (from leucine 194 to C-terminus) was deleted and the coding sequence for XBP1-DN was inserted in the MCS of the expression vector pXJ40-FLAG. As shown in **Figure 3-7d**, expression of FLAG-tag XBP1-DN could be clearly detected by Western blot using antibody against FLAG-tag. Multiple bands were observed possibly because the truncated protein underwent post-translational modifications. Compared with the vector control, overexpression of XBP1-DN significantly increased IBV-induced PARP cleavage from 13% to 20% at 19 hpi, and from 29% to 60% at 22 hpi (**Figure 3-7d**). The pro-apoptotic effect of XBP1-DN was also evidenced by the more complete cleavage of the IBV N protein. This observation was reproducible and statistically significant (**Figure 3-7e**), suggesting that inhibition of XBP1s by overexpressing XBP1-DN markedly potentiated IBV-induced apoptosis. The result confirmed that the two isoforms of XBP1 exhibited opposing activities during IBV infection: XBP1u was weakly pro-apoptotic, whereas XBP1s was anti-apoptotic.

3.2.8 JNK and Akt are involved in the anti-apoptotic function of IRE1

Previous studies have demonstrated that ER stress-induced apoptosis could be mediated by IRE1-dependent activation of the JNK pathway, whereas signaling through the pro-survival PI3K/Akt pathway antagonized ER stress-induced apoptosis [216,344]. Therefore, we continued to investigate the involvement of JNK and Akt in IBV-induced apoptosis. First, the activation of JNK induced by IBV infection was examined in IRE1-knockdown H1299 cells. As shown in **Figure 3-8a**, H1299 cells were transfected with siIRE1 or non-targeting control siRNA (siNC) before infected with IBV at MOI~2 or mock infected. Knockdown of IRE1 was revealed by Western blot analysis. Knockdown of IRE1 resulted in an earlier onset of IBV-induced PARP cleavage, which was also more prominent compared with the negative control of the same time point (**Figure 3-8a**). Notably, JNK phosphorylation could be detected in the control cells at 16 and 20 hpi, indicating that IBV replication activated the JNK pathway at late stage of infection. Surprisingly, activation of JNK was not abolished in the IRE1-knockdown cells infected with IBV as expected. In fact, JNK phosphorylation was drastically potentiated in IRE1-knockdown cells, as compared with the control. Moreover, phosphorylated JNK was also detectable earlier (12 hpi) in IRE1-knockdown cells (**Figure 3-8a**). Therefore, JNK activation was unlikely mediated by IRE1 in IBV-infected cells, and IRE1 might even be responsible for repressing the phosphorylation of JNK during IBV infection. As for the Akt kinase, significant phosphorylation could be detected as early as 8 hpi in the infected control cells, which sustained to 20 hours post infection (**Figure 3-8a**). Thus, in terms of temporal control, Akt was activated before JNK but was also inactivated earlier. Interestingly, in H1299 cells transfected with siIRE1, significant phosphorylation of Akt was detected at a later time point (12 hpi), which diminished rapidly from 16 hpi onwards. Because JNK is presumably pro-apoptotic and Akt anti-apoptotic, the hyper-phosphorylation of JNK and hypo-phosphorylation of Akt correlated well with the potentiated IBV-induced PARP cleavage observed in the IRE1-knockdown cells (**Figure 3-8a**).

Next we moved on to confirm that the opposing activities of Akt and JNK indeed contribute to apoptosis regulation during IBV infection. A gain-of-function approach was used to study the Akt kinase. Previous studies have shown that, when a myristoylation signal sequence is fused to N terminus of Akt (myr-AKT), the protein becomes constitutively active [333]. H1299 cells were transfected with myr-AKT or the pcDNA3.1 vector control before infected with IBV

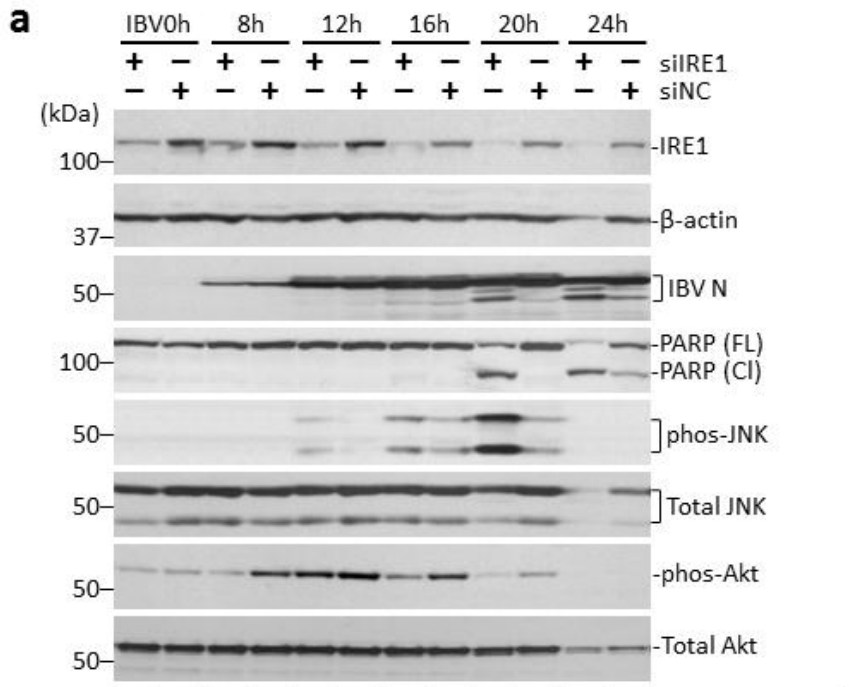

0	0	0	0	0	0	8	0	63	0	77	34	PARP Clv. (%)
0	0	0	0	**1**	0	2.1	1.3	12	1.5	0	0	phos-JNK/JNK
1	1.5	1.1	5.9	7.3	9.3	2.8	6.3	0.2	1.6	0	0	phos-Akt/Akt

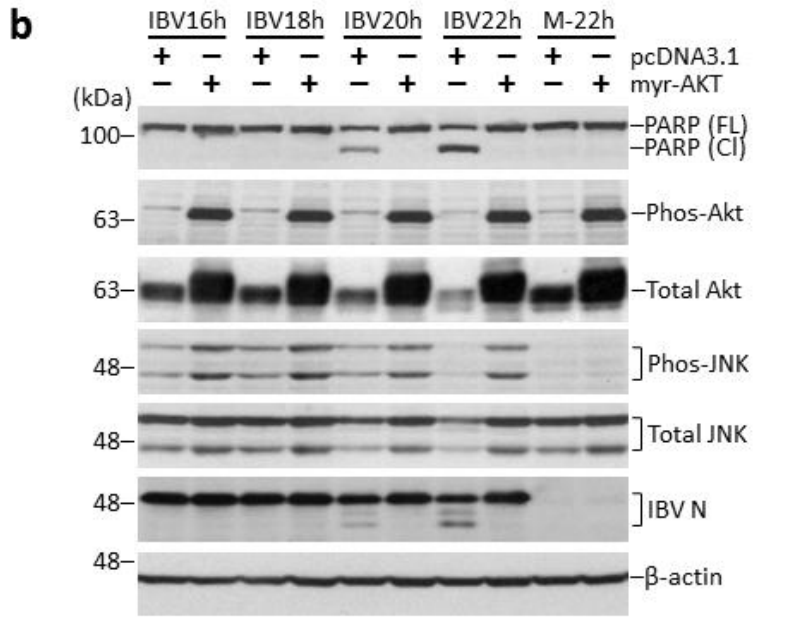

0	0	0	0	40	0	57	0	0	0	PARP Clv. (%)
1	2.7	1.7	2.4	0.8	1.6	0.3	1.4	0.1	0.1	Phospho-JNK

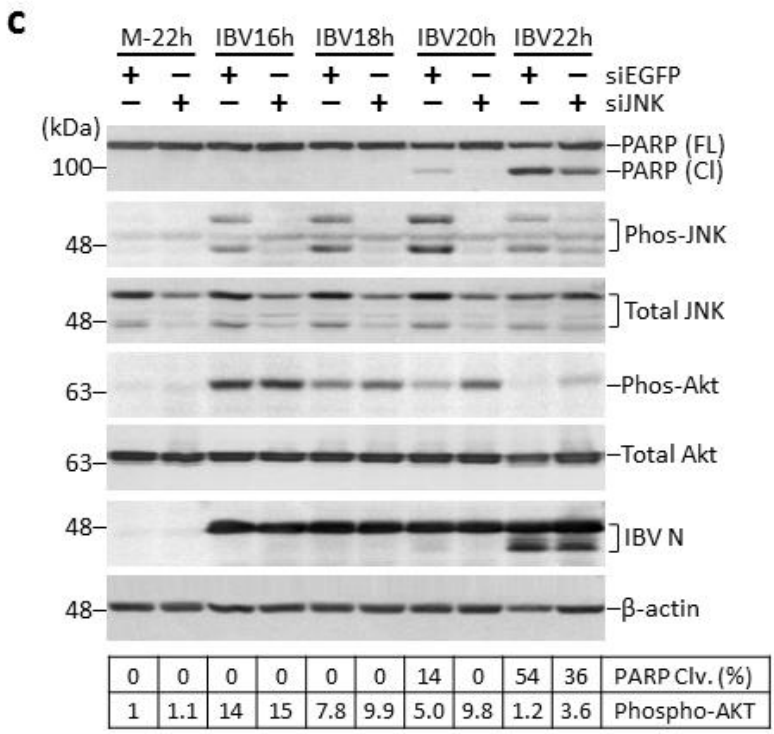

Figure 3-8 JNK and Akt are involved in the anti-apoptotic function of IRE1

(a) JNK is hyper-phosphorylated and Akt is hypo-phosphorylated in IRE1-knockdown cells infected with IBV. H1299 cells were transfected with siIRE1 or non-target siRNA before infected with IBV at MOI~2 and harvested at the indicated time points. Western blot analysis was performed using antibodies against IRE1, IBV N, PARP, phosphorylated-JNK (phos-JNK), total JNK, phosphorylated-Akt (phos-Akt) and total Akt. Beta-actin was included as loading control. Sizes of protein ladders in kDa were indicated on the left. Percentage of PARP cleavage was calculated as in Figure 3-5a. Degree of JNK or Akt phosphorylation was calculated as the band intensity of phosphorylated kinase divided by the band intensity of the corresponding total kinase.

(b) Constitutively active Akt promotes JNK phosphorylation and protects cells from IBV-induced apoptosis. H1299 cells were transfected with pcDNA3.1 or pcDNA3.1-myr-AKT1. At 24 hours post transfection, cells were infected with IBV at MOI~2 or mock infected. Western blot analysis and quantification were performed as in (a).

(c) Knockdown of JNK enhances Akt phosphorylation and partially inhibits IBV-induced apoptosis. H1299 cells were transfected with siJNK or siEGFP for 48 hours before infected with IBV or mock infected. Western blot analysis and quantification were performed as in (a).

at MOI~2 or mock infected. As shown in **Figure 3-8b**, expression of the constitutively active Akt was evidenced by the significantly stronger signal of the phosphorylated Akt and total Akt bands compared with the control. Interestingly, overexpression of active Akt seemed to promote IBV-induced JNK phosphorylation. In the myr-AKT transfected cells, JNK phosphorylation was more prominent and sustained from 16 to 22 hours post infection (**Figure 3-8b**). In contrast, JNK phosphorylation was relatively lower and diminished at 22 hpi in the control cells, possibly due to the extensive cell death and reduction of total JNK protein (**Figure 3-8b**). Expression of the constitutively active Akt did not significantly affect IBV replication, as determined by the similar levels of IBV N protein at 16 and 18 hpi. In the vector control, IBV induced PARP cleavage from 20 hpi onwards. In sharp contrast, in cells transfected with myr-AKT, IBV-induced PARP cleavage was completely abolished throughout the time-course experiment. The absence of apoptosis induction was also revealed by the lack of IBV N cleavage bands in cells expressing myr-AKT (**Figure 3-8b)**. Thus, although AKT enhanced IBV-induced JNK phosphorylation, it is predominantly pro-survival and protected cells from apoptosis during IBV infection.

In another experiment, the knockdown approach was used to study the involvement of JNK in IBV-induced apoptosis. As shown in **Figure 3-8c**, H1299 cells were transfected with siJNK or siEGFP, before infected with IBV or mock infected. Knockdown of JNK was determined by the lower levels of total JNK in the siJNK transfected cells. Moreover, IBV-induced JNK phosphorylation was barely detectable in the JNK-knockdown cells, except for the very weak signal at 22 hpi. Knockdown of JNK did not significantly affect IBV replication, as suggested by the similar levels of IBV N protein in JNK-knockdown cells and the control (**Figure 3-8c**). In the negative control, a low level (~14%) of PARP cleavage could be observed at 20 hpi and considerable (~54%) PARP cleavage was detected at 22 hpi. In contrast, PARP cleavage was absence at 20 hpi and partially reduced to ~36% at 22 hpi in cells transfected with siJNK (**Figure 3-8c**). Notably, IBV-induced Akt phosphorylation was similar at 16 hpi in the JNK-knockdown cells and the control cells. In the subsequent time points, the level of phosphorylated Akt rapidly diminished in the negative control and was barely detectable at 22 hpi. On the other hand, Akt phosphorylation was relatively higher in the JNK-knockdown cells of the same time point and sustained throughout the time course experiment (**Figure 3-8c**). Taken together, the result suggested that JNK served a pro-apoptotic role during IBV infection, possibly by suppressing phosphorylation of the anti-apoptotic Akt.

3.3 UPREGULATION OF CHOP DURING IBV INFECTION AND ITS INVOLVEMENT IN REGULATING IBV-INDUCED APOPTOSIS

3.3.1 IBV infection activates the PERK-eIF2α-ATF4-CHOP pathway

After investigating the IRE1-XBP1 pathway, we turned to another branch of UPR, namely the PERK-eIF2α-ATF4-CHOP signaling pathway. As described in **section 1.3.2**, the integrated stress response can be initiated by four eIF2α kinases – PKR, PERK, GCN2 and HRI. Because HRI is primarily expressed in erythroid cells in response to heme deficiency, studies on coronavirus-induced ISR has been focused on the other three eIF2α kinases. Previous data from this group has demonstrated that PKR is activated at early stage of IBV infection but rapidly dephosphorylated from 12 hpi onwards [195]. To look at the activation of PERK, H1299 cells were infected with IBV at MOI~2 and harvested at different time points. Mock infected cells were also included as a negative control. As shown in **Figure 3-9a**, the protein level of total PERK was not significantly affected by IBV infection and remained stable throughout the time course. In contrast, the level of phosphorylated PERK was significantly elevated in IBV-infected cells compared with the mock infected cells. Phosphorylation of PERK sustained till 16 hpi, after which the signal rapidly reduced to background level (**Figure 3-9a**). The dramatic inactivation of PERK between 16 and 20 hpi resembled that of PKR, suggesting that similar negative feedback mechanisms might be involved. Consistent with the pattern of PERK, eIF2α was significantly phosphorylated in IBV-infected H1299 cells starting from 8 hpi. Phosphorylation of eIF2α sustained till 16 hpi and rapidly reduced to background level from 20 hpi onwards, whereas the protein level of total eIF2α was stable throughout the course of infection (**Figure 3-9a**). Thus, the PERK branch of UPR was activated at the early stage of IBV infection. Together with PKR, IBV-induced phosphorylation of PERK might contribute to the transient activation of eIF2α.

Although eIF2α phosphorylation is associated with global translation attenuation, certain genes (such as ATF4 and CHOP) are indeed preferentially expressed during ISR (**Figure 3-9b**). The expression of these genes during IBV infection at protein level was also determined by Western blot. As shown in **Figure 3-9a**, the transcription factor ATF4 was undetectable in mock infected cells but was significantly induced in IBV-infected cells at 12 hpi. The protein level of

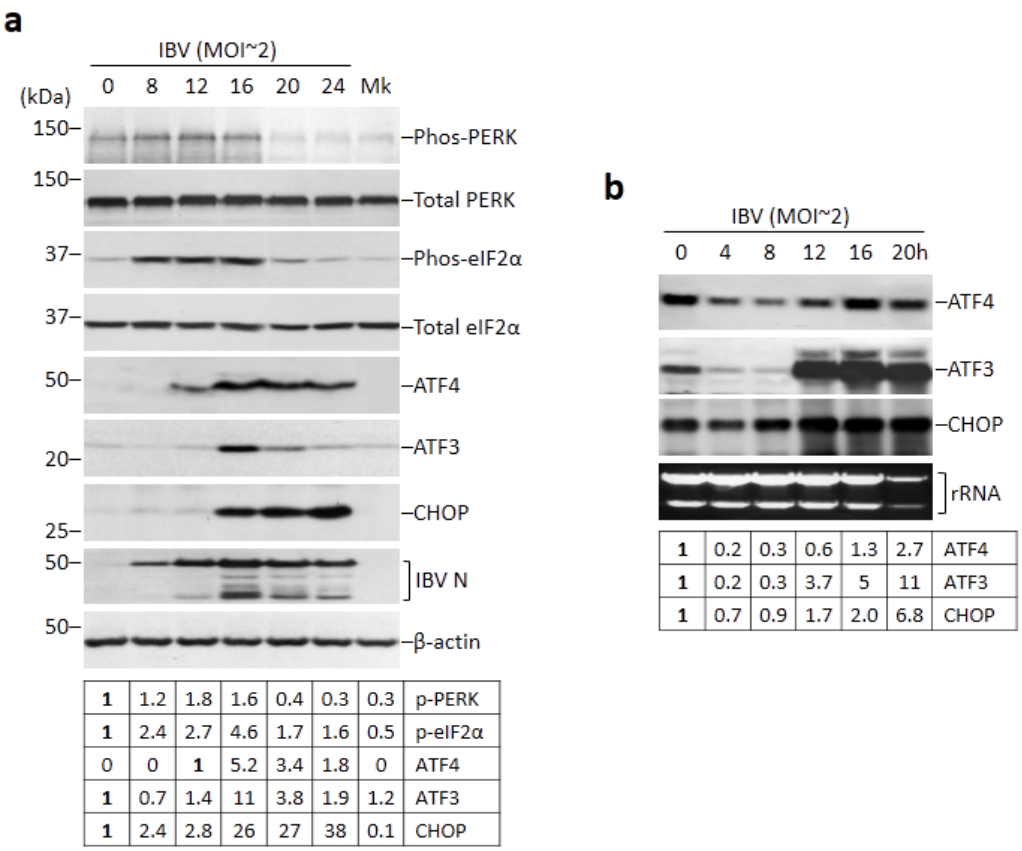

1	1.2	1.8	1.6	0.4	0.3	0.3	p-PERK
1	2.4	2.7	4.6	1.7	1.6	0.5	p-eIF2α
0	0	**1**	5.2	3.4	1.8	0	ATF4
1	0.7	1.4	11	3.8	1.9	1.2	ATF3
1	2.4	2.8	26	27	38	0.1	CHOP

1	0.2	0.3	0.6	1.3	2.7	ATF4
1	0.2	0.3	3.7	5	11	ATF3
1	0.7	0.9	1.7	2.0	6.8	CHOP

Figure 3-9 IBV infection activates the PERK-eIF2α-ATF4-CHOP pathway

(a) The PERK branch of UPR is activated in IBV-infected H1299 cells. H1299 cells were infected with IBV at MOI~2 and harvested at the indicated time points. Cells incubated with mock (Mk) cell lysates for 24 hours were included as negative control. Western blot analysis was performed using antibodies against phosphorylated-PERK (phos-PERK), total PERK, phos-eIF2α, total eIF2α, ATF4, ATF3, CHOP and IBV N. Beta-actin was included as loading control. Sizes of protein ladders in kDa were indicated on the left. Degree of PERK and eIF2α phosphorylation was calculated as the band intensity of phosphorylated protein divided by the band intensity of the corresponding total protein. The abundance of ATF4, ATF3 and CHOP was calculated by the band intensity divided by that of the corresponding β-actin band.

(b) H1299 cells were infected as in (a). Total RNA were extracted at the indicated time points and subjected to Northern blot analysis. Ethidium bromide staining of the 28S and 18S ribosomal RNA (rRNA) was used as loading control. The abundance of ATF4, ATF3 and CHOP mRNAs was calculated as the band intensity divided by that of the corresponding rRNA bands.

ATF4 peaked at 16 hpi and slightly reduced afterwards, although remained detectable till the end of the time course. ATF4 has been shown to induce another UPR-related transcription factor known as ATF3. As shown in **Figure 3-9a**, basal level of ATF3 protein could be observed in mock infected cells. The expression of ATF3 was significantly induced by IBV infection at 16 hpi, which rapidly reduced afterwards and returned to basal level at 24 hpi. Another UPR-related gene known to be activated by ATF4 and ATF3 is the transcription factor CHOP, which is closely associated with ER-stress induced apoptosis. As shown in **Figure 3-9a**, CHOP protein was undetectable in the mock infected cells. At early stage of infection (0-12 hpi), a low level of CHOP could be observed. At 16 hpi, a drastic increase in the protein level of CHOP was detected, which continued to accumulate till the end of the time course.

The mRNA levels of ATF4, ATF3 and CHOP in IBV-infected H1299 cells were also determined by Northern blot. As shown in **Figure 3-9b**, the ATF4 mRNA slightly reduced at the early stage of infection but marginally increased at 16 and 20 hpi. This was not unexpected, because the induction of ATF4 via eIF2α phosphorylation has been shown to occur at the translation level rather than at the transcription level. In contrast, the mRNA levels of ATF3 and CHOP slightly reduced at early time points but significantly increased from 12 hpi to the end of the time course experiment (**Figure 3-9b**). This suggested that both ATF3 and CHOP were dramatically induced by IBV infection at the transcription level, which was most likely mediated by the up-regulated ATF4 protein. Taken together, UPR-related transcription factors are significantly induced in IBV-infected cells at late stage of infection. Thus, although rapidly inactivated, the transient activation of PKR and PERK was sufficient to trigger the downstream eIF2α-ATF4 -CHOP signaling pathway.

3.3.2 Both PKR and PERK are involved in the up-regulation of CHOP and apoptosis induction during IBV infection

To confirm that the up-regulation of CHOP observed in IBV-infected cells was indeed mediated by upstream signaling via PKR or PERK, loss-of-function experiment using RNA interference was performed. As shown in **Figure 3-10a**, H1299 cells were transfected with siPKR, siPERK or non-targeting negative control siRNA (siNC) before infected with IBV at MOI~2 or mock infected. Successful knockdown of PKR or PERK could be clearly determined by Western blot analysis. Knockdown of PKR or PERK did not significantly affect IBV replication, as determined by the similar levels of IBV N protein compared with the negative control (**Figure 3-10a**) and the similar virus titers in the culture supernatants (**Figure 3-10b**). Although the virus titers for PKR-knockdown cells at early time points (8 and 12 hpi) were lower compared with the PERK-knockdown cells or the control, no significant difference was observed at later time points (16, 20 and 24 hpi). Therefore, similar to the SARS-CoV [192], IBV was also not sensitive to the antiviral activity of PKR *in vitro*.

The induction of CHOP by IBV infection was determined by Western blot. As shown in **Figure 3-10a**, CHOP was undetectable in all mock infected cells but significantly up-regulated in the IBV-infected siNC control. In sharp contrast, IBV-induced up-regulation of CHOP was dramatically reduced in the PKR-knockdown cells and partially reduced in the PERK-knockdown cells at 16 and 19 hpi. At 22 hpi, the protein levels of CHOP were significantly lower in both knockdown cells compared with the negative control (**Figure 3-10a**). Notably, the pattern of PARP cleavage correlated well with the induction of CHOP. Significant PARP cleavage could be observed at 19 and 22 hpi in the control cells. In contrast, cleavage of PARP was barely detectable in the PKR-knockdown cells and significantly reduced in the PERK-knockdown cells (**Figure 3-10a**). Taken together, the result demonstrated that PKR, and to a lower degree PERK, were required for the up-regulation of CHOP induced by IBV infection. Moreover, both PKR and PERK contributed to IBV-induced apoptosis *in vitro*, possibly via the induction of the pro-apoptotic transcription factor CHOP.

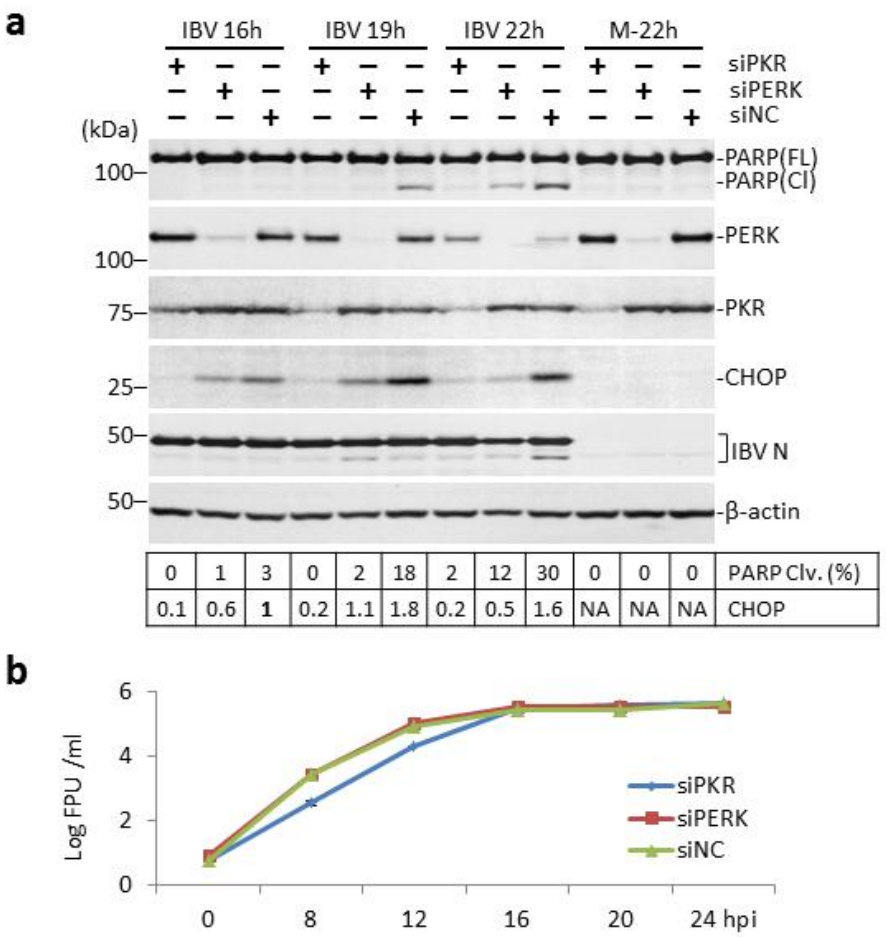

Figure 3-10 Involvement of PERK and PKR in the up-regulation of CHOP and apoptosis induction during IBV infection

(a) H1299 cells were transfected with siPKR, siPERK or siNC before infected with IBV at MOI~2 or mock infected. Protein lysates were harvested at the indicated time points and subjected to Western blot analysis using antibodies against PARP, PERK, PKR, CHOP and IBV N. Beta-actin was included as loading control. Sizes of protein ladders in kDa were indicated on the left. Percentage of PARP cleavage was calculated as in Figure 3-5a. Relative amount of CHOP was determined as the band intensity of CHOP normalized to GAPDH, with the 16 hpi sample of siNC-transfected cells set as one. NA, not applicable.

(b) Knockdown of PERK or PKR does not significantly affect IBV replication in H1299 cells. H1299 cells were transfected with siPERK, siPKR or siNC before infected with IBV at MOI~2. Culture supernatants were harvested at 0, 8, 12, 16, 20 and 24 hpi and subjected to plaque assay analysis using Vero cells. Virus titers were expressed as the logarithm of plaque forming units (PFU) per ml of supernatants.

3.3.3 Overexpression of CHOP promotes IBV-induced apoptosis

To obtain direct evidence that CHOP contributes to IBV-induced apoptosis, the overexpression approach was adopted. The coding sequence of CHOP was fused with FLAG-tag and the resulting construct was transfected into H1299 cells at different dosages (50-800ng). At 24 hours post transfection, cells were infected with IBV at MOI~2 or mock infected for 22 hours. As shown in **Figure 3-11a**, the expression of FLAG-tag CHOP could be detected in a dosage-dependent manner in the transfected cells but was undetectable in control cells transfected with the empty vector. Overexpression of CHOP did not significantly affect IBV replication, as revealed by the similar levels of IBV N protein compared with the control cells. IBV infection induced ~23% PARP cleavage in the negative control at 22h. Notably, transfection of as little as 50ng pXJ40-FLAG-CHOP significantly increased IBV-induced PARP cleavage to ~54%, while transfection of higher amount of DNA further promoted the cleavage of PARP (**Figure 3-11a**). Only background level of PARP cleavage could be detected in the mock infected cells, therefore the observed pro-apoptotic activity of CHOP was specific during IBV infection.

A few functional domains and modification sites have been previously identified for CHOP (**Figure 3-11b**). The region from amino acid 10 to 18 is critical for protein degradation and interaction with the repressor protein Tribbles homolog 3 (TRIB3) [345]. The MAP kinase p38 has been shown to phosphorylate CHOP at Ser79 and Ser82, which enhances its transcription activity [346]. Finally, the C-terminal bZIP domain is required for DNA binding. In particular, Leu134 and Leu141 are the two critical residues in the leucine zipper region [237]. To determine which element is required for the pro-apoptotic function of CHOP during IBV infection, a series of mutants were generated. In the point mutants, either the conserved serines (Ser79/Ser82) or the conserved leucines (Leu134/Leu141) were mutated into alanines. In the deletion mutants, either 9 or 18 amino acids at the N-terminus were deleted (**Figure 3-11b**). These constructs were transfected into H1299 cells, with the wild type CHOP as positive control and empty vector as negative control. Cells were then infected with IBV at MOI~2 for 19 or 22 hours. As described above, IBV induced PARP cleavage in the negative control, which was potentiated in cells transfected with wild type CHOP **(Figure 3-11c)**. Unexpectedly, the levels of PARP cleavage were similar for all the mutants compared with wild type CHOP, suggesting that none of these elements was necessary for the pro-apoptotic activity during IBV infection.

To identify the region required for the pro-apoptotic activity of CHOP, further deletion was made at the N-terminus. Two additional deletion mutants were generated, one with the N-terminal 36 amino acids deleted (ΔN36) and the other with the N-terminal 70 amino acids deleted (ΔN70). No alteration was attempted in the bZIP domain because such mutations might disrupt normal folding of the protein. H1299 cells were transfected with the vector control, wild type CHOP or the two new deletion mutants before infected with IBV at MOI~2 or mock infected. As shown in **Figure 3-11d**, expression of both wild type and mutant constructs could be detected by Western blot against FLAG-tag. Notably, the protein levels of ΔN36-CHOP and ΔN70-CHOP was significantly higher than that of wild type CHOP. This was expected, because previous studies have shown that the N-terminus of CHOP is required for efficient degradation of the protein. Deletion of the N-terminus thus rendered the mutant proteins more stable and accumulating at higher amount. Nonetheless, transfection of all CHOP constructs did not affect IBV replication, as determined by the similar levels of IBV N protein compared with the control.

As shown above and in **Figure 3-11d**, IBV induced PARP cleavage in the negative control, which was significantly enhanced in cells transfected with wild type CHOP. In cells transfected with ΔN36-CHOP, IBV-induced PARP cleavage was lower compared with cells transfected with wild type CHOP at 19 hpi, but the difference became marginal at 22 hpi. In contrast, IBV-induced PARP cleavage was dramatically reduced in cells transfected with ΔN70-CHOP at both 19 and 22 hpi. In fact, the degree of PARP cleavage in ΔN70-CHOP-transfected cells were even lower than the vector control, suggesting that ΔN70-CHOP might serve as a dominant negative mutant that suppressed the pro-apoptotic activity of endogenous CHOP. Taken together, the result demonstrated that the region spanning amino acids 36-70 of CHOP might be required for its pro-apoptotic function during IBV infection.

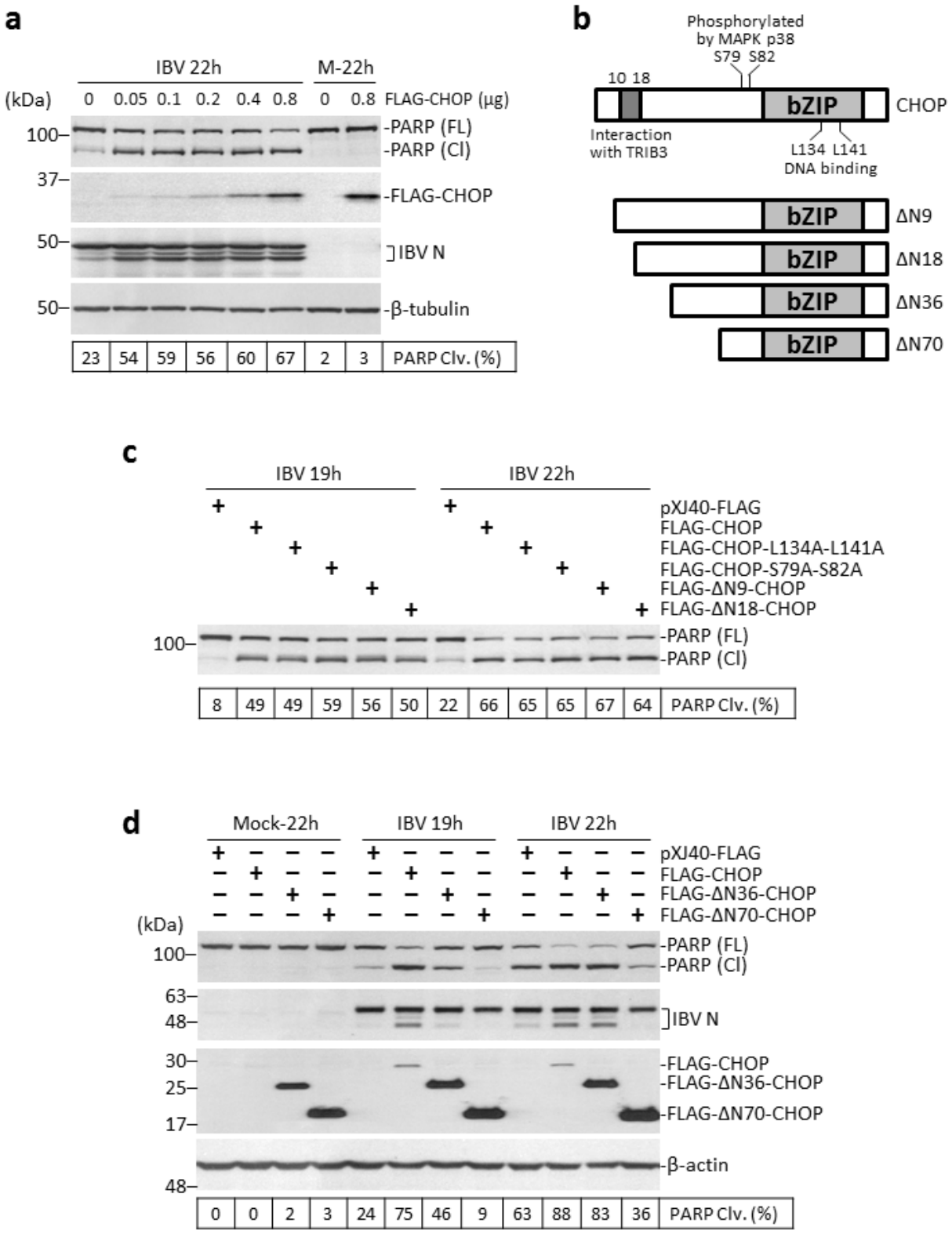
a
IBV 22h
M-22h
(kDa)
0 0.05 0.1 0.2 0.4 0.8 0 0.8 FLAG-CHOP (μg)
100–
-PARP (FL)
-PARP (Cl)
37–
-FLAG-CHOP
50–
IBV N
50–
-β-tubulin
23 54 59 56 60 67 2 3 PARP Clv. (%)
b
Phosphorylated by MAPK p38
S79 S82
10 18
bZIP
CHOP
Interaction with TRIB3
L134 L141
DNA binding
ΔN9
ΔN18
ΔN36
ΔN70
c
IBV 19h
IBV 22h
pXJ40-FLAG
FLAG-CHOP
FLAG-CHOP-L134A-L141A
FLAG-CHOP-S79A-S82A
FLAG-ΔN9-CHOP
FLAG-ΔN18-CHOP
100–
-PARP (FL)
-PARP (Cl)
8 49 49 59 56 50 22 66 65 65 67 64 PARP Clv. (%)
d
Mock-22h
IBV 19h
IBV 22h
pXJ40-FLAG
FLAG-CHOP
FLAG-ΔN36-CHOP
FLAG-ΔN70-CHOP
(kDa)
100–
-PARP (FL)
-PARP (Cl)
63–
48–
IBV N
30–
25–
17–
-FLAG-CHOP
-FLAG-ΔN36-CHOP
-FLAG-ΔN70-CHOP
48–
-β-actin
0 0 2 3 24 75 46 9 63 88 83 36 PARP Clv. (%)

Figure 3-11 Overexpression of CHOP promotes IBV-induced apoptosis

(a) H1299 cells plated in 12-well plate were transfected with 0, 50, 100, 200, 400 or 800ng of pXJ40-FLAG-CHOP plasmid DNA. Appropriate amount of empty vector (pXJ40-FLAG) was incorporated so that total amount of DNA transfected for each well was 0.8μg. At around 24 hours post transfection, cells were infected with IBV at MOI~2 or mock infected. Protein lysates were harvested at the indicated time points and subjected to Western blot analysis using antibodies against PARP, FLAG-tag and IBV N. Beta-tubulin was included as loading control. Sizes of protein ladders in kDa were indicated on the left. Percentage of PARP cleavage was calculated as in Figure 3-5a.

(b) Schematic diagram showing the functional domains, modification sites and critical residues of CHOP. The four deletion mutants were also shown. Not drawn to scale.

(c) H1299 cells were transfected with pXJ40-FLAG, pXJ40-FLAG-CHOP, pXJ40-FLAG-CHOP-L134A-L141A, pXJ40-FLAG-CHOP-S79A-S82A, pXJ40-FLAG-ΔN9-CHOP or pXJ40-FLAG-ΔN18-CHOP before infected with IBV at MOI~2 for 19 or 22 hours. Western blot and quantification was performed as in (a).

(d) The N-terminal region from amino acid 36 to 70 is required for the pro-apoptotic activity of CHOP during IBV infection. H1299 cells were transfected with pXJ40-FLAG, pXJ40-FLAG-CHOP, pXJ40-FLAG-ΔN36-CHOP or pXJ40-FLAG-ΔN70-CHOP before infected with IBV or mock infected. Western blot and quantification was performed as in (a).

3.3.4 CHOP enhances IBV-induced apoptosis by suppressing phosphorylation of the pro-survival MAP kinase ERK

To further confirm the involvement of CHOP in IBV-induced apoptosis, the siRNA knockdown approach was adopted. H1299 cells were transfected with siCHOP or siEGFP before infected with IBV at MOI~2 or mock infected. As shown in **Figure 3-12a**, CHOP was undetectable in the mock infected cells but significantly induced in the control cells infected with IBV. In contrast, the CHOP protein was completely undetectable in cells transfected with siCHOP (**Figure 3-12a**). Knockdown of CHOP did not significantly affect IBV replication, as indicated by the similar levels of IBV N protein and supernatant virus titers compared with the control (**Figure 3-12b**). Consistent with the overexpression experiments, CHOP exhibited a pro-apoptotic activity during IBV infection, as the cleavage of PARP was dramatically reduced in the CHOP-knockdown cells compared with the control (**Figure 3-12a**).

Previous studies have shown that the MAP kinase ERK is implicated in CHOP-mediated apoptosis [347]. The protein level of total ERK was not affected by IBV infection or knockdown of CHOP. In the negative control, phosphorylation of ERK was barely detectable in the mock infected cells but drastically increased at the late stage of infection (**Figure 3-12a**). Interestingly, IBV-induced ERK phosphorylation occurred earlier and was more pronounced in the CHOP-knockdown cells compared with the control, suggesting that CHOP might promote apoptosis by suppressing the activation of ERK during IBV infection.

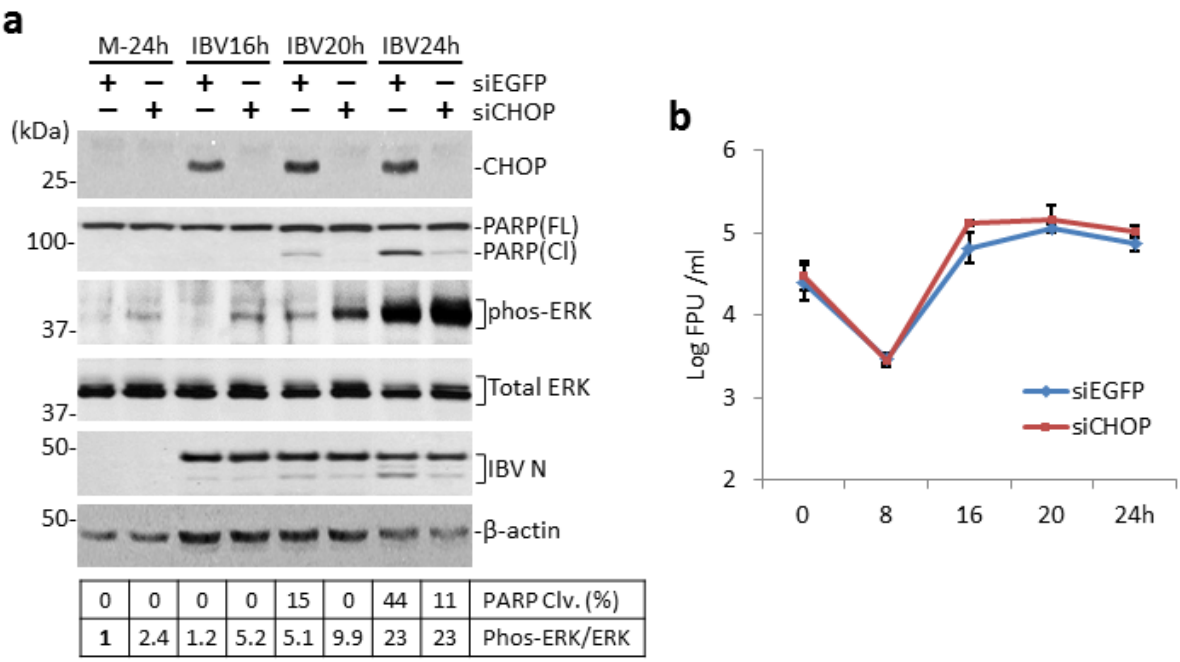

Figure 3-12 CHOP promotes IBV-induced apoptosis by suppressing the phosphorylation of the pro-survival MAP kinase ERK

(a) Knockdown of CHOP inhibits IBV-induced apoptosis and promotes phosphorylation of the ERK kinase. H1299 cells were transfected with siEGFP or siCHOP before infected with IBV at MOI~2 or mock infected. Protein lysates were harvested at the indicated time points and subjected to Western blot analysis using antibodies against CHOP, PARP, phosphorylated ERK (phos-ERK), total ERK and IBV N. Beta-actin was included as loading control. Sizes of protein ladders in kDa were indicated on the left. Percentage of PARP cleavage was calculated as in Figure 3-5a. Percentages of ERK phosphorylation were calculated as the band intensities of phosphorylated-ERK divided by the band intensities of the corresponding total ERK protein.

(b) Knockdown of CHOP does not significantly affect IBV replication in H1299 cells. H1299 cells were transfected with soEGFP or siCHOP before infected with IBV at MOI~2. Culture supernatants were harvested at 0, 8, 12, 16, 20 and 24 hpi and subjected to plaque assay analysis using Vero cells. Virus titers were expressed as the logarithm of plaque forming units (PFU) per ml of supernatants.

It has been well established that inhibition of ERK may trigger apoptosis in cells [348]. To confirm that ERK serves a pro-survival function during IBV infection, H1299 cells were transfected with siERK or siEGFP before infected with IBV. As shown in **Figure 3-13**, knockdown of ERK could be clearly determined by the reduced protein levels of both phosphorylated ERK and total ERK in cells transfected with siERK. Although knockdown of ERK did not significantly affect IBV replication, the virus-induced PARP cleavage was significantly potentiated in the ERK-knockdown cells compared with the control (**Figure 3-13**). This supported that ERK was required for cell survival during IBV infection and suggested that suppression of ERK phosphorylation might be one mechanism whereby CHOP induced apoptosis in IBV-infected cells.

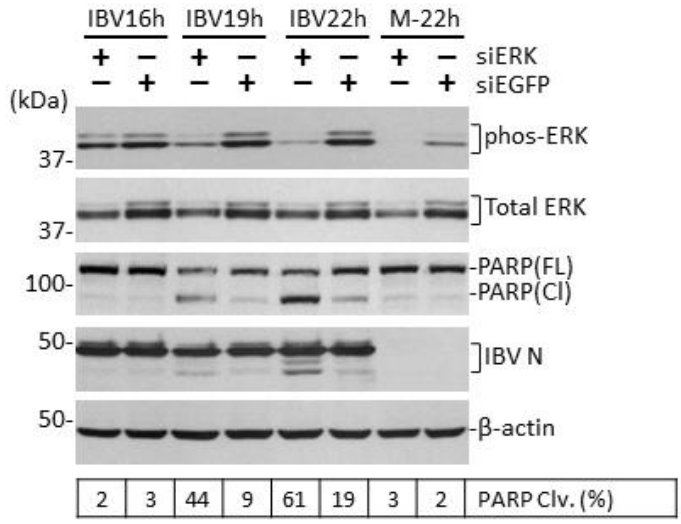

Figure 3-13 ERK protects IBV-infected H1299 cells from apoptotic cell death.

H1299 cells were transfected with siEGFP or siERK before infected with IBV at MOI~2 or mock infected. Protein lysates were harvested at the indicated time points and subjected to Western blot analysis using antibodies against phosphorylated ERK (phos-ERK), total ERK, PARP and IBV N. Beta-actin was included as loading control. Sizes of protein ladders in kDa were indicated on the left. Percentage of PARP cleavage was calculated as in Figure 3-5a.

3.3.5 CHOP and IRE1 differentially regulate death receptor 5 (DR5)

One recent study has shown that unmitigated ER stress promotes apoptosis through activation of DR5 [349]. In this model, signaling from the PERK branch of UPR induces CHOP, which transcriptionally activates DR5. On the other hand, mRNA decay mediated by the RNase activity of IRE1 depletes the transcript of DR5 to promote adaptation and cell survival. If the ER stress persists, accumulated DR5 protein undergoes ligand-independent activation, which activates caspase 8 and induces apoptosis (**Figure 3-14a**). To see whether a similar mechanism applies to IBV-induced apoptosis, modulation of DR5 mRNA by IRE1 and CHOP during IBV infection was investigated. H1299 cells were transfected with siIRE1, siCHOP or siEGFP before infected with IBV at MOI~2 or mock infected. As shown in **Figure 3-14b**, the mRNA levels of IRE1 and CHOP were significantly reduced by transfection of the respective siRNA compared with the control. Interestingly, compared with the control, the mRNA level of IRE1 was higher in the CHOP-knockdown cells, whereas the mRNA level of CHOP was also higher in the IRE1-knockdown cells. This reciprocity suggested that the PERK and IRE1 branch of UPR might regulate each other at the transcription level.

As shown in previous sections, knockdown of either IRE1 or CHOP did not affect IBV replication, as suggested by the similar level of IBV positive stranded genomic RNA compared with control (**Figure 3-14b**). Notably, the mRNA level of DR5 in the control cells increased ~4-fold at 16 hpi and ~6-fold at 19 hpi compared with the mock infected cells, suggesting that DR5 was induced during IBV infection. Importantly, the up-regulation of DR5 was potentiated in the IRE1-knockdown cells but partially suppressed in the CHOP-knockdown cells (**Figure 3-14b**). Therefore, CHOP and IRE1 indeed modulated the mRNA level of DR5 during IBV infection. Although functional studies have not been performed on DR5, it is likely that DR5 contributed to IBV-induced apoptosis in a similar manner as in cells under prolonged ER stress.

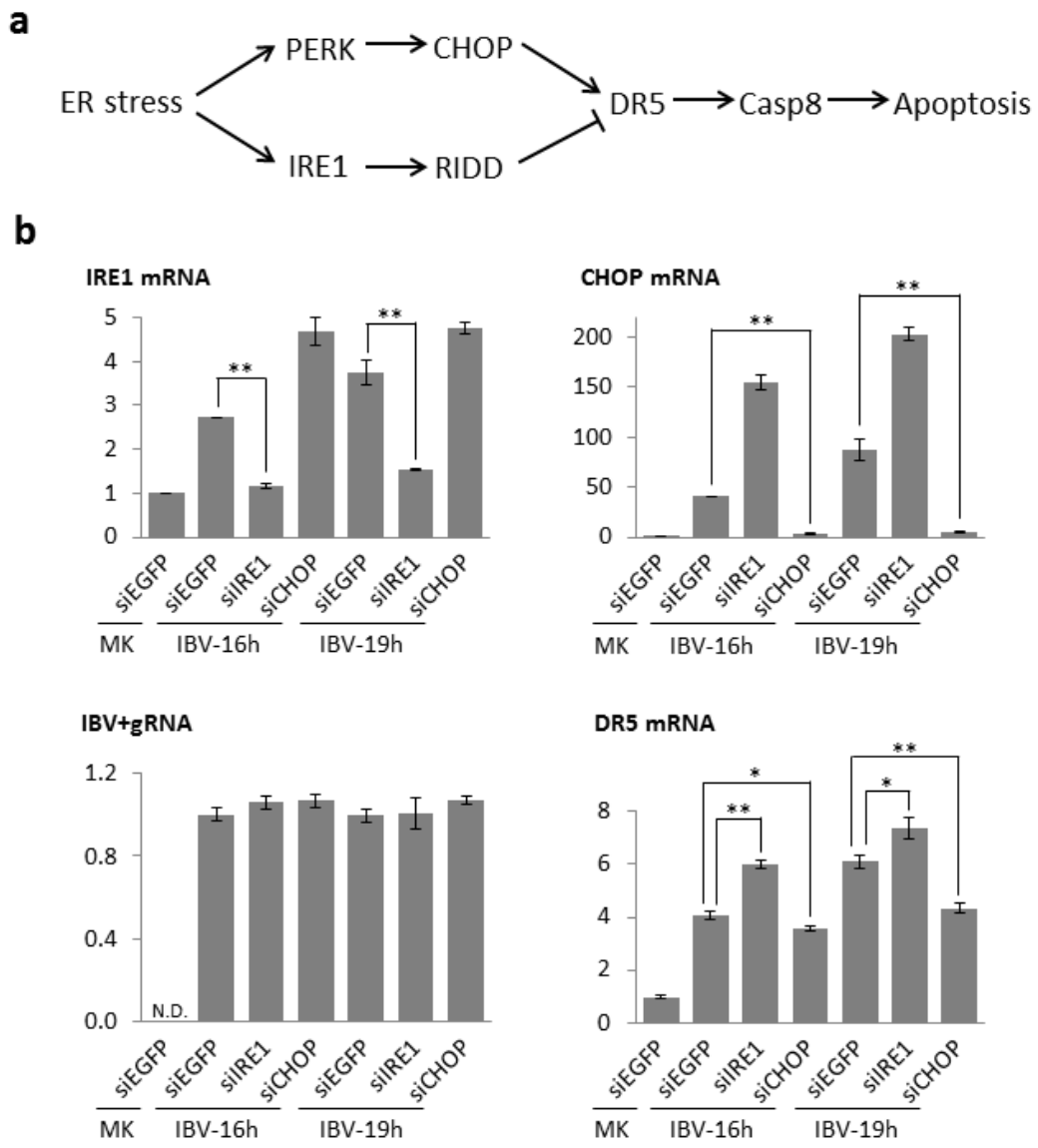

Figure 3-14 CHOP and IRE1 modulate the mRNA of DR5 during IBV infection

(a) Schematic diagram showing how UPR regulates DR5 activation and mediates ER stress-induced apoptosis. Arrows indicate activation and blunt arrow suppression.

(b) CHOP and IRE1 modulate the mRNA of DR5 during IBV infection. H1299 cells were transfected with siIRE1, siCHOP or siEGFP before infected with IBV at MOI~2 or mock infected. Total RNA was extracted and subjected to real time RT-PCR analysis. Fold inductions of genes were calculated using GAPDH as internal references and normalized to the mock infected siEGFP-transfected sample.. Asterisks indicate significant differences between indicated samples and mock (*, $P<0.05$; **, $P<0.01$).

3.4 THE ROLE OF UPR IN THE REGULATION OF IBV-INDUCED AUTOPHAGY

3.4.1 IBV infection induces complete autophagy

Autophagy is an evolutionarily conserved process activated under a variety of cellular stress. Several coronaviruses (such as SARS-CoV and MHV) have been shown to induce autophagy in the infected cells [143,147]. To determine whether IBV infection similarly induces autophagy, a time course experiment was performed. As shown in **Figure 3-15a**, H1299 cells were infected with IBV at MOI~2 or incubated with UV-IBV for the indicated period of time. The conversion of the LC3 protein from the non-lipidated LC3-I into the lipidated LC3-II form was generally used as an indicator of autophagy induction. According to a well-established guideline for autophagy study, the ratio between LC3-II and a loading control (such as β-actin or β-tubulin) should be used as a measurement of autophagy induction [140]. LC3-II/actin ratio remained stable from 0 to 8 hours in both IBV-infected cells and the UV-IBV control (**Figure 3-15a**). In cells infected with IBV, the LC3-II/actin ratio significantly increased at 12 hpi, peaked at 16 hpi and remained stable till the end of the time course. In cells incubated with UV-IBV, the LC3-II/actin ratio also gradually increased. However, LC3-II/actin ratio was always higher in the infected cells compared with control of the same time point after 12 hpi (**Figure 3-15a**).

The high "basal level" of autophagy induction in the negative control was likely due to the incubation of cells in serum-free medium, as serum deprivation has been shown to induce autophagy in cell culture [350]. The high basal level of endogenous LC3-II rendered it difficult to study the specific effect of IBV infection on autophagy induction. Therefore, we shifted to use another well-characterized autophagy reporter system in which the coding sequence of LC3 was fused with an N-terminal EGFP tag. H1299 cells were stably transfected the pEGFP-LC3 construct to generate the H1299-GFP-LC3 cell line. As shown in **Figure 3-15b**, H1299-GFP-LC3 cells were treated with a commonly used autophagy inducer called rapamycin. A considerable conversion of GFP-LC3-I into GFP-LC3-II was observed in the rapamycin-treated cells, whereas a very low level of GFP-LC3-II could be detected in the solvent control, suggesting that the GFP-LC3II to actin ratio might be used as an indicator of autophagy induction. The stable cells were infected with IBV at MOI~2 or incubated with UV-IBV. As

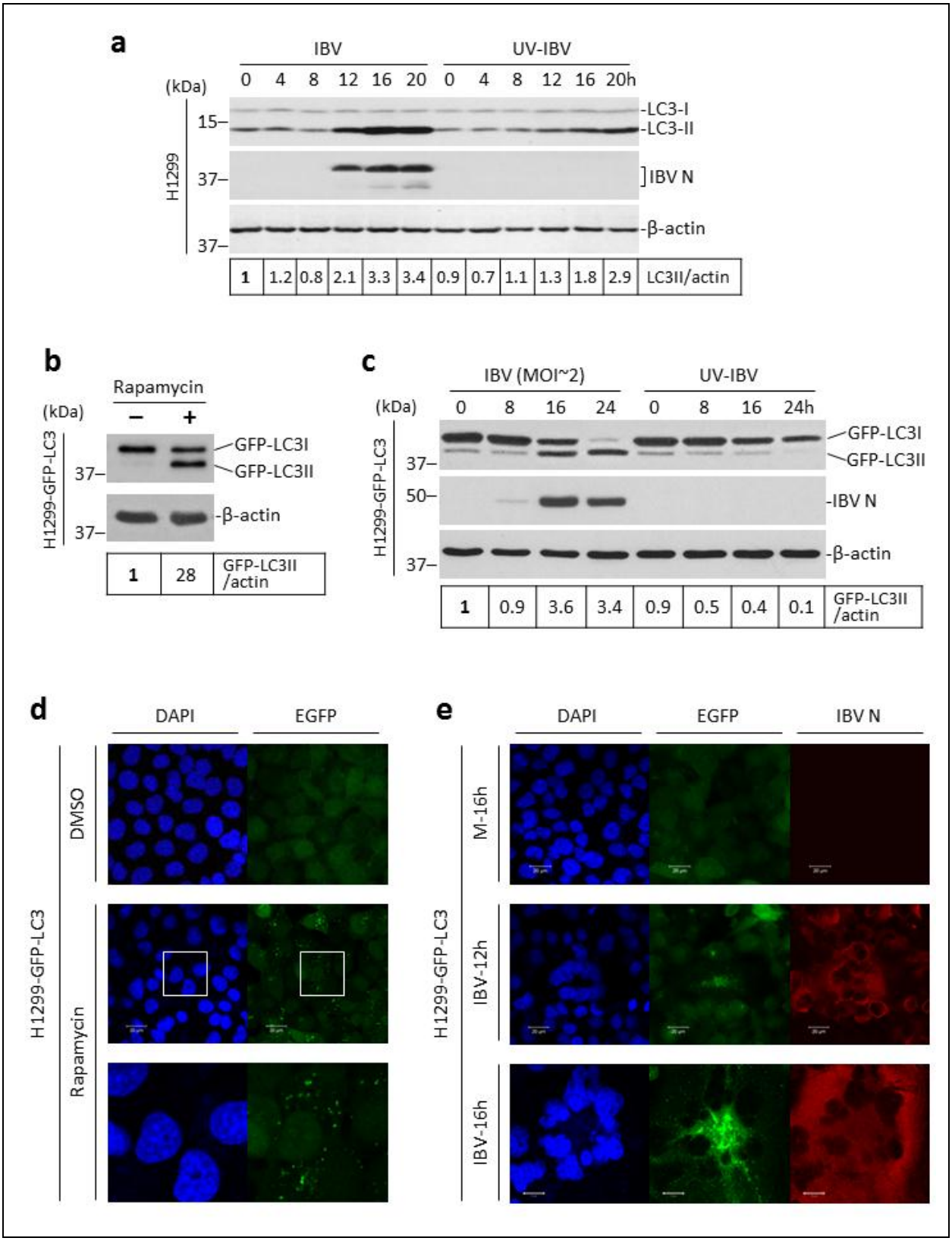
a
IBV
UV-IBV
0 4 8 12 16 20 0 4 8 12 16 20h
(kDa)
15–
37–
37–
H1299
-LC3-I
-LC3-II
IBV N
-β-actin
1 1.2 0.8 2.1 3.3 3.4 0.9 0.7 1.1 1.3 1.8 2.9 LC3II/actin
b
Rapamycin
– +
(kDa)
H1299-GFP-LC3
37–
37–
GFP-LC3I
GFP-LC3II
-β-actin
1 28 GFP-LC3II /actin
c
IBV (MOI~2)
UV-IBV
(kDa)
0 8 16 24 0 8 16 24h
H1299-GFP-LC3
37–
50–
37–
GFP-LC3I
GFP-LC3II
-IBV N
-β-actin
1 0.9 3.6 3.4 0.9 0.5 0.4 0.1 GFP-LC3II /actin
d
DAPI
EGFP
H1299-GFP-LC3
DMSO
Rapamycin
e
DAPI
EGFP
IBV N
H1299-GFP-LC3
M-16h
IBV-12h
IBV-16h

Figure 3-15 Induction of autophagy in cells infected with IBV

(a) Lipidation of endogenous LC3 during IBV infection. H1299 cells were infected with IBV at MOI~2 or incubated with UV-IBV. Protein lysates were harvested at the indicated time points and subjected to Western blot analysis using antibodies against LC3 and IBV N. Beta-actin was included as loading control. Sizes of protein ladders in kDa were indicated on the left. The ratio of LC3-II to corresponding β-actin band intensity was determined and normalized to the IBV-infected 0 hpi sample.

(b) H1299-GFP-LC3 cells were treated with 0.5μM rapamycin or same volume of DMSO for 5 hours before harvested for Western blot with EGFP antibody. Beta-actin was included as loading control. Sizes of protein ladders in kDa were indicated on the left. GFP-LC3II to actin ratio was determined similar as in (a).

(c) H1299-GFP-LC3 cells were infected with IBV as in (a) and subjected to Western blot using antibodies against EGFP and IBV N. Beta-actin was included as loading control. Sizes of protein ladders in kDa were indicated. GFP-LC3II to actin ratio was determined as in (b).

(d) H1299-GFP-LC3 cells were treated as in (b) and fixed. Cell nuclei were stained with DAPI. Fluorescent images were captured with confocal microscope. Highlighted region was enlarged in the bottom panel to show the GFP-LC3II puncta.

(e) H1299-GFP-LC3 cells were infected as in (c). Cells were harvested at the indicated time, fixed and stained with antibody against IBV N (red). Nuclei were stained with DAPI.

shown in **Figure 3-15c**, the band intensities of both GFP-LC3-I and GFP-LC3-II gradually decreased in cells incubated with UV-IBV, suggesting that the overexpressed protein were degraded during the time course. In the IBV-infected cells, although the total amount of GFP fusion protein also reduced by time, there was a significant conversion of GFP-LC3-I to GFP-LC3-II starting from 16 hpi. Indeed, the GFP-LC3II to actin ratio significantly increased at late stage of infection in the infected cells, but steadily decreased throughout the time course in the control cells (**Figure 3-15c**). The result suggested that IBV infection specifically activated autophagy induction, and the GFP-LC3 reporter system provided a more sensitive read-out with a lower level of basal activation compared with the endogenous LC3 protein.

The GFP-LC3 reporter provides another advantage: autophagy induction could be determined by the formation of GFP-LC3II puncta using fluorescent microscopy. As shown in **Figure 3-15d**, the GFP-LC3-I in DMSO treated cells was distributed diffusely in the cytoplasm. Rapamycin induced autophagy and the lipidation of GFP-LC3, thus cytosolic GFP-LC3-II puncta were clearly visible. Next, H1299-GFP-LC3 cells were infected with IBV or mock infected before subjected to immune staining using antibody against IBV N. As shown in **Figure 3-15e**, no specific signal for IBV N was detected in the mock infected cells and GFP-LC3 showed a diffuse pattern, suggesting an absence of autophagy induction. In cells infected with IBV for 12 hours, most cells were positively stained with IBV N protein, featuring an exclusive cytoplasmic localization as previously reported. Moreover, cluster of cells expressing high level of IBV N protein fused with each other to form multinucleated syncitia. Notably, GFP-LC3-II puncta could be readily detected inside these syncitia. On the other hand, in the surrounding mononucleated cells expressing low level of IBV N, the GFP-LC3 protein is still diffusely located in the cytoplasm (**Figure 3-15e**). At a later time point (16 hpi), infected cells underwent massive fusion and generated large syncytia, which were strongly stained with IBV N antibody. Moreover, extensive GFP-LC3-II puncta were observed scattering in the cytoplasm of the syncytia, but were excluded from the nuclei (**Figure 3-15e**). The result suggests that autophagy induction is dependent on the stage of IBV infection. Significant LC3 lipidation and puncta formation can be observed only at a relatively late stage of infection, when extensive syncitia are formed. As a result, cells would be harvested at a late time point (~16 hpi) for all the following experiments where autophagy was studied using fluorescent labeled LC3.

Interestingly, GFP-LC3 puncta are found mostly in the enclosed cytoplasmic space of the syncytia, compared with the peripheral space. This is possibly due to the morphology of the ‘dome-shaped’ syncytia formed in the H1299 cells infected with IBV. During sample preparation for immunofluorescence, cytoplasmic contents such as LC3 puncta became more enriched in the center due to different thickness across the syncytium, resulting in a seemingly uneven distribution pattern. On the other hand, a more evenly distributed pattern of GFP-LC3 puncta could be observed in Vero cells infected with IBV, because more ‘flatten’ syncytia are formed in this cell line (data not shown). To obtain a better resolution of the whole syncytia at a 3D level, confocal imaging using z-stack reconstruction could be used in future experiments.

Nonetheless, accumulation of endogenous LC3 or GFP-LC3 could be a result of inhibited degradation of autophagosomes rather than *de novo* induction of autophagy. These two mechanisms could be differentiated using chloroquine (CQ), a chemical inhibiting lysosomal degradation of autophagosomes [140]. As shown in **Figure 3-16a**, H1299-GFP-LC3 cells were either infected with IBV at MOI~2 or mock infected. Treatment of CQ slightly increased GFP-LC3-II/actin ratio in the mock infected cells, suggesting that 5μM CQ was able to block autophagosome degradation. Treatment of CQ did not significantly affect IBV replication, as indicated by similar level of IBV S protein compared with the solvent control. As shown above, IBV infection significantly increased the GFP-LC3-II/actin ratio compared with mock infected cells. Notably, treatment of CQ in the IBV-infected cells further increased the GFP-LC3-II/actin ratio (**Figure 3-16a**). The result suggested that IBV-induced accumulation of GFP-LC3II could be further enhanced by inhibition of autophagosomal degradation. Therefore, the observed increase of GFP-LC3-II/actin in IBV-infected cells was likely due to *de novo* increase of autophagy induction.

To confirm this, a tandem fluorescence construct ptfLC3 was used [331]. In this reporter construct, LC3 is fused with monomeric red fluoresence protein (mRFP) and GFP in tandem at the N-terminal. Inside the autophagic cell, both green and red fluorescence could be detected for the pH neutral autophagosomes. However, as the autophagosomes fuse with lysosomes, GFP is quenched by the low pH environment whereas mRFP remains fluorescent. Therefore, only red but not green fluoresence could be detected for the autolysosomes. When H1299 stably expressing ptfLC3 was infected with IBV in the presence of CQ, high levels of both green and red fluorescent signals could be detected, which overlapped extensively (**Figure 3-16b**). In sharp contrast, in the same cells infected with IBV without CQ treatment, both green and red fluorescent signals were reduced. Importantly, a large proportion of red fluorescent puncta did not overlap with the green fluorescent signal. This signified the presence of both autophagosomes and autolysosomes in IBV-infected cells. Taken together, the result demonstrated that IBV infection induced complete autophagy, which proceeds to the stage of lysosomal fusion.

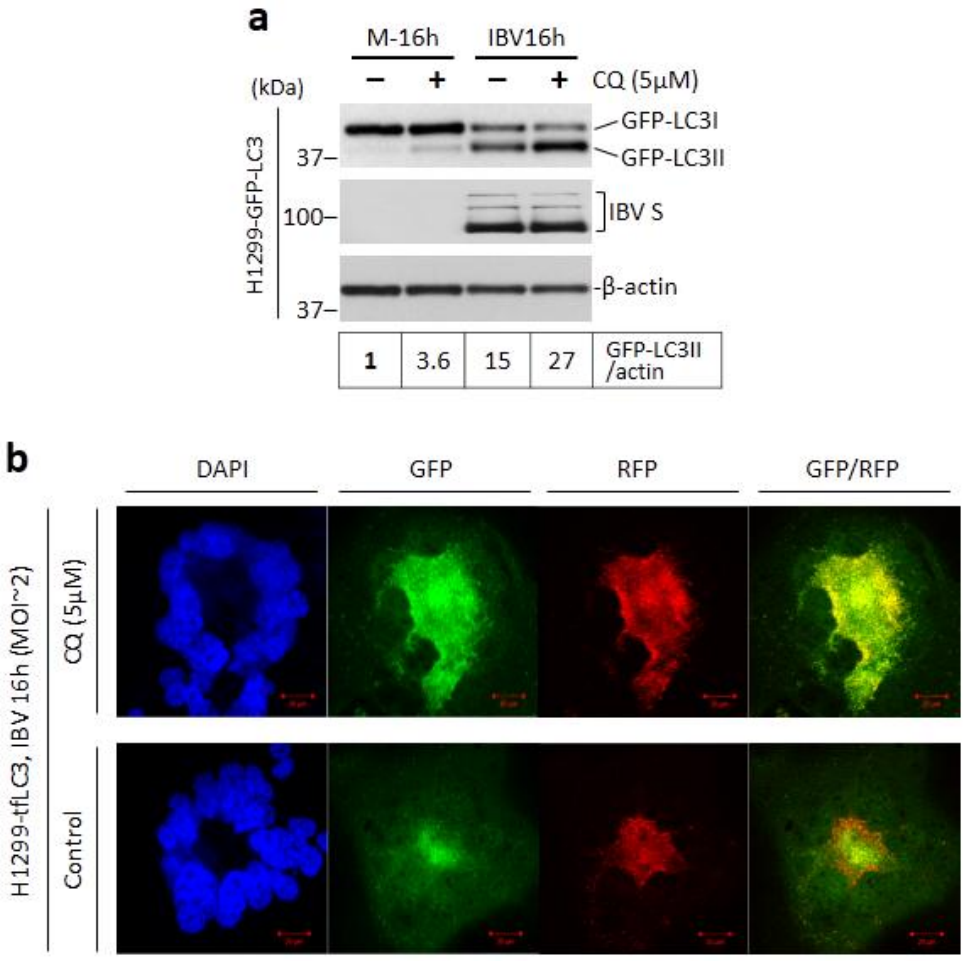

Figure 3-16 IBV infection induces complete autophagy

(a) H1299-GFP-LC3 cells were infected with IBV at MOI~2 or mock infected. After 2 hours of adsorption, cells were washed and treated with 5μM chloroquine or equal volume of PBS and incubated before harvested. Cell lysates were subjected to Western blot as in Figure 3-14c except that antibody of IBV S was used in place of IBV N. Beta-actin was included as loading control. Sizes of protein ladders in kDa were indicated. GFP-LC3II to actin ratio was determined as in Figure 3-14b.

(b) H1299-tfLC3 cells were infected with IBV at MOI~2. After 2 hours of adsorption, cells were washed and treated with 5μM chloroquine or equal volume of PBS. Cells were harvest and fixed, and cell nuclei were stained as in Figure 3-14d. The fluorescent images from GFP and RFP channels were merged to show the co-localization of GFP and RFP.

3.4.2 ATG5 but not Beclin1 is required for IBV-induced autophagy

Autophagy is a highly regulated process and involves a large number of proteins encoded by the autophagy-related genes (ATGs), such as ATG5 and ATG6 (also known as beclin 1, or BECN1) [132]. To study the role of BECN1 and ATG5 in the IBV-induced autophagy, H1299 cells were transfected with siATG5, siBECN1 or siEGFP before infected with IBV at MOI~2. As shown in **Figure 3-17a**, knockdown of ATG5 and BECN1 could be determined by the reduced protein levels in the Western blot. Knockdown of either gene did not significantly affect IBV replication, as suggested by similar level of IBV N protein compared with the negative control. As previously shown, IBV infection induced a ~2-fold increase of LC3-II/actin ratio in the siEGFP control (**Figure 3-17a**). Notably, no significant increase of LC3-II/actin ratio could be detected in the ATG5-knockdown IBV-infected cells. On the other hand, in cells transfected with siBECN1, the LC3-II/actin ratio was considerably higher than the mock infected cells, although slightly lower than the IBV-infected siEGFP control (**Figure 3-17a**).

The high basal level of autophagy in the mock infected cells prompted us to use the H1299-GFP-LC3 cells. As shown in **Figure 3-17b**, similar knockdown experiment was performed in H1299-GFP-LC3 cells and the knockdown efficiency was determined as described above. A non-targeting siRNA (siNC) was used to replace siEGFP because siEGFP would suppress the expression of the EGFP-LC3 reporter protein. As expected, low level of GFP-LC3 lipidation was observed in all the mock infected cells. In cells transfected with siNC, ~5-fold and ~3-fold increase in the GFP-LC3-II/actin ratio could be observed at 16 hpi and 20 hpi respectively, indicating a significant autophagy induction (**Figure 3-17b**). Similar increase in the GFP-LC3-II/actin ratio could be observed in the IBV-infected BECN1-knockdown cells. In sharp contrast, in the ATG5-knockdown cells infected with IBV, the GFP-LC3-II/actin ratio remained at a similar level as the mock infected cells, indicating a lack of autophagy induction. The result was further confirmed with immunofluorescence. As shown in **Figure 3-17c**, significant GFP-LC3-II punta formation induced by IBV infection could be observed in the siNC or siBECN1-transfected cells, but not in ATG5-knockdown cells. Taken together, autophagy induced by IBV infection was dependent on the host protein ATG5 but not BECN1.

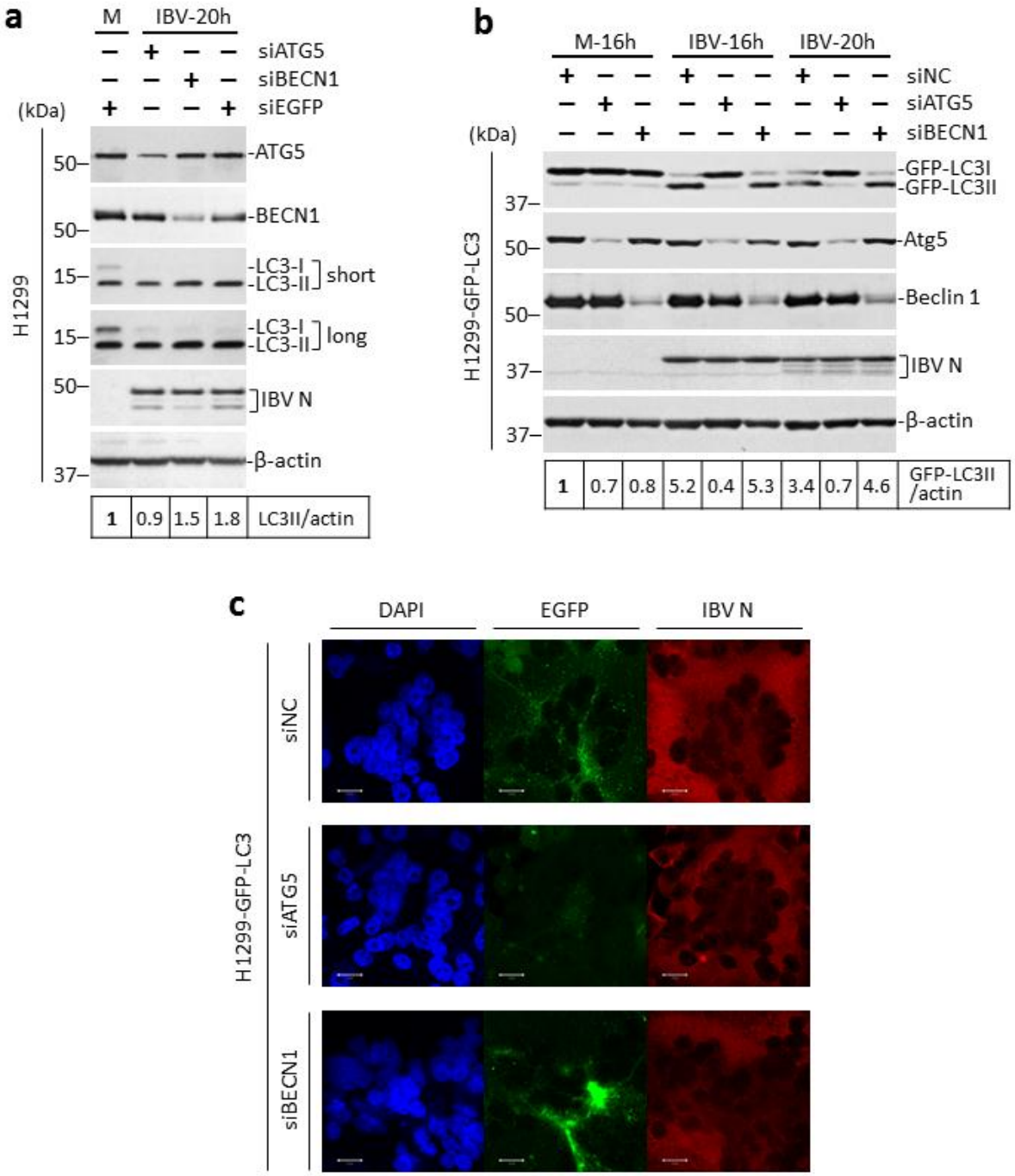
a
M
IBV-20h
siATG5
siBECN1
siEGFP
(kDa)
H1299
50–
-ATG5
50–
-BECN1
15–
-LC3-I
-LC3-II
short
15–
-LC3-I
-LC3-II
long
50–
IBV N
37–
-β-actin
1
0.9
1.5
1.8
LC3II/actin
b
M-16h
IBV-16h
IBV-20h
siNC
siATG5
siBECN1
(kDa)
H1299-GFP-LC3
37–
-GFP-LC3I
-GFP-LC3II
50–
-Atg5
50–
-Beclin 1
37–
IBV N
37–
-β-actin
1
0.7
0.8
5.2
0.4
5.3
3.4
0.7
4.6
GFP-LC3II /actin
c
DAPI
EGFP
IBV N
H1299-GFP-LC3
siNC
siATG5
siBECN1

Figure 3-17 IBV-induced autophagy requires ATG5 but not BECN1.

(a) H1299 cells were transfected with siATG5, siBECN1 or siEGFP before infected with IBV at MOI~2 or mock infected. Protein lysates were harvested at the indicated time points and subjected to Western blot analysis using antibodies against ATG5, BECN1, LC3 and IBV N. Beta-actin was included as loading control. Sizes of protein ladders in kDa were indicated on the left. The LC3-II/actin ratio was determined as in **Figure 3-15a**.

(b) H1299-GFP-LC3 cells were transfected and infected as in (a) before harvested for Western blot using antibodies against ATG5, BECN1, GFP and IBV N. Beta-actin was included as loading control. Sizes of protein ladders in kDa were indicated on the left. GFP-LC3II to actin ratio was determined as in **Figure 3-15b**.

(c) H1299-GFP-LC3 cells were infected as in (b). Cells were harvested at the indicated time, fixed and stained with antibody against IBV N (red). Nuclei were stained with DAPI.

3.4.3 The UPR sensor IRE1 is involved in IBV-induced autophagy

Previous studies have shown that ER stress could induce autophagy, which is dependent on the signaling via the IRE1-JNK pathway [218]. To investigate the involvement of IRE1-XBP1 pathway in IBV-induced autophagy, H1299 cells were transfected with siIRE1, siXBP1 or siEGFP before infected with IBV at MOI~2. As shown in **Figure 3-18a**, successful knockdown of IRE1 and XBP1 could be determined by Western blot and RT-PCR respectively. Compared with the mock control, both siXBP1 and siEGFP-transfected cells had a significant increase in the LC3-II/actin ratio after infected with IBV for 20 hours. Notably, knockdown of IRE1 slightly inhibited IBV-induced autophagy, as indicated by the reduced LC3-II/actin ratio compared with the infected siEGFP control (**Figure 3-18a**). To validate the result, H1299-GFP-LC3 cells were similarly transfected, and siATG5 was included as a positive control. As shown in **Figure 3-18b**, the knockdown of ATG5, IRE1 and XBP1 was determined by either Western blot or RT-PCR. Consistent with the data presented above, IBV infection increased the GFP-LC3-II/actin ratio in cells transfected with siNC. A similar autophagy induction was also detected in the XBP1-knockdown cells. In contrast, lipidation of GFP-LC3-II was significantly inhibited in cells transfected with siATG5 or siIRE1 (**Figure 3-18b**). Consistently, GFP-LC3-II puncta was readily observed in IBV-infected control and XBP1-knockdown cells, but was present at very low level in either ATG5- or IRE1-knockdown cells (**Figure 3-18c**).

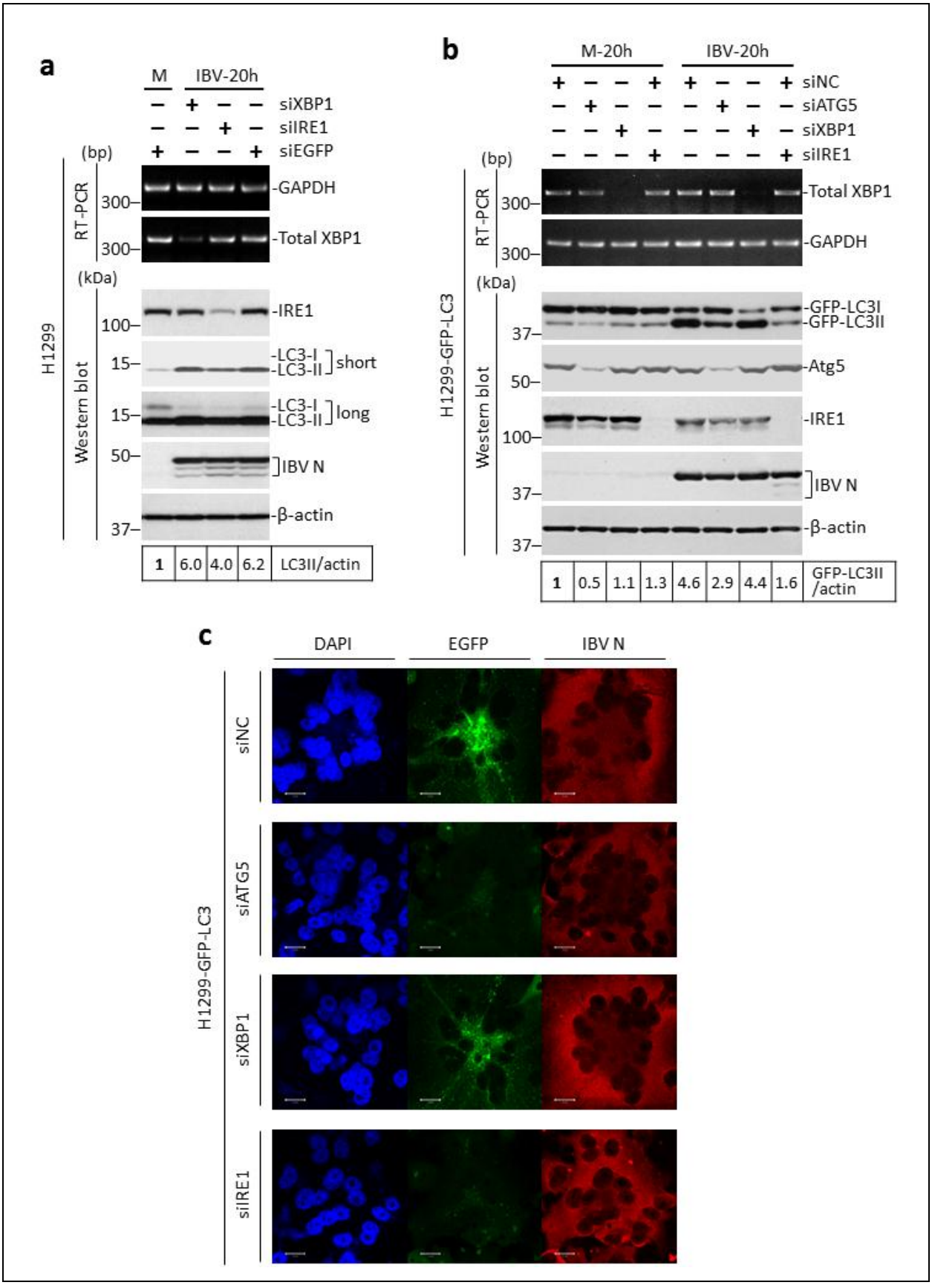
a
M
IBV-20h
siXBP1
siIRE1
siEGFP
(bp)
RT-PCR
300
GAPDH
300
Total XBP1
H1299
(kDa)
Western blot
100
IRE1
15
LC3-I
LC3-II
short
15
LC3-I
LC3-II
long
50
IBV N
37
β-actin
1
6.0
4.0
6.2
LC3II/actin
b
M-20h
IBV-20h
siNC
siATG5
siXBP1
siIRE1
(bp)
RT-PCR
300
Total XBP1
300
GAPDH
H1299-GFP-LC3
(kDa)
Western blot
37
GFP-LC3I
GFP-LC3II
50
Atg5
100
IRE1
37
IBV N
37
β-actin
1
0.5
1.1
1.3
4.6
2.9
4.4
1.6
GFP-LC3II /actin
c
DAPI
EGFP
IBV N
H1299-GFP-LC3
siNC
siATG5
siXBP1
siIRE1

Figure 3-18 IBV-induced autophagy requires the UPR sensor IRE1.

(a) H1299 cells in duplicate were transfected with siXBP1, siIRE1 or siEGFP before infected with IBV at MOI~2 or mock infected. Protein lysates were harvested at the indicated time points and subjected to Western blot analysis using antibodies against IRE1, LC3 and IBV N. Beta-actin was included as loading control. Both a short and long exposure blot of LC3 were shown. Sizes of protein ladders in kDa were indicated on the left. The LC3-II/actin ratio was determined as in **Figure 3-15a**. In the second set of cells, total RNA was extracted and subjected to RT-PCR using primers specific for XBP1 and GAPDH. Sizes of DNA ladders in bp were indicated on the left.

(b) H1299-GFP-LC3 cells induplicate were transfected and infected as in (a) before harvested for Western blot using antibodies against ATG5, IRE1, GFP and IBV N. Beta-actin was included as loading control. Sizes of protein ladders in kDa were indicated on the left. GFP-LC3II to actin ratio was determined as in **Figure 3-15b**. In the second set of cells, total RNA was extracted and subjected to RT-PCR using primers specific for XBP1 and GAPDH. Sizes of DNA ladders in bp were indicated on the left.

(c) H1299-GFP-LC3 cells were infected as in (b). Cells were harvested at the indicated time, fixed and stained using antibodies against IBV N (red). Nuclei were stained with DAPI.

To see whether the other two branches of UPR (ATF6 and PERK) also play a similar function in IBV-induced autophagy, similar knockdown experiments were performed in the H1299-GFP-LC3 cells using the respective siRNAs. As shown in **Figure 3-19a** and **b**, efficient knockdown of ATG5, ATF6, PERK or CHOP could be determined by RT-PCR or Western blot analysis. The replication of IBV was not significantly affected by the silencing of ATG5, ATF6, PERK or CHOP, as indicated by the similar level of IBV N protein compared with the siNC control of the same time point. Consistent with the result above, knockdown of ATG5 partially reduced the lipidation of GFP-LC3-II induced by IBV infection. In contrast, in ATF6-, PERK-, or CHOP-knockdown cells infected with IBV, the GFP-LC3-II/actin ratios were all similar to the control of the same time point (**Figure 3-19a and b**). Taken together, it appeared that IRE1, but not the other two branches of UPR, was required for IBV-induced autophagy.

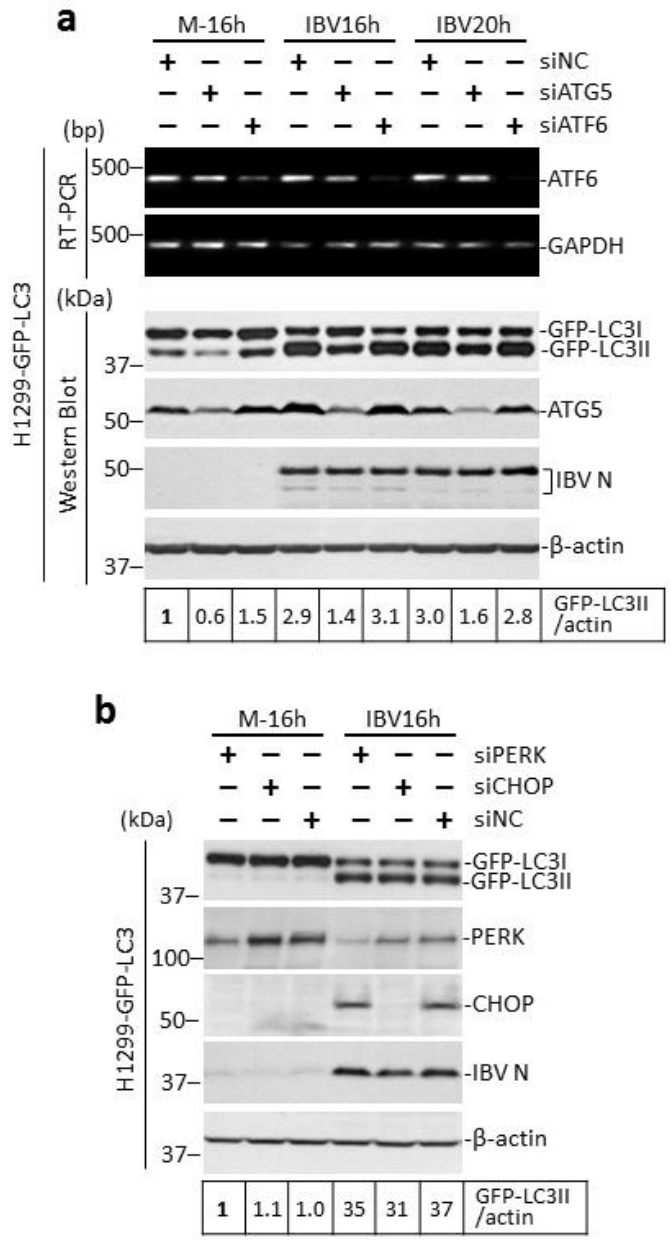

Figure 3-19 IBV-induced autophagy does not require ATF6 or PERK.

(a) H1299-GFP-LC3 cells in duplicate were transfected with siATG5, siATF6 or siNC and infected as in Figure 3-17b. Western blot, RT-PCR, and quantification of the GFP-LC3-II/actin ratio were performed similarly as described in Figure 3-17b.

(e) H1299-GFP-LC3 cells were transfected with siPERK, siCHOP or siNC and infected as in Figure 3-17b. Western blot, RT-PCR, and quantification of GFP-LC3-II/actin ratio were performed similarly as in Figure 3-17b.

3.5 THE ROLE OF UPR IN THE REGULATION OF INNATE IMMUNE RESPONSE DURING IBV INFECTION

3.5.1 The AP-1 and NF-κB binding sites are required for IBV-induced activation of the IL-8 promoter

Next, we investigated the involvement of UPR in the innate immune response activated during IBV infection. Particular interest was placed in the pro-inflammatory cytokine IL-8, because previous studies have shown induction of IL-8 in cells overexpressing the MHV spike protein or in cells under ER stress [155,260]. Three known response elements have been identified in the promoter of IL-8, which are binding sites for AP-1, NF-κB and CEBP/β respectively. To study the requirement for these response elements in the induction of IL-8 during IBV infection, a series of IL-8 luciferase reporter constructs were obtained [334]. In the wild type construct, the IL-8 promoter was fused with coding sequence of the firefly luciferase (Fluc). In the mutant constructs, individual response elements were mutated (**Figure 3-20a**).

HEK293 cells were co-transfected with the IL-8 reporters and the TK-Rluc control. In the TK-Rluc construct, the expression of renilla luciferase (Rluc) is controlled by the promoter of the house-keeping gene thymidine kinase (TK), thus it could serve as a control for the transfection efficiency. The transfected cells were infected with IBV at MOI~2 or mock infected for 24 hours before lysed for luciferase assay. As shown in **Figure 3-20b**, IBV infection induced the IL-8 promoter by ~5-fold in cells transfected with the wild type reporter. This is consistent with the ~6-fold induction of the endogenous IL-8 mRNA in IBV infected HEK293 cells compared with the mock infected control (**Figure 3-20c**). Compared with the WT IL-8 reporter, mutations in either the AP-1 or NF-κB site dramatically reduced the IBV-induced activation of the IL-8 promoter (**Figure 3-20b**). In contrast, removal of the CEBP/β element only marginally affected the activation of IL-8 promoter by IBV. Therefore, the AP-1 and NF-κB binding sites in the IL-8 promoter were essential in the induction of IL-8 during IBV infection. Notably, AP-1 and NF-κB mutant reporters also had reduced activity in the mock infected cells compared with the wild type control. This might suggest that the AP-1 and NF-κB response elements were also required for the basal activation of IL-8 promoter.

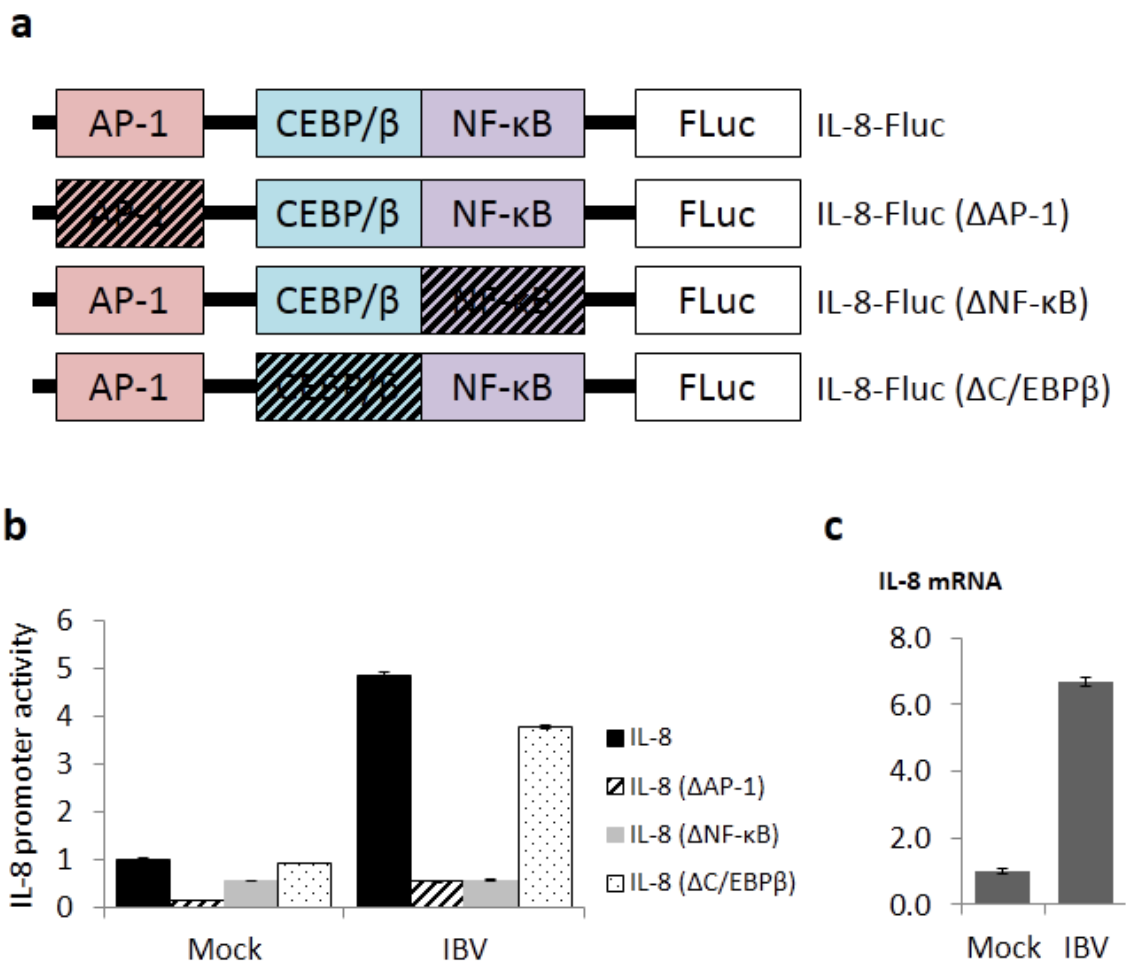

Figure 3-20 IBV-induced activation of IL-8 gene involves both AP-1 and NF-κB binding sites.

(a) Schematic diagram showing the arrangement of AP-1, NF-κB and CEBP/β binding sites in the IL-8 reporter constructs used in the following experiment. Shaded boxes indicate the mutations that abolish the respective response elements.

(b) HEK293 cells were transfected with the IL-8 reporters listed in (a) and TK-Rluc plasmid before infected with IBV at MOI~2 or mock infected. At 24 hpi, cells were lysed and the relative luciferase activity (Fluc/Rluc) was measured. The ratios were normalized to the value of mock infected cells transfected with wild type IL-8 reporter. Experiment was performed three times and result of one representative experiment is shown.

(c) Another set of cells in (b) transfected with wild type reporter were subjected to RNA extraction and RT-qPCR to determine the amount of endogenous IL-8 mRNA.

3.5.2 XBP1 is required for the induction of pro-inflammatory cytokines and type I interferon during IBV infection

To study the involvement of UPR in cytokine production during IBV infection, the knockdown approach was adopted. Since the AP-1 and NF-κB binding sites were found important for the activation of IL-8 promoter, the corresponding transcription factors (the upstream kinase JNK and the p65 subunit of NF-κB) were used as putative positive control. On the other hand, the three important UPR-related bZIP transcription factors – ATF6, CHOP and XBP1, were chosen as knockdown targets in this experiment.

As shown in **Figure 3-21a**, H1299 cells were transfected with siEGFP, siNFκB, siJNK, siATF6, siCHOP or siXBP1 before infected with IBV at MOI~2. Quantitative PCR result showed that IBV infection induced the expression of all tested genes compared with the mock infected control in cells transfected with siEGFP. Transfection of individual siRNA significantly reduced the mRNA level of the targeted gene compared with the siEGFP control (**Figure 3-21a**). The pro-inflammatory cytokines IL-6 and IL-8, as well as IFN-β, were chosen for analysis. Consistent with the IL-8 luciferase reporter experiment, IBV infection significantly induced the IL-8 mRNA level by more than 20-fold compared with mock infected cells in the siEGFP control (**Figure 3-21b**). Interestingly, knockdown of NF-κB, JNK, ATF6, CHOP or XBP1 all drastically reduced the IBV-induced IL-8 expression compared with the siEGFP control. Notably, knockdown of NF-κB almost completely abolished the IL-8 induction by IBV infection. As for IL-6, infection with IBV induced gene expression by ~3-fold in the negative control. Knockdown of ATF6 or XBP1 slightly reduced the IBV-induced IL-6 expression compared with the siEGFP control. Surprisingly, IL-6 induction seemed unaffected in cells transfected with siNFκB (**Figure 3-21b**). Finally, a moderate induction (~3.5-fold) of IFN-β mRNA by IBV infection was observed in the siEGFP control. Knockdown of all tested genes reduced IBV-induced IFN-β expression, particularly in the NF-κB or XBP1-knockdown cells (**Figure 3-21b**). Transfection of all siRNA duplexes did not affect IBV replication, as revealed by the similar level of IBV positive stranded gRNA and similar virus titers in the supernatant compared with the siEGFP control (**Figure 3-21c**). Taken together, the UPR-related transcription factor XBP1 might serve a certain function in the induction of IL-8, IL-6 and IFN-β during IBV infection.

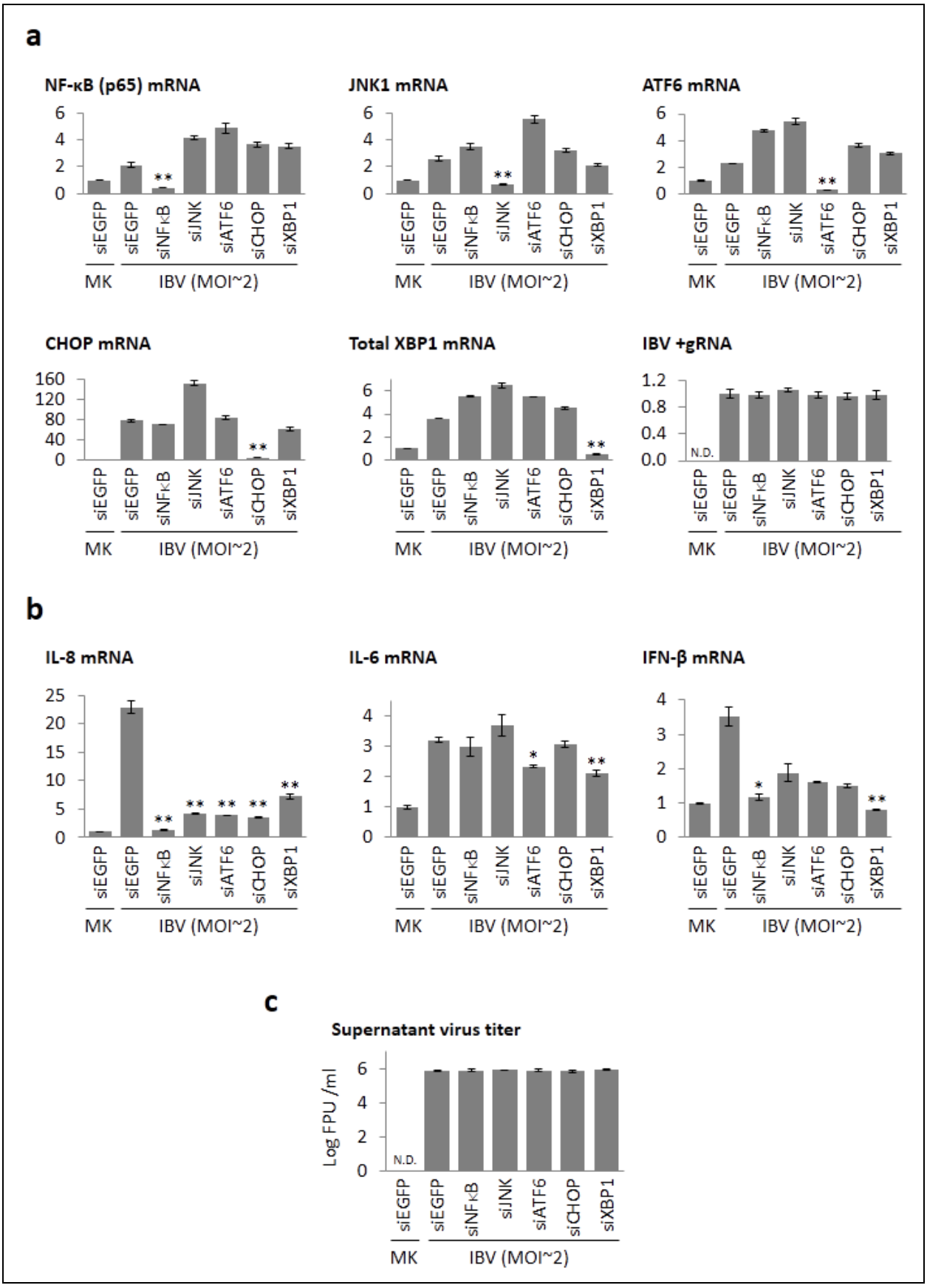
a
NF-κB (p65) mRNA
JNK1 mRNA
ATF6 mRNA
CHOP mRNA
Total XBP1 mRNA
IBV +gRNA
N.D.
b
IL-8 mRNA
IL-6 mRNA
IFN-β mRNA
c
Supernatant virus titer
Log FPU /ml
siEGFP
siNFκB
siJNK
siATF6
siCHOP
siXBP1
MK
IBV (MOI~2)

Figure 3-21 XBP1 is required for induction of cytokines in IBV-infected cells.

(a) H1299 cells were transfected with siEGFP, siNFκB, siJNK, siATF6, siCHOP or siXBP1 before infected with IBV at MOI~2 or mock infected. At 20 hpi, cells were harvested and total RNA was subjected to RT-qPCR analysis. Fold induction of specific genes were calculated using GAPDH as internal references and normalized to the siEGFP transfected mock-infected sample. Asterisks denotes significant differences between the indicated sample and the IBV-infected siEGFP control (**, $P<0.01$).

(b) The relative mRNA levels of IL-8, IL-6 and IFN-β in the samples described in (a). Fold induction of genes were calculated as in (a). Asterisks denotes significant differences between indicated sample and the IBV-infected siEGFP control (*, $P<0.05$; **, $P<0.01$).

(c) The levels of IBV positive stranded gRNA and the supernatant virus titers in (a) were determined as described above. N.D, not determined.

3.5.3 Overexpression of XBP1s enhances the expression of IL-8 and IFN-β induced by IBV infection

To confirm the involvement of XBP1 in innate immune response during IBV infection and to identify which one of two XBP1 isoforms was responsible, the transient overexpression approach was adopted. H1299 cells were transfected with the EGFP-fusion proteins as described above. The corresponding vector pEGFP-C1 was used as control. As shown in **Figure 3-22a**, expression of EGFP-XBP1u and EGFP-XBP1s could be determined using EGFP specific antibody. Transfected cells were infected with IBV at MOI~2 or mock infected and the extracted total RNA was subjected to RT-qPCR analysis. As shown in **Figure 3-22b**, overexpression of XBP1s but not XBP1u dramatically increased the mRNA level of ERdj4 induced by IBV infection, as compared with the EGFP control. Therefore the ectopic XBP1s demonstrated its function as a potent transcription factor. Transfection of the XBP1 fusion proteins did not significantly affect IBV replication, as evidenced by the similar level of IBV N protein (**Figure 3-22a**) and similar IBV positive stranded gRNA (**Figure 3-22b**) compared with control.

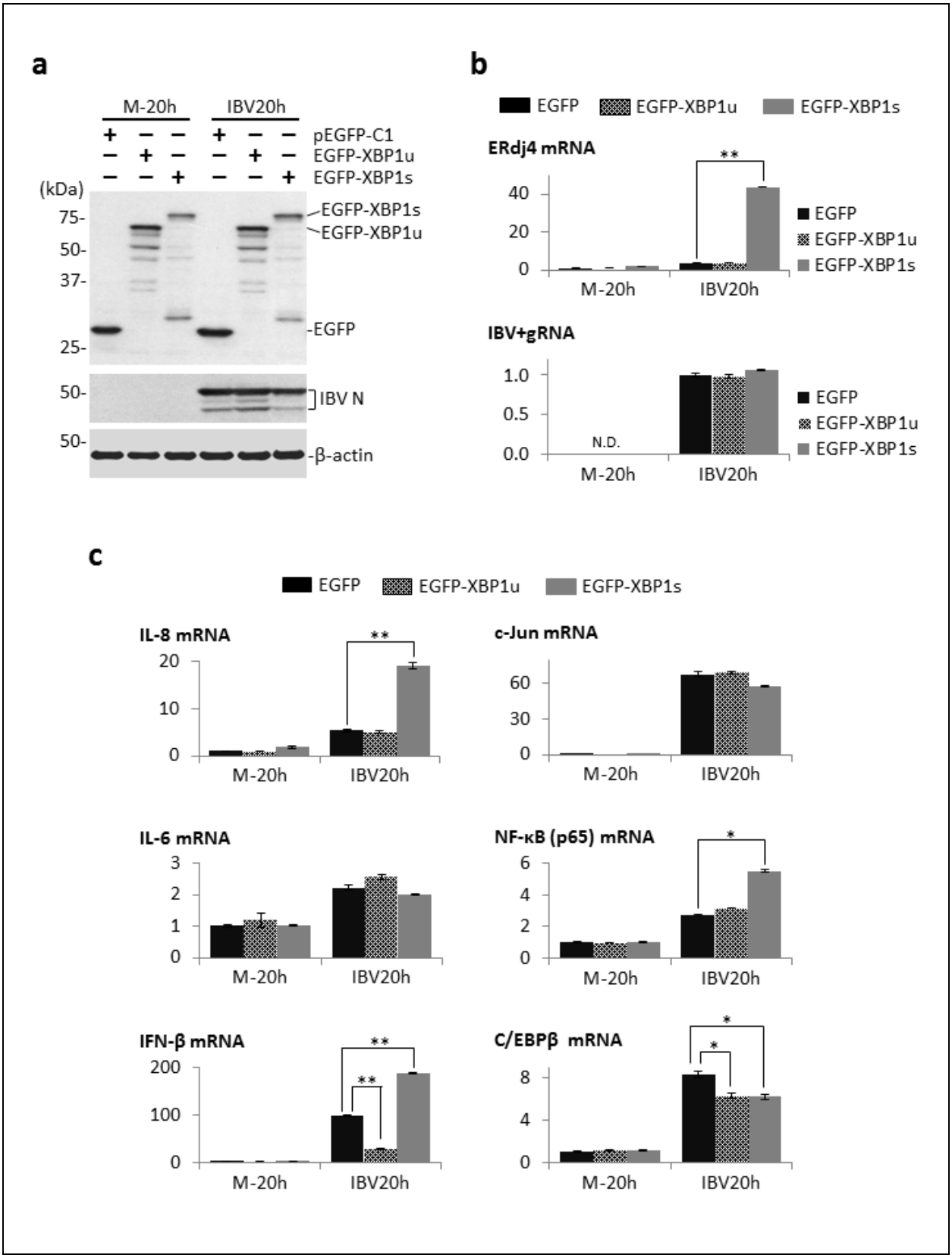
a
M-20h
IBV20h
pEGFP-C1
EGFP-XBP1u
EGFP-XBP1s
(kDa)
75-
50-
37-
25-
50-
50-
EGFP-XBP1s
EGFP-XBP1u
-EGFP
IBV N
-β-actin
b
EGFP
EGFP-XBP1u
EGFP-XBP1s
ERdj4 mRNA
**
40
20
0
M-20h
IBV20h
IBV+gRNA
1.0
0.5
0.0
N.D.
c
IL-8 mRNA
c-Jun mRNA
IL-6 mRNA
NF-κB (p65) mRNA
IFN-β mRNA
C/EBPβ mRNA
*

Figure 3-22 Overexpression of XBP1s, but not XBP1u, enhances the expression of IL-8 and IFN-β induced by IBV infection.

(a) H1299 cells were transfected with pEGFP-C1, pEGFP-XBP1u or pEGFP-XBP1s in duplicate before infected with IBV at MOI~2 or mock. One set of cells were lysed for protein and subjected to Western blot analysis using antibodies against EGFP and IBV N. Beta-actin was included as loading control. Sizes of protein ladders in kDa were indicated.

(b) Another set of transfected cells as described in (a) were subjected to RT-qPCR as in Figure 3-18a. Fold induction of specific genes were calculated using GAPDH as internal references and normalized to the pEGFP-C1 transfected mock-infected sample. Asterisks indicate significant differences (**, $P<0.01$). N.D, not determined.

(c) The relative mRNA levels of IL-8, IL-6, IFN-β and IL-8 related transcription factors in the samples described in (a). Fold induction of genes were calculated as in (b). Asterisks indicate significant differences between two samples (*, $P<0.05$; **, $P<0.01$).

We then looked at the expression of cytokines and IFN-β. As shown in **Figure 3-22c**, compared with the mock infected cells, IBV infection induced IL-8 expression by ~5-fold in the EGFP control. This induction of IL-8 transcription was markedly lower than the ~20-fold increase observed in the siEGFP control cells infected with IBV shown in **Figure 3-21b.** The reason for this difference was not known, although it might be due to the different transfection procedures. Transfection of siRNA was performed using the Lipofectamine RNAiMAX reagent, whereas transfection of plasmid DNA was done using the Lipofectamine 2000 (LP2000) reagent. According to the manufacturer, the RNAiMAX reagent causes lower cell toxicity compared with the LP2000. Moreover, overexpression of the EGFP protein may also further cause cell toxicity in the plasmid DNA-transfected cells. Therefore, siRNA-transfected cells might experience less stress and grew in a better condition compared with the plasmid DNA-transfected cells, which might explain the relatively higher level of IL-8 transcription when infected with IBV. Notably, compared with the vector control, the level of IBV-induced IL-8 expression was significantly enhanced to ~20-fold in cells expressing EGFP-XBP1s. This enhancement was not observed in cells transfected with EGFP-XBP1u, suggesting that the transactivation domain of XBP1 was required for this enhancement effect. In contrast, induction of IL-6 in the IBV-infected cells was

not significantly affected by the overexpression of either EGFP-XBP1u or EGFP-XBP1s (**Figure 3-22c**).

As for IFN-β, a huge induction of IFN-β by IBV infection by ~100-fold was observed in the EGFP control. This value was significantly higher compared with the induction observed in the knockdown experiment (**Figure 3-21b**). The reason for this difference was not known, but the different transfection reagents used might contribute. Alternatively, the plasmid DNA might be recognized as PAMP by the transfected cells, and thus synergistically enhanced the IBV-induced IFN-β expression. This high level of IFN-β transcription per se could potentially affect IBV replication by up-regulating the interferon stimulated genes (ISGs). However, significant reduction of IBV genome replication/transcription or the supernatant titers was not observed, when compared with untransfected H1299 cells (data not shown). Therefore, it is possible that this increase in IFN-β transcription did not lead to an effective antiviral response due to some uncharacterized counter mechanisms by IBV (such as translation attenuation). Also, because a relatively high MOI is used in this experiment, almost all cells are infected in the primary infection. Therefore, even though a high level of IFN-β is induced, the antiviral effect might not be readily detectable due to the rapid course of infection.

Importantly, compared with the EGFP control, the mRNA level of IFN-β was significantly higher in the IBV-infected cells transfected with EGFP-XBP1s, but significantly lower in IBV-infected cells transfected with EGFP-XBP1u (**Figure 3-22c**). Taken together, the result confirms that the spliced form of XBP1 contributes to the induction of IL-8 and IFN-β during IBV infection, whereas the unspliced form might negatively regulate IFN-β expression.

As mentioned above, the IL-8 promoter contains binding sites for AP-1, NF-κB and CEBP/β. To see whether overexpression of XBP1s directly affected the mRNA levels of these transcription factors, the relative fold changes of these transcripts were also determined. As shown in **Figure 3-22c**, the mRNA level of c-Jun was not significantly affected by the transfection of XBP1 plasmids. Overexpression of EGFP-XBP1s, but not EGFP-XBP1u, seemed to increase the expression of NF-κB (p65) in the infected cells, as compared with the EGFP control. As for CEBP/β, compared with the EGFP control, transfection of both EGFP-XBP1u and EGFP-XBP1s slightly reduced the mRNA level of CEBP/β in the infected cells.

3.5.4 Overexpression of XBP1s enhances IBV-induced IL-8 and IFN-β expression in NF-κB-knockdown H1299 cells

As mentioned above, the transcription factor NF-κB is known to be a crucial regulator of pro-inflammatory and innate immune response during coronavirus infections. It is possible that the observed enhancement of XBP1s on IBV-induced IL-8 and IFN-β expression is achieved via modulation of NF-κB. To this end, H1299 cells were first transfected with siEGFP or siNFκB, then transfected with pEGFP-C1 or pEGFP-XBP1s, and finally infected with IBV at MOI~2 or mock infected. As shown in **Figure 3-23a**, knockdown of NF-κB could be determined by the reduced protein amount of the p65 subunit. The expression of the EGFP-XBP1s fusion protein was also detectable using antibody specific for XBP1. Transfection of siRNA or plasmid DNA did not significantly affect the replication of IBV, as determined by the similar amount of IBV N protein and the similar level of positive stranded genomic RNA (**Figure 3-23a and b**) among the infected samples. Overexpression of EGFP-XBP1s significantly enhanced the IBV-induced ERdj4 expression in cells transfected with either siEGFP or siNFκB (**Figure 3-23b**). Therefore, the activity of XBP1s as a transcription factor regulating downstream UPR genes was not affected by the knockdown of NF-κB.

The induction of IL-8 and IFN-β was also determined by RT-qPCR. As shown in **Figure 3-23b**, compared with the mock infected control, the mRNA levels of both IL-8 and IFN-β were significantly increased in the siEGFP-transfected cells infected with IBV, which were further potentiated when XBP1s was overexpressed. As expected, knockdown of NF-κB almost completely abolished the IL-8 and IFN-β induction, suggesting that NF-κB was crucial in trans-activating IL-8 and IFN-β during IBV infection. Notably, when XBP1s was overexpressed in the NF-κB-knockdown cells, a significant induction of both IL-8 and IFN-β could be observed, compared with the infected NF-κB-knockdown cells transfected with the vector (**Figure 3-23b**). This suggested that the ability of XBP1s to enhance IBV-induced IL-8 and IFN-β expression remained detectable when NF-κB was knockdown. Nonetheless, the induction of IL-8 and IFN-β were still remarkably lower in the NF-κB-knockdown cells compared with the siEGFP control, suggesting that overexpression of XBP1s could only partially compensate for the reduction of IL-8 and IFNβ expression.

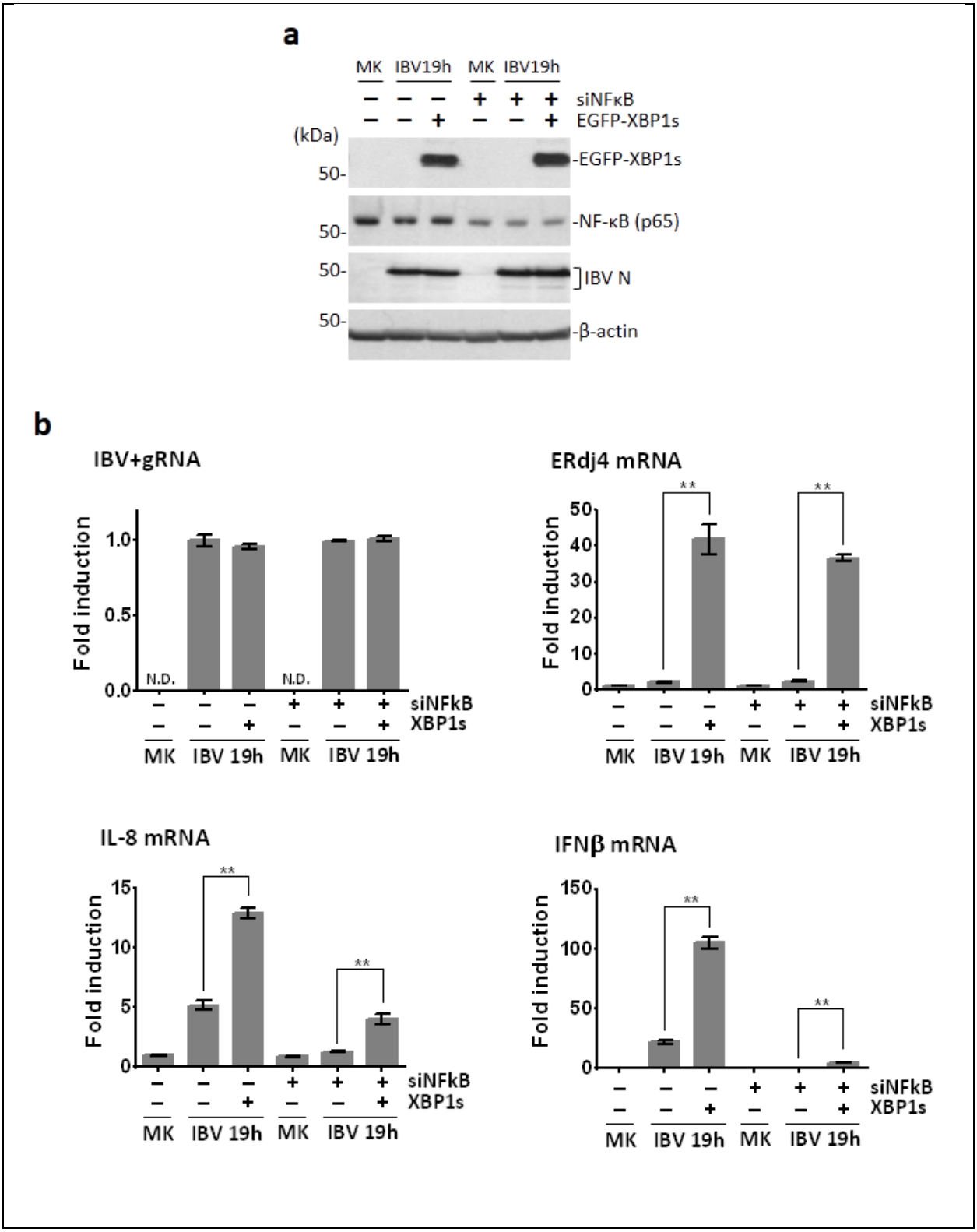
a
MK
IBV19h
MK
IBV19h
siNFκB
EGFP-XBP1s
(kDa)
50-
-EGFP-XBP1s
50-
-NF-κB (p65)
50-
IBV N
50-
-β-actin
b
IBV+gRNA
Fold induction
1.0
0.5
0.0
N.D.
N.D.
siNFkB
XBP1s
MK
IBV 19h
MK
IBV 19h
ERdj4 mRNA
Fold induction
50
40
30
20
10
0
**
**
siNFkB
XBP1s
MK
IBV 19h
MK
IBV 19h
IL-8 mRNA
Fold induction
15
10
5
0
**
**
siNFkB
XBP1s
MK
IBV 19h
MK
IBV 19h
IFNβ mRNA
Fold induction
150
100
50
0
**
**
siNFkB
XBP1s
MK
IBV 19h
MK
IBV 19h

Figure 3-23 Overexpression of XBP1s enhances IBV-induced IL-8 and IFN-β expression in NF-κB-knockdown H1299 cells

(a) H1299 cells in duplicate were first transfected with either siEGFP (-) or siNFκB (+) for 24 hours. The cells were then further transfected with either pEGFP-C1 (-) or pEGFP-XBP1s for another 24 hours before infected with IBV at MOI~2 or mock. One set of cells were lysed for protein and subjected to Western blot using antibodies against XBP1, NF-κB and IBV N. Beta-actin was used as loading control. Sizes of protein ladders were indicated.

(b) Another set of transfected cells as described in (a) were subjected to RT-qPCR as in Figure 3-18a. Fold induction of specific genes were calculated using GAPDH as internal references and normalized to the siNFκB/pEGFP-C1 transfected mock-infected sample. Asterisks indicate significant differences (**, $P<0.01$). N.D, not determined.

3.6 DISCUSSION

3.6.1. Activation of the IRE1 pathway during IBV infection

Previous studies have shown that activation of the IRE1 branch of UPR is either absence or incomplete in cells infected with SARS-CoV or MHV [155,191]. In SARS-CoV-infected cells, the E protein prevents efficient splicing of XBP1 mRNA by IRE1[221]. As for MHV, although IRE1effectively splices the XBP1 mRNA, the spliced XBP1 protein is not produced due to global translation attenuation, leading to the lack of downstream signaling [191]. In this study, we have demonstrated that the IRE1 pathway is activated during IBV infection. Significant splicing of the XBP1 mRNA could be observed at late stage of IBV infection, together with dramatic induction of downstream UPR genes such as ERdj4. Moreover, knockdown of IRE1 or XBP1 by RNAi attenuated pathway activation, whereas overexpression of wild type IRE1 or the spliced form of XBP1 potentiated downstream signaling induced by IBV infection. Taken together, the result suggest that unlike betacoronaviruses (such as MHV or SARS-CoV), IBV infection induces ER stress and activates the IRE1-XBP1 pathway.

Previously it has been shown that overexpression of the S protein of MHV but not SARS-CoV induces XBP1 splicing in cell culture [155]. We have also detected dosage dependent activation of the IRE1-XBP1 pathway in cells transfected with IBV S protein. As a large and highly glycosylated transmembrane protein massively synthesized during replication, the S protein has been commonly recognized as the major culprit that triggers cellular stress responses. Recent studies have also identified functional interaction between the SARS-CoV S protein and a ER protein chaperone called calnexin [159]. It is therefore interesting to further investigate the detailed mechanisms of ER stress induced by coronavirus S protein. In fact, preliminary data have shown that mutations at several putative N-glycosylation sites partially abolish XBP1 mRNA splicing in cells overexpressing the IBV S protein. Therefore, the extensive glycosylation of S protein inside the ER lumen might be responsible for the ER stress induced by coronavirus infections. However, reverse genetic experiments aiming to mutate these sites in the IBV genome proved difficult, as the same glycosylation sites seemed to be essential for the fusion activity of the S protein. Finally, other mechanisms such as DMVs formation and/or membrane depletion might also be involved and required further studies in the future.

Many studies on virus-induced activation of the IRE1-XBP1 pathway have utilized the specific IRE1 inhibitor DBSA [351,352]. DBSA has been shown to selectively inhibit the RNase activity of IRE1 without significantly affecting other known RNases (such as RNaseL) [339]. However, similar to all inhibitor approaches, DBSA may act on unknown cellular factors that regulate virus replication. In this study, treatment of DBSA at 10μM was sufficient to suppress IBV-induced XBP1 mRNA splicing in Vero cells without affecting IBV replication. However, as low as 5μM DBSA was found to significantly inhibit IBV replication in H1299 cells. Therefore, the sensitivity towards DBSA might be different depending on the cell line used. Since the activation of the IRE1 pathway *per se* was dependent on virus replication, the observed reduction of XBP1 splicing might be due to non-specific effects of DBSA instead of IRE1 inhibition. Therefore, cautions should be taken to interpret result from such inhibitor studies and conclusions need to be fortified by other functional approaches such as knockdown/knockout and/or overexpression experiments.

The XBP1 splicing assay has been commonly used as a golden standard to access the activation of IRE1-XBP1 pathway. Using primer pairs that amplify both isoforms of the XBP1 mRNAs, the method allows relatively accurate estimation of XBP1 mRNA splicing. However, the major drawback of this approach is the lack of sensitivity. Due to the small size difference (26nt), the RT-PCR products of XBP1u and XBP1s were often not well separated in agarose gel electrophoresis. If the band intensity of XBP1s is significantly weaker, the pre-dominant XBP1u band usually masks the signal of XBP1s, leading to a false negative result. In this study, XBP1 splicing was not detected until late stage infection (24 hpi) using the gel-based XBP1 splicing assay. This led to the seemingly contradictory finding that induction of downstream UPR genes (such as ERdj4) occurred in the absence of XBP1 splicing. Further quantitative PCR experiment using primers specific for XBPs revealed that IBV infection indeed triggered significant XBP1 splicing as early as 20 hpi. The result suggested that the gel-based assay might fail to detect low level of XBP1 splicing, which was usually associated with virus infection. Nonetheless, as a potent transcription factor, the low amount of XBP1s protein was sufficient to induce the expression of downstream genes. Therefore, although convenient and straight forward, the traditional gel-based splicing assay should be supplemented with quantitative PCR analysis on the transcript levels of XBP1s and the downstream UPR target genes.

3.6.2. Activation of the PERK branch of UPR in IBV-infected cells

Phosphorylation of eIF2α has been detected in cells infected with MHV, SARS-CoV and TGEV [191,192,194]. In this and a previous study from our group, activation of eIF2α and its two upstream kinases (PKR and PERK) has been observed at the early stage of IBV infection [156,195]. Interestingly, phosphorylation of eIF2α does not sustain and global translation attenuation is not detected, possibly due to the dephosphorylation of eIF2α by PP1 [195]. Similar to PKR, phosphorylation of PERK in IBV-infected cells was found to occur only transiently at the early stage of infection. Rapidly inactivation of PKR and PERK might be mediated by P58IPK [353,354]. With an eIF2α homology domain, P58IPK has been shown to directly interact with PKR, inhibiting its auto-phosphorylation and activity [355]. Expression of P58IPK is induced under ER stress by the transcription factor ATF6 and XBP1, constituting a negative feedback mechanism among the three UPR branches [206,356]. It has been shown that the molecular chaperone heat shock protein 40 (hsp40) binds to and inhibits the activity of P58IPK [357]. Intriguingly, influenza virus infection promotes dissociation of the hsp40-P58IPK complex, thereby activating P58IPK to counteract the translation attenuation induced by the PKR-eIF2α pathway [357]. This exemplifies viral mechanisms to counteract host antiviral response and demonstrates the importance of ISR in suppressing virus replication. In this study, we have detected up-regulation of P58IPK mRNA during IBV infection. However, the functional involvement of P58IPK in coronavirus replication and pathogenesis would require further investigations.

Although eIF2α activation is observed in cells infected with several coronaviruses, the induction of downstream genes has not been well characterized. For instance, induction of CHOP is not detected in MHV-infected cells, which has been attributed to the sustained translation suppression due to eIF2α phosphorylation [191]. Since significant translation attenuation is not observed during IBV infection (due to the rapid inactivation of PKR, PERK and eIF2α), activation of the downstream ATF4-ATF3-CHOP could be readily observed [156]. In particular, significant induction of the transcription factor CHOP has been detected at both mRNA and protein level at late stage of infection. The dramatic and sustained up-regulation of CHOP in turn induces the PP1 regulatory subunit GADD34, which facilitates dephosphorylation of eIF2α and restores translation. In this study, knockdown experiments have shown that both

PKR and PERK contribute to the IBV-induced up-regulation of CHOP. In particular, induction of CHOP is almost completely abolished in PKR-knockdown cells infected with IBV. Therefore, it seems the transient activation of PKR and PERK is sufficient to trigger the downstream ISR pathway during IBV infection. Whereas PKR is interferon-inducible and activated by binding of dsRNA, PERK is activated by accumulation of unfolded proteins in the ER lumen. The different activation mechanisms and the converging effect on the downstream signaling pathway may ensure the induction of CHOP, in spite of the numerous viral counter mechanisms.

3.6.3. UPR and IBV-induced apoptosis

There has been extensive studies on the involvement of UPR in ER-stress induced apoptosis [167]. In the initial stage of ER stress, the UPR is generally considered pro-survival. Translation attenuation, ERAD and RIDD reduce the ER burden, whereas induction of ER chaperones enhances the folding capacity. All of these aim to restore the ER homeostasis and facilitate adaptation to ER stress. However, in unmitigated persistent ER stress, prolonged RIDD activation and induction of pro-apoptotic proteins are detrimental to cell survival and promote apoptotic cell death. In this study, the involvement of the IRE1-XBP1 pathway and CHOP in IBV-induced apoptosis is studied in mechanistic detail.

The anti-apoptotic nature of IRE1 was clearly demonstrated by the potentiated apoptosis in the IRE1-knockdown cells infected with IBV compared with the control, evidenced by the more prominent cleavage of PARP, caspase 3, 8 and 9. On the other hand, overexpression of wild type IRE1, but not its kinase dead or RNase deletion mutants, partially reduced IBV-induced apoptosis, suggesting that both the kinase and RNase activities were required for the anti-apoptotic function of IRE1. Surprisingly, knockdown of XBP1, the splicing substrate of IRE1, seemed to inhibit apoptosis in IBV-infected cells. Since both the unspliced and spliced isoform of XBP1 were targeted by siXBP1, we hypothesized that the two isoforms might have opposing functions during IBV infection. Overexpression experiments clearly demonstrated that whereas XBP1u was weakly pro-apoptotic, XBP1s was anti-apoptotic in cells infected with IBV. A dominant negative form of XBP1 (XBP1-DN) was generated by removing the proteasome degradation motif in XBP1u. When cells were transfected with XBP1-DN, IBV-induced apoptosis was found significantly potentiated compared with the vector control. Taken together,

the anti-apoptotic function of IRE1 may be explained, at least in part, by the conversion of pro-apoptotic XBP1u to anti-apoptotic XBP1s.

Previous studies have also demonstrated that the kinase activity of IRE1 could activate the JNK signaling pathway to induce apoptosis [216]. In this study, however, ER-stress induced apoptosis did not seem to be mediated by the IRE1-JNK pathway in IBV-infected cells. In fact, phosphorylation of JNK induced by IBV infection was much more pronounced in the IRE1-knockdown cells compared with the control. Therefore, JNK was likely activated by alternative upstream kinases (such as MKK4/MKK7 as described in the next chapter). Along with the hyper-phosphorylation of JNK, we have also detected a hypo-phosphorylation of Akt in the IRE1-knockdown cells infected with IBV. Akt has been demonstrated to play an important role in cell survival under ER stress [358]. Phosphorylation of Akt preceded JNK activation during IBV infection, while overexpression of constitutively active Akt abolished IBV-induced apoptosis. Notably, Akt phosphorylation sustained longer in cells transfected with siJNK compared with the control, suggesting a counteraction between the two pathways. Indeed, it has been shown that JNK inhibits the survival signals of Akt by phosphorylating the 14-3-3 protein [312]. It is quite likely that the antagonizing actions of Akt and JNK determine cell death or survival at late stage of IBV infection. In this sense, the anti-apoptotic function of IRE1 may be mediated by modulating the phosphorylation status of Akt and JNK.

The transcription factor CHOP has been attributed to the apoptosis induced in cells under persistent ER stress. A number of mechanisms have been proposed to explain CHOP-induced apoptosis, including aggravation of ER burden by restoring protein translation [185], induction of pro-apoptotic proteins such as ERO1α, Bim and DR5 [185,238,239] or suppression of pro-survival proteins such as Bcl2 and Akt [237,359]. In this study, we have clearly demonstrated the pro-apoptotic function of CHOP during IBV infection by the knockdown and overexpression approaches. Moreover, we proposed that CHOP might facilitate IBV-induced apoptosis by suppressing the activation of ERK, a pro-survival MAP kinase. Surprisingly, the pro-apoptotic activity of CHOP in IBV-infected cells were dependent on the amino acids 36-70 region in the N-terminal, but not its DNA binding bZIP domain. The interacting partners and detailed mechanisms of CHOP-induced apoptosis during IBV infection remained to be investigated.

Finally, we have also demonstrated that IRE1 and CHOP differentially modulated the mRNA level of DR5. Recent studies have shown that the mRNA of DR5 is induced by CHOP but degraded by the RIDD activity of IRE1 [349]. Consistently, the mRNA level of DR5 was found lower in CHOP-knockdown cells and higher in IRE1-knockdown cells infected with IBV, as compared with control. Accumulation of DR5 protein might promote ligand-independent activation of caspase 8 in IBV-infected cells, as in cells under persistent ER stress [349]. Nonetheless, determination of DR5 at the protein level and further functional studies are required to elucidate its role in IBV-induced apoptosis. **Figure 3-22** summarizes the mechanisms that UPR might use to modulate apoptosis during IBV infection.

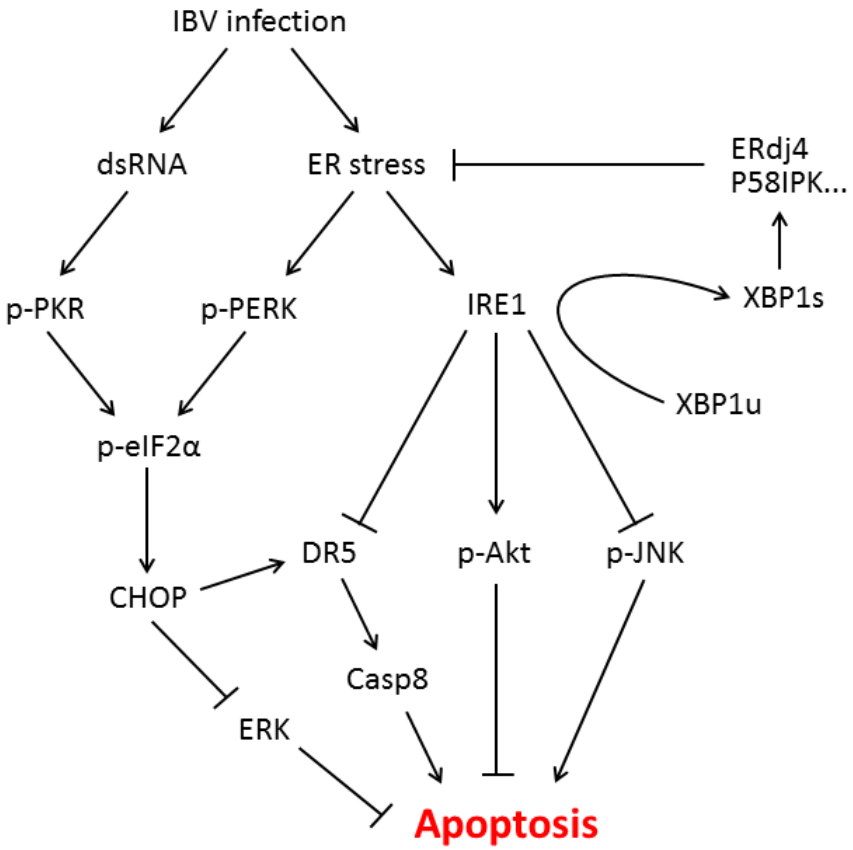

Figure 3-24 The involvement of UPR in IBV-induced apoptosis.

Schematic diagram showing the mechanisms where UPR modulates ER-stress induced apoptosis during IBV infection. Pointed arrows indicate activation. Blunt-ended lines indicate inhibition.

3.6.4. IBV-induced autophagy and the involvement of IRE1

A growing number of viruses have been demonstrated to induce autophagy in infected cells [62,360,361]. For certain viruses such as poliovirus, coxsackievirus B3 and HCV, autophagy is induced by the viruses and promotes viral replication. Whereas for other viruses such as Sindbis virus, vesicular stomatitis virus and HSV-1, autophagy acts as a host defence mechanism to either eliminate the virus or to activate the innate immune response [137]. One recent study has demonstrated that IBV infection induces autophagy in infected Vero cells and identified nsp6 as the viral protein that triggers autophagosome formation [89]. Here, we confirmed the IBV-induced autophagy with another mammalian cell lines (H1299) and a stable cell line expressing the autophagy marker GFP-LC3. Moreover, using the lysosome acidification inhibitor chloroquine and the tandem fluorescent LC3 reporter, we demonstrated that IBV induced complete autophagy flux that proceeded to the lysosomal fusion stage.

In agreement with previous studies in IBV and MHV, knockdown of ATG5 inhibited the viral induced autophagy but did not significantly affect coronavirus replication. Interestingly, when another autophagy related gene, BECN1 was silenced by siRNA, IBV infection was still able to induce autophagy. During starvation induced autophagy, the ULK1 protein complex is activated and recruits a second protein complex containing BECN1, Vsp15 and a class III PI3K, called Vps34. Activated Vps34 phorphorylates PI3 to PI3P, which recruits effectors such as DFCP1 and WIPI for isolated membrane nucleation. On the other hand, ATG5 binds toATG12 and forms one of the two ubiquitin-like conjugates, which is essential for membrane elongation [362]. Since IBV-induced autophagy is independent of BECN1 but dependent on ATG5, it is likely that other signal transducers are activated in response to IBV infection, which initiates BECN1-independent membrane nucleation and converges to the canonical autophagy pathway only at the elongation stage where ATG5 is required.

We then moved on to study the involvement of UPR in IBV-induced autophagy. Knockdown experiments showed that among the three UPR sensors, only IRE1 was required for IBV-induced lipidation of GFP-LC3. Also, knockdown of XBP1 failed to inhibit IBV-induced autophagy. However, as discussed above, the two isoforms of XBP1 might exhibit distinct functions. Therefore, the role of XBP1 in autophagy induction should be further investigated

using the overexpression approach and the dominant negative mutant. In fact, previous studies have shown that the IRE1-JNK pathway was responsible for ER-stress induced autophagy [218]. In the study conducted by Ogata et al., induction of autophagy is observed in cells treated with ER stress inducers, which is inhibited when IRE1 is knockout or JNK is inhibited [218]. However, as discussed above, the phosphorylation of JNK observed in IBV-infected cells was not mediated by IRE1. Therefore, it is quite unlikely that the IRE1-JNK pathway contribute to autophagy induction during IBV infection.

3.6.5. UPR and innate immune response during IBV infection

The innate immunity constitutes the first line of defense against coronavirus infections, although uncontrolled innate immune response may also lead to inflammation and other immunopathologies associated with coronavirus infections [245]. In this study, we also attempted to unravel potential involvement of the UPR in regulating innate immune response induced by IBV infection. Previous studies have shown that IL-8 was induced in MHV-infected cells and cells transfected with S protein of MHV [155]. Using the luciferase based reporter, it was found that the IL-8 promoter was also activated in IBV-infected cells, which required functional binding sites for AP-1 and NF-κB. Moreover, the mRNA levels of IL-8 and IFN-β significantly increased in cells infected with IBV. Knockdown of NF-κB or the UPR-related transcription factor XBP1 significantly reduced IBV-induced up-regulation of IL-8 and IFN-β compared with the control. On the other hand, overexpression of XBP1s but not XBP1u drastically enhanced the induction of IL-8 and IFN-β induced by IBV infection.

In this study, we have shown that overexpression of XBP1s induced the mRNA level of NF-κB compared with the control. However, when NF-κB was knocked down by siRNA, transfection of XBP1s was still capable of enhancing IBV-induced IL-8 and IFN-β expression. Nonetheless, caution should be taken when interpreting from this experiment. First of all, because the transient transfections of siRNAs and plasmid DNAs were preformed separately, a mixed population of transfected cells was expected. Cells might be only transfected with the siRNA/plasmid DNA, dually transfected with both, or non-transfected at all. To overcome this, future experiments need to be done using NF-κB knock-out or stably knockdown cells. Secondly, even though the mRNA and protein levels of NF-κB were significantly reduced in the

knockdown cells, a low amount of NF-κB was still detectable. It might be possible that this remaining NF-κB was enough to mediate the enhancement effect of XBP1s. To rule out this possibility, a cell line with NF-κB completely knocked out should be used. Therefore, it is still too early to conclude that the action of XBP1 on IBV-induced IL-8 and IFN-β expression is totally independent of NF-κB.

There are several other possible mechanisms whereby XBP1s facilitates the production of pro-inflammatory cytokines and type-I interferon. First, XBP1s may directly bind to the promoter sequences of these genes and activates transcription. Indeed, recent studies have identified putative XBP1 binding sites in the promoters of IL-6, TNF-α and IFN-β [271,273]. So far, similar response element for XBP1 has not been identified in the promoter of IL-8 and DNA binding gel shift assay could be performed to search for potential binding sites. Secondly, XBP1s may modulate the activity of one or more of the key transcription factors, such as c-Jun, NF-κB, CEBP/β and IRF3/IRF7. Expression of cytokines and chemokines could also be promoted by post-translational modification (such as phosphorylation and sumoylation) and nuclear translocation of these key regulatory factors, which should be determined in future experiments. Finally, XBP1s may also promote the activity of key transcription factors by protein-protein interactions. The CHOP protein has been shown to interact with CEBP/β and the co-activator protein p300/CBP [345]. Similar activities of XBP1s may facilitate binding of the transcription factors and assembly of the enhanceosome structure to induce cytokine production.

Notably, preliminary results in this study have been focusing on the induction of cytokines at the mRNA level. More detailed experiments need to be performed to examine the role of UPR in the translation, processing, secretion and signaling of cytokines in IBV-infected cells. The translation and processing of cytokines could be determined by Western blot analysis, whereas the secretion level could be measured using immunoassay (such as ELISA). The signaling of cytokines involved multiple transduction pathways, which might require specific reporter and/or assay systems. Moreover, the preliminary results were obtained using a single cell line of epithelial origin (H1299 cells). Because innate immune cells such as DCs and monocytes are more specialized in the production and secretion of cytokines, future experiments using these cells are necessary. To do this, however, such a cell line needs to be obtained or established, which is both permissive to IBV infection and competent in UPR signaling.

Chapter Four:

Activation of JNK pathway during IBV infection and its involvement in regulating IBV-induced apoptosis and innate immune response

4.1 BACKGROUND AND INTRODUCTION

JNK is a MAP kinase known to be activated by a diversity of cellular stress and pro-inflammatory cytokines [276]. Activation of JNK has been observed in cells infected with MHV or SARS-CoV [262,291], as well as in cells transfected with the S, N, accessory protein 3a, 3b or 7a of SARS-CoV [128,292,293,296]. Previous studies on coronavirus-induced JNK activation have been focused on its involvement in virus persistency and cell survival [295,363]. However, the upstream signaling pathway responsible for JNK activation during coronavirus infections has not been investigated in detail.

In Chapter Three of this thesis, we have shown that the IRE1 branch of UPR protects infected cells from IBV-induced apoptosis, at least in part by suppressing the activation of JNK. In most experiments, high level of JNK phosphorylation is usually associated with enhanced IBV-induced apoptosis. Therefore, we decided to characterize the molecular mechanism behind the pro-apoptotic activity of JNK in the context of IBV infection. We also attempted to determine involvement of the two known JNK upstream kinases (MKK4 and MKK7) in JNK activation induced by IBV infection.

Among the three MAP kinases, p38 is best characterized as the mediator of pro-inflammatory response. In fact, previous studies have shown that induction of IL-6 and IL-8 in coronavirus-infected cells is dependent on the activation of p38 [262,263]. On the other hand, the role of JNK in the innate immune response during coronavirus infections has not been fully determined. In the previous chapter, we have already shown that the knockdown of JNK indeed reduced IBV-induced expression of IL-8 and IFN-β. In this chapter, additional experiments using the overexpression approach will be presented to demonstrate the importance of JNK in the regulation of cytokine production during IBV infection.

4.2 RESULT

4.2.1. The JNK pathway is activated during IBV infection

To determine whether the JNK pathway is activated during IBV infection, H1299 cells were either infected with IBV at MOI~2 or mock infected. As shown in **Figure 4-1**, the level of total JNK remained relatively unchanged throughout the time course experiment in both the IBV-infected cells and the mock infected control. No phosphorylated JNK could be observed in the mock control, whereas phosphorylated JNK could be detected starting from 12 hpi in the IBV-infected cells. Phosphorylated JNK continued to accumulate and peaked at 20 hpi, followed by a rapid reduction to background level at 24 hpi (**Figure 4-1**). The phosphorylation of c-Jun, a direct substrate of JNK, was also determined. As shown in **Figure 4-1**, a low level of background c-Jun phosphorylation could be detected in the mock infected cells and in early time point of IBV-infected cells. This might be due to basal activation of c-Jun by other kinases or non-specific detection by the antibody. At 16 hpi, an abrupt increase of phosphorylated c-Jun was observed, which slowly subsided in later time points. Interestingly, the total protein level of c-Jun was also slightly higher at 16-24 hpi, compared with early time points of the infected cells or the mock control. This suggested that phosphorylation of c-Jun might stabilize the protein in H1299 cells infected with IBV.

The activation of two known JNK upstream kinases was also determined. Total protein levels of both MKK4 and MKK7 remained the same in both IBV-infected and mock infected cells. For MKK4, a basal level of phosphorylation was detected at 0 hpi, which gradually increased and peaked at the last time point collected (24 hpi). Phosphorylated MKK4 also stably accumulated in the mock infected control, although to a lower level compared with IBV-infected cells of the same time point (**Figure 4-1**). As for MKK7, no detectable phosphorylation was picked up in the mock infected cells, whereas a drastic increase of phosphorylated MKK7 was detected at 16 hpi. The amount of phosphorylated MKK7 slowly decreased afterwards, although remained at a considerable high level even at 24 hpi (**Figure 4-1**). Judging from the degree of phosphorylation above basal level and the temporal profile of activation, it seemed more likely that IBV-induced JNK phosphorylation was mediated by MKK7 instead of MKK4.

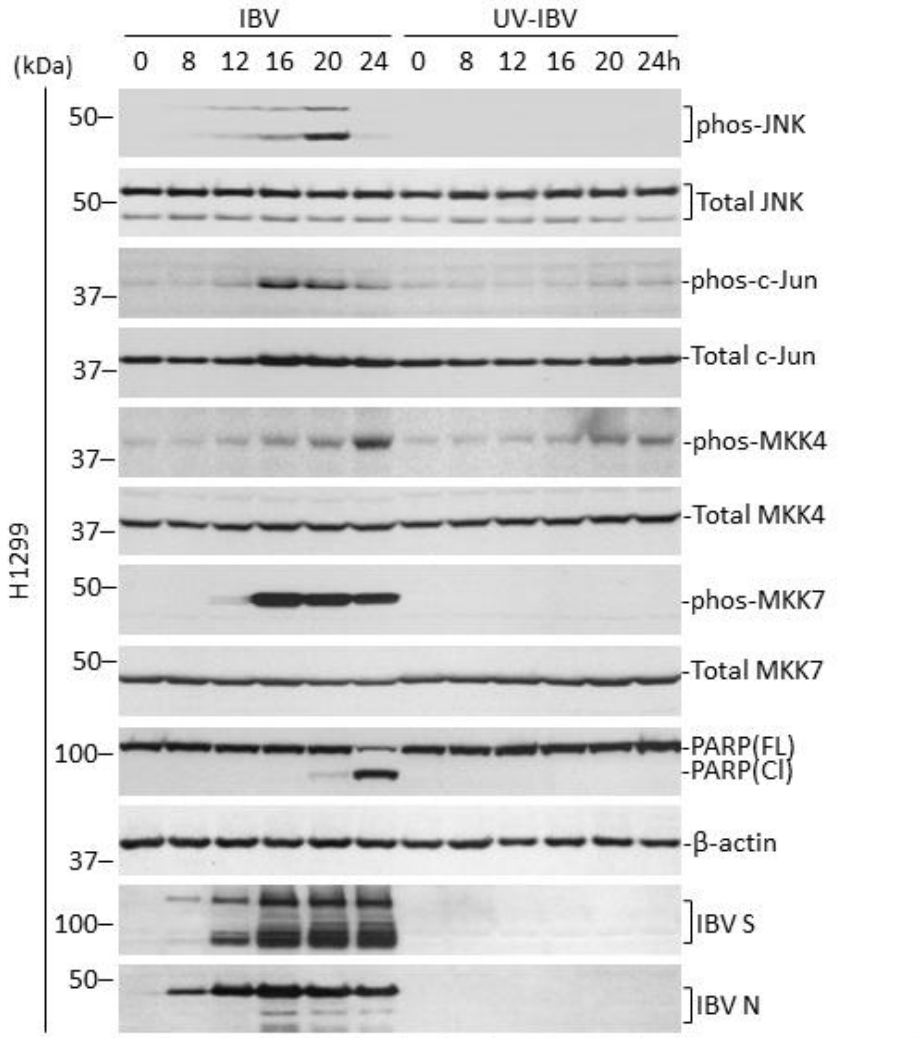

0	**1**	5.1	10	27	1.8	0	0	0	0	0	0	phos-JNK/JNK
1	0.8	1.9	4.9	4.6	2.7	1.0	1.0	1.0	1.0	0.9	1.4	phos-c-Jun/c-Jun
1	1.0	1.8	3.2	4.3	10	1	1.2	1.2	1.7	4.1	4.0	phos-MKK4/MKK4
0	0	**1**	12	14	10	0	0	0	0	0	0	phos-MKK7/MKK7

Figure 4-1 Activation of JNK pathway during IBV infection in H1299 cells

H1299 cells were infected with IBV at MOI~2 or mock infected. Protein lysates were harvested at the indicated time points and subjected to Western blot analysis using the indicated antibodies. Beta-tubulin was included as loading control. Sizes of protein ladders in kDa were indicated on the left. Degree of protein phosphorylation was calculated as the band intensity of phosphorylated protein divided by the band intensity of the corresponding total protein respectively.

To validate the result, a similar time course experiment was performed on another mammalian cell line Huh-7. As shown in **Figure 4-2**, IBV infection induced JNK phosphorylation in Huh-7 cells similar to the H1299 cells, except that the signal seemed to be stronger and remained at high level even at 24 hpi. A high degree of c-Jun phosphorylation above the basal level was also detected in IBV-infected Huh-7 cells. However, unlike in H1299 cells, phosphorylation of c-Jun seemed to destabilize the protein, as the amount of total c-Jun was found reduced at late time points (20 and 24 hpi) in the Huh-7 cells (**Figure 4-2**). On the other hand, only minimum level of MKK4 phosphorylation was observed, except in the 24 hpi sample. Also, compared with H1299 cells, phosphorylation of MKK7 occurred earlier at 12 hpi and was also inactivated faster in Huh-7 cells (**Figure 4-2**). Phosphorylated MKK7 could be barely detected in the 20 and 24 hpi samples, possibly also due to a reduction of the total MKK7 protein. Taken together, the result suggested that the JNK pathway was effectively activated in IBV-infected cells, and phosphorylation of JNK seemed to be mediated by the upstream kinase MKK7. Notably, JNK activation also preceded IBV-induced PARP cleavage in both H1299 and Huh-7 cells, suggesting a functional involvement in regulating IBV-induced apoptotic cell death (**Figure 4-1 and 4-2**).

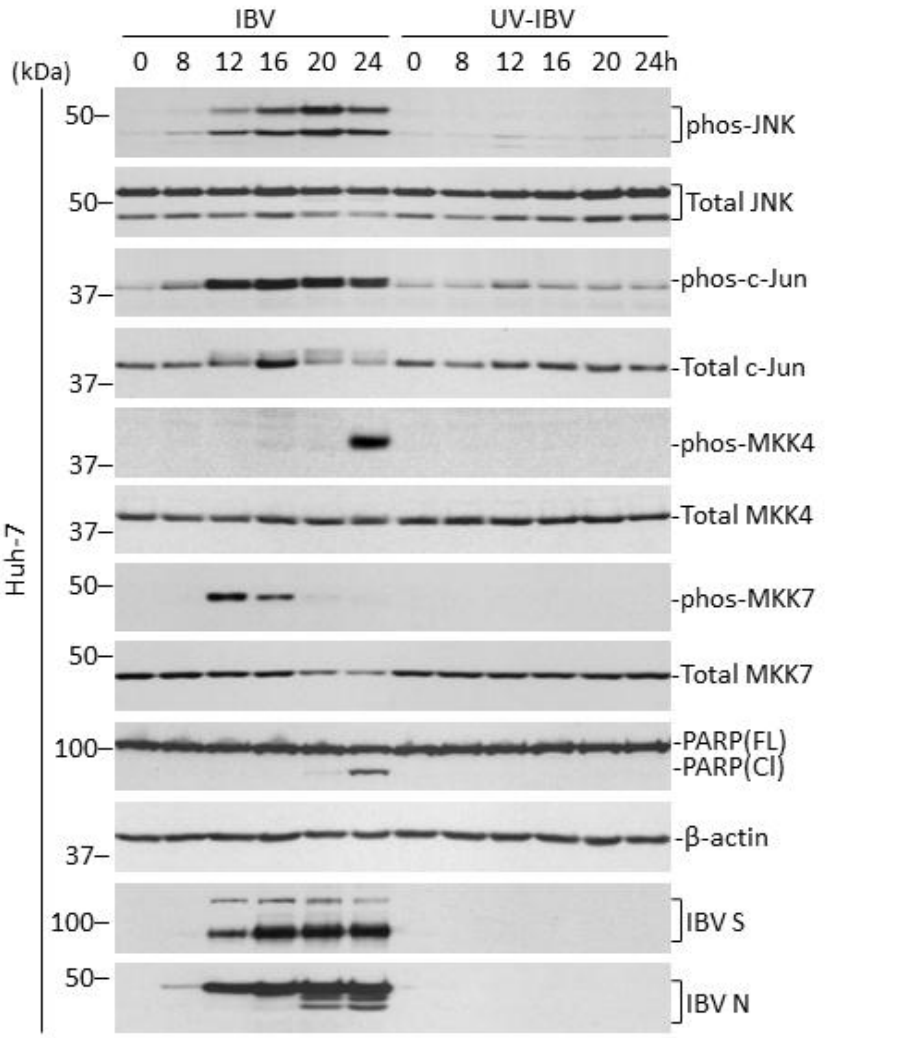

1	5.1	30	44	81	69	2.1	1.4	2.8	1.0	1.9	1.8	phos-JNK/JNK
1	3.2	5.9	3.4	8.0	11	1.3	1.6	2.3	1.4	1.4	1.5	phos-c-Jun/c-Jun
0	0	0	**1**	0.7	15	0	0	0	0	0	0	phos-MKK4/MKK4
0	0	**1**	0.6	0.1	0.1	0	0	0	0	0	0	phos-MKK7/MKK7

Figure 4-2 Activation of JNK pathway during IBV infection in Huh-7 cells.

Huh-7 cells were infected with IBV or mock infected as in Figure 4-1. Western blot analysis and quantification were performed as in Figure 4-1.

4.2.2. Overexpression of MKK7 promotes JNK phosphorylation and induction of IL-8 during IBV infection

To further validate the role of upstream MKKs in JNK activation during IBV infection, the coding sequences of MKK4 and MKK7 were amplified and inserted into the mammalian expression vector pXJ40FLAG. H1299 cells were transfected with pXJ40FLAG-MKK4, pXJ40FLAG-MKK7 or the empty vector before infected with IBV at MOI~2 or mock infected for 20 hours. As shown in **Figure 4-3a**, expression of FLAG-tag MKK4 and MKK7 could be determined by Western blot using the FLAG antibody. As expected, phosphorylated MKK4 was detected at a significantly higher level in cells transfected with FLAG-MKK4, as compared with the vector control. Prominent phosphorylation of MKK4 occurred in the IBV-infected cells but not in the mock infected cells, suggesting that activation of the ectopic MKK4 was dependent on activation of upstream kinases during IBV infection (**Figure 4-3a**). Surprisingly, MKK7 phosphorylation was detected at a similar level in all transfected cells, although a significant higher level of total MKK7 was observed in cells transfected with FLAG-MKK7. It was possible that the phosphorylated MKK7 antibody only recognized the endogenous protein but not the ectopic phosphorylated FLAG-MKK7. Transfection of MKK4 or MKK7 did not significantly affect IBV replication, as determined by the similar levels of IBV N protein and IBV positive stranded genomic RNA compared with the vector control (**Figure 4-3a and c**).

The activation of JNK and c-Jun induced by IBV infection was then examined in the transfected cells. In the vector control, a moderate increase of JNK and c-Jun phosphorylation was observed in the infected cells compared with the mock infected cells (**Figure 4-3a**). Surprisingly, overexpression of MKK4 indeed reduced both the basal level and the IBV-induced phosphorylation of JNK and c-Jun. It might be possible that the overly active MKK4 signal triggered some negative feedback mechanisms, which in turn suppressed the downstream activation of JNK/c-Jun. On the other hand, both JNK and c-Jun were more efficiently phosphorylated in the infected cells transfected with FLAG-MKK7 compared with the vector control (**Figure 4-3a**). Even the basal activation of JNK and c-Jun in the mock infected cells was slightly higher in the FLAG-MKK7 transfected cells compared with the control. Thus, the ectopic FLAG-MKK7 was functionally active and promoted phosphorylation of JNK and c-Jun induced by IBV infection.

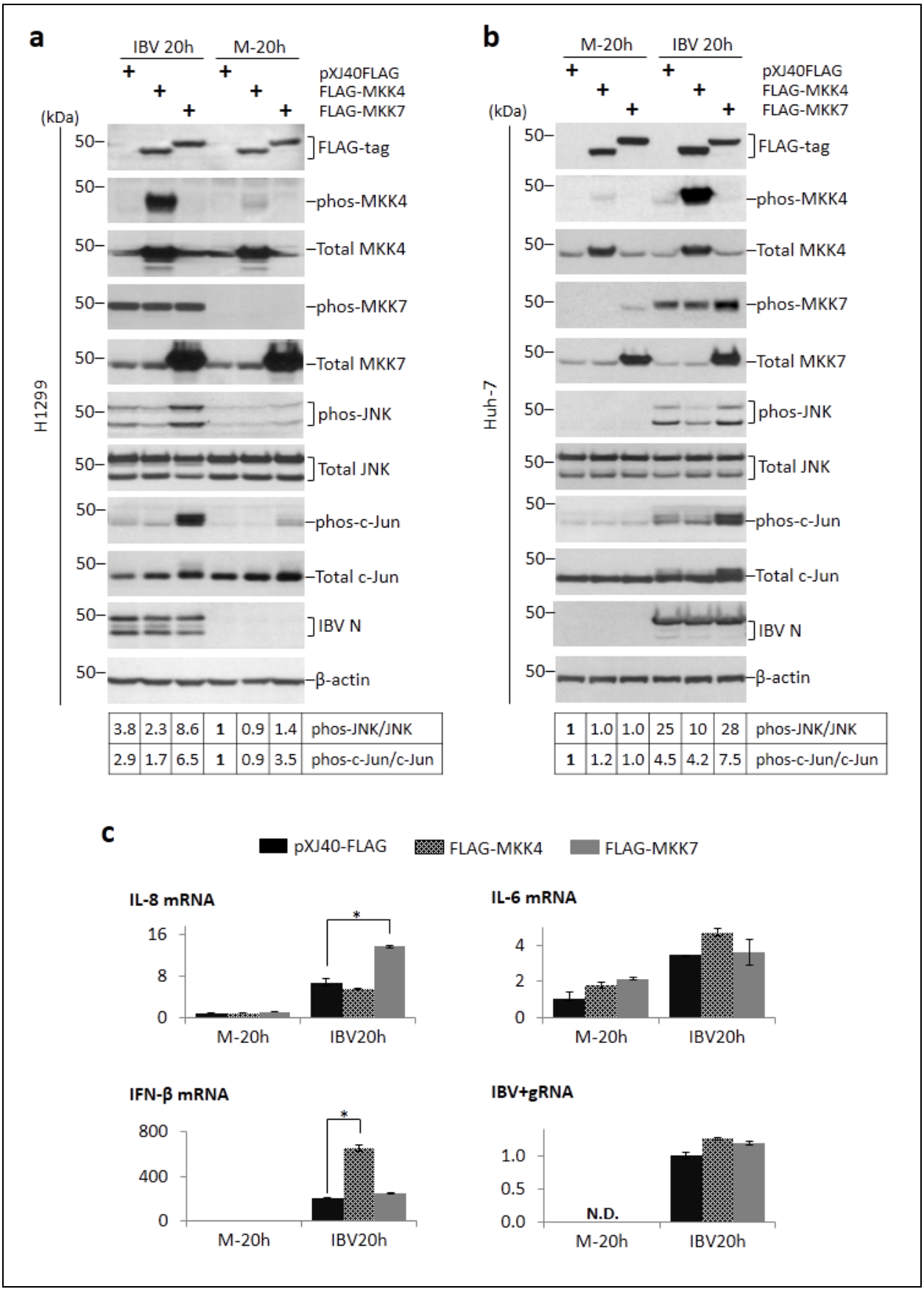
a
IBV 20h
M-20h
pXJ40FLAG
FLAG-MKK4
FLAG-MKK7
(kDa)
H1299
50–
FLAG-tag
phos-MKK4
Total MKK4
phos-MKK7
Total MKK7
phos-JNK
Total JNK
phos-c-Jun
Total c-Jun
IBV N
β-actin
3.8 2.3 8.6 1 0.9 1.4 phos-JNK/JNK
2.9 1.7 6.5 1 0.9 3.5 phos-c-Jun/c-Jun
b
M-20h
IBV 20h
Huh-7
1 1.0 1.0 25 10 28 phos-JNK/JNK
1 1.2 1.0 4.5 4.2 7.5 phos-c-Jun/c-Jun
c
pXJ40-FLAG
FLAG-MKK4
FLAG-MKK7
IL-8 mRNA
IL-6 mRNA
IFN-β mRNA
IBV+gRNA
N.D.
M-20h
IBV20h

Figure 4-3 Overexpression of MKK7 promotes IBV-induced JNK phosphorylation and IL-8 expression at the mRNA level.

(a) Overexpressing MKK7 promotes JNK/c-Jun phosphorylation in H1299 cells. H1299 cells were transfected with pXJ40FLAG, pXJ40FLAG-MKK4 or pXJ40FLAG-MKK7 before infected with IBV mock infected for 20 hours. Protein lysates were harvested at the indicated time points and subjected to Western blot analysis using the indicated antibodies. Beta-actin was included as loading control. Sizes of protein ladders in kDa were indicated on the left. Degree of protein phosphorylation was calculated as in Figure 4-1.

(b) MKK7 promotes the activation of JNK pathway in Huh-7 cells. Cells were transfected and infected as in (a). Western blot and quantification were performed as in (a).

(c) Overexpressing MKK7 promotes IL-8 induction in IBV-infected cells. A second set of H1299 cells in (a) were harvested for total RNA. Quantitative RT-PCR was performed as in Figure 3-18a. Fold induction of genes were calculated using GAPDH as internal references and normalized to the pXJ40FLAG transfected mock-infected sample. Asterisks indicate significant differences between two indicated samples (*, $P<0.05$).

The same experiment was also performed in Huh-7 cells. Unlike in H1299 cells, a slightly higher level of phosphorylated MKK7 was indeed detected in Huh-7 cells transfected with FLAG-MKK7 (**Figure 4-3b**). Similar to the H1299 cells, although the ectopically expressed FLAG-MKK4 was highly phosphorylated, it actually reduced IBV-induced JNK phosphorylation compared with the vector control. Although phosphorylated JNK was only marginally increased in cells transfected with FLAG-MKK7, the level of c-Jun phosphorylation was found significantly higher compared with the control (**Figure 4-3b**). Taken together, result from Huh-7 cells also supported an important role of MKK7 in IBV-induced activation of the JNK pathway.

To see whether the hyper-phosphorylated JNK in cells overexpressing FLAG-MKK7 contributed to cytokine induction, the mRNA levels of IL-8, IL-6 and IFN-β were determined by quantitative RT-PCR. As shown in **Figure 4-3c**, significant up-regulation of IL-8 and IFN-β mRNA could be detected in the IBV-infected H1299 cells transfected with the vector plasmid. Notably, overexpression of FLAG-MKK7 further promoted the induction of IL-8, but has no detectable effect on the expression of IL-6 and IFN-β (**Figure 4-3c**). Interestingly, transcription of IFN-β was found significantly up-regulated in cells transfected with FLAG-MKK4. This might be attributed to the function of p38, which is also known to be phosphorylated by MKK4.

4.2.3. Overexpression of MKK7 promotes IBV-induced apoptosis

It has been well established that JNK activation was involved in apoptosis induced by a variety of stimuli and stress. Since overexpression of MKK7 was found to promote JNK phosphorylation in IBV-infected cells, we continued to investigate its effect on IBV-induced apoptosis. Additionally, we would like to investigate why the ectopically expressed FLAG-MKK7 could not be detected by the phosphorylated MKK7 antibody (**Figure 4-3a and b**). Therefore a few mutants of MKK7 were generated by site-directed mutagenesis. In the K149M mutant, the lysine 149 in MKK7 critical for ATP binding was mutated to methionine. In the STS-3E mutant, serine 271, threonine 275 and serine 277 were mutated to glutamates. These residues were normally phosphorylated by upstream MKKKs to activate MKK7. Therefore the STS-3E was considered a "phosphomimetic" mutant of active MKK7. Finally in the STS-3A mutant, the same three residues were mutated to alanines, which rendered the protein incapable of being phosphorylated by upstream kinases.

First, we would like to characterize the behavior of these MKK7 constructs in cells under a condition known to activate the JNK pathway. H1299 cells were transfected with vector, wild type MKK7 or the three mutants for 24 hours. The transfected cells were then irradiated with UVC, which has been widely used as a positive control treatment to activate the JNK pathway. As shown in **Figure 4-4a**, UVC treatment induced moderate JNK phosphorylation in the vector control. Transfection of wild type MKK7 enhanced UVC-induced JNK phosphorylation by ~2.2-fold. The level of phosphorylated JNK in cells transfected with the K149M mutant was slightly lower than the control, suggesting that the ATP-binding mutant might serve as a dominant negative mutant that inhibited the endogenous MKK7 (**Figure 4-4a**). The STS-3E mutant promoted UVC-induced JNK activation similarly as the wild type MKK7. This was unexpected, as previous publications have treated the STS-3E as a constitutively active mutant. It was also not expected that cells transfected with the STS-3A mutant actually had a similar level of JNK phosphorylation compared with the vector control (**Figure 4-4a**). This indicated that the STS-3A mutant, unlike the K149M mutant, was not dominant negative in UVC-treated cells.

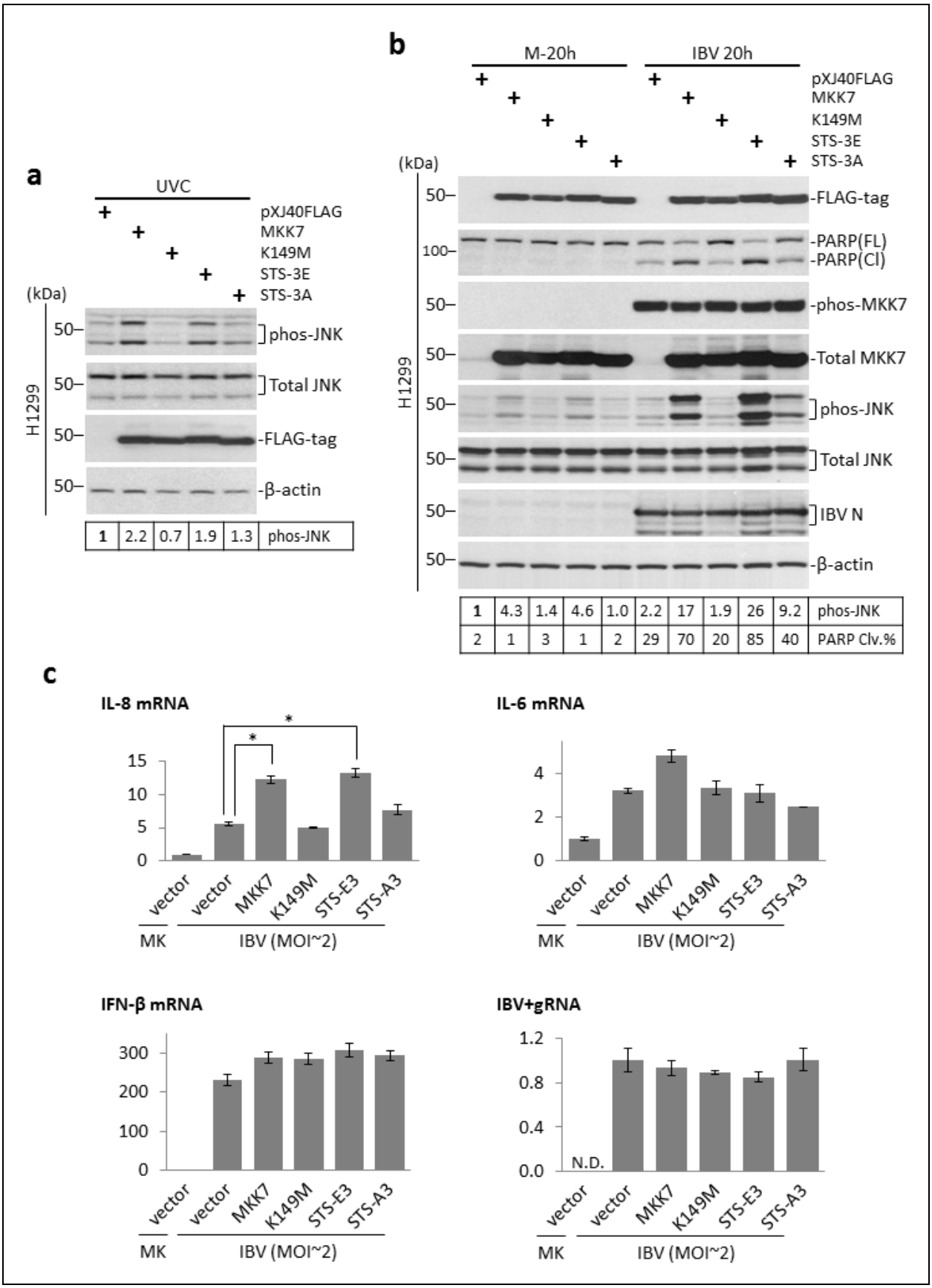
a
UVC
pXJ40FLAG
MKK7
K149M
STS-3E
STS-3A
(kDa)
50–
phos-JNK
Total JNK
FLAG-tag
β-actin
H1299
1 2.2 0.7 1.9 1.3 phos-JNK
b
M-20h
IBV 20h
pXJ40FLAG
MKK7
K149M
STS-3E
STS-3A
(kDa)
50–
100–
FLAG-tag
PARP(FL)
PARP(Cl)
phos-MKK7
Total MKK7
phos-JNK
Total JNK
IBV N
β-actin
H1299
1 4.3 1.4 4.6 1.0 2.2 17 1.9 26 9.2 phos-JNK
2 1 3 1 2 29 70 20 85 40 PARP Clv.%
c
IL-8 mRNA
IL-6 mRNA
IFN-β mRNA
IBV+gRNA
vector
MKK7
K149M
STS-E3
STS-A3
MK
IBV (MOI~2)
N.D.

Figure 4-4 Overexpression of MKK7 or its phosphomimetic mutant promotes IBV-induced apoptosis and IL-8 expression in H1299 cells

(a) H1299 cells were transfected with pXJ40-FLAG, pXJ40FLAG-MKK7, pXJ40FLAG-MKK7-K149M, pXJ40FLAG-MKK7-STS-3E or pXJ40FLAG-MKK7-STS-3A. After 24 hours, cells were irradiated with UVC (10mJ) and incubated for another 1 hour. Protein lysates were harvested and subjected to Western blot analysis using the indicated antibodies. Beta-tubulin was included as loading control. Sizes of protein ladders in kDa were indicated on the left. Degree of JNK phosphorylation was calculated as in Figure 4-1a.

(b) H1299 cells in duplicate were transfected as in (a) before infected with IBV at MOI~2 or mock infected for 20 hours. One set of cells were harvested for protein and subjected to Western blot analysis using the indicated antibodies. Beta-tubulin was included as loading control. Sizes of protein ladders in kDa were indicated on the left. Degree of JNK phosphorylation was calculated as in Figure 4-1a. Percentage of PARP cleavage was determined as in Figure 3-5a.

(c) A second set of cells in (b) were harvested for total RNA. Quantitative RT-PCR was performed as in Figure 3-18a. Fold induction of genes were calculated using GAPDH as internal references and normalized to the pXJ40FLAG transfected mock-infected sample. Asterisks indicate significant differences between two samples (*, $P<0.05$).

H1299 cells similar transfected were then infected with IBV at MOI~2 or mock infected for 20 hours. As shown in **Figure 4-4b**, expression of wild type MKK7 and the three mutants were determined by the anti-FLAG antibody. Phosphorylation of MKK7 was detected in the IBV-infected cells but not the mock infected control. The level of phosphorylated MKK7 was similar among all transfected samples, even for the vector control. Because the phosphorylation sites were removed in the STS-3A mutant, the phosphorylated MKK7 detected in STS-3A transfected cells should represent only the endogenous MKK7 protein. Therefore, it was concluded that the phosphorylated MKK7 antibody indeed could only detect the endogenous protein, but not the ectopically expressed protein.

Notably, in spite of the similar level of MKK7 phosphorylation detected, different level of IBV-induced JNK phosphorylation was observed. Transfection of wild type or the STS-3E mutant of MKK7 significantly increased the level of phosphorylated JNK in IBV-infected cells, as compared with the vector (**Figure 4-4b**). Transfection of the K149M mutant slightly reduced IBV-induced JNK phosphorylation. Interestingly, in IBV-infected cells transfected with the STS-3A mutant, the level of phosphorylated JNK was higher than the vector control, although not as high as in cells transfected with the wild type MKK7 or the STS-3E mutant (**Figure 4-4b**). To determine the degree of apoptosis induction, the apoptotic marker PARP was used. The PARP cleavage percentages were found to correlate well with the level of JNK phosphorylation. Moderate PARP cleavage was detected in vector control, which was slightly reduced in K149M, slightly increased in STS-3A, and considerably increased in cells transfected with wild type MKK7 or STS-3E (**Figure 4-4b**).

The induction of cytokines was also determined by quantitative RT-PCR. As shown in **Figure 4-4c**, the IBV-induced up-regulation of IL-8 mRNA also demonstrated a similar pattern as the JNK phosphorylation profile. IBV-infected cells transfected with wild type MKK7 or the STS-3E mutant had a significantly higher level of IL-8, compared with the vector control. Whereas the mRNA level of IL-8 was similar for the K149M mutant, and only marginally higher in cells transfected with the STS-3A mutant. The expression of IL-6 and IFN-β seemed to be independent on the transfection of MKK7 or its mutants (**Figure 4-4c**). Transfection of all MKK7 constructs did not significantly affect IBV replication, as determined by the similar levels of IBV N protein or positive stranded gRNA (**Figure 4-4b and c**) compared with control.

Similar transfection experiment was performed in Huh-7 cells. As shown in **Figure 4-5a**, the IBV-induced phosphorylation of MKK7 was found higher in cells transfected with wild type MKK7, K149M or the STS-3A mutant. Nonetheless, the phosphorylation of JNK showed a similar pattern as in H1299 cells: only wild type MKK7 and STS-3E, but not K149M or STS-3A, significantly enhanced IBV-induced JNK phosphorylation compared with the vector control (**Figure 4-5a**). The PARP cleavage pattern was also found to correlate with JNK activation, as observed for H1299 cells. Since IBV N was found at slightly different levels in the transfected cells, plaque assay was performed for the supernatants collected from infected cells. As shown in **Figure 4-5b,** similar virus titers were detected in all the samples compared with the vector control, suggesting that transfected of MKK7 or its mutants did not affect IBV replication in Huh-7 cells. Taken together, it seemed that both the ATP binding site and phosphorylation by up-stream kinases were required for MKK7 to activate JNK. Moreover, the MKK7-dependent JNK phosphorylation seemed to play an important role in the regulation of IBV-induced apoptosis and expression of IL-8 at the mRNA level.

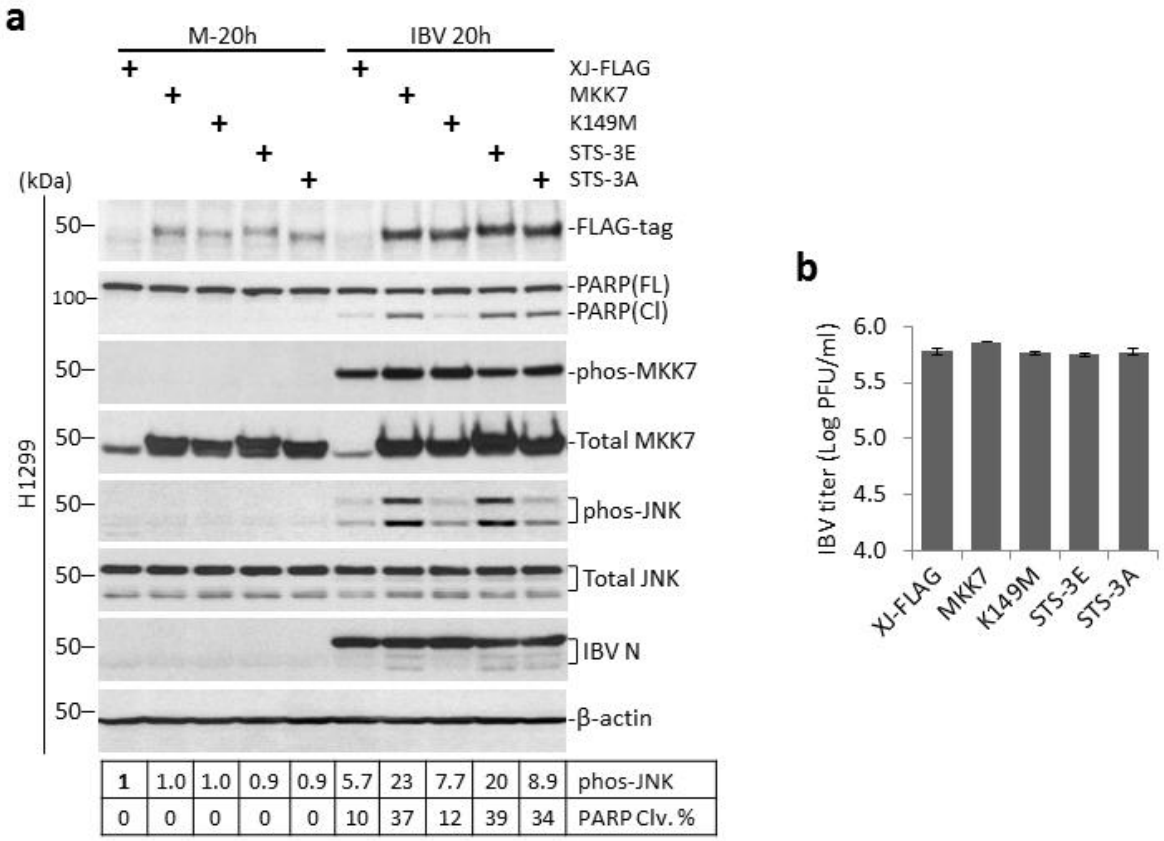

Figure 4-5 Overexpression of MKK7 or its phosphomimetic mutant promotes IBV-induced apoptosis in Huh-7 cells

(a) Overexpressing MKK7 promotes the IBV-induced apoptosis in Huh-7 cells. Transfection, infection, Western blot and data analysis were performed as in Figure 4-4b.

(b) The culture supernatants of IBV-infected Huh-7 cells in (a) were subjected to plaque assay analysis. Virus titers were expressed as the logarithm of PFU per ml of supernatants.

4.2.4. Overexpression of constitutively active JNK promotes IBV-induced apoptosis and cytokine production

Previous studies have shown that, when JNK is fused with its upstream kinase MKK7, the protein becomes constitutively active [332]. We obtained this construct and investigated the effect of constitutively active JNK on IBV replication and cellular responses. As a negative control, the conserved Thr-Pro-Tyr motif in JNK was modified to Ala-Pro-Phe (APF), which rendered the kinase unable to be phosphorylated. As shown in **Figure 4-6a**, H1299 cells were transfected with pcDNA-MKK7-JNK1 or pcDNA-MKK7-JNK1(APF), before infected with IBV at MOI~2 or mock infected. The expression level of MKK7-JNK1 was found slightly higher than the APF mutant, possibly due to differences in post-translational modification (such as degradation). Ectopic JNK1 inside the fusion protein was efficiently phosphorylated in cells transfected with MKK7-JNK1 but not the APF mutant, as determined by the antibody specific for phosphorylated JNK (**Figure 4-6a**). Notably, phosphorylation of the endogenous JNK was also promoted in cells transfected with MKK7-JNK1 compared with the APF control, whereas the total amount of endogenous JNK was not significantly affected. Transfection of MKK7-JNK1 enhanced the phosphorylation of c-Jun in both mock infected and IBV-infected cells as compared with the APF control, indicating that the constitutively active JNK indeed activated the downstream pathway. No PARP cleavage could be detected in the mock infected cells. In cells infected with IBV, percentage of PARP cleavage was found significantly higher in cells transfected with MKK7-JNK1, as compared with the APF control (**Figure 4-6a**). On the other hand, no significant difference in the level of IBV N was observed between cells transfected with MKK7-JNK1 or MKK7-JNK1(APF).

A similar transfection and infection experiment was performed in the Huh-7 cells. As shown in **Figure 4-6b**, transfection of MKK7-JNK1 had a similar effect on the phosphorylation of endogenous JNK and c-Jun in Huh-7 cells. Also, a significantly higher percentage of PARP cleavage was detected at 24 hpi in Huh-7 cells transfected with MKK7-JNK1 compared with the APF control (**Figure 4-6b**). Therefore, the result suggested that overexpression of constitutively active JNK did not affect IBV replication but promoted IBV-induced apoptosis.

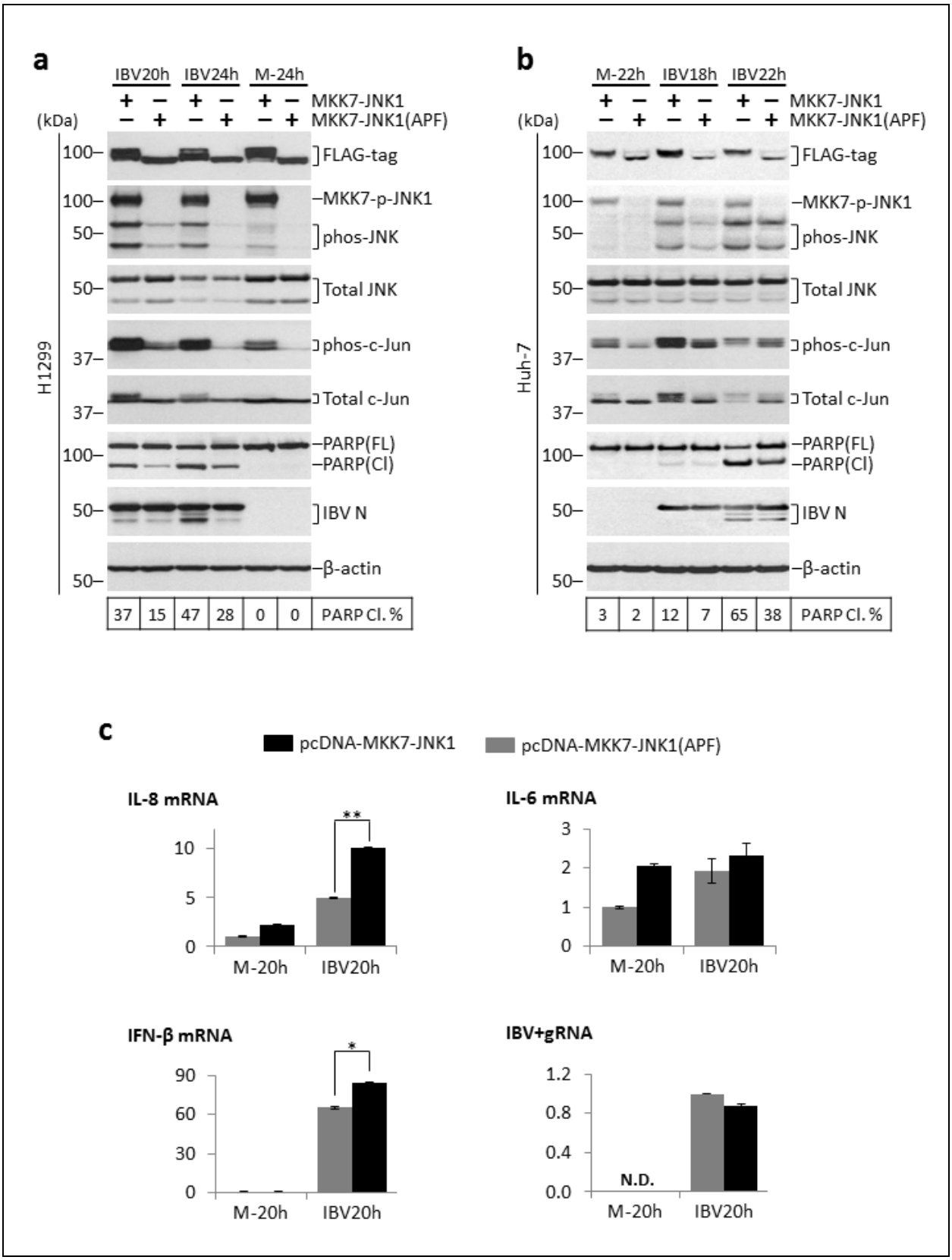
a
IBV20h
IBV24h
M-24h
MKK7-JNK1
MKK7-JNK1(APF)
(kDa)
H1299
100–
FLAG-tag
100–
–MKK7-p-JNK1
50–
phos-JNK
50–
Total JNK
37–
phos-c-Jun
37–
Total c-Jun
100–
–PARP(FL)
–PARP(Cl)
50–
IBV N
50–
–β-actin
37 15 47 28 0 0 PARP Cl. %
b
M-22h
IBV18h
IBV22h
MKK7-JNK1
MKK7-JNK1(APF)
(kDa)
Huh-7
FLAG-tag
–MKK7-p-JNK1
phos-JNK
Total JNK
phos-c-Jun
Total c-Jun
–PARP(FL)
–PARP(Cl)
IBV N
–β-actin
3 2 12 7 65 38 PARP Cl. %
c
pcDNA-MKK7-JNK1
pcDNA-MKK7-JNK1(APF)
IL-8 mRNA
**
M-20h
IBV20h
IL-6 mRNA
IFN-β mRNA
*
IBV+gRNA
N.D.

Figure 4-6 Overexpression of constitutively active form of JNK promotes IBV-induced apoptosis and cytokine production

(a) H1299 cells in duplicate were transfected with pcDNA-MKK7-JNK1 or pcDNA-MKK7-JNK1(APF), before infected with IBV at MOI~2 or mock infected. One set of cells were harvested for protein at the indicated time points and subjected to Western blot analysis using the indicated antibodies. Beta-tubulin was included as loading control. Sizes of protein ladders in kDa were indicated on the left. Degree of JNK phosphorylation and the percentage of PARP cleavage was determined as in Figure 4-4b.

(b) Huh-7 cells were transfected and infected similarly as in (a). Western blot analysis and data quantification were performed as in (a).

(c) A second set of cells in (a) were harvested for total RNA. Quantitative RT-PCR was performed as in Figure 3-18a. Fold induction of genes were calculated using GAPDH as internal references and normalized to the pcDNA-MKK7-JNK1(APF) transfected mock-infected sample. Asterisks indicate significant differences between two indicated samples (**, $P<0.01$; *, $P<0.05$).

The induction of cytokines in transfected H1299 cells was also determined by quantitative RT-PCR. As shown in **Figure 4-6c**, compared with the APF control, transfection of MKK7-JNK1 did not significantly affect the mRNA level of positive stranded IBV genomic RNA or the expression of IL-6. On the other hand, induction of IFN-β was moderately increased, whereas induction of IL-8 was markedly increased in the MKK7-JNK1-transfected cells compared with the APF control. Therefore, overexpression of constitutively active JNK actually enhanced IBV-induced IL-8 and IFN-β expression at the mRNA level.

4.2.5. The JNK inhibitor SP600125 suppresses JNK phosphorylation and apoptosis during IBV infection

The result presented above has been relied on the gain-of-function approach. To gain a more complete understanding of JNK's function during IBV infection, we turned to the loss-of-function approach. Several specific JNK inhibitors have been developed so far, and an anthrapyrazolone compound called SP600125 is the most widely used and well-characterized [364]. Because IBV-induced JNK phosphorylation was more intense in Huh-7 cells, we first studied the effect of SP600125 in this cell line.

As shown in **Figure 4-7a**, Huh-7 cells were first infected with IBV at MOI~2 or mock infected. After 4 hours of adsorption, the unbound virus was removed and cells were treated with increasing doses of SP600125 (from 0 to 50μM) for 20 hours. In the DMSO solvent control, IBV infection induced prominent JNK phosphorylation compared with the mock infected cells. Treatment of as low as 10μM SP600125 significantly reduced IBV-induced phosphorylated JNK by ~60% (**Figure 4-7a**). However, further increase of SP600125 concentration did not markedly suppressed JNK phosphorylation further. This low level of JNK activation might be mediated by other mechanisms resistant to the action of SP600125. Notably, treatment of SP600125 at 10μM did not significantly affect the level of IBV N compared with the DMSO control (**Figure 4-7a**). On the other hand, increasing amounts of SP600125 dosage dependently reduced the level of IBV N protein. This was validated by plaque assay of the culture supernatant. Treatment of SP600125 at 20μM or above was found to significantly reduce the IBV titers in Huh-7 cells (**Figure 4-7b**). Taken together, it seemed that the JNK inhibitor SP600125 significantly inhibited IBV replication at concentration higher than 10μM.

Since JNK phosphorylation was induced by IBV replication, we decided to use lower dosage of SP600125 in the subsequent experiments. As shown in **Figure 4-7c**, Huh-7 cells were infected and treated with SP600125 at lower concentrations (0-8μM). The total amount of JNK was not affected by the treatment of SP600125. Moreover, IBV replication was also not significantly affected, as determined by the similar amount of IBV N protein compared with the DMSO-treated control.

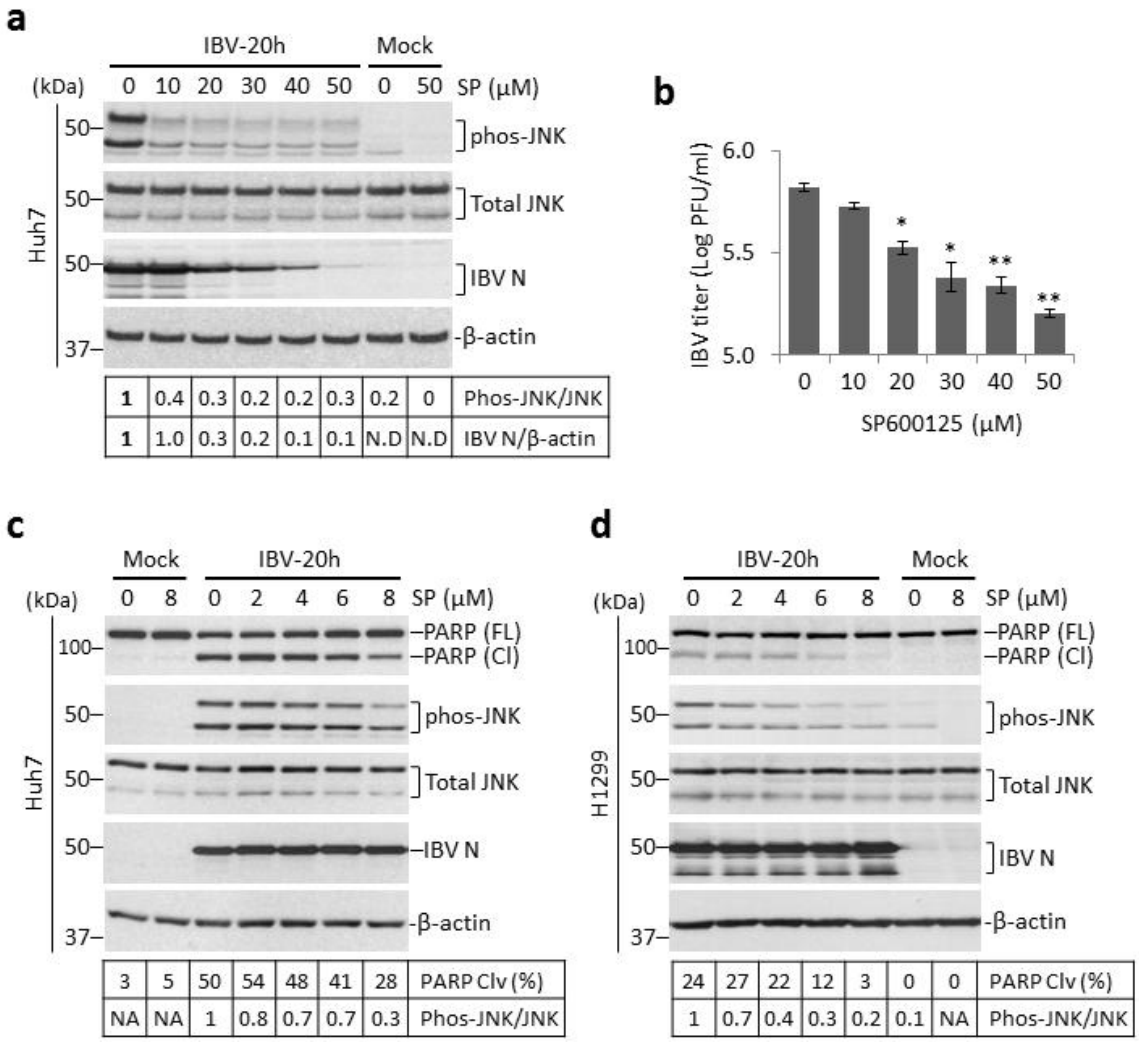

Figure 4-7 SP600125 suppresses IBV-induced JNK phosphorylation and apoptosis

(a) Huh-7 cells were infected with IBV or mock infected. After 4 hours, cells were treated with SP600125 (SP) at the indicated concentrations or same volume of DMSO for 20 hours. Cell lysates were subjected to Western blot analysis using the indicated antibodies. JNK phosphorylation and PARP cleavage was determined as in Figure 4-3b.

(b) The culture supernatants in (a) were subjected to plaque assay analysis. Virus titers were expressed as the logarithm of PFU per ml of supernatants.

(c) Huh-7 cells were infected and treated with SP600125 at lower concentrations as in (a). Western blot analysis and data quantification were performed as in (a).

(d) H1299 cells were infected and treated with SP600125 as in (c). Western blot analysis and data quantification were performed as in (a).

Notably, the protein level of phosphorylated JNK reduced dosage dependently with increasing concentration of SP600125 used. Moreover, the percentage of PARP cleavage was also reduced in a dosage dependent manner in cells treated with SP600125 (**Figure 4-7c**). In Huh-7 cells treated with 8μM SP600125, IBV-induced PARP cleavage was reduced nearly by half compared with the IBV-infected DMSO control. Similar experiments were also performed in H1299 cells. As shown in **Figure 4-7d**, treatment of increasing dosages of SP600125 also reduced JNK phosphorylation and PARP cleavage induced by IBV infection in H1299 cells. Similar to Huh-7 cells, the replication of IBV was not significantly affected in H1299 cells treated with SP600125 at concentration as high as 8μM (**Figure 4-7d**). Taken together, the inhibitor experiments demonstrated that at low concentration, inhibition of JNK phosphorylation by SP600125 suppressed apoptosis induced by IBV infection.

4.2.6. Knockdown of JNK, but not c-Jun, attenuates IBV-induced apoptosis

The reduced IBV-induced apoptosis observed in SP600125-treated cells could have been due to other uncharacterized off-target effects of the compound. Therefore, to validate the result we shifted to the RNAi approach. The functional knockdown of JNK was first examined in cells subjected to positive control treatment. As shown in **Figure 4-8a**, H1299 cells transfected with siEGFP or siJNK were irradiated with UVC. In the siEGFP control, UVC induced significant phosphorylation of both JNK and c-Jun (**Figure 4-8a**). In cells transfected with siJNK, the amounts of total JNK and phosphorylated JNK were both reduced compared with the siEGFP control. Although the level of total c-Jun was not affected, UVC-induced phosphorylation of c-Jun was suppressed in cells transfected with siJNK (**Figure 4-8a**). The data suggested that transfection of siJNK attenuated the activation of JNK pathway in UVC-irradiated cells.

Next, H1299 cells transfected with siEGFP or siJNK were infected with IBV at MOI~2 or mock infected. As shown in **Figure 4-8b**, significant phosphorylation of JNK and c-Jun was detected in IBV-infected cells in the siEGFP control. Knockdown of JNK drastically reduced the protein levels of both phosphorylated and total JNK. The amount of phosphorylated c-Jun was also lower in the JNK-knockdown cells compared with the control, suggesting a successful inhibition of the JNK signaling pathway (**Figure 4-8b**). Notably, IBV induced significant PARP cleavage in the siEGFP control at 20 and 22 hpi, which was partially reduced in cells transfected with siJNK. Moreover, when compared with the siEGFP control of the same time point, the JNK-knockdown cells had a higher amount of the anti-apoptotic Bcl2 protein, but a slightly lower amount of the pro-apoptotic BAK1 protein (**Figure 4-8b**). Knockdown of JNK did not significantly affect IBV replication, as indicated by the similar level of IBV N protein.

The same knockdown experiment was also performed in Huh-7 cells. As shown in **Figure 4-8c**, siJNK reduced the levels of phosphorylated JNK and c-Jun in IBV-infected Huh-7 cells. The siRNA knockdown efficiency was not as high as in H1299 cells, as considerable level of phosphorylated JNK could still be detected in the JNK-knockdown Huh-7 cells. Nonetheless, transfection of the siJNK partially reduced IBV-induced PARP cleavage and modulated the protein levels of Bcl2 and BAK1, similar to what happened in the H1299 cells (**Figure 4-8c**). Therefore, the result demonstrated that knockdown of JNK suppressed IBV-induced apoptosis, possibly by up-regulating anti-apoptotic Bcl2 and down-regulating pro-apoptotic BAK1.

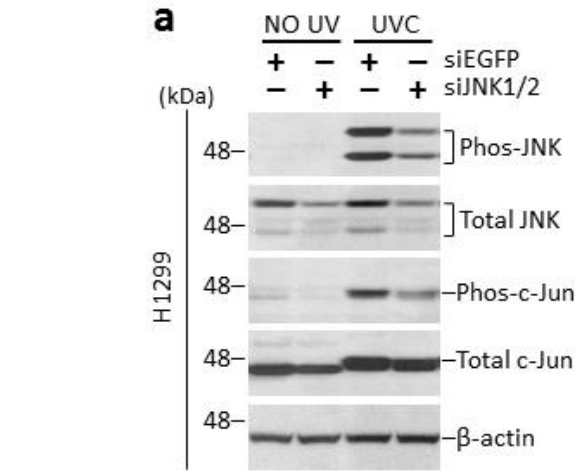

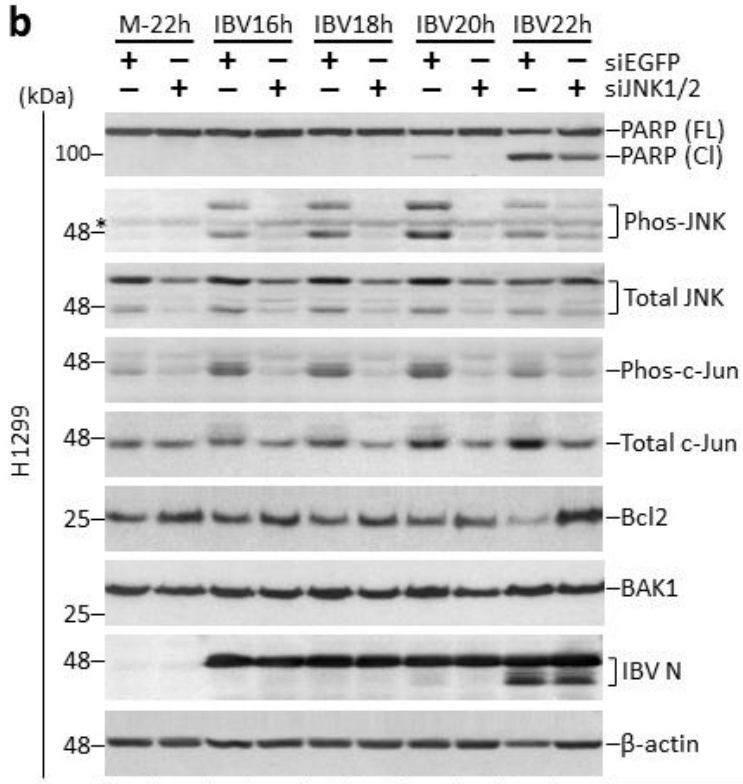

0	0	0	0	0	0	14	0	54	36	PARP Clv (%)
1	1.5	1.0	1.3	0.9	1.2	0.9	1.2	0.5	1.9	Bcl2
1	1.0	1.2	1.0	1.3	1.0	1.4	0.9	1.7	1.2	BAK1

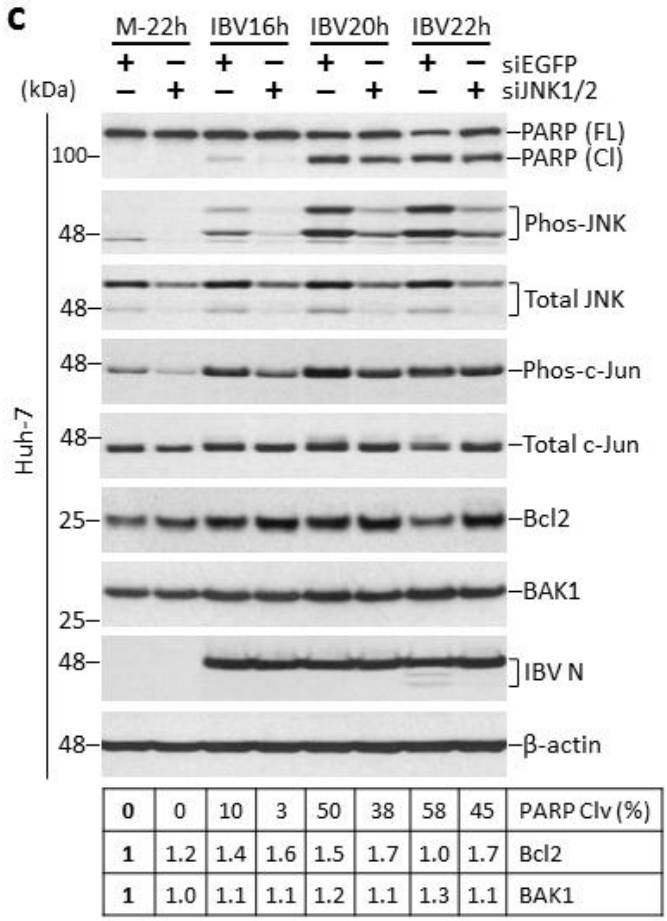

0	0	10	3	50	38	58	45	PARP Clv (%)
1	1.2	1.4	1.6	1.5	1.7	1.0	1.7	Bcl2
1	1.0	1.1	1.1	1.2	1.1	1.3	1.1	BAK1

Figure 4-8 Knockdown of JNK attenuates IBV-induced apoptosis

(a) H1299 cells were transfected with siEGFP or siJNK for 48 hours. Cells were then irradiated with 40mJ UVC and incubated for another 1 hour. Protein lysates were subjected to Western blot analysis using the indicated antibodies. Beta-actin was included as loading control. JNK phosphorylation was determined as in Figure 4-3b.

(b) H1299 cells were transfected with siEGFP or siJNK before infected with IBV at MOI~2 or mock infected. Cells were harvested at indicated time points and subjected to Western blot analysis using the indicated antibodies. Beta-actin was included as loading control. Percentage of PARP cleavage was determined as in Figure 3-5a. Relative amount of Bcl2 or BAK1 was determined as the band intensity normalized to GAPDH, with the mock infected sample of siEGFP-transfected cells set as one.

(c) Huh-7 cells were transfected and infected as in (b). Cells were harvested and subjected for Western blot analysis as in (b). Percentage of PARP cleavage and the relative abundance of Bcl2 or BAK1was determined as in (b).

To see whether the pro-apoptotic activity of JNK was mediated via c-Jun, additional knockdown experiments were performed. As shown in **Figure 4-9a**, H1299 cells were transfected with siEGFP or sic-Jun before infected with IBV or mock infected. Successful knockdown of c-Jun could be determined by the reduced amount of both phosphorylated c-Jun and total c-Jun in cells transfected with sic-Jun, as compared with the siEGFP control. Knockdown of c-Jun did not significantly affect IBV replication, as determined by the similar level of IBV N protein. Surprisingly, a significantly higher percentage of PARP cleavage could be detected in c-Jun-knockdown cells compared with the siEGFP control of the same time point (**Figure 4-9a**). When the same knockdown experiment was performed in Huh-7 cells, a similar enhanced PARP cleavage was also observed in cells transfected with sic-Jun (**Figure 4-9b**). Taken together, it seemed that unlike JNK, c-Jun might serve a pro-survival function during IBV infection and protect the infected cells from IBV-induced apoptosis.

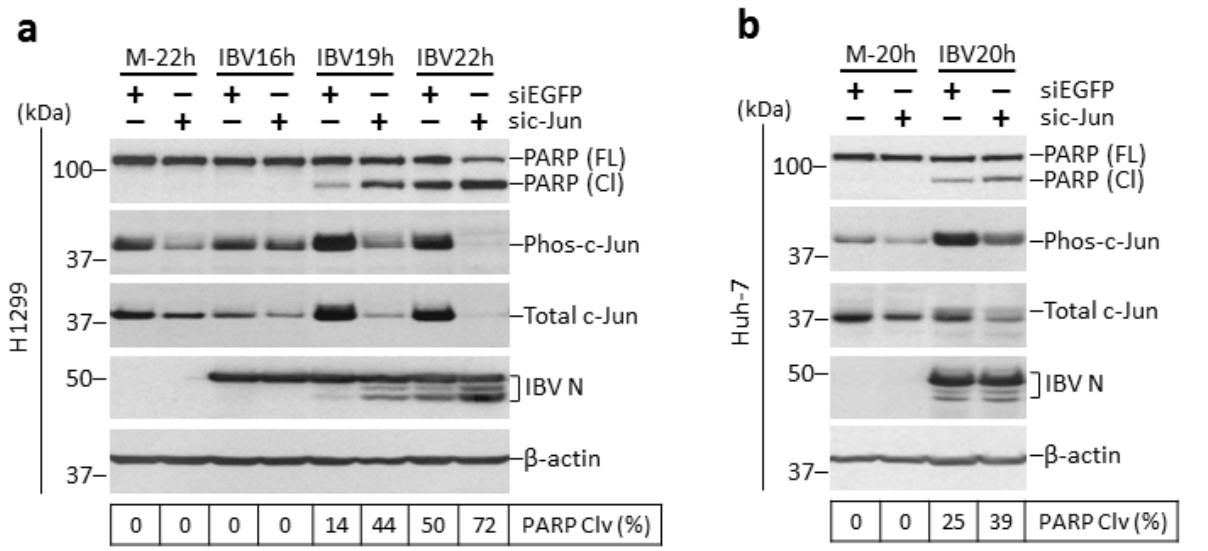

Figure 4-9 Knockdown of c-Jun potentiates IBV-induced apoptosis

(a) H1299 cells were transfected with siEGFP or sic-Jun before infected with IBV at MOI~2 or mock infected. Cells were harvested at indicated time points and subjected to Western blot analysis using the indicated antibodies. Beta-actin was included as loading control. Percentage of PARP cleavage was determined as in Figure 3-5a.

(b) Huh-7 cells were transfected and infected as in (a). Western blot analysis and quantification of PARP cleavage was performed as in (a).

4.2.7. Overexpression of Bcl2 inhibits IBV-induced apoptosis

Previous studies have shown that overexpression of Bcl2 does not affect SARS-CoV replication but inhibits apoptosis induced in the infected cells [125]. In the result obtained above, a higher level of Bcl2 protein was found to associate with reduced apoptosis in JNK-knockdown cells at the late stage of IBV infection (**Figure 4-8b and c**). Furthermore, JNK has also been demonstrated to directly phosphorylate Bcl2 at Ser70, inhibiting its anti-apoptotic activity in cells treated with pacilitaxel [313]. We therefore hypothesized that the pro-apoptotic activity of JNK might be mediated through its inhibition of the anti-apoptotic protein Bcl2. The coding sequence of Bcl2 was amplified and cloned in the mammalian expression vector pXJ40-FLAG. A mutant (S70A) was generated, in which the serine 70 reported to be phosphorylated by JNK was mutated into alanine. H1299 cells were transfected with empty vector, Bcl2 or the S70A mutant before infected with IBV at MOI~2 or mock infected. As shown in **Figure 4-10a**, the expression of FLAG-Bcl2 and FLAG-Bcl2-S70A could be detected at similar level by Western blot. When the membrane was probed with antibody specific for phosphorylated Bcl2 at Serine 70, signals were detected only in cells transfected with wild type Bcl2 but not in the vector or mutant-transfected cells. Thus, endogenous Bcl2 might not undergo significant phosphorylation at serine 70, or the level was lower than the detection limit of this antibody. Notably, a high level of phosphorylated Bcl2 could be detected in the mock infected cells transfected with FLAG-Bcl2, where no JNK phosphorylation was observed (**Figure 4-10a**). These suggested that phosphorylation of the ectopic Bcl2 was not dependent on IBV replication or JNK activation, and might rather be mediated by other constitutively active kinase(s) in the cells.

In the vector control, IBV infection triggered significant PARP cleavage at 20 and 24 hpi (**Figure 4-10a**). In cells transfected with FLAG-Bcl2 and FLAG-Bcl2(S70A), PARP cleavage was completely abolished at 20 hpi and significantly reduced at 24 hpi. Notably, there was no significant difference in IBV-induced PARP cleavage between cells transfected with wild type Bcl2 and the S70A mutant of the same time point. Thus phosphorylation at serine 70 seemed to be non-essential for the anti-apoptotic function of Bcl2 during IBV infection.

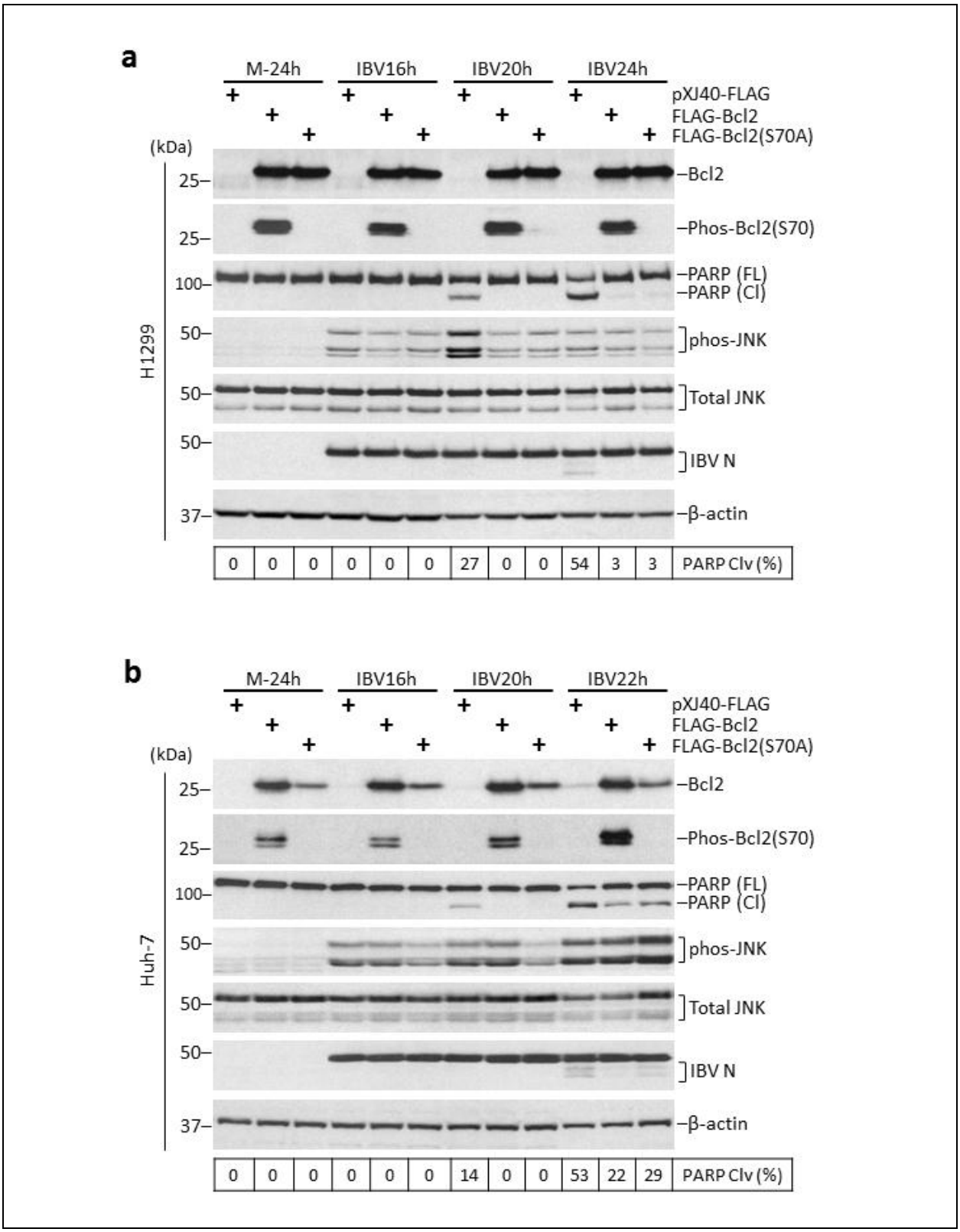
a
M-24h
IBV16h
IBV20h
IBV24h
pXJ40-FLAG
FLAG-Bcl2
FLAG-Bcl2(S70A)
(kDa)
25–
Bcl2
25–
Phos-Bcl2(S70)
100–
PARP (FL)
PARP (Cl)
50–
phos-JNK
50–
Total JNK
50–
IBV N
37–
β-actin
H1299
0 0 0 0 0 0 27 0 0 54 3 3 PARP Clv (%)
b
M-24h
IBV16h
IBV20h
IBV22h
pXJ40-FLAG
FLAG-Bcl2
FLAG-Bcl2(S70A)
(kDa)
25–
Bcl2
25–
Phos-Bcl2(S70)
100–
PARP (FL)
PARP (Cl)
50–
phos-JNK
50–
Total JNK
50–
IBV N
37–
β-actin
Huh-7
0 0 0 0 0 0 14 0 0 53 22 29 PARP Clv (%)

Figure 4-10 Overexpression of Bcl2 inhibits IBV-induced apoptosis

(a) H1299 cells were transfected with pXJ40-FLAG, pXJ40-FLAG-Bcl2 or pXJ40-FLAG-Bcl2(S70A) before infected with IBV at MOI~2 or mock infected. Cells were harvested at indicated time points and subjected to Western blot analysis using the indicated antibodies. Beta-tubulin was included as loading control. Sizes of protein ladders in kDa were indicated on the left. Percentage of PARP cleavage was determined as in Figure 3-5a.

(b) Huh-7 cells were transfected and infected as in (a). Western blot analysis and quantification of PARP cleavage was determined as in (a).

The same experiment was performed in Huh-7 cells. As shown in **Figure 4-10b**, the protein expression level of Bcl2(S70A) was lower than that of the wild type protein. It might be possible that phosphorylation of Bcl2 at serine 70 stabilized the protein in Huh-7 cells. Similar to the H1299 cells, phosphorylation of endogenous Bcl2 was not observed. Phosphorylation of the ectopic Bcl2 could be detected in the mock infected cells, although the level seemed to increase at late stage of infection (**Figure 4-10b**). As in H1299 cells, overexpression of Bcl2 and Bcl2(S70A) inhibited PARP cleavage induced by IBV infection, as compared with the vector control. Compared with the Bcl2-transfected cells, a slightly higher PARP cleavage was observed in the Bcl2(S70A)-transfected cells at 24 hpi (**Figure 4-10b**). This seemingly reduced anti-apoptotic activity could be explained by the lower protein level of Bcl2 in cells transfected with Bcl2(S70A) at 24 hpi. Taken together, the result suggested that IBV infection did not induce detectable phosphorylation of endogenous Bcl2. Although ectopically expressed Bcl2 was phosphorylated at serine 70, it was not mediated by JNK and did not significantly affect the anti-apoptotic activity of Bcl2 during IBV infection.

4.2.8. Overexpression of DUSP1 reduced JNK phosphorylation, apoptosis induction and IL-8 mRNA expression in IBV-infected cells

It has been shown that activated MAP kinases are dephosphorylated by proteins called dual specificity protein phosphatases (DUSPs) [365]. Previous data from our group has also shown that IBV infection induces expression of DUSP1, which dephosphorylates the p38 kinase and modulates the induction of IL-6 and IL-8 in IBV-infected cells [263]. However, it is unknown whether DUSP1 also regulates activation of the JNK pathway IBV infection. To this end, the coding sequence of DUSP1 was amplified and inserted into the pXJ40-FLAG vector. H1299 cells were transfected with empty vector or FLAG-DUSP1 before infected with IBV or mock infected. As shown in **Figure 4-11a**, expression of FLAG-DUSP1 could be identified by Western blot. The protein level of FLAG-DUSP1 was lower in the IBV-infected cells compared with the mock control, suggesting that IBV infection might modulate expression or stability of DUSP1. Although the protein level of total JNK was comparable, IBV-induced phosphorylation of JNK was found significantly reduced in cells overexpressing FLAG-DUSP1, as compared with the vector control (**Figure 4-11a**). This suggested that the transfected FLAG-DUSP1was functionally active as a phosphatase of JNK in IBV-infected cells. Interestingly, the protein levels of phosphorylated ERK and p38 were only marginally reduced in the DUSP1-transfected cells compared with the control (**Figure 4-11a**). It could be possible that other DUSPs might be responsible for the dephosphorylation of ERK or p38 in IBV-infected cells. Notably, the percentage of PARP cleavage at late stage of IBV infection was found to be slightly reduced in cells overexpressing FLAG-DUSP1 (**Figure 4-11a**). Transfection of DUSP1 did not significantly affect IBV replication, as suggested by the similar level of IBV N protein.

As for the cytokines and IFNβ, overexpression of DUSP1 was found to moderately reduce the mRNA level of IL-8 induced by IBV infection, whereas induction of IL-6 and IFN-β was not significantly affected (**Figure 4-11b**). This result further confirmed that the level of IBV-induced IL-8 was tightly associated with the phosphorylation status of JNK in the infected cells. Taken together, overexpression of DUSP1 suppressed JNK phosphorylation in IBV-infected H1299 cells, which was associated with a reduced apoptosis induction and IL-8 mRNA expression.

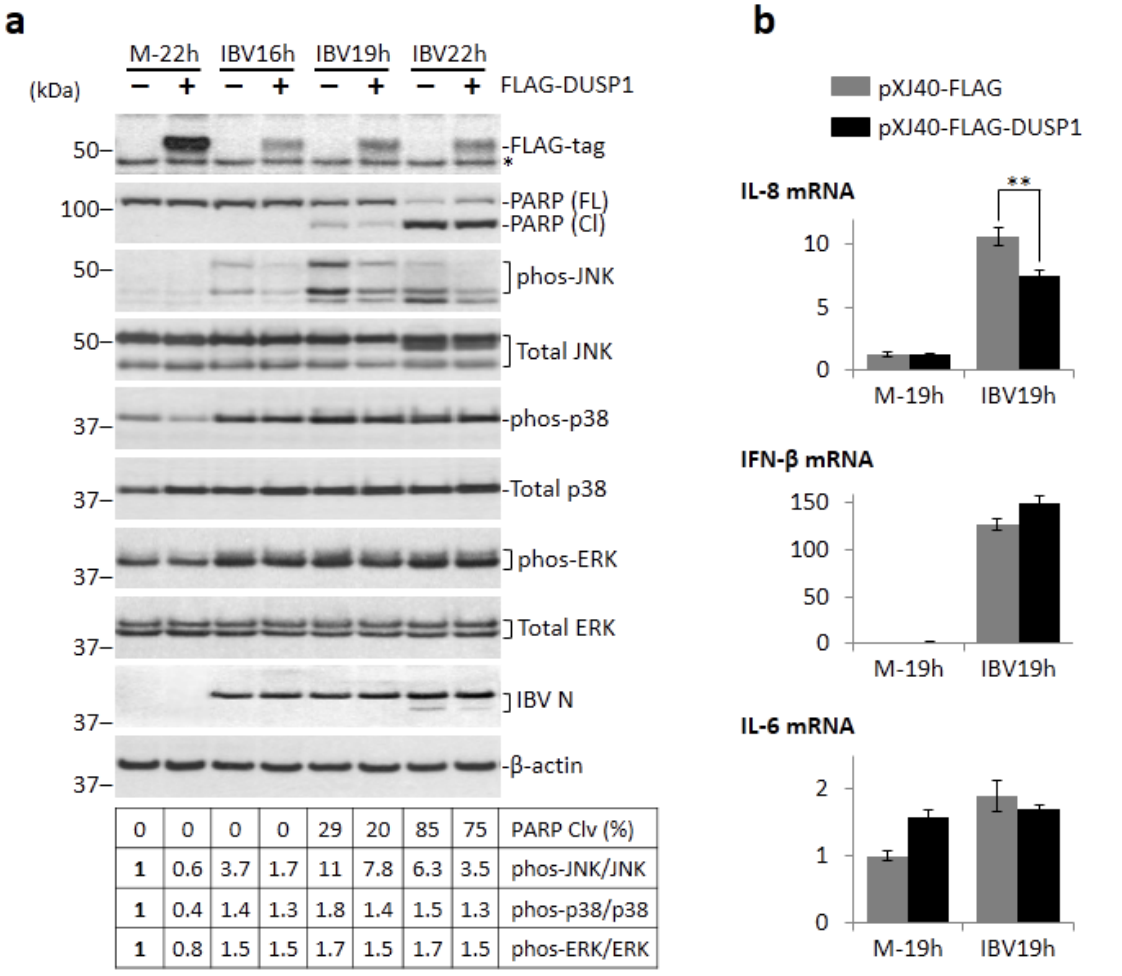

0	0	0	0	29	20	85	75	PARP Clv (%)
1	0.6	3.7	1.7	11	7.8	6.3	3.5	phos-JNK/JNK
1	0.4	1.4	1.3	1.8	1.4	1.5	1.3	phos-p38/p38
1	0.8	1.5	1.5	1.7	1.5	1.7	1.5	phos-ERK/ERK

Figure 4-11 Overexpression of DUSP1 reduced JNK phosphorylation, apoptosis induction and IL-8 mRNA expression in IBV-infected H1299 cells

(a) H1299 cells in duplicate were transfected with pXJ40-FLAG or pXJ40-FLAG-DUSP1 before infected with IBV or mock infected. Cells were harvested at indicated time points and subjected to Western blot analysis using the indicated antibodies. Beta-tubulin was included as loading control. Sizes of protein ladders in kDa were indicated on the left. Asterisk indicates a non-specific band detected by the anti-FLAG antibody. Degree of phosphorylation and percentage of PARP cleavage was determined as in Figure 4-1a.

(b) A second set of cells in (a) were harvested for total RNA and subjected to RT-qPCR as in Figure 3-18a. Fold induction of genes were calculated using GAPDH as internal references and normalized to the pXJ40-FLAG transfected mock-infected samples. Asterisk indicates significant differences between two samples (**, $P<0.01$).

4.3 DISCUSSION

4.3.1. Activation of the JNK pathway during IBV infection

Previous studies on coronavirus-induced JNK activation have been focused on individual viral proteins. Viral proteins were either transiently transfected using the cationic-liposome method [128,292,296] or the lentivirus vectors [293]. In both cases, the expression level of these proteins would be different from that in an actual infection. Moreover, physical and/or functional interactions between multiple viral proteins could not be recreated using the overly simplified overexpression approach. In two studies, phosphorylation of JNK was clearly detected in cells infected with MHV [262] and SARS-CoV [291]. Because phosphorylated JNK was not detected (or only at basal level) in the mock infected cells or in cells incubated with UV-inactivated virus, it was concluded that coronavirus replication induced JNK phosphorylation. However, activation of the downstream substrates of JNK (such as c-Jun) was not determined. Thus it was unknown whether the phosphorylated JNK was functionally active. Therefore, molecular mechanisms of the complete JNK signaling pathway during coronavirus infections remained largely unexplored.

In this study, we used the gammacoronavirus IBV as a model and characterized the phosphorylation status of JNK, its upstream MKKs (MKK4 and MKK7) and its downstream substrate c-Jun during a time course infection. It was found that IBV induced significant phosphorylation of MKK7, JNK and c-Jun starting from 12 hpi in the infected cells. Notably, phosphorylation of MKK4 was only apparent at the very late time point of infection (24 hpi). Moreover, transfection of MKK7 but not MKK4 promoted the phosphorylation of JNK and c-Jun in the IBV-infected cells. Therefore, based on the activation kinetics and overexpression data, it is more likely that IBV-induced activation of JNK is mediated by MKK7, but not MKK4.

We then continued to use a series of mutant constructs to determine which functional domain(s) is required for MKK7 to mediate JNK phosphorylation in the IBV-infected cells. Using the FLAG-tag and total MKK7 antibody, it is found that ectopic wild type MKK7 as well as the K149M, STS-3E and STS-3A mutants were expressed to a similar level in the transfected cells. Interestingly, when phosphor-specific MKK7 antibody was used to probe for the same membrane, similar band intensities were determined for all transfected samples including the vector control. This data suggested that the phosphor-specific MKK7 antibody could only detect

the endogenous level of phosphor-MKK7 but not the ectopic expressed FLAG-tag proteins, although the reason remained unknown. Also, ectopic expression of either wild type or mutated forms of MKK7 appeared to have minimal effect on IBV-induced phosphorylation of the endogenous MKK7, as detected by Western blot. Nonetheless, the JNK activation data strongly supported that the overexpressed wild type and STS-3E mutants were functionally active, as significantly higher levels of IBV-induced JNK phosphorylation were detected compared with the vector control in both H1299 and Huh-7 cells. Moreover, overexpression of the K149M mutant reduced IBV-induced JNK activation in H1299 cells, suggesting that the dominant negative mutant might compete with the endogenous MKK7 for the substrate. As for the STS-3A mutant, it slightly enhanced IBV-induced JNK activation compared with the vector control, but the catalytic activity was significantly lower compared with wild type MKK7 and the STS-3E mutant. This suggested that both the ATP binding activity and the phosphorylation sites of MKK7 were required for optimal activation of JNK during IBV infection.

Nonetheless, further experiments are needed to validate the results. First of all, other detection techniques should be used to study JNK activation during IBV infection. In this thesis, phosphorylation levels of JNK and other relevant proteins were determined by Western blot to serve as the marker of pathway activation. Although highly sensitive, false positive/negative result might sometimes arise depending on the quality and specificity of the antibodies. For examples, the phospho-MKK7 antibody was unable to detect ectopic FLAG-tag wild type proteins as mentioned above. Likewise, the phosphor-JNK antibody only detects the dual phosphorylated (Thr183/Tyr185) protein and the phosphor-c-Jun antibody only detects the c-Jun protein phosphorylated at Ser63 but not on the other sites. Although these questions could be addressed using other specific antibodies, alternative approaches might also be adopted. For instance, *in vitro* kinase activity assays could be performed on cell lysates harvested at different time points to obtain direct activity read-out on the individual kinase in the JNK pathway. Also, systems such as the AP-1 promoter luciferase reporter could be used to determine the transcription activity of c-Jun and other substrates of the JNK pathway. Secondly, loss-of-function experiments using specific inhibitors and/or gene knockdown/knockout should be performed to confirm the involvement of individual players in the JNK pathway. Importantly, the ultimate upstream kinase(s) responsible for the initial trigger of the JNK pathway upon IBV infection remained to be identified in the future.

4.3.2. Inhibition of IBV replication by JNK inhibitor SP600125

The JNK inhibitor SP600125 has been used in several studies on coronavirus-induced JNK activation. In general, a concentration from 10μM to 40 μM was used to inhibit JNK phosphorylation [291,292,296,327]. However, as shown by result from this study, treatment of SP600125 at concentrations higher than 10μM inhibited IBV replication in a dosage dependent manner. Since JNK phosphorylation was induced by coronavirus replication, interpreting the specific effect of JNK inhibition would be impossible if virus replication *per se* was affected. Therefore, the result from inhibitor studies needs to be supplemented with further experiments using other loss-of-function approaches, such as more specific inhibitors or RNAi.

In fact, the compound SP600125 has also been shown to inhibit replication of other viruses. In one study, treatment of SP600125 inhibited the morphogenesis of poxviruses in multiple cell lines [366]. The inhibition was independent of JNK, because similar antiviral effect was not observed in JNK1/2 knockout cells infected with poxviruses [366]. SP600125 also inhibited the infectivity of vesicular stomatitis virus (VSV) [367]. Although transcription and translation of viral proteins were not affected, SP600125 was shown to induce a post-translational modification in the VSV glycoprotein and decrease its fusion activity [367]. In contrast, treatment of SP600125 and another JNK inhibitor AS601245 has been shown to enhance the HCV genome replication but inhibit viral entry [368]. Further experiments identified a host factor called MAP kinase interacting serine/threonine kinase 1 (MKNK1), which was involved in HCV entry and non-specifically inhibited by SP600125 [368]. As for coronavirus, the mechanism behind the antiviral activity of SP600125 remains to be investigated in the future.

4.3.3. Involvement of the JNK pathway in IBV-induced apoptosis

There have been limited studies on the involvement of JNK in coronavirus-induced apoptosis. In one study, inhibition of JNK by SP600125 was found to suppress caspase-dependent apoptosis induced by overexpression of the SARS-CoV ORF6 protein [153]. As presented in the previous chapter, hyper-phosphorylation of JNK associated with the enhanced apoptosis observed in the IRE1-knockdown cells infected with IBV. To investigate the role of JNK in IBV-induced apoptosis, both gain-of-function and loss-of-function approaches were adopted. Overexpression of the upstream kinase MKK7 or the constitutively active form of JNK

both promoted PARP cleavage in IBV-infected cells, as compared with the respective controls. On the other hand, inhibition of JNK phosphorylation, knockdown of JNK by siRNA, and overexpression of the negative regulator DUSP1 all suppressed IBV-induced apoptosis. Therefore, JNK behaved as a pro-apoptotic protein during IBV infection.

Interestingly, when the JNK substrate c-Jun was knockdown, IBV-induced PARP cleavage was enhanced. This suggested that unlike JNK, c-Jun served as a survival factor in IBV-infected cells. Indeed, previous studies have shown that the pro-apoptotic activities of JNK could be mediated independent of c-Jun under certain stimuli [303]. For example, both vinblastine and taxol are microtubule inhibitors that induce JNK-dependent apoptosis with similar kinetics. Although both chemicals induced c-Jun expression, phosphorylation of c-Jun could be observed only in cells treated with vinblastine but not taxol [304]. Moreover, apoptosis induced by DNA damage has been shown to be mediated by JNK-dependent phosphorylation of the transcription factor p53 or p73 [305,306]. Thus, apoptosis induced by IBV infection might also involve uncharacterized mechanisms independent of c-Jun.

JNK has been shown to translocate to the mitochondria and modify multiple Bcl2 family proteins, such as BAD, Bid, Bim and Bcl2 [297]. In this study, the BAK1 protein was found slightly down-regulated whereas the Bcl2 protein was up-regulated in JNK-knockdown cells infected with IBV. Previously data from this group has demonstrated that IBV infection induces the expression of BAK1 at both mRNA and protein levels [236]. Moreover, knockdown of BAK1 reduced the PARP cleavage and DNA fragmentation in IBV-infected cells, suggesting a pro-apoptotic role of the protein during coronavirus infections [236]. On the other hand, it has been demonstrated that overexpression of Bcl2 protects cells from apoptosis induced by SARS-CoV [125]. Similar anti-apoptotic activity of Bcl2 was also revealed by the overexpression experiments in this study, although the putative JNK phosphorylation site at serine 70 was found to be irrelevant. To conclude, the pro-apoptotic function of JNK during IBV infection might be mediated by modulating the Bcl2 family proteins. For example, JNK might induce the transcription and/or translation of these proteins, or affect their activity or stability by protein interactions or phosphorylation. Further experiments are required to uncover these mechanisms.

Notably, previous studies have shown that the JNK signaling pathway is necessary for the maintenance of cells persistently infected with SARS-CoV [294,295]. Establishment of persistent SARS-CoV infection was observed in cells after the apoptotic events. It is possible that JNK serves as a pro-apoptotic protein at the acute phase of SARS-CoV infection, but shifts to become a pro-survival factor in cells persistently infected with SARS-CoV.

4.3.4. The role of JNK in innate immune response during IBV infection

Several studies have focused on the implication of MAP kinases in the innate immune response during coronavirus infections, specifically production of pro-inflammatory cytokines. Activation of p38 has been shown to be important for the production of IL-6 in MHV-infected cells [262], TNF-α and IL-1β in FIPV-infected cells [369], as well as IL-6 and IL-8 in IBV-infected cells [263]. On the other hand, activation of ERK has been found to be required for the phosphorylation of Runt related transcription factor, isoform b (RunX1b), a transcription factor that regulated induction of cytokines (such as IL-2) and chemokines (such as MIP-1α) during SARS-CoV infection [370]. Finally, activation of JNK has been demonstrated to mediate induction of TNF-α and IL-6 in MHV-infected cells [327] and expression of IL-8 in cells overexpressing the SARS-CoV S protein [326]. Moreover, it has also been shown that ERK and p38 participate in the pathogenesis of murine viral fulminant hepatitis by up-regulating the synthesis of hepatic fibrinogen-like protein 2 [371]. However, majority of these studies have relied on the use of inhibitors and the detailed mechanisms were not fully investigated.

In this study, we look at the involvement of JNK pathway in the production of IL-6, IL-8 and IFN-β during IBV infection. It was found that mRNA level of IL-8 (but not IL-6 or IFNβ) was highly correlated with the phosphorylation status of JNK in IBV-infected cells. The result was consistent with the experiments presented in the previous chapter, where knockdown of JNK was shown to reduce the IBV-induced expression of IL-8. The most simplified explanation would be JNK-mediated activation of c-Jun, which forms the AP-1 complex that directly binds to the IL-8 promoter and activates gene transcription. However, as demonstrated by the opposing function of JNK and c-Jun in IBV-induced apoptosis, the JNK-dependent induction of IL-8 might also involve uncharacterized mechanisms independent of c-Jun. Moreover, it would be interesting to investigate potential cross-talks between the ER stress and JNK signaling pathway in regulating cytokine production during infection with IBV and other coronaviruses.

Chapter Five:

Conclusions and future directions

The work presented in this dissertation focuses on the molecular characterization of cellular stress response during coronavirus infections, using the gammacoronavirus IBV as a model. This chapter lists the main conclusions from the work done so far and suggests the future experiments for further investigation.

5.1 INDUCTION OF UPR DURING IBV INFECTION AND ITS INVOLVEMENT IN IBV-INDUCED APOPTOSIS AND INNATE IMMUNE RESPONSE

5.1.1 Main conclusions

Main conclusions from experiments presented in Chapter 3 are listed as follows:

- Both the IRE1-XBP1 pathway and the PERK/PKR-eIF2α-ATF4-CHOP pathway are activated during IBV infection.
- IRE1 protects IBV-infected cells from apoptosis by mediating the splicing of XBP1 mRNA, converting it from pro-apoptotic XBP1u to anti-apoptotic XBP1s.
- IRE1 also exerts the anti-apoptotic function by modulating the phosphorylation status of the pro-apoptotic kinase JNK and the pro-survival kinase Akt.
- Both PERK and PKR contribute to the IBV-induced up-regulation of CHOP, which promotes apoptosis by suppressing the anti-apoptotic MAP kinase ERK.
- IBV infection induces complete autophagy, which is ATG5-dependent and BECN1-independent; IRE1 is also involved in IBV-induced autophagy induction.
- Induction of IL-8 in IBV-infected cells requires the AP-1 and NF-κB binding sites in the promoter sequence and involves the transcription activation by XBP1s.

5.1.2 Unanswered questions and future directions

The activation of IRE1 and PERK branches of UPR during IBV infection and their involvement in IBV-induced apoptosis has been experimentally validated in this study. However, some questions remain unsettled, as presented below together with proposed future work:

- The viral signals of IBV-induced ER stress have not been fully elucidated. Results from this and previous studies have attributed the ER stress to the coronavirus S proteins. However, the domains or regions in the S protein responsible have not been identified.

Moreover, the involvement of alternative mechanisms (such as membrane rearrangement and lipid depletion) should be examined in greater detail.

- Activation of the third branch of UPR, namely the ATF6 signaling pathway, was not investigated in this study. Under ER stress, the cytosolic domain of ATF6 releases from the ER and translocates into the nucleus, activating multiple ER protein chaperones and ERAD components to restore ER homeostasis. Induction of ATF6 during IBV infection should be determined at both mRNA and protein levels. Activation of ATF6 could also be identified by the proteolytic cleavage of the protein using Western blot and the increase in transcription activity using ERSE containing luciferase reporters. Also, the functional implications of this UPR branch in coronavirus replication and regulation of host responses remain to be characterized.
- Activation of the three branches of UPR during coronavirus infections is tightly regulated and closely related. For example, eIF2α phosphorylation mediated by PERK/PKR is inactivated at the early stage of infection, whereas significant IRE1-mediated XBP1 mRNA splicing occurs only at a later stage of infection. The mechanism behind the temporal control and potential cross-talks will require further studies.
- The mechanism of IBV-induced autophagy has not been fully investigated. Although IRE1 was shown to participate in autophagy induction during IBV infection, the downstream signaling event was not determined. Overexpression experiments using XBP1 and its mutants should be performed. The recently identified autophagy-independent function of LC3-I in coronavirus-induced DMV formation should also be examined in cells infected with IBV [146]. Also, the relationship between coronavirus-induced ER stress, autophagy and innate immunity should be examined in detail.
- Involvement of XBP1s in the induction of IL-8 during IBV infection has only been determined at the mRNA level. The protein expression of IL-8 should be determined by Western blot and the amount of secreted IL-8 in the supernatant should be determined by immunoassays such as ELISA. Moreover, mechanisms whereby XBP1s enhances IL-8 expression need to be characterized in molecular detail.

5.2 ACTIVATION OF JNK PATHWAY DURING IBV INFECTION AND ITS INVOLVEMENT IN IBV-INDUCED APOPTOSIS AND INNATE IMMUNE RESPONSE

5.2.1 Main conclusions

Main conclusions from experiments presented in Chapter 4 are listed as follows:

- IBV infection activates the MKK7/JNK/c-Jun signaling pathway.
- MKK7 but not MKK4, is responsible for the JNK phosphorylation in IBV-infected cells. The kinase activity of MKK7 is required for activation of JNK.
- JNK activation promotes induction of apoptosis during IBV infection. This pro-apoptotic activity is not mediated by c-Jun, but may involve the modulation of Bcl2 family proteins such as Bcl2 and BAK1.
- Activation of JNK also contributes to the production of pro-inflammatory cytokine IL-8 in IBV-infected cells at the mRNA level.

5.2.2 Unanswered questions and future directions

In this study, activation of JNK and the upstream MKK7 was investigated in two mammalian cell lines infected with IBV. However, only preliminary experiments have been perform to determine its involvement in IBV-induced apoptosis and innate immune response. Future experiments are proposed as below to answer these questions:

- The viral signals of IBV-induced JNK phosphorylation have not been identified. Transient transfection of individual structural and non-structural proteins of IBV could be performed to determine which protein(s) activate JNK. Once identified, mutants could be generated to identify the regions or positions responsible for JNK activation. Moreover, recombinant IBV could be generated to incorporate the mutations, and the effect on IBV replication and host response would be determined. Nonetheless, the JNK pathway may be activated by a specific stage of the IBV infection process but not necessarily one or more of the viral protein(s).
- Loss-of-function approach should be adopted to validate the involvement of MKK7 in IBV-induced JNK phosphorylation. MKK7-knockdown cells or cell lines with

endogenous MKK7 gene deleted/mutated could be used. When these cells are transfected with wild type or the various MKK7 mutants, the result would be easier to interpret due to a reduced level of the endogenous protein.

- The upstream MKKKs responsible for IBV-induced MKK7 phosphorylation have not been identified. Specific siRNAs that target the fourteen known MKKKs could be designed and transfected into cells before IBV infection. The phosphorylation of MKK7 could be determined and compared with the siEGFP control. Once identified, the MKKK(s) could be amplified and cloned into mammalian expression vector and validated by overexpression experiments. Further studies would focus on the molecular mechanisms on how IBV infection activates the identified MKKK(s).
- How JNK regulates the level of Bcl2 family proteins during IBV infection is unknown. In this study, we have shown that phosphorylation of Bcl2 at serine 70 is not catalyzed by JNK and has no significant effect on its anti-apoptotic activity. Therefore, modulation of Bcl2 and other Bcl2 family proteins by activated JNK should be mediated by other uncharacterized mechanisms. The induction of Bcl2 family proteins at both mRNA and protein levels, as well as their sub-cellular localization, stability and activities, should be determined in JNK-knockdown cells or cells with constitutively active JNK.
- How JNK specifically enhances the induction of IL-8 in IBV-infected cells remains unknown. All cytokines examined in this study (IL-6, IL-8 and IFNβ) contain the AP-1 binding site in their promoters. Yet only the expression of IL-8 was found closely regulated by JNK activation. This suggested that additional regulatory mechanisms might be involved. Moreover, the potential cross-talks between UPR-induced and JNK-induced IL-8 expression also needs to be further examined. Finally, the mechanism by which MKK4 overexpression enhances IBV-induced IFN-β expression should be examined.
- The regulation of JNK and other MAP kinases by DUSP1 and other DUSPs during IBV infection is still not completely characterized. Further functional studies using the knockdown approach or specific inhibitors should be done. Importantly, the implication of DUSPs in the regulation of IBV-induced pro-inflammatory response and innate immunity should be further addressed.

5.3 FINAL REMARKS

Both the UPR and the JNK signaling pathway are evolutionarily conserved stress response pathways activated during coronavirus infections. Stress response pathways have been demonstrated to crosstalk with major cellular signaling pathways and constitute a major aspect of coronavirus-host interaction. On one hand, coronavirus-induced stress response can activate or promote host antiviral mechanisms, thus limiting the spread of the virus. On the other hand, certain stress response pathways may be adopted by the virus to facilitate replication and pathogenesis, whereas aberrant signaling can also contribute to detrimental inflammatory response and immunopathologies. Therefore, it is hoped that the findings reported in this dissertation may inspire future investigation on coronavirus-induced stress response, thereby facilitating the discovery of new antiviral agents and development of better and safer vaccines against coronavirus infections.

Reference

1. Hamre D, Procknow JJ (1966) A new virus isolated from the human respiratory tract. Experimental Biology and Medicine 121: 190-193.
2. Kaye HS, Ong SB, Dowdle WR (1972) Detection of coronavirus 229E antibody by indirect hemagglutination. Applied microbiology 24: 703-707.
3. van der Hoek L (2006) Human coronaviruses: what do they cause? Antiviral therapy 12: 651-658.
4. Peiris J, Guan Y, Yuen K (2004) Severe acute respiratory syndrome. Nature medicine 10: S88-S97.
5. Ksiazek TG, Erdman D, Goldsmith CS, Zaki SR, Peret T, et al. (2003) A novel coronavirus associated with severe acute respiratory syndrome. The New England journal of medicine 348: 1953-1966.
6. Peiris J, Lai S, Poon L, Guan Y, Yam L, et al. (2003) Coronavirus as a possible cause of severe acute respiratory syndrome. The Lancet 361: 1319-1325.
7. Gu J, Gong E, Zhang B, Zheng J, Gao Z, et al. (2005) Multiple organ infection and the pathogenesis of SARS. The Journal of experimental medicine 202: 415-424.
8. Li W, Shi Z, Yu M, Ren W, Smith C, et al. (2005) Bats are natural reservoirs of SARS-like coronaviruses. Science 310: 676-679.
9. Wang L, Eaton B (2007) Bats, civets and the emergence of SARS. Wildlife and Emerging Zoonotic Diseases: the Biology, Circumstances and Consequences of Cross-Species Transmission: 325-344.
10. Ge XY, Li JL, Yang XL, Chmura AA, Zhu G, et al. (2013) Isolation and characterization of a bat SARS-like coronavirus that uses the ACE2 receptor. Nature 503: 535-538.
11. de Groot RJ, Baker SC, Baric RS, Brown CS, Drosten C, et al. (2013) Middle East respiratory syndrome coronavirus (MERS-CoV): announcement of the Coronavirus Study Group. Journal of virology 87: 7790-7792.
12. Graham RL, Donaldson EF, Baric RS (2013) A decade after SARS: strategies for controlling emerging coronaviruses. Nature Reviews Microbiology 11: 836-848.
13. Alagaili AN, Briese T, Mishra N, Kapoor V, Sameroff SC, et al. (2014) Middle East respiratory syndrome coronavirus infection in dromedary camels in Saudi Arabia. MBio 5: e00884-00814.
14. Baker DG (1998) Natural pathogens of laboratory mice, rats, and rabbits and their effects on research. Clinical microbiology reviews 11: 231-266.
15. Bender SJ, Weiss SR (2010) Pathogenesis of murine coronavirus in the central nervous system. Journal of Neuroimmune Pharmacology 5: 336-354.
16. Clark M (1993) Bovine coronavirus. British Veterinary Journal 149: 51-70.
17. Laude H, Van Reeth K, Pensaert M (1993) Porcine respiratory coronavirus: molecular features and virus-host interactions. Veterinary research 24: 125-150.
18. Song D, Park B (2012) Porcine epidemic diarrhoea virus: a comprehensive review of molecular epidemiology, diagnosis, and vaccines. Virus genes 44: 167-175.
19. Cavanagh D (2007) Coronavirus avian infectious bronchitis virus. Veterinary research 38: 281-297.
20. Masters PS (2006) The molecular biology of coronaviruses. Advances in virus research 66: 193-292.
21. Gorbalenya AE, Snijder EJ, Spaan WJ (2004) Severe acute respiratory syndrome coronavirus phylogeny: toward consensus. Journal of virology 78: 7863-7866.
22. Woo PC, Lau SK, Lam CS, Lau CC, Tsang AK, et al. (2012) Discovery of seven novel mammalian and avian coronaviruses in Deltacoronavirus supports bat coronaviruses as the gene source of Alphacoronavirus and Betacoronavirus and avian coronaviruses as the gene source of Gammacoronavirus and Deltacoronavirus. Journal of virology: JVI. 06540-06511.
23. Sugiyama K, Amano Y (1981) Morphological and biological properties of a new coronavirus associated with diarrhea in infant mice. Archives of virology 67: 241-251.

24. de Groot RJ (2006) Structure, function and evolution of the hemagglutinin-esterase proteins of corona-and toroviruses. Glycoconjugate journal 23: 59-72.
25. Lai MM (1990) Corona virus: organization, replication and expression of genome. Annual Reviews in Microbiology 44: 303-303.
26. de Haan CA, Volders H, Koetzner CA, Masters PS, Rottier PJ (2002) Coronaviruses maintain viability despite dramatic rearrangements of the strictly conserved genome organization. Journal of virology 76: 12491-12502.
27. Bosch B, Rottier P (2008) Nidovirus entry into cells. Nidoviruses ASM Press, Washington, DC: 157-178.
28. Cavanagh D, Davis PJ, Pappin DJ, Binns MM, Boursnell ME, et al. (1986) Coronavirus IBV: partial amino terminal sequencing of spike polypeptide S2 identifies the sequence Arg-Arg-Phe-Arg-Arg at the cleavage site of the spike precursor propolypeptide of IBV strains Beaudette and M41. Virus research 4: 133-143.
29. de Haan CA, Stadler K, Godeke G-J, Bosch BJ, Rottier PJ (2004) Cleavage inhibition of the murine coronavirus spike protein by a furin-like enzyme affects cell-cell but not virus-cell fusion. Journal of virology 78: 6048-6054.
30. Matsuyama S, Ujike M, Morikawa S, Tashiro M, Taguchi F (2005) Protease-mediated enhancement of severe acute respiratory syndrome coronavirus infection. Proceedings of the National Academy of Sciences of the United States of America 102: 12543-12547.
31. Wong SK, Li W, Moore MJ, Choe H, Farzan M (2004) A 193-amino acid fragment of the SARS coronavirus S protein efficiently binds angiotensin-converting enzyme 2. The Journal of biological chemistry 279: 3197-3201.
32. Kubo H, Yamada YK, Taguchi F (1994) Localization of neutralizing epitopes and the receptor-binding site within the amino-terminal 330 amino acids of the murine coronavirus spike protein. Journal of virology 68: 5403-5410.
33. Godet M, Grosclaude J, Delmas B, Laude H (1994) Major receptor-binding and neutralization determinants are located within the same domain of the transmissible gastroenteritis virus (coronavirus) spike protein. Journal of virology 68: 8008-8016.
34. Schwegmann-Wessels C, Al-Falah M, Escors D, Wang Z, Zimmer G, et al. (2004) A novel sorting signal for intracellular localization is present in the S protein of a porcine coronavirus but absent from severe acute respiratory syndrome-associated coronavirus. Journal of Biological Chemistry 279: 43661-43666.
35. Winter C, Schwegmann-Wessels C, Neumann U, Herrler G (2008) The spike protein of infectious bronchitis virus is retained intracellularly by a tyrosine motif. Journal of virology 82: 2765-2771.
36. Opstelten D, de Groote P, Horzinek MC, Vennema H, Rottier P (1993) Disulfide bonds in folding and transport of mouse hepatitis coronavirus glycoproteins. Journal of virology 67: 7394-7401.
37. Yamada Y, Liu XB, Fang SG, Tay FPL, Liu DX (2009) Acquisition of Cell–Cell Fusion Activity by Amino Acid Substitutions in Spike Protein Determines the Infectivity of a Coronavirus in Cultured Cells. PloS one 4: e6130.
38. Jacobs L, van der Zeijst B, Horzinek M (1986) Characterization and translation of transmissible gastroenteritis virus mRNAs. Journal of virology 57: 1010-1015.
39. Cavanagh D, Davis PJ (1988) Evolution of avian coronavirus IBV: sequence of the matrix glycoprotein gene and intergenic region of several serotypes. The Journal of general virology 69: 621-629.
40. Nal B, Chan C, Kien F, Siu L, Tse J, et al. (2005) Differential maturation and subcellular localization of severe acute respiratory syndrome coronavirus surface proteins S, M and E. Journal of general virology 86: 1423-1434.
41. De Haan CA, Vennema H, Rottier PJ (2000) Assembly of the coronavirus envelope: homotypic interactions between the M proteins. Journal of virology 74: 4967-4978.

42. Hogue B, Machamer C (2008) Coronavirus structural proteins and virus assembly. Nidoviruses ASM Press, Washington, DC: 179-200.
43. Wang J, Fang S, Xiao H, Chen B, Tam JP, et al. (2009) Interaction of the coronavirus infectious bronchitis virus membrane protein with β-actin and its implication in virion assembly and budding. PloS one 4: e4908.
44. Siu K-L, Kok K-H, Ng M-HJ, Poon VK, Yuen K-Y, et al. (2009) Severe acute respiratory syndrome coronavirus M protein inhibits type I interferon production by impeding the formation of TRAF3· TANK· TBK1/IKKε complex. Journal of Biological Chemistry 284: 16202-16209.
45. Liu DX, Inglis SC (1991) Association of the infectious bronchitis virus 3c protein with the virion envelope. Virology 185: 911-917.
46. Maeda J, Repass JF, Maeda A, Makino S (2001) Membrane topology of coronavirus E protein. Virology 281: 163-169.
47. Corse E, Machamer CE (2002) The cytoplasmic tail of infectious bronchitis virus E protein directs Golgi targeting. Journal of virology 76: 1273-1284.
48. Liao Y, Yuan Q, Torres J, Tam J, Liu D (2006) Biochemical and functional characterization of the membrane association and membrane permeabilizing activity of the severe acute respiratory syndrome coronavirus envelope protein. Virology 349: 264-275.
49. Lim K, Liu D (2001) The Missing Link in Coronavirus Assembly RETENTION OF THE AVIAN CORONAVIRUS INFECTIOUS BRONCHITIS VIRUS ENVELOPE PROTEIN IN THE PRE-GOLGI COMPARTMENTS AND PHYSICAL INTERACTION BETWEEN THE ENVELOPE AND MEMBRANE PROTEINS. Journal of Biological Chemistry 276: 17515-17523.
50. Vennema H, Godeke GJ, Rossen JW, Voorhout WF, Horzinek MC, et al. (1996) Nucleocapsid-independent assembly of coronavirus-like particles by co-expression of viral envelope protein genes. The EMBO journal 15: 2020-2028.
51. Bos EC, Luytjes W, van der Meulen HV, Koerten HK, Spaan WJ (1996) The production of recombinant infectious DI-particles of a murine coronavirus in the absence of helper virus. Virology 218: 52-60.
52. DeDiego ML, Álvarez E, Almazán F, Rejas MT, Lamirande E, et al. (2007) A severe acute respiratory syndrome coronavirus that lacks the E gene is attenuated in vitro and in vivo. Journal of virology 81: 1701-1713.
53. Kuo L, Masters PS (2003) The small envelope protein E is not essential for murine coronavirus replication. Journal of virology 77: 4597-4608.
54. Liao Y, Lescar J, Tam J, Liu D (2004) Expression of SARS-coronavirus envelope protein in< i> Escherichia coli</i> cells alters membrane permeability. Biochemical and biophysical research communications 325: 374-380.
55. Madan V, García MdJ, Sanz MA, Carrasco L (2005) Viroporin activity of murine hepatitis virus E protein. FEBS letters 579: 3607-3612.
56. Torres J, Parthasarathy K, Lin X, Saravanan R, Kukol A, et al. (2006) Model of a Putative Pore: The Pentameric< i> α</i>-Helical Bundle of SARS Coronavirus E Protein in Lipid Bilayers. Biophysical journal 91: 938-947.
57. Verdiá-Báguena C, Nieto-Torres JL, Alcaraz A, DeDiego ML, Torres J, et al. (2012) Coronavirus E protein forms ion channels with functionally and structurally-involved membrane lipids. Virology 432: 485-494.
58. Siddell S (1995) The coronaviridae. New York: Plenum Press. xviii, 418 p. p.
59. Hurst KR, Kuo L, Koetzner CA, Ye R, Hsue B, et al. (2005) A major determinant for membrane protein interaction localizes to the carboxy-terminal domain of the mouse coronavirus nucleocapsid protein. Journal of virology 79: 13285-13297.

60. Chen H, Gill A, Dove BK, Emmett SR, Kemp CF, et al. (2005) Mass spectroscopic characterization of the coronavirus infectious bronchitis virus nucleoprotein and elucidation of the role of phosphorylation in RNA binding by using surface plasmon resonance. Journal of virology 79: 1164-1179.
61. Stohlman SA, Baric RS, Nelson GN, Soe LH, Welter LM, et al. (1988) Specific interaction between coronavirus leader RNA and nucleocapsid protein. Journal of virology 62: 4288-4295.
62. Wong J, Zhang J, Si X, Gao G, Mao I, et al. (2008) Autophagosome supports coxsackievirus B3 replication in host cells. Journal of virology 82: 9143-9153.
63. Hogue BG (1995) Bovine coronavirus nucleocapsid protein processing and assembly. Advances in experimental medicine and biology 380: 259-263.
64. Baric R, Nelson G, Fleming J, Deans R, Keck J, et al. (1988) Interactions between coronavirus nucleocapsid protein and viral RNAs: implications for viral transcription. Journal of virology 62: 4280-4287.
65. Tahara SM, Dietlin TA, Bergmann CC, Nelson GW, Kyuwa S, et al. (1994) Coronavirus translational regulation: leader affects mRNA efficiency. Virology 202: 621-630.
66. Zúñiga S, Sola I, Moreno JL, Sabella P, Plana-Durán J, et al. (2007) Coronavirus nucleocapsid protein is an RNA chaperone. Virology 357: 215-227.
67. Brierley I, Boursnell ME, Binns MM, Bilimoria B, Blok VC, et al. (1987) An efficient ribosomal frame-shifting signal in the polymerase-encoding region of the coronavirus IBV. The EMBO journal 6: 3779-3785.
68. Ziebuhr J, Snijder EJ, Gorbalenya AE (2000) Virus-encoded proteinases and proteolytic processing in the Nidovirales. Journal of General Virology 81: 853-879.
69. Angelini MM, Akhlaghpour M, Neuman BW, Buchmeier MJ (2013) Severe Acute Respiratory Syndrome Coronavirus Nonstructural Proteins 3, 4, and 6 Induce Double-Membrane Vesicles. MBio 4: e00524-00513.
70. Xu X, Liu Y, Weiss S, Arnold E, Sarafianos SG, et al. (2003) Molecular model of SARS coronavirus polymerase: implications for biochemical functions and drug design. Nucleic acids research 31: 7117-7130.
71. Imbert I, Guillemot JC, Bourhis JM, Bussetta C, Coutard B, et al. (2006) A second, non-canonical RNA-dependent RNA polymerase in SARS Coronavirus. The EMBO journal 25: 4933-4942.
72. Seybert A, Posthuma CC, van Dinten LC, Snijder EJ, Gorbalenya AE, et al. (2005) A complex zinc finger controls the enzymatic activities of nidovirus helicases. Journal of virology 79: 696-704.
73. Eckerle LD, Lu X, Sperry SM, Choi L, Denison MR (2007) High fidelity of murine hepatitis virus replication is decreased in nsp14 exoribonuclease mutants. Journal of virology 81: 12135-12144.
74. Eckerle LD, Becker MM, Halpin RA, Li K, Venter E, et al. (2010) Infidelity of SARS-CoV Nsp14-exonuclease mutant virus replication is revealed by complete genome sequencing. PLoS pathogens 6: e1000896.
75. Ivanov KA, Hertzig T, Rozanov M, Bayer S, Thiel V, et al. (2004) Major genetic marker of nidoviruses encodes a replicative endoribonuclease. Proceedings of the National Academy of Sciences of the United States of America 101: 12694-12699.
76. Posthuma CC, Nedialkova DD, Zevenhoven-Dobbe JC, Blokhuis JH, Gorbalenya AE, et al. (2006) Site-directed mutagenesis of the nidovirus replicative endoribonuclease NendoU exerts pleiotropic effects on the arterivirus life cycle. Journal of virology 80: 1653-1661.
77. Chen Y, Cai H, Pan Ja, Xiang N, Tien P, et al. (2009) Functional screen reveals SARS coronavirus nonstructural protein nsp14 as a novel cap N7 methyltransferase. Proceedings of the National Academy of Sciences 106: 3484-3489.
78. von Grotthuss M, Wyrwicz LS, Rychlewski L (2003) mRNA cap-1 methyltransferase in the SARS genome. Cell 113: 701-702.

79. Kamitani W, Narayanan K, Huang C, Lokugamage K, Ikegami T, et al. (2006) Severe acute respiratory syndrome coronavirus nsp1 protein suppresses host gene expression by promoting host mRNA degradation. Proceedings of the National Academy of Sciences 103: 12885-12890.
80. Lokugamage KG, Narayanan K, Huang C, Makino S (2012) Severe acute respiratory syndrome coronavirus protein nsp1 is a novel eukaryotic translation inhibitor that represses multiple steps of translation initiation. Journal of virology 86: 13598-13608.
81. Chen C-J, Sugiyama K, Kubo H, Huang C, Makino S (2004) Murine coronavirus nonstructural protein p28 arrests cell cycle in G0/G1 phase. Journal of virology 78: 10410-10419.
82. Wathelet MG, Orr M, Frieman MB, Baric RS (2007) Severe acute respiratory syndrome coronavirus evades antiviral signaling: role of nsp1 and rational design of an attenuated strain. Journal of virology 81: 11620-11633.
83. Graham RL, Sims AC, Baric RS, Denison MR (2006) The nsp2 proteins of mouse hepatitis virus and SARS coronavirus are dispensable for viral replication. The Nidoviruses: Springer. pp. 67-72.
84. Putics Á, Filipowicz W, Hall J, Gorbalenya AE, Ziebuhr J (2005) ADP-ribose-1"-monophosphatase: a conserved coronavirus enzyme that is dispensable for viral replication in tissue culture. Journal of virology 79: 12721-12731.
85. Lindner HA, Fotouhi-Ardakani N, Lytvyn V, Lachance P, Sulea T, et al. (2005) The papain-like protease from the severe acute respiratory syndrome coronavirus is a deubiquitinating enzyme. Journal of virology 79: 15199-15208.
86. Clementz MA, Chen Z, Banach BS, Wang Y, Sun L, et al. (2010) Deubiquitinating and interferon antagonism activities of coronavirus papain-like proteases. Journal of virology 84: 4619-4629.
87. Frieman M, Ratia K, Johnston RE, Mesecar AD, Baric RS (2009) Severe acute respiratory syndrome coronavirus papain-like protease ubiquitin-like domain and catalytic domain regulate antagonism of IRF3 and NF-κB signaling. Journal of virology 83: 6689-6705.
88. Clementz MA, Kanjanahaluethai A, O'Brien TE, Baker SC (2008) Mutation in murine coronavirus replication protein nsp4 alters assembly of double membrane vesicles. Virology 375: 118-129.
89. Cottam EM, Maier HJ, Manifava M, Vaux LC, Chandra-Schoenfelder P, et al. (2011) Coronavirus nsp6 proteins generate autophagosomes from the endoplasmic reticulum via an omegasome intermediate. Autophagy 7: 1335-1347.
90. Zhai Y, Sun F, Li X, Pang H, Xu X, et al. (2005) Insights into SARS-CoV transcription and replication from the structure of the nsp7–nsp8 hexadecamer. Nature structural & molecular biology 12: 980-986.
91. Egloff M-P, Ferron F, Campanacci V, Longhi S, Rancurel C, et al. (2004) The severe acute respiratory syndrome-coronavirus replicative protein nsp9 is a single-stranded RNA-binding subunit unique in the RNA virus world. Proceedings of the National Academy of Sciences of the United States of America 101: 3792-3796.
92. Sutton G, Fry E, Carter L, Sainsbury S, Walter T, et al. (2004) The nsp9 replicase protein of SARS-coronavirus, structure and functional insights. Structure 12: 341-353.
93. Matthes N, Mesters JR, Coutard B, Canard B, Snijder EJ, et al. (2006) The non-structural protein Nsp10 of mouse hepatitis virus binds zinc ions and nucleic acids. FEBS letters 580: 4143-4149.
94. Ivanov KA, Thiel V, Dobbe JC, van der Meer Y, Snijder EJ, et al. (2004) Multiple enzymatic activities associated with severe acute respiratory syndrome coronavirus helicase. Journal of virology 78: 5619-5632.
95. Li W, Zhang C, Sui J, Kuhn JH, Moore MJ, et al. (2005) Receptor and viral determinants of SARS-coronavirus adaptation to human ACE2. The EMBO journal 24: 1634-1643.
96. Kuo L, Godeke GJ, Raamsman MJ, Masters PS, Rottier PJ (2000) Retargeting of coronavirus by substitution of the spike glycoprotein ectodomain: crossing the host cell species barrier. Journal of virology 74: 1393-1406.

97. Li W, Moore MJ, Vasilieva N, Sui J, Wong SK, et al. (2003) Angiotensin-converting enzyme 2 is a functional receptor for the SARS coronavirus. Nature 426: 450-454.
98. Williams RK, Jiang GS, Holmes KV (1991) Receptor for mouse hepatitis virus is a member of the carcinoembryonic antigen family of glycoproteins. Proceedings of the National Academy of Sciences of the United States of America 88: 5533-5536.
99. Raj VS, Mou H, Smits SL, Dekkers DH, Müller MA, et al. (2013) Dipeptidyl peptidase 4 is a functional receptor for the emerging human coronavirus-EMC. Nature 495: 251-254.
100. Winter C, Schwegmann-Weßels C, Cavanagh D, Neumann U, Herrler G (2006) Sialic acid is a receptor determinant for infection of cells by avian Infectious bronchitis virus. Journal of general virology 87: 1209-1216.
101. Mohandas DV, Dales S (1991) Endosomal association of a protein phosphatase with high dephosphorylating activity against a coronavirus nucleocapsid protein. FEBS letters 282: 419-424.
102. Asanaka M, Lai M (1993) Cell fusion studies identified multiple cellular factors involved in mouse hepatitis virus entry. Virology 197: 732-741.
103. Oostra M, Hagemeijer MC, van Gent M, Bekker CP, te Lintelo EG, et al. (2008) Topology and membrane anchoring of the coronavirus replication complex: not all hydrophobic domains of nsp3 and nsp6 are membrane spanning. Journal of virology 82: 12392-12405.
104. Knoops K, Kikkert M, Van Den Worm SHE, Zevenhoven-Dobbe JC, Van Der Meer Y, et al. (2008) SARS-coronavirus replication is supported by a reticulovesicular network of modified endoplasmic reticulum. PLoS biology 6: e226.
105. Maier HJ, Hawes PC, Cottam EM, Mantell J, Verkade P, et al. (2013) Infectious bronchitis virus generates spherules from zippered endoplasmic reticulum membranes. MBio 4: e00801-00813.
106. Sawicki S, Sawicki D (1998) A new model for coronavirus transcription. Advances in experimental medicine and biology 440: 215-220.
107. Sola I, Mateos-Gomez PA, Almazan F, Zuñiga S, Enjuanes L (2011) RNA-RNA and RNA-protein interactions in coronavirus replication and transcription. RNA biology 8: 237-248.
108. Liu D, Inglis S (1992) Internal entry of ribosomes on a tricistronic mRNA encoded by infectious bronchitis virus. Journal of virology 66: 6143-6154.
109. Liu D, Inglis S (1992) Identification of two new polypeptides encoded by mRNA5 of the coronavirus infectious bronchitis virus. Virology 186: 342-347.
110. Klumperman J, Locker JK, Meijer A, Horzinek MC, Geuze HJ, et al. (1994) Coronavirus M proteins accumulate in the Golgi complex beyond the site of virion budding. Journal of virology 68: 6523-6534.
111. Stertz S, Reichelt M, Spiegel M, Kuri T, Martínez-Sobrido L, et al. (2007) The intracellular sites of early replication and budding of SARS-coronavirus. Virology 361: 304-315.
112. Ye R, Montalto-Morrison C, Masters PS (2004) Genetic analysis of determinants for spike glycoprotein assembly into murine coronavirus virions: distinct roles for charge-rich and cysteine-rich regions of the endodomain. Journal of virology 78: 9904-9917.
113. Luo H, Wu D, Shen C, Chen K, Shen X, et al. (2006) Severe acute respiratory syndrome coronavirus membrane protein interacts with nucleocapsid protein mostly through their carboxyl termini by electrostatic attraction. The international journal of biochemistry & cell biology 38: 589-599.
114. Narayanan K, Makino S (2001) Cooperation of an RNA packaging signal and a viral envelope protein in coronavirus RNA packaging. Journal of virology 75: 9059-9067.
115. Taylor RC, Cullen SP, Martin SJ (2008) Apoptosis: controlled demolition at the cellular level. Nature reviews Molecular cell biology 9: 231-241.
116. Nicholson DW (1999) Caspase structure, proteolytic substrates, and function during apoptotic cell death. Cell death and differentiation 6: 1028-1042.

117. Taylor RC, Cullen SP, Martin SJ (2008) Apoptosis: controlled demolition at the cellular level. Nature Reviews Molecular Cell Biology 9: 231-241.
118. Elmore S (2007) Apoptosis: a review of programmed cell death. Toxicologic pathology 35: 495-516.
119. Li H, Zhu H, Xu C, Yuan J (1998) Cleavage of BID by caspase 8 mediates the mitochondrial damage in the Fas pathway of apoptosis. Cell 94: 491-501.
120. Tan YJ, Lim SG, Hong W (2007) Regulation of cell death during infection by the severe acute respiratory syndrome coronavirus and other coronaviruses. Cellular microbiology 9: 2552-2561.
121. Liu C, Xu H, Liu D (2001) Induction of caspase-dependent apoptosis in cultured cells by the avian coronavirus infectious bronchitis virus. Journal of virology 75: 6402-6409.
122. Eleouet JF, Chilmonczyk S, Besnardeau L, Laude H (1998) Transmissible gastroenteritis coronavirus induces programmed cell death in infected cells through a caspase-dependent pathway. Journal of virology 72: 4918-4924.
123. Yan H, Xiao G, Zhang J, Hu Y, Yuan F, et al. (2004) SARS coronavirus induces apoptosis in Vero E6 cells. Journal of medical virology 73: 323-331.
124. Ren L, Yang R, Guo L, Qu J, Wang J, et al. (2005) Apoptosis induced by the SARS-associated coronavirus in Vero cells is replication-dependent and involves caspase. DNA and cell biology 24: 496-502.
125. Bordi L, Castilletti C, Falasca L, Ciccosanti F, Calcaterra S, et al. (2006) Bcl-2 inhibits the caspase-dependent apoptosis induced by SARS-CoV without affecting virus replication kinetics. Archives of virology 151: 369-377.
126. Lu W, Zheng BJ, Xu K, Schwarz W, Du L, et al. (2006) Severe acute respiratory syndrome-associated coronavirus 3a protein forms an ion channel and modulates virus release. Proceedings of the National Academy of Sciences 103: 12540-12545.
127. Wilson L, Mckinlay C, Gage P, Ewart G (2004) SARS coronavirus E protein forms cation-selective ion channels. Virology 330: 322-331.
128. Surjit M, Liu B, Jameel S, Chow VTK, Lal SK (2004) The SARS coronavirus nucleocapsid protein induces actin reorganization and apoptosis in COS-1 cells in the absence of growth factors. Biochemical Journal 383: 13.
129. Yuan X, Shan Y, Zhao Z, Chen J, Cong Y (2005) G0/G1 arrest and apoptosis induced by SARS-CoV 3b protein in transfected cells. Virol J 2: 198-0024.
130. Eleouet JF, Slee EA, Saurini F, Castagne N, Poncet D, et al. (2000) The viral nucleocapsid protein of transmissible gastroenteritis coronavirus (TGEV) is cleaved by caspase-6 and -7 during TGEV-induced apoptosis. Journal of virology 74: 3975-3983.
131. Diemer C, Schneider M, Seebach J, Quaas J, Frösner G, et al. (2008) Cell type-specific cleavage of nucleocapsid protein by effector caspases during SARS coronavirus infection. Journal of molecular biology 376: 23-34.
132. Yang Z, Klionsky DJ (2010) Eaten alive: a history of macroautophagy. Nature cell biology 12: 814-822.
133. Kuma A, Hatano M, Matsui M, Yamamoto A, Nakaya H, et al. (2004) The role of autophagy during the early neonatal starvation period. Nature 432: 1032-1036.
134. Kroemer G, Mariño G, Levine B (2010) Autophagy and the integrated stress response. Molecular cell 40: 280-293.
135. Maiuri MC, Zalckvar E, Kimchi A, Kroemer G (2007) Self-eating and self-killing: crosstalk between autophagy and apoptosis. Nature reviews Molecular cell biology 8: 741-752.
136. Mizushima N, Levine B, Cuervo AM, Klionsky DJ (2008) Autophagy fights disease through cellular self-digestion. Nature 451: 1069-1075.
137. Kim HJ, Lee S, Jung JU (2010) When autophagy meets viruses: a double-edged sword with functions in defense and offense. Seminars in immunopathology 32: 323-341.

138. Hosokawa N, Hara T, Kaizuka T, Kishi C, Takamura A, et al. (2009) Nutrient-dependent mTORC1 association with the ULK1–Atg13–FIP200 complex required for autophagy. Molecular biology of the cell 20: 1981-1991.
139. Levine B, Deretic V (2007) Unveiling the roles of autophagy in innate and adaptive immunity. Nature reviews Immunology 7: 767-777.
140. Klionsky DJ, Abeliovich H, Agostinis P, Agrawal DK, Aliev G, et al. (2008) Guidelines for the use and interpretation of assays for monitoring autophagy in higher eukaryotes. Autophagy 4: 151-175.
141. Mehrpour M, Esclatine A, Beau I, Codogno P (2010) Overview of macroautophagy regulation in mammalian cells. Cell research 20: 748-762.
142. Prentice E, McAuliffe J, Lu X, Subbarao K, Denison MR (2004) Identification and characterization of severe acute respiratory syndrome coronavirus replicase proteins. Journal of virology 78: 9977-9986.
143. Prentice E, Jerome WG, Yoshimori T, Mizushima N, Denison MR (2004) Coronavirus replication complex formation utilizes components of cellular autophagy. The Journal of biological chemistry 279: 10136-10141.
144. Snijder EJ, van der Meer Y, Zevenhoven-Dobbe J, Onderwater JJ, van der Meulen J, et al. (2006) Ultrastructure and origin of membrane vesicles associated with the severe acute respiratory syndrome coronavirus replication complex. Journal of virology 80: 5927-5940.
145. de Haan CAM, Reggiori F (2008) Are nidoviruses hijacking the autophagy machinery? Autophagy 4: 276.
146. Reggiori F, Monastyrska I, Verheije MH, Cali T, Ulasli M, et al. (2010) Coronaviruses Hijack the LC3-I-positive EDEMosomes, ER-derived vesicles exporting short-lived ERAD regulators, for replication. Cell host & microbe 7: 500-508.
147. Zhao Z, Thackray LB, Miller BC, Lynn TM, Becker MM, et al. (2007) Coronavirus replication does not require the autophagy gene ATG5. Autophagy 3: 581-585.
148. Ron D, Walter P (2007) Signal integration in the endoplasmic reticulum unfolded protein response. Nature reviews Molecular cell biology 8: 519-529.
149. Tang BS, Chan K-h, Cheng VC, Woo PC, Lau SK, et al. (2005) Comparative host gene transcription by microarray analysis early after infection of the Huh7 cell line by severe acute respiratory syndrome coronavirus and human coronavirus 229E. Journal of virology 79: 6180-6193.
150. Yeung YS, Yip CW, Hon CC, Chow KYC, Ma I, et al. (2008) Transcriptional profiling of Vero E6 cells over-expressing SARS-CoV S2 subunit: Insights on viral regulation of apoptosis and proliferation. Virology 371: 32-43.
151. Chan CP, Siu KL, Chin KT, Yuen KY, Zheng B, et al. (2006) Modulation of the unfolded protein response by the severe acute respiratory syndrome coronavirus spike protein. Journal of virology 80: 9279-9287.
152. Minakshi R, Padhan K, Rani M, Khan N, Ahmad F, et al. (2009) The SARS Coronavirus 3a protein causes endoplasmic reticulum stress and induces ligand-independent downregulation of the type 1 interferon receptor. PloS one 4: e8342.
153. Ye Z, Wong CK, Li P, Xie Y (2008) A SARS-CoV protein, ORF-6, induces caspase-3 mediated, ER stress and JNK-dependent apoptosis. Biochimica et biophysica acta 1780: 1383-1387.
154. Sung SC, Chao CY, Jeng KS, Yang JY, Lai M (2009) The 8ab protein of SARS-CoV is a luminal ER membrane-associated protein and induces the activation of ATF6. Virology 387: 402-413.
155. Versteeg GA, Van De Nes PS, Bredenbeek PJ, Spaan WJM (2007) The coronavirus spike protein induces endoplasmic reticulum stress and upregulation of intracellular chemokine mRNA concentrations. Journal of virology 81: 10981-10990.

156. Liao Y, Fung TS, Huang M, Fang SG, Zhong Y, et al. (2013) Up-regulation of CHOP/GADD153 during Coronavirus Infectious Bronchitis Virus Infection Modulates Apoptosis by Restricting Activation of the Extracellular Signal-Regulated Kinase Pathway. Journal of virology 87: 8124-8134.
157. Fung TS, Liu DX (2014) Coronavirus infection, ER stress, apoptosis and innate immunity. Frontiers in Microbiology 5: 1-13.
158. Delmas B, Laude H (1990) Assembly of coronavirus spike protein into trimers and its role in epitope expression. Journal of virology 64: 5367-5375.
159. Fukushi M, Yoshinaka Y, Matsuoka Y, Hatakeyama S, Ishizaka Y, et al. (2012) Monitoring S protein maturation in the endoplasmic reticulum by calnexin is important for the infectivity of severe acute respiratory syndrome-coronavirus. Journal of virology 86: 11745-11753.
160. Favreau DJ, Desforges M, St-Jean JR, Talbot PJ (2009) A human coronavirus OC43 variant harboring persistence-associated mutations in the S glycoprotein differentially induces the unfolded protein response in human neurons as compared to wild-type virus. Virology 395: 255-267.
161. Miller S, Krijnse-Locker J (2008) Modification of intracellular membrane structures for virus replication. Nature Reviews Microbiology 6: 363-374.
162. David-Ferreira J, Manaker R (1965) An electron microscope study of the development of a mouse hepatitis virus in tissue culture cells. The Journal of cell biology 24: 57-78.
163. Gosert R, Kanjanahaluethai A, Egger D, Bienz K, Baker SC (2002) RNA replication of mouse hepatitis virus takes place at double-membrane vesicles. Journal of virology 76: 3697-3708.
164. Testerink N, van der Sanden MH, Houweling M, Helms JB, Vaandrager AB (2009) Depletion of phosphatidylcholine affects endoplasmic reticulum morphology and protein traffic at the Golgi complex. Journal of lipid research 50: 2182-2192.
165. van der SANDEN M, Houweling M, van GOLDE L, VAANDRAGER A (2003) Inhibition of phosphatidylcholine synthesis induces expression of the endoplasmic reticulum stress and apoptosis-related protein CCAAT/enhancer-binding protein-homologous protein (CHOP/GADD153). Biochem J 369: 643-650.
166. Sriburi R, Jackowski S, Mori K, Brewer JW (2004) XBP1 a link between the unfolded protein response, lipid biosynthesis, and biogenesis of the endoplasmic reticulum. The Journal of cell biology 167: 35-41.
167. Szegezdi E, Logue SE, Gorman AM, Samali A (2006) Mediators of endoplasmic reticulum stress-induced apoptosis. EMBO reports 7: 880-885.
168. Bertolotti A, Zhang Y, Hendershot LM, Harding HP, Ron D (2000) Dynamic interaction of BiP and ER stress transducers in the unfolded-protein response. Nature cell biology 2: 326-332.
169. Krishnan N, Fu C, Pappin DJ, Tonks NK (2011) H2S-Induced sulfhydration of the phosphatase PTP1B and its role in the endoplasmic reticulum stress response. Science signaling 4: ra86.
170. Shi Y, Vattem KM, Sood R, An J, Liang J, et al. (1998) Identification and characterization of pancreatic eukaryotic initiation factor 2 α-subunit kinase, PEK, involved in translational control. Molecular and cellular biology 18: 7499-7509.
171. De Haro C, Mendez R, Santoyo J (1996) The eIF-2alpha kinases and the control of protein synthesis. The FASEB Journal 10: 1378-1387.
172. Kimball SR (1999) Eukaryotic initiation factor eIF2. The international journal of biochemistry & cell biology 31: 25-29.
173. Harding HP, Novoa I, Zhang Y, Zeng H, Wek R, et al. (2000) Regulated translation initiation controls stress-induced gene expression in mammalian cells. Molecular cell 6: 1099-1108.
174. Acharya P, Chen J-J, Correia MA (2010) Hepatic heme-regulated inhibitor (HRI) eukaryotic initiation factor 2α kinase: A protagonist of heme-mediated translational control of CYP2B enzymes and a modulator of basal endoplasmic reticulum stress tone. Molecular pharmacology 77: 575-592.

175. McEwen E, Kedersha N, Song B, Scheuner D, Gilks N, et al. (2005) Heme-regulated inhibitor kinase-mediated phosphorylation of eukaryotic translation initiation factor 2 inhibits translation, induces stress granule formation, and mediates survival upon arsenite exposure. Journal of Biological Chemistry 280: 16925-16933.
176. Sood R, Porter AC, Olsen DA, Cavener DR, Wek RC (2000) A mammalian homologue of GCN2 protein kinase important for translational control by phosphorylation of eukaryotic initiation factor-2α. Genetics 154: 787-801.
177. CLEMENS MJ, ELIA A (1997) The double-stranded RNA-dependent protein kinase PKR: structure and function. Journal of interferon & cytokine research 17: 503-524.
178. Sadler A, Williams B (2007) Structure and function of the protein kinase R. Interferon: The 50th Anniversary: Springer. pp. 253-292.
179. Dever TE, Feng L, Wek RC, Cigan AM, Donahue TF, et al. (1992) Phosphorylation of initiation factor 2α by protein kinase GCN2 mediates gene-specific translational control of GCN4 in yeast. Cell 68: 585-596.
180. Vattem KM, Wek RC (2004) Reinitiation involving upstream ORFs regulates ATF4 mRNA translation in mammalian cells. Proceedings of the National Academy of Sciences of the United States of America 101: 11269-11274.
181. Ameri K, Harris AL (2008) Activating transcription factor 4. The international journal of biochemistry & cell biology 40: 14-21.
182. Chen H, Pan Y-X, Dudenhausen EE, Kilberg MS (2004) Amino acid deprivation induces the transcription rate of the human asparagine synthetase gene through a timed program of expression and promoter binding of nutrient-responsive basic region/leucine zipper transcription factors as well as localized histone acetylation. Journal of Biological Chemistry 279: 50829-50839.
183. He CH, Gong P, Hu B, Stewart D, Choi ME, et al. (2001) Identification of activating transcription factor 4 (ATF4) as an Nrf2-interacting protein Implication for heme oxygenase-1 gene regulation. Journal of Biological Chemistry 276: 20858-20865.
184. FAWCETT T, MARTINDALE J, GUYTON K, HAI T, HOLBROOK N (1999) Complexes containing activating transcription factor (ATF)/cAMP-responsive-element-binding protein (CREB) interact with the CCAAT/enhancer-binding protein (C/EBP)–ATF composite site to regulate Gadd153 expression during the stress response. Biochem J 339: 135-141.
185. Marciniak SJ, Yun CY, Oyadomari S, Novoa I, Zhang Y, et al. (2004) CHOP induces death by promoting protein synthesis and oxidation in the stressed endoplasmic reticulum. Genes & development 18: 3066.
186. Brush MH, Weiser DC, Shenolikar S (2003) Growth arrest and DNA damage-inducible protein GADD34 targets protein phosphatase 1α to the endoplasmic reticulum and promotes dephosphorylation of the α subunit of eukaryotic translation initiation factor 2. Molecular and cellular biology 23: 1292-1303.
187. Han J, Back SH, Hur J, Lin Y-H, Gildersleeve R, et al. (2013) ER-stress-induced transcriptional regulation increases protein synthesis leading to cell death. Nature cell biology 15: 481-490.
188. Zorzitto J, Galligan CL, Ueng JJ, Fish EN (2006) Characterization of the antiviral effects of interferon-α against a SARS-like coronoavirus infection in vitro. Cell research 16: 220-229.
189. Ye Y, Hauns K, Langland JO, Jacobs BL, Hogue BG (2007) Mouse hepatitis coronavirus A59 nucleocapsid protein is a type I interferon antagonist. Journal of virology 81: 2554-2563.
190. Roth-Cross JK, Martínez-Sobrido L, Scott EP, García-Sastre A, Weiss SR (2007) Inhibition of the alpha/beta interferon response by mouse hepatitis virus at multiple levels. Journal of virology 81: 7189-7199.

191. Bechill J, Chen Z, Brewer JW, Baker SC (2008) Coronavirus infection modulates the unfolded protein response and mediates sustained translational repression. Journal of virology 82: 4492-4501.
192. Krähling V, Stein DA, Spiegel M, Weber F, Mühlberger E (2009) Severe acute respiratory syndrome coronavirus triggers apoptosis via protein kinase R but is resistant to its antiviral activity. Journal of virology 83: 2298-2309.
193. Siu K-L, Chan C-P, Kok K-H, Woo PC, Jin D-Y (2014) Comparative analysis of the activation of unfolded protein response by spike proteins of severe acute respiratory syndrome coronavirus and human coronavirus HKU1. 4: 1-9.
194. Cruz JL, Sola I, Becares M, Alberca B, Plana J, et al. (2011) Coronavirus gene 7 counteracts host defenses and modulates virus virulence. PLoS pathogens 7: e1002090.
195. Wang X, Liao Y, Yap PL, Png KJ, Tam JP, et al. (2009) Inhibition of protein kinase R activation and upregulation of GADD34 expression play a synergistic role in facilitating coronavirus replication by maintaining de novo protein synthesis in virus-infected cells. Journal of virology 83: 12462-12472.
196. Korennykh A, Walter P (2012) Structural basis of the unfolded protein response. Annual review of cell and developmental biology 28: 251-277.
197. Zhou J, Liu CY, Back SH, Clark RL, Peisach D, et al. (2006) The crystal structure of human IRE1 luminal domain reveals a conserved dimerization interface required for activation of the unfolded protein response. Proceedings of the National Academy of Sciences of the United States of America 103: 14343-14348.
198. Liu CY, Schröder M, Kaufman RJ (2000) Ligand-independent dimerization activates the stress response kinases IRE1 and PERK in the lumen of the endoplasmic reticulum. Journal of Biological Chemistry 275: 24881-24885.
199. Credle JJ, Finer-Moore JS, Papa FR, Stroud RM, Walter P (2005) On the mechanism of sensing unfolded protein in the endoplasmic reticulum. Proceedings of the National Academy of Sciences of the United States of America 102: 18773-18784.
200. Pincus D, Chevalier MW, Aragón T, van Anken E, Vidal SE, et al. (2010) BiP binding to the ER-stress sensor Ire1 tunes the homeostatic behavior of the unfolded protein response. PLoS biology 8: e1000415.
201. Sidrauski C, Walter P (1997) The transmembrane kinase Ire1p is a site-specific endonuclease that initiates mRNA splicing in the unfolded protein response. Cell 90: 1031-1039.
202. Yoshida H, Matsui T, Yamamoto A, Okada T, Mori K (2001) XBP1 mRNA is induced by ATF6 and spliced by IRE1 in response to ER stress to produce a highly active transcription factor. Cell 107: 881-891.
203. Hooks KB, Griffiths-Jones S (2011) Conserved RNA structures in the non-canonical Hac1/Xbp1 intron. RNA Biology 8: 552-556.
204. Yamamoto K, Yoshida H, Kokame K, Kaufman RJ, Mori K (2004) Differential contributions of ATF6 and XBP1 to the activation of endoplasmic reticulum stress-responsive cis-acting elements ERSE, UPRE and ERSE-II. Journal of biochemistry 136: 343-350.
205. Glimcher L (2010) XBP1: the last two decades. Annals of the rheumatic diseases 69: i67-i71.
206. Lee AH, Iwakoshi NN, Glimcher LH (2003) XBP-1 regulates a subset of endoplasmic reticulum resident chaperone genes in the unfolded protein response. Molecular and cellular biology 23: 7448-7459.
207. Yamamoto K, Suzuki N, Wada T, Okada T, Yoshida H, et al. (2008) Human HRD1 promoter carries a functional unfolded protein response element to which XBP1 but not ATF6 directly binds. Journal of biochemistry 144: 477-486.

208. Gao B, Lee SM, Chen A, Zhang J, Zhang DD, et al. (2008) Synoviolin promotes IRE1 ubiquitination and degradation in synovial fibroblasts from mice with collagen-induced arthritis. EMBO reports 9: 480-485.
209. Yoshida H, Oku M, Suzuki M, Mori K (2006) pXBP1 (U) encoded in XBP1 pre-mRNA negatively regulates unfolded protein response activator pXBP1 (S) in mammalian ER stress response. The Journal of cell biology 172: 565-575.
210. Tirosh B, Iwakoshi NN, Glimcher LH, Ploegh HL (2006) Rapid turnover of unspliced Xbp-1 as a factor that modulates the unfolded protein response. Journal of Biological Chemistry 281: 5852-5860.
211. Hollien J, Weissman JS (2006) Decay of endoplasmic reticulum-localized mRNAs during the unfolded protein response. Science 313: 104-107.
212. Hollien J, Lin JH, Li H, Stevens N, Walter P, et al. (2009) Regulated Ire1-dependent decay of messenger RNAs in mammalian cells. The Journal of cell biology 186: 323-331.
213. Oikawa D, Tokuda M, Hosoda A, Iwawaki T (2010) Identification of a consensus element recognized and cleaved by IRE1α. Nucleic acids research: gkq452.
214. Han D, Lerner AG, Vande Walle L, Upton J-P, Xu W, et al. (2009) IRE1α kinase activation modes control alternate endoribonuclease outputs to determine divergent cell fates. Cell 138: 562-575.
215. Maurel M, Chevet E, Tavernier J, Gerlo S (2014) Getting RIDD of RNA: IRE1 in cell fate regulation. Trends in biochemical sciences 39: 245-254.
216. Urano F, Wang X, Bertolotti A, Zhang Y, Chung P, et al. (2000) Coupling of stress in the ER to activation of JNK protein kinases by transmembrane protein kinase IRE1. Science 287: 664-666.
217. Nishitoh H, Matsuzawa A, Tobiume K, Saegusa K, Takeda K, et al. (2002) ASK1 is essential for endoplasmic reticulum stress-induced neuronal cell death triggered by expanded polyglutamine repeats. Genes & development 16: 1345-1355.
218. Ogata M, Hino S, Saito A, Morikawa K, Kondo S, et al. (2006) Autophagy is activated for cell survival after endoplasmic reticulum stress. Molecular and cellular biology 26: 9220-9231.
219. Wei Y, Sinha S, Levine B (2008) Dual role of JNK1-mediated phosphorylation of Bcl-2 in autophagy and apoptosis regulation. Autophagy 4: 949-951.
220. Castillo K, Rojas-Rivera D, Lisbona F, Caballero B, Nassif M, et al. (2011) BAX inhibitor-1 regulates autophagy by controlling the IRE1α branch of the unfolded protein response. The EMBO journal 30: 4465-4478.
221. DeDiego ML, Nieto-Torres JL, Jiménez-Guardeño JM, Regla-Nava JA, Álvarez E, et al. (2011) Severe Acute Respiratory Syndrome Coronavirus Envelope Protein Regulates Cell Stress Response and Apoptosis. PLoS pathogens 7: e1002315.
222. Shen J, Chen X, Hendershot L, Prywes R (2002) ER stress regulation of ATF6 localization by dissociation of BiP/GRP78 binding and unmasking of Golgi localization signals. Developmental cell 3: 99-111.
223. Hong M, Luo S, Baumeister P, Huang J-M, Gogia RK, et al. (2004) Underglycosylation of ATF6 as a novel sensing mechanism for activation of the unfolded protein response. Journal of Biological Chemistry 279: 11354-11363.
224. Nadanaka S, Okada T, Yoshida H, Mori K (2007) Role of disulfide bridges formed in the luminal domain of ATF6 in sensing endoplasmic reticulum stress. Molecular and cellular biology 27: 1027-1043.
225. Ye J, Rawson RB, Komuro R, Chen X, Davé UP, et al. (2000) ER stress induces cleavage of membrane-bound ATF6 by the same proteases that process SREBPs. Molecular cell 6: 1355-1364.
226. Yoshida H, Okada T, Haze K, Yanagi H, Yura T, et al. (2001) Endoplasmic reticulum stress-induced formation of transcription factor complex ERSF including NF-Y (CBF) and activating transcription

factors 6α and 6β that activates the mammalian unfolded protein response. Molecular and cellular biology 21: 1239-1248.
227. Adachi Y, Yamamoto K, Okada T, Yoshida H, Harada A, et al. (2008) ATF6 is a transcription factor specializing in the regulation of quality control proteins in the endoplasmic reticulum. Cell structure and function 33: 75-89.
228. Guan Y, Zheng B, He Y, Liu X, Zhuang Z, et al. (2003) Isolation and characterization of viruses related to the SARS coronavirus from animals in southern China. Science 302: 276-278.
229. Sano R, Reed JC (2013) ER stress-induced cell death mechanisms. Biochimica et Biophysica Acta (BBA)-Molecular Cell Research 1833: 3460-3470.
230. Mizutani T, Fukushi S, Saijo M, Kurane I, Morikawa S (2004) Phosphorylation of p38 MAPK and its downstream targets in SARS coronavirus-infected cells. Biochemical and biophysical research communications 319: 1228-1234.
231. An S, Chen CJ, Yu X, Leibowitz JL, Makino S (1999) Induction of apoptosis in murine coronavirus-infected cultured cells and demonstration of E protein as an apoptosis inducer. Journal of virology 73: 7853-7859.
232. Chau TN, Lee KC, Yao H, Tsang TY, Chow TC, et al. (2004) SARS-associated viral hepatitis caused by a novel coronavirus: Report of three cases. Hepatology 39: 302-310.
233. Haagmans BL, Egberink HF, Horzinek MC (1996) Apoptosis and T-cell depletion during feline infectious peritonitis. Journal of virology 70: 8977-8983.
234. Liu C, Xu HY, Liu DX (2001) Induction of caspase-dependent apoptosis in cultured cells by the avian coronavirus infectious bronchitis virus. Journal of virology 75: 6402-6409.
235. Li FQ, Tam JP, Liu DX (2007) Cell cycle arrest and apoptosis induced by the coronavirus infectious bronchitis virus in the absence of p53. Virology 365: 435-445.
236. Zhong Y, Liao Y, Fang S, Tam JP, Liu DX (2012) Up-regulation of mcl-1 and bak by coronavirus infection of human, avian and animal cells modulates apoptosis and viral replication. PloS one 7: e30191.
237. McCullough KD, Martindale JL, Klotz L-O, Aw T-Y, Holbrook NJ (2001) Gadd153 sensitizes cells to endoplasmic reticulum stress by down-regulating Bcl2 and perturbing the cellular redox state. Molecular and cellular biology 21: 1249-1259.
238. Puthalakath H, O'Reilly LA, Gunn P, Lee L, Kelly PN, et al. (2007) ER stress triggers apoptosis by activating BH3-only protein Bim. Cell 129: 1337-1349.
239. Yamaguchi H, Wang H-G (2004) CHOP is involved in endoplasmic reticulum stress-induced apoptosis by enhancing DR5 expression in human carcinoma cells. Journal of Biological Chemistry 279: 45495-45502.
240. Gotoh T, Oyadomari S, Mori K, Mori M (2002) Nitric oxide-induced apoptosis in RAW 264.7 macrophages is mediated by endoplasmic reticulum stress pathway involving ATF6 and CHOP. Journal of Biological Chemistry 277: 12343-12350.
241. Nakanishi K, Sudo T, Morishima N (2005) Endoplasmic reticulum stress signaling transmitted by ATF6 mediates apoptosis during muscle development. The Journal of cell biology 169: 555-560.
242. Morishima N, Nakanishi K, Nakano A (2011) Activating transcription factor-6 (ATF6) mediates apoptosis with reduction of myeloid cell leukemia sequence 1 (Mcl-1) protein via induction of WW domain binding protein 1. Journal of Biological Chemistry 286: 35227-35235.
243. Nakagawa T, Zhu H, Morishima N, Li E, Xu J, et al. (2000) Caspase-12 mediates endoplasmic-reticulum-specific apoptosis and cytotoxicity by amyloid-β. Nature 403: 98-103.
244. Hitomi J, Katayama T, Eguchi Y, Kudo T, Taniguchi M, et al. (2004) Involvement of caspase-4 in endoplasmic reticulum stress-induced apoptosis and Aβ-induced cell death. The Journal of cell biology 165: 347-356.

245. Perlman S, Dandekar AA (2005) Immunopathogenesis of coronavirus infections: implications for SARS. Nature reviews Immunology 5: 917-927.
246. Huang KJ, Su IJ, Theron M, Wu YC, Lai SK, et al. (2005) An interferon-γ-related cytokine storm in SARS patients. Journal of medical virology 75: 185-194.
247. Jiang Y, Xu J, Zhou C, Wu Z, Zhong S, et al. (2005) Characterization of cytokine/chemokine profiles of severe acute respiratory syndrome. American journal of respiratory and critical care medicine 171: 850-857.
248. Smith JA (2014) A new paradigm: innate immune sensing of viruses via the unfolded protein response. Frontiers in Microbiology 5.
249. Hayden MS, Ghosh S (2012) NF-κB, the first quarter-century: remarkable progress and outstanding questions. Genes & development 26: 203-234.
250. Libermann TA, Baltimore D (1990) Activation of interleukin-6 gene expression through the NF-kappa B transcription factor. Molecular and cellular biology 10: 2327-2334.
251. Kunsch C, Rosen CA (1993) NF-kappa B subunit-specific regulation of the interleukin-8 promoter. Molecular and cellular biology 13: 6137-6146.
252. Wang J, Basagoudanavar SH, Wang X, Hopewell E, Albrecht R, et al. (2010) NF-κB RelA subunit is crucial for early IFN-β expression and resistance to RNA virus replication. The Journal of Immunology 185: 1720-1729.
253. Balachandran S, Beg AA (2011) Defining emerging roles for NF-κB in antivirus responses: revisiting the interferon-β enhanceosome paradigm. PLoS pathogens 7: e1002165.
254. Wang W, Ye L, Ye L, Li B, Gao B, et al. (2007) Up-regulation of IL-6 and TNF-α induced by SARS-coronavirus spike protein in murine macrophages via NF-κB pathway. Virus research 128: 1-8.
255. Dosch SF, Mahajan SD, Collins AR (2009) SARS coronavirus spike protein-induced innate immune response occurs via activation of the NF-κB pathway in human monocyte macrophages in vitro. Virus research 142: 19-27.
256. Karin M, Ben-Neriah Y (2000) Phosphorylation meets ubiquitination: the control of NF-κB activity. Annual review of immunology 18: 621-663.
257. Kanarek N, London N, Schueler-Furman O, Ben-Neriah Y (2010) Ubiquitination and Degradation of the Inhibitors of NF-κB. Cold Spring Harbor perspectives in biology 2: a000166.
258. Jiang H-Y, Wek SA, McGrath BC, Scheuner D, Kaufman RJ, et al. (2003) Phosphorylation of the α subunit of eukaryotic initiation factor 2 is required for activation of NF-κB in response to diverse cellular stresses. Molecular and cellular biology 23: 5651-5663.
259. Tam AB, Mercado EL, Hoffmann A, Niwa M (2012) ER stress activates NF-κB by integrating functions of basal IKK activity, IRE1 and PERK. PloS one 7: e45078.
260. Park S-H, Choi HJ, Yang H, Do KH, Kim J, et al. (2010) Endoplasmic reticulum stress-activated C/EBP homologous protein enhances nuclear factor-κB signals via repression of peroxisome proliferator-activated receptor γ. Journal of Biological Chemistry 285: 35330-35339.
261. Yamazaki H, Hiramatsu N, Hayakawa K, Tagawa Y, Okamura M, et al. (2009) Activation of the Akt-NF-κB pathway by subtilase cytotoxin through the ATF6 branch of the unfolded protein response. The Journal of Immunology 183: 1480-1487.
262. Banerjee S, Narayanan K, Mizutani T, Makino S (2002) Murine coronavirus replication-induced p38 mitogen-activated protein kinase activation promotes interleukin-6 production and virus replication in cultured cells. Journal of virology 76: 5937-5948.
263. Liao Y, Wang X, Huang M, Tam JP, Liu DX (2011) Regulation of the p38 mitogen-activated protein kinase and dual-specificity phosphatase 1 feedback loop modulates the induction of interleukin 6 and 8 in cells infected with coronavirus infectious bronchitis virus. Virology 420: 106-116.

264. Boutros T, Nantel A, Emadali A, Tzimas G, Conzen S, et al. (2008) The MAP Kinase Phosphatase-1 MKP-1/DUSP1 Is a Regulator of Human Liver Response to Transplantation. American Journal of Transplantation 8: 2558-2568.
265. Li B, Yi P, Zhang B, Xu C, Liu Q, et al. (2011) Differences in endoplasmic reticulum stress signalling kinetics determine cell survival outcome through activation of MKP-1. Cellular signalling 23: 35-45.
266. Gora S, Maouche S, Atout R, Wanherdrick K, Lambeau G, et al. (2010) Phospholipolyzed LDL induces an inflammatory response in endothelial cells through endoplasmic reticulum stress signaling. The FASEB Journal 24: 3284-3297.
267. Blohmke CJ, Mayer ML, Tang AC, Hirschfeld AF, Fjell CD, et al. (2012) Atypical activation of the unfolded protein response in cystic fibrosis airway cells contributes to p38 MAPK-mediated innate immune responses. The Journal of Immunology 189: 5467-5475.
268. Clavarino G, Cláudio N, Dalet A, Terawaki S, Couderc T, et al. (2012) Protein phosphatase 1 subunit Ppp1r15a/GADD34 regulates cytokine production in polyinosinic: polycytidylic acid-stimulated dendritic cells. Proceedings of the National Academy of Sciences 109: 3006-3011.
269. Clavarino G, Cláudio N, Couderc T, Dalet A, Judith D, et al. (2012) Induction of GADD34 Is necessary for dsRNA-dependent interferon-β production and participates in the control of chikungunya virus infection. PLoS pathogens 8: e1002708.
270. Gu M, Ouyang C, Lin W, Zhang T, Cao X, et al. (2014) Phosphatase Holoenzyme PP1/GADD34 Negatively Regulates TLR Response by Inhibiting TAK1 Serine 412 Phosphorylation. The Journal of Immunology 192: 2846-2856.
271. Martinon F, Chen X, Lee A-H, Glimcher LH (2010) TLR activation of the transcription factor XBP1 regulates innate immune responses in macrophages. Nature immunology 11: 411-418.
272. Hu F, Yu X, Wang H, Zuo D, Guo C, et al. (2011) ER stress and its regulator X-box-binding protein-1 enhance polyIC-induced innate immune response in dendritic cells. European journal of immunology 41: 1086-1097.
273. Zeng L, Liu Y-P, Sha H, Chen H, Qi L, et al. (2010) XBP-1 couples endoplasmic reticulum stress to augmented IFN-β induction via a cis-acting enhancer in macrophages. The Journal of Immunology 185: 2324-2330.
274. Cho JA, Lee A-H, Platzer B, Cross B, Gardner BM, et al. (2013) The unfolded protein response element IRE1α senses bacterial proteins invading the ER to activate RIG-I and innate immune signaling. Cell host & microbe 13: 558-569.
275. Keshet Y, Seger R (2010) The MAP kinase signaling cascades: a system of hundreds of components regulates a diverse array of physiological functions. MAP Kinase Signaling Protocols: Springer. pp. 3-38.
276. Kyriakis JM, Avruch J (2001) Mammalian mitogen-activated protein kinase signal transduction pathways activated by stress and inflammation. Physiological reviews 81: 807-869.
277. Nishimoto S, Nishida E (2006) MAPK signalling: ERK5 versus ERK1/2. EMBO reports 7: 782-786.
278. Natoli G, Costanzo A, Ianni A, Templeton DJ, Woodgett JR, et al. (1997) Activation of SAPK/JNK by TNF receptor 1 through a noncytotoxic TRAF2-dependent pathway. Science 275: 200-203.
279. Ninomiya-Tsuji J, Kishimoto K, Hiyama A, Inoue J-i, Cao Z, et al. (1999) The kinase TAK1 can activate the NIK-IκB as well as the MAP kinase cascade in the IL-1 signalling pathway. Nature 398: 252-256.
280. Atfi A, Djelloul S, Chastre E, Davis R, Gespach C (1997) Evidence for a role of Rho-like GTPases and stress-activated protein kinase/c-Jun N-terminal kinase (SAPK/JNK) in transforming growth factor β-mediated signaling. Journal of Biological Chemistry 272: 1429-1432.
281. Davis RJ (2000) Signal transduction by the JNK group of MAP kinases. Inflammatory Processes: Molecular Mechanisms and Therapeutic Opportunities 21: 13.

282. Johnson GL, Nakamura K (2007) The c-jun kinase/stress-activated pathway: regulation, function and role in human disease. Biochimica et Biophysica Acta (BBA)-Molecular Cell Research 1773: 1341-1348.
283. Constant SL, Dong C, Yang DD, Wysk M, Davis RJ, et al. (2000) JNK1 is required for T cell-mediated immunity against Leishmania major infection. The Journal of Immunology 165: 2671-2676.
284. Smeal T, Binetruy B, Mercola DA, Birrer M, Karin M (1991) Oncogenic and transcriptional cooperation with Ha-Ras requires phosphorylation of c-Jun on serines 63 and 73.
285. Gupta S, Campbell D, Derijard B, Davis RJ (1995) Transcription factor ATF2 regulation by the JNK signal transduction pathway. Science 267: 389-393.
286. Cavigelli M, Dolfi F, Claret F-X, Karin M (1995) Induction of c-fos expression through JNK-mediated TCF/Elk-1 phosphorylation. The EMBO journal 14: 5957.
287. Fuchs SY, Adler V, Pincus MR, Ronai Ze (1998) MEKK1/JNK signaling stabilizes and activates p53. Proceedings of the National Academy of Sciences 95: 10541-10546.
288. Park J, Liu AY (2001) JNK phosphorylates the HSF1 transcriptional activation domain: role of JNK in the regulation of the heat shock response. Journal of cellular biochemistry 82: 326-338.
289. Hess J, Angel P, Schorpp-Kistner M (2004) AP-1 subunits: quarrel and harmony among siblings. Journal of cell science 117: 5965-5973.
290. Jeffrey KL, Camps M, Rommel C, Mackay CR (2007) Targeting dual-specificity phosphatases: manipulating MAP kinase signalling and immune responses. Nature Reviews Drug Discovery 6: 391-403.
291. Mizutani T, Fukushi S, Murakami M, Hirano T, Saijo M, et al. (2004) Tyrosine dephosphorylation of STAT3 in SARS coronavirus-infected Vero E6 cells. FEBS letters 577: 187-192.
292. Varshney B, Lal SK (2011) SARS-CoV accessory protein 3b induces AP-1 transcriptional activity through activation of JNK and ERK pathways. Biochemistry 50: 5419-5425.
293. Kanzawa N, Nishigaki K, Hayashi T, Ishii Y, Furukawa S, et al. (2006) Augmentation of chemokine production by severe acute respiratory syndrome coronavirus 3a/X1 and 7a/X4 proteins through NF-κB activation. FEBS letters 580: 6807-6812.
294. Mizutani T, Fukushi S, Saijo M, Kurane I, Morikawa S (2005) JNK and PI3k/Akt signaling pathways are required for establishing persistent SARS-CoV infection in Vero E6 cells. Biochimica et Biophysica Acta (BBA)-Molecular Basis of Disease 1741: 4-10.
295. Mizutani T, Fukushi S, Ishii K, Sasaki Y, Kenri T, et al. (2006) Mechanisms of establishment of persistent SARS-CoV-infected cells. Biochemical and biophysical research communications 347: 261-265.
296. Liu M, Yang Y, Gu C, Yue Y, Wu KK, et al. (2007) Spike protein of SARS-CoV stimulates cyclooxygenase-2 expression via both calcium-dependent and calcium-independent protein kinase C pathways. The FASEB Journal 21: 1586-1596.
297. Dhanasekaran DN, Reddy EP (2008) JNK signaling in apoptosis. Oncogene 27: 6245-6251.
298. Tournier C, Hess P, Yang DD, Xu J, Turner TK, et al. (2000) Requirement of JNK for stress-induced activation of the cytochrome c-mediated death pathway. Science 288: 870-874.
299. Behrens A, Sibilia M, Wagner EF (1999) Amino-terminal phosphorylation of c-Jun regulates stress-induced apoptosis and cellular proliferation. Nature genetics 21: 326-329.
300. Uehara T, Bennett B, Sakata ST, Satoh Y, Bilter GK, et al. (2005) JNK mediates hepatic ischemia reperfusion injury. Journal of hepatology 42: 850-859.
301. Ferrandi C, Ballerio R, Gaillard P, Giachetti C, Carboni S, et al. (2004) Inhibition of c-Jun N-terminal kinase decreases cardiomyocyte apoptosis and infarct size after myocardial ischemia and reperfusion in anaesthetized rats. British journal of pharmacology 142: 953-960.
302. Fan M, Chambers TC (2001) Role of mitogen-activated protein kinases in the response of tumor cells to chemotherapy. Drug Resistance Updates 4: 253-267.

303. Björkblom B, Vainio JC, Hongisto V, Herdegen T, Courtney MJ, et al. (2008) All JNKs can kill, but nuclear localization is critical for neuronal death. Journal of Biological Chemistry 283: 19704-19713.
304. Kolomeichuk SN, Terrano DT, Lyle CS, Sabapathy K, Chambers TC (2008) Distinct signaling pathways of microtubule inhibitors–vinblastine and Taxol induce JNK-dependent cell death but through AP-1-dependent and AP-1-independent mechanisms, respectively. FEBS journal 275: 1889-1899.
305. Oleinik N, Krupenko N, Krupenko S (2007) Cooperation between JNK1 and JNK2 in activation of p53 apoptotic pathway. Oncogene 26: 7222-7230.
306. Jones E, Dickman M, Whitmarsh A (2007) Regulation of p73-mediated apoptosis by c-Jun N-terminal kinase. Biochem J 405: 617-623.
307. Kharbanda S, Saxena S, Yoshida K, Pandey P, Kaneki M, et al. (2000) Translocation of SAPK/JNK to mitochondria and interaction with Bcl-xL in response to DNA damage. Journal of Biological Chemistry 275: 322-327.
308. Deng Y, Ren X, Yang L, Lin Y, Wu X (2003) A JNK-dependent pathway is required for TNFα-induced apoptosis. Cell 115: 61-70.
309. Lei K, Davis RJ (2003) JNK phosphorylation of Bim-related members of the Bcl2 family induces Bax-dependent apoptosis. Proceedings of the National Academy of Sciences 100: 2432-2437.
310. Donovan N, Becker EB, Konishi Y, Bonni A (2002) JNK phosphorylation and activation of BAD couples the stress-activated signaling pathway to the cell death machinery. Journal of Biological Chemistry 277: 40944-40949.
311. Tsuruta F, Sunayama J, Mori Y, Hattori S, Shimizu S, et al. (2004) JNK promotes Bax translocation to mitochondria through phosphorylation of 14-3-3 proteins. The EMBO journal 23: 1889-1899.
312. Sunayama J, Tsuruta F, Masuyama N, Gotoh Y (2005) JNK antagonizes Akt-mediated survival signals by phosphorylating 14-3-3. The Journal of cell biology 170: 295-304.
313. Yamamoto K, Ichijo H, Korsmeyer SJ (1999) BCL-2 is phosphorylated and inactivated by an ASK1/Jun N-terminal protein kinase pathway normally activated at G2/M. Molecular and cellular biology 19: 8469-8478.
314. Verma G, Datta M (2012) The critical role of JNK in the ER-mitochondrial crosstalk during apoptotic cell death. Journal of cellular physiology 227: 1791-1795.
315. Verma G, Bhatia H, Datta M (2013) JNK1/2 regulates ER–mitochondrial Ca2+ cross-talk during IL-1β–mediated cell death in RINm5F and human primary β-cells. Molecular biology of the cell 24: 2058-2071.
316. Verma G, Datta M (2010) IL-1β induces ER stress in a JNK dependent manner that determines cell death in human pancreatic epithelial MIA PaCa-2 cells. Apoptosis 15: 864-876.
317. Arthur JSC, Ley SC (2013) Mitogen-activated protein kinases in innate immunity. Nature reviews immunology 13: 679-692.
318. Kawai T, Akira S (2006) TLR signaling. Cell Death & Differentiation 13: 816-825.
319. Shim J-H, Xiao C, Paschal AE, Bailey ST, Rao P, et al. (2005) TAK1, but not TAB1 or TAB2, plays an essential role in multiple signaling pathways in vivo. Genes & development 19: 2668-2681.
320. Sato S, Sanjo H, Takeda K, Ninomiya-Tsuji J, Yamamoto M, et al. (2005) Essential function for the kinase TAK1 in innate and adaptive immune responses. Nature immunology 6: 1087-1095.
321. Wang C, Deng L, Hong M, Akkaraju GR, Inoue J-i, et al. (2001) TAK1 is a ubiquitin-dependent kinase of MKK and IKK. Nature 412: 346-351.
322. Fitzgerald KA, McWhirter SM, Faia KL, Rowe DC, Latz E, et al. (2003) IKKε and TBK1 are essential components of the IRF3 signaling pathway. Nature immunology 4: 491-496.
323. Meylan E, Burns K, Hofmann K, Blancheteau V, Martinon F, et al. (2004) RIP1 is an essential mediator of Toll-like receptor 3–induced NF-κB activation. Nature immunology 5: 503-507.

324. Panne D, Maniatis T, Harrison SC (2007) An atomic model of the interferon-β enhanceosome. Cell 129: 1111-1123.
325. Karin M (1995) The regulation of AP-1 activity by mitogen-activated protein kinases. Journal of Biological Chemistry 270: 16483-16486.
326. Chang Y-J, Liu CY-Y, Chiang B-L, Chao Y-C, Chen C-C (2004) Induction of IL-8 release in lung cells via activator protein-1 by recombinant baculovirus displaying severe acute respiratory syndrome-coronavirus spike proteins: identification of two functional regions. The Journal of Immunology 173: 7602-7614.
327. Yu D, Zhu H, Liu Y, Cao J, Zhang X (2009) Regulation of proinflammatory cytokine expression in primary mouse astrocytes by coronavirus infection. Journal of virology 83: 12204-12214.
328. Li FQ, Xiao H, Tam JP, Liu DX (2005) Sumoylation of the nucleocapsid protein of severe acute respiratory syndrome coronavirus. FEBS letters 579: 2387-2396.
329. Ng LF, Liu DX (1998) Identification of a 24-kDa polypeptide processed from the coronavirus infectious bronchitis virus 1a polyprotein by the 3C-like proteinase and determination of its cleavage sites. Virology 243: 388-395.
330. Xiao H, Xu LH, Yamada Y, Liu DX (2008) Coronavirus spike protein inhibits host cell translation by interaction with eIF3f. PLoS One 3: e1494.
331. Kimura S, Noda T, Yoshimori T (2007) Dissection of the autophagosome maturation process by a novel reporter protein, tandem fluorescent-tagged LC3. Autophagy 3: 452-460.
332. Lei K, Nimnual A, Zong W-X, Kennedy NJ, Flavell RA, et al. (2002) The Bax subfamily of Bcl2-related proteins is essential for apoptotic signal transduction by c-Jun NH2-terminal kinase. Molecular and cellular biology 22: 4929-4942.
333. Jacquin M, Chiche J, Zunino B, Bénéteau M, Meynet O, et al. (2013) GAPDH binds to active Akt, leading to Bcl-xL increase and escape from caspase-independent cell death. Cell Death & Differentiation 20: 1043-1054.
334. Murayama T, Ohara Y, Obuchi M, Khabar K, Higashi H, et al. (1997) Human cytomegalovirus induces interleukin-8 production by a human monocytic cell line, THP-1, through acting concurrently on AP-1-and NF-kappaB-binding sites of the interleukin-8 gene. Journal of virology 71: 5692-5695.
335. Laemmli UK (1970) Cleavage of structural proteins during the assembly of the head of bacteriophage T4. Nature 227: 680-685.
336. Meir O, Dvash E, Werman A, Rubinstein M (2010) C/EBP-β regulates endoplasmic reticulum stress–triggered cell death in mouse and human models. PloS one 5: e9516.
337. Calfon M, Zeng H, Urano F, Till JH, Hubbard SR, et al. (2002) IRE1 couples endoplasmic reticulum load to secretory capacity by processing the XBP-1 mRNA. Nature 415: 92-96.
338. HIROTA M, KITAGAKI M, ITAGAKI H, AIBA S (2006) Quantitative measurement of spliced XBP1 mRNA as an indicator of endoplasmic reticulum stress. The Journal of toxicological sciences 31: 149-156.
339. Volkmann K, Lucas JL, Vuga D, Wang X, Brumm D, et al. (2011) Potent and selective inhibitors of the inositol-requiring enzyme 1 endoribonuclease. Journal of Biological Chemistry 286: 12743-12755.
340. Yoneda T, Imaizumi K, Oono K, Yui D, Gomi F, et al. (2001) Activation of caspase-12, an endoplastic reticulum (ER) resident caspase, through tumor necrosis factor receptor-associated factor 2-dependent mechanism in response to the ER stress. The Journal of biological chemistry 276: 13935-13940.
341. Hitomi J, Katayama T, Taniguchi M, Honda A, Imaizumi K, et al. (2004) Apoptosis induced by endoplasmic reticulum stress depends on activation of caspase-3 via caspase-12. Neuroscience letters 357: 127-130.

342. Eléouët JF, Slee EA, Saurini F, Castagné N, Poncet D, et al. (2000) The viral nucleocapsid protein of transmissible gastroenteritis coronavirus (TGEV) is cleaved by caspase-6 and-7 during TGEV-induced apoptosis. Journal of virology 74: 3975-3983.
343. Yu CY, Hsu YW, Liao CL, Lin YL (2006) Flavivirus infection activates the XBP1 pathway of the unfolded protein response to cope with endoplasmic reticulum stress. Journal of virology 80: 11868-11880.
344. Kato H, Nakajima S, Saito Y, Takahashi S, Katoh R, et al. (2011) mTORC1 serves ER stress-triggered apoptosis via selective activation of the IRE1–JNK pathway. Cell Death & Differentiation 19: 310-320.
345. Ohoka N, Hattori T, Kitagawa M, Onozaki K, Hayashi H (2007) Critical and functional regulation of CHOP (C/EBP homologous protein) through the N-terminal portion. Journal of biological chemistry 282: 35687-35694.
346. Wang X, Ron D (1996) Stress-induced phosphorylation and activation of the transcription factor CHOP (GADD153) by p38 MAP kinase. Science 272: 1347-1349.
347. Lu T-H, Tseng T-J, Su C-C, Tang F-C, Yen C-C, et al. (2014) Arsenic induces reactive oxygen species-caused neuronal cell apoptosis through JNK/ERK-mediated mitochondria-dependent and GRP 78/CHOP-regulated pathways. Toxicology letters 224: 130-140.
348. Xia Z, Dickens M, Raingeaud J, Davis RJ, Greenberg ME (1995) Opposing effects of ERK and JNK-p38 MAP kinases on apoptosis. Science 270: 1326-1331.
349. Lu M, Lawrence DA, Marsters S, Acosta-Alvear D, Kimmig P, et al. (2014) Opposing unfolded-protein-response signals converge on death receptor 5 to control apoptosis. Science 345: 98-101.
350. Steiger-Barraissoul S, Rami A (2009) Serum deprivation induced autophagy and predominantly an AIF-dependent apoptosis in hippocampal HT22 neurons. Apoptosis 14: 1274-1288.
351. Hassan IH, Zhang MS, Powers LS, Shao JQ, Baltrusaitis J, et al. (2011) Influenza A viral replication is blocked by inhibition of the inositol requiring enzyme 1 (IRE1) stress pathway. The Journal of biological chemistry 287: 4679-4689.
352. Hassan I, Gaines KS, Hottel WJ, Wishy RM, Miller SE, et al. (2014) Inositol-requiring Enzyme 1 Inhibits Respiratory Syncytial Virus Replication. Journal of Biological Chemistry 289: 7537-7546.
353. Lee TG, Tang N, Thompson S, Miller J, Katze MG (1994) The 58,000-dalton cellular inhibitor of the interferon-induced double-stranded RNA-activated protein kinase (PKR) is a member of the tetratricopeptide repeat family of proteins. Molecular and cellular biology 14: 2331-2342.
354. Yan W, Frank CL, Korth MJ, Sopher BL, Novoa I, et al. (2002) Control of PERK eIF2α kinase activity by the endoplasmic reticulum stress-induced molecular chaperone P58IPK. Proceedings of the National Academy of Sciences 99: 15920-15925.
355. Polyak SJ, Tang N, Wambach M, Barber GN, Katze MG (1996) The P58 cellular inhibitor complexes with the interferon-induced, double-stranded RNA-dependent protein kinase, PKR, to regulate its autophosphorylation and activity. Journal of Biological Chemistry 271: 1702-1707.
356. van Huizen R, Martindale JL, Gorospe M, Holbrook NJ (2003) P58IPK, a novel endoplasmic reticulum stress-inducible protein and potential negative regulator of eIF2α signaling. Journal of biological chemistry 278: 15558-15564.
357. Melville MW, Tan S-L, Wambach M, Song J, Morimoto RI, et al. (1999) The cellular inhibitor of the PKR protein kinase, P58IPK, is an influenza virus-activated co-chaperone that modulates heat shock protein 70 activity. Journal of biological chemistry 274: 3797-3803.
358. Hu P, Han Z, Couvillon AD, Exton JH (2004) Critical role of endogenous Akt/IAPs and MEK1/ERK pathways in counteracting endoplasmic reticulum stress-induced cell death. Journal of Biological Chemistry 279: 49420-49429.

359. Bromati CR, Lellis-Santos C, Yamanaka TS, Nogueira TC, Leonelli M, et al. (2011) UPR induces transient burst of apoptosis in islets of early lactating rats through reduced AKT phosphorylation via ATF4/CHOP stimulation of TRB3 expression. American Journal of Physiology-Regulatory, Integrative and Comparative Physiology 300: R92-R100.
360. Ke PY, Chen SS (2011) Activation of the unfolded protein response and autophagy after hepatitis C virus infection suppresses innate antiviral immunity in vitro. The Journal of clinical investigation 121: 37-56.
361. Heaton NS, Randall G (2011) Dengue virus and autophagy. Viruses 3: 1332-1341.
362. Levine B, Mizushima N, Virgin HW (2011) Autophagy in immunity and inflammation. Nature 469: 323-335.
363. Mizutani T, Fukushi S, Saijo M, Kurane I, Morikawa S (2004) Importance of Akt signaling pathway for apoptosis in SARS-CoV-infected Vero E6 cells. Virology 327: 169-174.
364. Bennett BL, Sasaki DT, Murray BW, O'Leary EC, Sakata ST, et al. (2001) SP600125, an anthrapyrazolone inhibitor of Jun N-terminal kinase. Proceedings of the National Academy of Sciences of the United States of America 98: 13681-13686.
365. Camps M, Nichols A, Arkinstall S (2000) Dual specificity phosphatases: a gene family for control of MAP kinase function. The FASEB Journal 14: 6-16.
366. Pereira AC, Soares-Martins JA, Leite FG, Da Cruz AF, Torres AA, et al. (2012) SP600125 inhibits Orthopoxviruses replication in a JNK1/2-independent manner: Implication as a potential antipoxviral. Antiviral research 93: 69-77.
367. Marozin S, Altomonte J, Apfel S, Dinh PX, De Toni EN, et al. (2012) Posttranslational Modification of Vesicular Stomatitis Virus Glycoprotein, but Not JNK Inhibition, Is the Antiviral Mechanism of SP600125. Journal of virology 86: 4844-4855.
368. Kim S, Ishida H, Yamane D, Yi M, Swinney DC, et al. (2013) Contrasting roles of mitogen-activated protein kinases in cellular entry and replication of hepatitis C virus: MKNK1 facilitates cell entry. Journal of virology 87: 4214-4224.
369. Regan AD, Cohen RD, Whittaker GR (2009) Activation of p38 MAPK by feline infectious peritonitis virus regulates pro-inflammatory cytokine production in primary blood-derived feline mononuclear cells. Virology 384: 135-143.
370. Varshney B, Agnihotram S, Tan Y-J, Baric R, Lal SK (2012) SARS coronavirus 3b accessory protein modulates transcriptional activity of RUNX1b. PloS one 7: e29542.
371. Xu Gl, Chen J, Yang F, Li Gq, Zheng Lx, et al. (2014) C5a/C5aR pathway is essential for the pathogenesis of murine viral fulminant hepatitis by way of potentiating Fgl2/fibroleukin expression. Hepatology.